

Noise Generation by Airfoils and Rotors with Porous and Serrated Trailing Edges

Author:

Jiang, Chaoyang

Publication Date:

2020

DOI:

<https://doi.org/10.26190/unsworks/2025>

License:

<https://creativecommons.org/licenses/by/4.0/>

Link to license to see what you are allowed to do with this resource.

Downloaded from <http://hdl.handle.net/1959.4/100115> in <https://unsworks.unsw.edu.au> on 2024-04-18

Noise Generation by Airfoils and Rotors with Porous and Serrated Trailing Edges

Chaoyang Jiang

A thesis presented for the degree of
Doctor of Philosophy



School of Mechanical and Manufacturing Engineering
Faculty of Engineering
University of New South Wales
Australia

July 2020



Thesis/Dissertation Sheet

Surname/Family Name	:	Jiang
Given Name/s	:	Chaoyang
Abbreviation for degree as given in the University calendar	:	PhD
Faculty	:	Engineering
School	:	Mechanical and Manufacturing Engineering
Thesis Title	:	Noise Generation by Airfoils and Rotors with Porous and Serrated Trailing Edges

Abstract

Trailing-edge (TE) noise is an important noise source for airfoil applications that operate near populated areas. This thesis aims to develop novel (porous, serrated, and porous-serrated) geometries for the TE noise control of airfoils/rotors and investigate their noise generation mechanisms.

First, the acoustic absorption of ten additively manufactured porous specimens is characterised to facilitate the design of porous TE geometries. The aeroacoustic performance and near-wake characteristics of eleven novel TE designs are then measured at various velocities in UNSW Anechoic Wind Tunnel. Their noise attenuation performance on laminar-transitional boundary layer TE (LBL-TE) and turbulent boundary layer TE (TBL-TE) noise are evaluated. Fluctuating velocity results indicate that the proposed designs influence LBL-TE noise generation by altering the flow characteristics around the TE. A TBL-TE noise intensity factor is proposed to relate near-wake flow statistics to TBL-TE noise generation, showing good consistency with the measured TBL-TE noise level. A high-frequency-broadband noise increase is observed for all porous TE designs.

Moreover, the aeroacoustic performance of three sets of rotor blades with integrated novel TEs is evaluated at various pitch angles and RPMs on UNSW Rotor rig. Compared with serrated blades, porous blades show better low-frequency noise attenuation. At frequencies where the porous structures have good acoustic absorption, porous blades can effectively control TE noise at all operating conditions, indicating the acoustic absorption may contribute to TE noise attenuation by altering the acoustic scattering efficiency.

In addition, Large-Eddy Simulations (LES) are performed on a porous and a reference airfoil. Flowcs-Williams and Hawkins (FWH) acoustic analogy results of porous airfoil capture the high-frequency excessive noise and agree well with single microphone measurements. Flow simulation results reveal that the TBL-TE noise reduction for porous TE is mainly due to an attenuation of convection velocity and spanwise correlation, and the excessive noise is originated from the interaction of the permeated turbulent flow and pore geometries. Finally, a wind turbine noise prediction model based on a noise scaling function is proposed. It accurately predicts the noise spectra and overall noise levels of a full-scale wind turbine using the aerodynamic and acoustic data of lab-scale airfoil models.

Declaration relating to disposition of project thesis/dissertation.

I hereby grant the University of New South Wales or its agents a non-exclusive licence to archive and to make available (including to members of the public) my thesis or dissertation in whole or part in the University libraries in all forms of media, now or here after known. I acknowledge that I retain all intellectual property rights which subsist in my thesis or dissertation, such as copyright and patent rights, subject to applicable law. I also retain the right to use all or part of my thesis or dissertation in future works (such as articles or books).

I also authorise University Microfilms to use the abstract of my thesis in Dissertation Abstracts International.

The University recognises that there may be exceptional circumstances requiring restrictions on copying or conditions on use. Requests for restriction for a period of up to 2 years must be made in writing. Requests for a longer period of restriction may be considered in exceptional circumstances and require the approval of the Dean of Graduate Research

FOR OFFICE USE ONLY Date of completion of requirements for Award:

ORIGINALITY STATEMENT

I hereby declare that this submission is my own work and to the best of my knowledge it contains no materials previously published or written by another person, or substantial proportions of material which have been accepted for the award of any other degree or diploma at UNSW or any other educational institution, except where due acknowledgement is made in the thesis. Any contribution made to the research by others, with whom I have worked at UNSW or elsewhere, is explicitly acknowledged in the thesis. I also declare that the intellectual content of this thesis is the product of my own work, except to the extent that assistance from others in the project's design and conception or in style, presentation and linguistic expression is acknowledged.

COPYRIGHT STATEMENT

I hereby grant the University of New South Wales or its agents a non-exclusive licence to archive and to make available (including to members of the public) my thesis or dissertation in whole or part in the University libraries in all forms of media, now or here after known. I acknowledge that I retain all intellectual property rights which subsist in my thesis or dissertation, such as copyright and patent rights, subject to applicable law. I also retain the right to use all or part of my thesis or dissertation in future works (such as articles or books).

For any substantial portions of copyright material used in this thesis, written permission for use has been obtained, or the copyright material is removed from the final public version of the thesis.

AUTHENTICITY STATEMENT

I certify that the Library deposit digital copy is a direct equivalent of the final officially approved version of my thesis. No emendation of content has occurred and if there are any minor variations in formatting, they are the result of the conversion to digital format.

UNSW is supportive of candidates publishing their research results during their candidature as detailed in the UNSW Thesis Examination Procedure.

Publications can be used in the candidate's thesis in lieu of a Chapter provided:

- The candidate contributed **greater than 50%** of the content in the publication and are the "primary author", i.e. they were responsible primarily for the planning, execution and preparation of the work for publication.
- The candidate has obtained approval to include the publication in their thesis in lieu of a Chapter from their Supervisor and Postgraduate Coordinator.
- The publication is not subject to any obligations or contractual agreements with a third party that would constrain its inclusion in the thesis.

☒ The candidate has declared that **some of the work described in their thesis has been published and has been documented in the relevant Chapters with acknowledgement.**

A short statement on where this work appears in the thesis and how this work is acknowledged within chapter/s:

The results from paper - "Acoustic absorption of porous materials produced by additive manufacturing with varying geometries" in Proceedings of ACOUSTICS 2017 is contained in Chapter 4 (Section 4.2).

The results from paper - "Experimental Investigation of Novel Porous-serrated Treatments on Airfoil Trailing Edge Noise Reduction" in 25th AIAA/CEAS Aeroacoustics Conference 2019 are contained in Chapter 5 (Section 5.2) and Chapter 6 (Section 6.2)

Acknowledgement of the work of other authors of these papers has been made in my Acknowledgements section.

Candidate's Declaration



I declare that I have complied with the Thesis Examination Procedure.

Abstract

Trailing-edge (TE) noise is an important noise source for airfoil applications that operate near populated areas. This thesis aims to develop novel (porous, serrated, and porous-serrated) geometries for the TE noise control of airfoils/rotors and investigate their noise generation mechanisms.

First, the acoustic absorption of ten additively manufactured porous specimens is characterised to facilitate the design of porous TE geometries. The aeroacoustic performance and near-wake characteristics of eleven novel TE designs are then measured at various velocities in UNSW Anechoic Wind Tunnel. Their noise attenuation performance on laminar-transitional boundary layer TE (LBL-TE) and turbulent boundary layer TE (TBL-TE) noise are evaluated. Fluctuating velocity results indicate that the proposed designs influence LBL-TE noise generation by altering the flow characteristics around the TE. A TBL-TE noise intensity factor is proposed to relate near-wake flow statistics to TBL-TE noise generation, showing good consistency with the measured TBL-TE noise level. A high-frequency-broadband noise increase is observed for all porous TE designs.

Moreover, the aeroacoustic performance of three sets of rotor blades with integrated novel TEs is evaluated at various pitch angles and RPMs on UNSW Rotor rig. Compared with serrated blades, porous blades show better low-frequency noise attenuation. At frequencies where the porous structures have good acoustic absorption, porous blades can effectively control TE noise at all operating conditions, indicating the acoustic absorption may contribute to TE noise attenuation by altering the acoustic scattering efficiency.

In addition, Large-Eddy Simulations (LES) are performed on a porous and a reference airfoil. Ffowcs-Williams and Hawkings (FWH) acoustic analogy results of porous airfoil capture the high-frequency excessive noise and agree well with single microphone measurements. Flow simulation results reveal that the TBL-TE noise reduction for porous TE is mainly due to an attenuation of convection velocity and spanwise correlation, and the excessive noise is originated from the interaction of the permeated turbulent flow and pore geometries.

Finally, a wind turbine noise prediction model based on a noise scaling function is proposed. It accurately predicts the noise spectra and overall noise levels of a full-scale wind turbine using the aerodynamic and acoustic data of lab-scale airfoil models.

Acknowledgements

Thank you to my supervisors, Professor Con Doolan and Dr. Danielle Moreau, for their support, encouragement and insightful discussions during the development of this thesis. I would also like to thank my co-supervisor, Dr. Jeoffrey Fischer, for his help in beamforming techniques and rotor experiments.

Thank you to Professor Weikang Jiang, Dr. Jianzheng Gao, Ryan McKay, Dr. Claudia Echeverria, Dr. Fabien Delhomme and Dr. Andre Almeida for affording me the collaboration opportunity. Also, I gratefully acknowledge Goldwind for providing valuable data.

Finally, thank you to my colleagues in Flow Noise Group, Dr. Charitha de Silva, Dr. Manuj Awasthi, Dr. Yendrew Yauwenas, Omear Saeed, Jiawei Tan, Yuchen Ding, Tingyi Zhang, Ziao Zhang, Sean McCreton, Angus Wills, Dr. Jun Zhang (former visiting scholar) and Ruixian Ma (former visiting student), for their help in experiments and numerical simulations.

My sincerest thanks to all of you.

Contents

Abstract	i
Acknowledgements	ii
List of Figures	xvi
List of Tables	xvii
Nomenclature	xxiv
1 Introduction	1
1.1 Background	1
1.2 Aims and Objectives	5
1.3 Thesis Structure	6
1.4 Publications	7
2 Literature Review	8
2.1 Overview	8
2.2 Airfoil Trailing-Edge Noise	9
2.2.1 Turbulent Boundary Layer Trailing-Edge Noise	9
2.2.2 Laminar-Transitional Boundary Layer Trailing-Edge Noise	13
2.3 Trailing-Edge Treatments for Noise Reduction	14
2.3.1 Effects of Trailing-Edge Sawtooth-Serrations on Turbulent Boundary Layer Trailing-Edge Noise	15
2.3.2 Effects of Porous Trailing-Edge Treatments on Turbulent Boundary Layer Trailing-Edge Noise	18
2.3.3 Effects of Novel Trailing-Edge Treatments on Turbulent Boundary Layer Trailing-Edge Noise	21
2.3.4 Effects of Trailing-Edge Treatments on Laminar-Transitional Boundary Layer Trailing-Edge Noise	23
2.3.5 Rotor Trailing-Edge Treatments	24
2.4 Summary and Research Gaps	24
3 Methodology	28
3.1 Overview	28
3.2 Acoustic Characterisation of the 3D Printed Porous Structures	29
3.2.1 Test Specimens	29
3.2.2 Measurement Setup and Theoretical Background	32
3.2.3 Maa’s Model of Micro-Perforated Panel	34

3.3	Anechoic Wind Tunnel Measurements	36
3.3.1	Facility	36
3.3.2	Test Models and Setup	40
3.3.3	Acoustic Beamforming	51
3.3.4	Hot-wire Anemometry	54
3.3.5	Aerodynamic Force Measurement	55
3.3.6	Aerodynamic Corrections	55
3.4	Rotor Rig Measurements	56
3.4.1	Facility	57
3.4.2	Rotor Blade Models and Test Setup	58
3.4.3	Phase-Averaged Beamforming	62
3.5	Numerical Simulation Methodology	65
3.5.1	Governing Equations	66
3.5.2	Subgrid-Scale Models	67
3.5.3	Computational Grid and Boundary Conditions	69
3.5.4	Grid Convergence Study	70
3.5.5	FWH Analogy	72
3.6	Uncertainty of Statistical Quantities	74
4	Acoustic Characterisation of Porous Structures	77
4.1	Overview	77
4.2	Acoustic Absorption of Micro-Tube Porous Structures	78
4.2.1	Effects of Porosity	78
4.2.2	Effects of Aspect Ratio	79
4.3	Acoustic Absorption of Micro-Perforated Housings with Air Gap and Foam Infill	81
4.4	Summary	84
5	Airfoil Trailing Edge Noise Reduction Using Porous and Serrated Edge Treatments	86
5.1	Overview	86
5.2	Laminar-Transitional Boundary Layer Trailing-Edge Noise	87
5.3	Turbulent Boundary Layer Trailing-Edge Noise	96
5.4	Summary	104
6	Flow Characteristics Around Porous and Serrated Trailing Edges	108
6.1	Overview	108
6.2	Flow Measurements in a Laminar-transitional Flow Regime	110
6.2.1	Mean Velocity Results	110
6.2.2	Fluctuating Velocity Results	114
6.3	Flow Measurements in a Turbulent Flow Regime	119
6.3.1	Mean Velocity Results	119

6.3.2	Fluctuating Velocity Results	121
6.3.3	TBL-TE noise Intensity Factor	127
6.4	Numerical Simulation of an Airfoil with Porous Trailing Edge	130
6.4.1	FWH Acoustic Analogy Results	131
6.4.2	Flow Simulation Results	135
6.5	Summary	156
7	Rotor Noise Reduction using Porous and Serrated Trailing-Edge Treatments	159
7.1	Overview	159
7.2	Beamforming Sound Maps	161
7.3	Noise Spectra Results	166
7.4	The Relationship between Noise Reduction and Sound Absorption Coefficient for the Porous Blade	179
7.5	Summary	180
8	Prediction Model for Wind Turbine Noise	183
8.1	Overview	183
8.2	Aerodynamic Results	184
8.2.1	Boundary Layer Properties	186
8.3	Acoustic Results	188
8.3.1	Beamforming Maps	188
8.3.2	Source Integration Results	188
8.4	Wind Turbine Noise Prediction Method	191
8.4.1	Principle	191
8.4.2	Corrections of Sound Propagation	199
8.4.3	Prediction Procedure	202
8.5	Prediction Results	204
8.5.1	Effects of Sound Propagation Corrections	205
8.5.2	Improvement of Wind Turbine Noise Prediction	206
8.6	Summary	207
9	Conclusions	208
9.1	Thesis Summary	208
9.2	Future Work	213
	References	215

List of Figures

1.1	Schematics of flow conditions that induce the airfoil self-noise: (a) TBL-TE noise; (b) LBL-TE noise; (c) bluntness vortex-shedding TE noise; (d) stall noise; (e) tip vortex-formation noise.	3
1.2	Thesis structure and the summarised contents for each chapter.	6
2.1	Sketch of the geometries of TE sawtooth serrations.	15
3.1	Geometries of the 3D printed micro-tube specimens and reference specimens: (a) schematic of micro-tube structures; photos of specimens with (b) different porosity ϕ , (c) different pore diameter d_0 and (d) different thickness h_0 ; (e) photos of reference specimens (from left to right): SR (3D printed solid resin with $h_0 = 10$ mm), 40PPI, 20PPI and 10PPI (aluminium foam with $\phi = 92\text{--}94\%$).	30
3.2	Geometries of the 3D printed micro-perforated housings: (a) with melamine resin foam (Basotect [®] foam) infill; (b) with an air gap; (c) schematic of the assembled specimen and its dimensions.	30
3.3	Acoustic characterisation setup:(a) measurement setup in-situ;(b) Schematic of impedance tube.	33
3.4	Schematics of (a) micro-perforated resonant absorber (micro-perforated panel with an air gap) and (b) its equivalent circuit.	34
3.5	Schematic of the UNSW Anechoic Wind Tunnel	37
3.6	Background noise measured in UAT at $U_\infty = 20, 30, 40$ and 50 m/s: (a) power spectral density (PSD); (b) overall sound pressure level (OASPL) over 250 to 10000 Hz.	37
3.7	Turbulence intensity measured by hot-wire and Cobra probe along the jet core center-line.	38
3.8	The hot-wire measurement results of the mean velocity profiles across the mid-plane of the contraction outlet at various downstream locations in (a) the y-direction and (b) the z-direction at $U_\infty = 30$ m/s.	39
3.9	The hot-wire measurement results of the turbulence intensity I_{uu} across the mid-plane of the contraction outlet at various downstream locations in (a) the y-direction and (b) the z-direction at 30 m/s.	39
3.10	Colormaps of the mean velocity ($U_\infty = 30$ m/s) measured by Cobra probe on the cross-stream planes at (a) $x/D_H = 0.25$ and (b) 0.5. Boundary of the test-section inlet is marked by the dashed black line.	40

3.11	Colormaps of the turbulence intensity ($U_\infty = 30$ m/s) measured by Cobra probe on the cross-stream planes at (a) $x/D_H = 0.25$ and (b) 0.5. Boundary of the test-section inlet is marked by the dashed black line.	40
3.12	CAD drawings of the airfoil model. (a) Model before assembly; (b) Model after assembly (dimensions included).	41
3.13	Schematics of the acoustic measurement setup for UAT Campaign 1: (a) perspective view; top view for (b) UAT Campaign 1a and (c) UAT Campaign 1b.	44
3.14	Flow measurement setup of UAT Campaign 1a: (a) Schematic of the measurement locations for hot-wire probes (y axis is positive out-of-plane); (b) Positions of hot-wire probes <i>in-situ</i>	45
3.15	Location of the flow measurement points for UAT Campaign 1b: (a) perspective view; (b) view normal to x axis; (c) view normal to y axis.	46
3.16	Schematic of the wind turbine and the locations of test model profile. . . .	48
3.17	CAD drawings of wind turbine airfoil model (a) S1 (b) transparent S1 (c) S1 Assembly exploded view	49
3.18	Schematics of the acoustic and aerodynamic force measurements setup for UAT Campaign 2: (a) perspective view; (b) top view.	50
3.19	Schematic of the boundary layer measurement setup for UAT Campaign 2. . . .	51
3.20	Schematic of the UNSW Rotor Rig.	57
3.21	Schematic of rotor geometries (view from the microphone array).	58
3.22	Schematic of rotor blade models: (a) Reference NACA0012 blade (Ref); blades with (b) porous TE (P), (c) cut-serrated TE (CutS) and (d) extended-serrated TE (ExtS).	59
3.23	Transparent drawing of the porous region in rotor blade P.	60
3.24	Aeroacoustic measurement setup for the rotor blades in-situ.	61
3.25	Schematic of the data segment used to perform the phase-averaged beam-forming for the rotor at desired phase angle.	63
3.26	Computational grids looked from spanwise direction: (a) full view; (b) near-field detailed view and FWH porous surface.	69
3.27	Detailed view of computational grids for the TE porous region in LES Case 2. . .	70
4.1	Sound absorption coefficient of (a) specimen P1 compared with solid reference specimen SR and porous aluminium specimens 40PPI, 20PPI and 10PPI; (b) specimens with identical thickness h_0 , pore diameter d_0 but different porosity ϕ : P1 ($\phi=11.53\%$), P2 ($\phi=8.20\%$) and P3 ($\phi=5.35\%$) compared with specimen SR.	79
4.2	Sound absorption coefficients of micro-tube specimens with same porosity ($\phi = 11.5\%$): (a) specimens with same thickness h_0 but different pore diameter d_0 ; (b) specimens with same pore diameter d_0 but different thickness h_0	80

4.3	Relationship between pore aspect ratio and peak sound absorption coefficient (all specimens have a similar porosity within 11.1–11.5%).	80
4.4	Sound absorption coefficient of specimens (a) PA1, (b) PA2, (c) PA3 and (d) PA4 compared with predictions using Maa’s model (bottom micro-perforated panel excluded).	82
4.5	Sound absorption coefficient of specimens (a) PF1, (b) PF2, (c) PF3 and (d) PF4 compared with that of specimens PA1–PA4.	83
4.6	Sound absorption coefficient of specimens PF1–PF4 compared with that of a Basotect [®] foam with 10 mm thickness (F10).	83
5.1	Beamforming sound maps for the natural-transitioned NACA 0012 airfoil with extensions (a) BL, (b) NS, (c) CS and (d) CSP at freestream velocity $U_\infty = 18$ m/s and frequency $f = 2520$ Hz (color bar scale in dB). Flow comes from left to right. Green rectangle is the position of airfoil model, and green dash-line is the leading edge of flat-plate extension (x and y correspond to horizontal (streamwise) and vertical coordinates).	88
5.2	Schematic of the positions of array microphones (black circles), airfoil model (green rectangle) and TE integration region (red rectangle) for UAT Campaign 1a.	89
5.3	Acoustic data for baseline (BL) case at $U_\infty = 18$ m/s. (a) Integrated narrow-band noise spectrum of baseline case (BL) compared to background noise (BG); (b) integrated 1/3 octave band noise spectrum of baseline case (Exp) compared to BPM predictions (BPM LBL-TE: level-corrected BPM prediction of LBL-TE noise; f_{LBL} : peak frequency of LBL-TE noise; f_b : peak frequency of bluntness vortex-shedding noise.)	89
5.4	Colormap of narrow-band noise spectra for the natural-transitioned NACA 0012 airfoil with baseline flat-plate extension (St_{δ^*} - Strouhal number based on displacement thickness δ^* ; f_b - peak frequency of bluntness vortex-shedding noise).	90
5.5	Colormaps of narrow-band noise attenuation ΔSPL for (a) narrow-serrated (NS), (b) wide-serrated (WS), (c) curved-serrated (CS) and (d) slitted-serrated (SS) extensions (St_{δ^*} - Strouhal number based on displacement thickness δ^* ; St_b - Strouhal number based on TE thickness b ; f_b - peak frequency of bluntness vortex-shedding noise).	92
5.6	Colormaps of narrow-band noise attenuation ΔSPL for (a) porous (P), (b) curved-serrated-porous (CSP), (c) narrow-porous-serrated (NPS), (d) narrow-serrated-porous (NSP), (e) wide-porous-serrated (WPS) and (f) wide-serrated-porous (WSP) extensions (St_{δ^*} - Strouhal number based on displacement thickness δ^* ; St_b - Strouhal number based on TE thickness b ; f_b - peak frequency of bluntness vortex-shedding noise).	93

5.7	The noise attenuation in overall sound pressure level $\Delta OASPL$ (log scale on x axis) over frequencies ranging from 0.25 kHz to 10 kHz for extensions CS, NS, WS, CSP, NSP, WSP and P at Reynolds number ranging from 1.9×10^5 to 3.2×10^5	95
5.8	Beamforming sound maps for the forced-transitioned airfoil with extensions (a) BL, (b) P, (c) NS, (d) CS, (e) NSP and (f) CSP at freestream velocity $U_\infty = 36$ m/s and frequency $f = 2520$ Hz (color bar scale in dB). Flow comes from left to right. Green rectangle is the position of airfoil model, and green dash-line is the leading edge of flat-plate extension (x and y correspond to horizontal (streamwise) and vertical coordinates).	97
5.9	Schematic of the positions of array microphones (black circles), airfoil model (green rectangle) and the integration regions of leading edge (blue rectangle) and TE (red rectangle) for UAT Campaign 1b.	98
5.10	Noise spectra integrated over the TE region for airfoil with baseline extension (BL-TE) and background noise without airfoil model (BG) at freestream velocity of 36 m/s.	99
5.11	Noise spectra integrated over the leading-edge (BL-LE) and trailing-edge (BL-TE) regions for the airfoil model with baseline extension at freestream velocity of 36 m/s (f_{TE} - critical frequency for TE noise dominance).	99
5.12	Colormaps of narrow-band noise spectra for (a) the forced-transitioned NACA 0012 airfoil with baseline flat-plate extension (f_{TE} - critical frequency for TE noise dominance; f_b - peak frequency of bluntness vortex-shedding noise) and (b) the BPM predictions of TBL-TE noise.	100
5.13	Colormaps of narrow-band noise attenuation ΔSPL for extensions (a) NS, (b) CS, (c) NSP, (d) CSP and (e) P (f_{TE} - critical frequency for TE noise dominance; St_b - Strouhal number based on TE thickness b ; f_b - peak frequency of bluntness vortex-shedding noise).	101
5.14	The noise attenuation in overall sound pressure level $\Delta OASPL$ (log scale on x axis) for extensions P, NS, CS, NSP and CSP at Reynolds numbers from 3.2×10^5 to 8×10^5 over (a) frequencies from 0.5 kHz to 10 kHz and frequency regions (b) R1' (TE turbulence noise), (c) R2' (TE bluntness noise) and (d) R3' (high-frequency broadband noise increase).	103
6.1	Mean velocity boundary-layer profiles measured at 1 mm upstream ($x/c = -0.171$) of baseline (BL-UP1), porous (P-UP3), narrow-serrated (NS-UP1) and slitted-serrated (SS-UP1) extensions. Note that UP1, UP2 and UP3 refer to the measurement positions as shown in Figure 3.14a.	110

6.2	Near-wake (1mm downstream of TE, $x/c = 0.004$) mean velocity profile for baseline extension (BL-P1) compared with that for (a) porous extension (P-P3); (b) narrow-serrated (NS-P1), curved-serrated (CS-P1) and wide-serrated (WS-P1) extensions; (c) slitted-serrated extension (SS-P1). Note that P1, P2 and P3 refer to the measurement positions as shown in Figure 3.14a.	111
6.3	Wake ($x/c = 0.004$) mean velocity profile for (a) curved-serrated (CS) and narrow-serrated (NS) extensions at different spanwise positions P1, P2 and P3 as shown in Figure 3.14a.	111
6.4	Trailing-edge boundary layer displacement thickness δ^* obtained from the near-wake measurements (at 1 mm downstream of TE, $x/c = 0.004$).	113
6.5	Velocity spectra maps (from 0.4 to 0.9 kHz, region R1) measured along vertical (y) direction in the near wake (at position P1, $x/c = 0.004$) of (a) baseline (BL), (b) curved-serrated (CS), (c) narrow-serrated (NS) and (d) slitted-serrated (SS) extensions (positive y axis corresponds to airfoil suction-side). Frequencies of the discrete tones of LBL-TE noise are marked by dashed white lines.	115
6.6	Velocity spectra maps (from 0.9 to 3 kHz, regions R2 and R3) measured along vertical (y) direction in the near wake (at position P1, $x/c = 0.004$) of (a) baseline (BL), (b) curved-serrated (CS), (c) narrow-serrated (NS) and (d) slitted-serrated (SS) extensions (positive y axis corresponds to airfoil suction-side).	116
6.7	Velocity spectra maps (from 3 to 10 kHz, region R4) measured along vertical (y) direction in the near wake (1mm downstream) of (a) baseline (BL) extension at position P1 and (b) porous (P) extension at position P3 (positive y axis corresponds to airfoil suction-side).	117
6.8	Fluctuating velocity $\sqrt{u'^2}/U_\infty$ integrated over (a) 0.4 to 0.9 kHz (region R1), (b) 0.9 to 3 kHz (R2 and R3), (c) 3 to 10 kHz (R4) measured along vertical (y) direction in the near wake ($x/c = 0.004$) of curved-serrated (CS-P1, -P2 and -P3), narrow-serrated (NS-P1, -P2 and -P3), slitted-serrated (SS-P1, -P2 and -P3) and all-porous (P-P3) extensions compared with that of baseline (BL-P1) extension (positive y axis corresponds to airfoil suction-side). Note that P1, P2 and P3 refer to the measurement positions as shown in Figure 3.14a.	118
6.9	Normalised mean velocity U/U_∞ measured in the near wake ($x/c = 0.008$) at spanwise locations (a) P1', (b) P2' and (3) P3'. For extensions BL and P, only data measured at one position (P1' for BL, P3' for P) are presented as their geometries are uniformly distributed along the span.	120
6.10	Contours of normalised mean velocity U/U_∞ measured in the near-wake plane ($x/c = 0.008$) for extensions (a) BL, (b) P, (c) NS, (d) CS and (e) CSP.	122

6.11	Turbulence intensity $\sqrt{u'^2}/U$ measured in the near wake ($x/c = 0.008$) at spanwise locations (a) P1', (b) P2' and (3) P3'. For extensions BL and P, only data measured at one position (P1' for BL, P3' for P) are presented as their geometries are uniformly distributed along the span.	123
6.12	Turbulence intensity $\sqrt{u'^2}/U$ measured in the near-wake plane ($x/c = 0.008$) for extensions (a) BL, (b) P, (c) NS, (d) CS and (e) CSP.	124
6.13	Turbulence integral length scale δ_{ILS} measured in the near wake ($x/c = 0.008$) at spanwise locations (a) P1', (b) P2' and (3) P3'. For extensions BL and P, only data measured at one position (P1' for BL, P3' for P) are presented as their geometries are uniformly distributed along the span. . . .	125
6.14	Contours of turbulence integral length scale δ_{ILS} measured in the near-wake plane ($x/c = 0.008$) for extensions (a) BL, (b) P, (c) NS, (d) CS and (e) CSP.	126
6.15	Velocity power spectra at the position of the highest velocity deficit. Frequency region R2' for bluntness vortex-shedding noise is marked in grey. . .	127
6.16	Contours of noise intensity factor I_{TN} measured in the near-wake plane ($x/c = 0.008$) for extensions (a) BL, (b) P, (c) NS, (d) CS and (e) CSP. . .	129
6.17	Comparison of the single-microphone measurement results (Exp.) and FWH acoustic analogy results (FWH): (a) sound pressure level SPL in 1/3 octave-bands; (b) noise reduction performance ΔSPL of the porous airfoil in 1/3 octave-bands.	133
6.18	Directivity plot of the far-field 1/3 octave-band acoustic pressure [Pa^2/Hz] for the reference airfoil (Ref) and airfoil with porous TE (Porous) at (a) 1.6 kHz, (b) 2 kHz, (c) 4 kHz, (d) 5 kHz, (e) 8 kHz and (f) 10 kHz.	134
6.19	Narrow-band FWH acoustic analogy results. Frequency regions of interest are marked in grey (R_l : TE noise reduction region; R_h : high-frequency noise increase region).	135
6.20	Distribution of pressure coefficient C_p over the reference airfoil compared with XFOIL prediction.	136
6.21	Sketch of the TE geometries of the porous airfoil (top view).	136
6.22	Instantaneous flow structures around the reference and porous airfoil TEs: (a) vorticity in spanwise plane; (b) iso-surfaces of λ_2 criteria colored by vorticity.	137
6.23	Contours of the normalised Reynolds normal-stress $\overline{u'u'}/U_\infty^2$ in spanwise planes at (a) PL1 and (b) PL2 of porous airfoil and (c) midspan plane of reference airfoil. Locations of $U = 0.99U_\infty$ are marked by white dashed lines.	137
6.24	Contours of the normalised Reynolds normal-stress $\overline{u'u'}/U_\infty^2$ bandpass-filtered within R_l in spanwise planes at (a) PL1 and (b) PL2 of porous airfoil and (c) midspan plane of reference airfoil. Locations of $U = 0.99U_\infty$ are marked by white dashed lines.	138

- 6.25 Contours of the normalised Reynolds normal-stress $\overline{u'u'}/U_\infty^2$ bandpass-filtered within R_h in spanwise planes at (a) PL1 and (b) PL2 of porous airfoil and (c) midspan plane of reference airfoil. Locations of $U = 0.99U_\infty$ are marked by white dashed lines. 138
- 6.26 Contours of the normalised Reynolds normal-stress $\overline{v'v'}/U_\infty^2$ in spanwise planes at (a) PL1 and (b) PL2 of porous airfoil and (c) midspan plane of reference airfoil. Locations of $U = 0.99U_\infty$ are marked by white dashed lines. 139
- 6.27 Contours of the normalised Reynolds normal-stress $\overline{v'v'}/U_\infty^2$ bandpass-filtered within R_l in spanwise planes at (a) PL1 and (b) PL2 of porous airfoil and (c) midspan plane of reference airfoil. Locations of $U = 0.99U_\infty$ are marked by white dashed lines. 139
- 6.28 Contours of the normalised Reynolds normal-stress $\overline{v'v'}/U_\infty^2$ bandpass-filtered within R_h in spanwise planes at (a) PL1 and (b) PL2 of porous airfoil and (c) midspan plane of reference airfoil. Locations of $U = 0.99U_\infty$ are marked by white dashed lines. 140
- 6.29 Schematic of the polar velocity components about the airfoil TE. 140
- 6.30 Contours of the magnitude of acoustic source term $|-2\widehat{u_r u_\theta}|/U_\infty^2$ in 1/3 octave band at 5 kHz in spanwise planes at (a) PL1 and (b) PL2 of porous airfoil and (c) midspan plane of reference airfoil. Locations of $U = 0.99U_\infty$ are marked by white dashed lines. 141
- 6.31 Contours of the magnitude of acoustic source term $|-2\widehat{u_r u_\theta}|/U_\infty^2$ in 1/3 octave band at 8 kHz in spanwise planes at (a) PL1 and (b) PL2 of porous airfoil and (c) midspan plane of reference airfoil. Locations of $U = 0.99U_\infty$ are marked by white dashed lines. 141
- 6.32 Contours of the spatial correlation of the vertical velocity fluctuations bandpass-filtered within frequency region R_l in spanwise planes at PL1 (middle column) and PL2 (left column) of porous airfoil and midspan plane of reference airfoil (right column) with reference points at $\delta_y = 0.1\delta$ and different streamwise location:(a)–(c) $x/c = -0.178$; (d)–(f) $x/c = -0.142$; (g)–(i) $x/c = -0.105$; (j)–(l) $x/c = -0.070$; (m)–(o) $x/c = -0.034$; (p)–(r) $x/c = -0.02$. Locations of the reference point are marked by blue crosses, and the boundary layer edges ($U = 0.99U_\infty$) are marked by black dashed lines. 144

- 6.33 Contours of the spatial correlation of the vertical velocity fluctuations bandpass-filtered within frequency region R_h in spanwise planes at PL1 (middle column) and PL2 (left column) of porous airfoil and midspan plane of reference airfoil (right column) with reference points at $\delta_y = 0.1\delta$ and different streamwise location:(a)–(c) $x/c = -0.178$; (d)–(f) $x/c = -0.142$; (g)–(i) $x/c = -0.105$; (j)–(l) $x/c = -0.070$; (m)–(o) $x/c = -0.034$; (p)–(r) $x/c = -0.02$. Locations of the reference point are marked by blue crosses, and the boundary layer edges ($U = 0.99U_\infty$) are marked by black dashed lines. 145
- 6.34 Contours of the spatial correlation of the pressure fluctuations bandpass-filtered within frequency region R_l at the suction surface of the porous (top) and reference (bottom) TEs with reference points at different streamwise location:(a) $x/c = -0.199$; (b) $x/c = -0.176$; (c) $x/c = -0.159$ (d) $x/c = -0.14$; (e) $x/c = -0.12$; (f) $x/c = -0.105$ (g) $x/c = -0.087$; (h) $x/c = -0.069$; (i) $x/c = -0.051$; (j) $x/c = -0.034$; (k) $x/c = -0.016$; (l) $x/c = -0.001$. Locations of the reference point are marked by blue crosses, and the pores are marked by black circles. 146
- 6.35 Contours of the spatial correlation of the pressure fluctuations bandpass-filtered within frequency region R_h at the suction surface of the porous (top) and reference (bottom) TEs with reference points at different streamwise location:(a) $x/c = -0.199$; (b) $x/c = -0.176$; (c) $x/c = -0.159$ (d) $x/c = -0.14$; (e) $x/c = -0.12$; (f) $x/c = -0.105$ (g) $x/c = -0.087$; (h) $x/c = -0.069$; (i) $x/c = -0.051$; (j) $x/c = -0.034$; (k) $x/c = -0.016$; (l) $x/c = -0.001$. Locations of the reference point are marked by blue crosses, and the pores are marked by black circles. 147
- 6.36 Locations of the reference point for analysing the space-time correlation and mean convection velocity. 148
- 6.37 Contours of the space-time correlation of the pressure fluctuations on the suction surface of the porous (top) and reference (bottom) TEs with respect to reference points: (a) P_{st1} ; (b) P_{st2} ; (c) P_{st3} ; (d) P_{st4} ; (e) P_{st5} and (f) P_{st6} . Locations of the pore wall are marked by black dashed lines. 149
- 6.38 Normalised mean convection velocity $\overline{U_c}/U_\infty$ on the suction surface of the porous and reference TEs with respect to reference points: (a) P_{st1} ; (b) P_{st2} ; (c) P_{st3} ; (d) P_{st4} ; (e) P_{st5} ; (f) P_{st6} ; (g) P_{st7} and (h) P_{st8} . Locations of the pore are marked in grey. 150
- 6.39 Locations of the selected pores for flow characterisation (marked in grey). . 151
- 6.40 Characteristics of the mass flow rate through pores PR1–PR5: (a) mean mass flow rate q_m ; (b) power spectral density of mass flow rate P_{qq} 151
- 6.41 Contours of the normalised RMS of wall pressure fluctuations bandpass-filtered within frequency region R_l in pores (a) PR1, (b) PR2, (c) PR3, (d) PR4 and (e) PR5. 152

6.42	Contours of the normalised RMS of wall pressure fluctuations bandpass-filtered within frequency region R_h in pores (a) PR1, (b) PR2, (c) PR3, (d) PR4 and (e) PR5.	153
6.43	Contours of the normalised RMS of wall pressure fluctuations bandpass-filtered within frequency region R_h on the suction surface of the (a) porous and (b) reference TEs. Locations of the pore are marked by black circles. .	154
6.44	Contours of the normalised RMS of wall pressure fluctuations bandpass-filtered within frequency region R_h on the suction surface of the (a) porous and (b) reference TEs. Locations of the pore are marked by black circles. .	155
6.45	Contours of the power spectral density of wall pressure at different stream-wise locations on the suction surface of the porous TE at spanwise locations (a) PL1 and (b) PL2; and (c) the reference TE at PL1. The Locations of pores PR1–PR5 are marked by black dashed lines, and locations of PL1 and PL2 are illustrated in Figure 6.21.	155
7.1	One-third-octave band beamforming maps at 4 kHz and 8 kHz for reference blades at RPM of 900 and pitch angle of 5° . Each row corresponds to the results processed by (a, b) CBF, (c, d) PABF 1 and (e, f) PABF 2	162
7.2	One-third-octave band beamforming maps at $f_{1/3} =$ (a) 4 kHz, (b) 5.04 kHz, (c) 6.35 kHz and (d) 8 kHz processed by PABF 2 for forced-transitioned blades Ref operating at RPM of 900 and pitch angle of 5° . The location of maximum noise level is marked by a white circle-cross symbol.	164
7.3	One-third-octave beamforming maps at 6.35 kHz processed by PABF 2 for forced-transitioned blades (a) Ref, (b) P, (c) CuS and (d) ExtS operating at RPM of 900 and pitch angle of 5°	165
7.4	Integration region (marked in green rectangle) of rotor beamforming maps.	166
7.5	Sketch of the rotor blade segmentation.	167
7.6	Schematic of the local aerodynamic environment of a blade segment. . . .	168
7.7	Lift coefficient estimations using Xfoil for a NACA0012 blade segment (tripped at 10% chord) at $Re_c = 2.08 \times 10^5$ in comparison with thin airfoil approximation.	169
7.8	BEMT results for the forced-transitioned reference blade at RPM of 900 and pitch angles of 5° and 10° : (a) local angle of attack, (b) induced velocity and (c) inflow velocity (data used for BPM predictions are marked in grey). .	170
7.9	BPM noise prediction compared with the integrated one-third-octave noise spectra for reference blade at RPM of 900 and pitch angles of (a) 0° , (b) 5° and (c) 10° (The TE-noise-dominant frequency range determined from the beamforming sound map is marked in grey).	171
7.10	One-third-octave band noise reduction ΔSPL for forced-transitioned blades P, ExtS and CutS at 800 RPM: pitch angles of (a) 0° , (c) 5° and (e) 10° , and 900 RPM: pitch angles of (b) 0° , (d) 5° and (f) 10° . (the frequency range for TBL-TE noise comparison is marked in grey)	174

7.11	Integrated noise spectra in one-third-octave band for the reference blade with naturally and forced transitioned boundary layers at RPM of 900 and pitch angles of (a) 0° , (b) 5° and (c) 10°	175
7.12	One-third-octave band noise reduction ΔSPL for naturally transitioned (untripped) blades P, ExtS and CutS at 800 RPM: pitch angles of (a) 0° , (c) 5° and (e) 10° , and 900 RPM: pitch angles of (b) 0° , (d) 5° and (f) 10° . (The frequency range for LBL-TE noise comparison is marked in grey). . .	176
7.13	Reduction in overall sound pressure level $\Delta OASPL$ over TE-turbulence-noise-sensitive frequencies for forced-transitioned blades with TE treatments at RPM of (a) 800 and (b) 900.	178
7.14	Reduction in overall sound pressure level $\Delta OASPL$ over TE-instability-noise-dominant frequencies for natural-transitioned blades with TE treatments at RPM of (a) 800 and (b) 900.	178
7.15	One-third-octave band noise reduction ΔSPL for (a) forced-transitioned and (b) natural-transitioned blade P at RPM of 800 and 900 and pitch angles of 0° , 5° and 10° (high-sound-absorption region marked in grey). . .	179
8.1	Aerodynamic performance for airfoils S1 to S5: (a) Lift curves, (b) drag curves, (c) lift to drag ratio and (d) drag polar.	185
8.2	Boundary layer velocity profiles on both sides of the airfoil for S1 at (a) $\alpha_g = 0^\circ$ and (b) 10° , and S5 at (c) $\alpha_g = 0^\circ$ and (d) 10°	187
8.3	Beamforming maps (color bar scale in dB) at 1260 Hz for airfoil models (a) S1, (b) S2, (c) S3, (d) S4 and (e) S5 at $\alpha_g = 0$ and $U_\infty = 30$ m/s. Flow comes from left to right. Green rectangle is the position of airfoil model, and the TE integration region is marked by a blue-dashed rectangle (x and y correspond to horizontal (streamwise) and vertical coordinates).	189
8.4	Integrated 1/3 octave band spectra (green squares) and spectra from BPM model (black dashed line, boundary layer parameters estimated by Xfoil) for S1 at the geometric angle of attack $\alpha_g =$ (a) 0° ; (b) 2° ; (c) 4° ; (d) 6° ; (e) 8° ; (f) 10° ; (g) 12° ; (h) 14° and (i) 16° at $U_\infty = 30$ m/s.	190
8.5	Integrated 1/3 octave band spectra (green square) and spectra from BPM model (black dashed line, boundary layer parameters estimated by Xfoil) for (a) S2; (b) S3; (c) S4 and (d) S5 at $\alpha_g = 0^\circ$ and $U_\infty = 30$ m/s.	191
8.6	Schematic of the discretisation of a wind turbine blade into n segments: $S_1, S_2, S_3, \dots, S_n$	192
8.7	Schematic of the flow condition encountered by a wind turbine blade element	192
8.8	TBL-TE noise prediction models employed in different radial positions along the blade.	196
8.9	Schematic of the angle definitions for the noise directivity function	199
8.10	Flow chart for the wind turbine noise prediction program using noise scaling function (NSF) and BPM model.	203
8.11	Schematic of the field-test setup.	204

8.12 Wind turbine noise prediction results using *NSF* with (a) no correction;
(b) directivity correction; (c) atmospheric correction; (d) directivity and
atmospheric corrections for wind turbine operating at $U_i = 9.5\text{ m/s}$ 205

8.13 Comparison of the prediction results between *NSF* method and BPM
model: (a) predicted noise spectra for the wind turbine operating at wind
speed of 9.5 m/s ; (b) predicted A-weighted overall sound power level for the
wind turbine operating at wind speeds U_i from 7 to 9.5 m/s 206

List of Tables

3.1	Geometric parameters of micro-tube specimens, reference specimen and porous aluminium specimens in MC Campaign 1.	31
3.2	Geometric parameters of micro-perforated housings with an air gap or acoustic foam infill in MC Campaign 2.	31
3.3	Summary of UAT measurements	36
3.4	Geometries for TE extensions tested in this study. The direction of free stream velocity U_∞ is also shown in the sketch (from top to bottom).	42
3.5	Geometric parameters for cambered airfoil models	49
3.6	Geometries of rotor blades with porous, cut-serrated and extended-serrated TEs.	61
3.7	The results of the grid convergence study for LES Case 2.	72
3.8	Statistical parameters and uncertainties for quantities presented in Chapters 3–8 (Exp.: Experimental; Num.: Numerical; HW: Hot-wire; Mic.: Microphone; F_s : sampling frequency).	76
5.1	Peak frequencies f_b and Strouhal numbers St_b of bluntness vortex-shedding noise for airfoil with baseline flat-plate extensions at freestream velocities ranging from 12 m/s to 20 m/s.	90
5.2	Geometric parameters of porous and serrated-porous extensions	95
5.3	Summary of the overall sound pressure level reduction $\Delta OASPL$ in LBL-TE noise for proposed novel TE treatments over low-to-moderate Reynolds numbers ($1.9\text{--}3.2 \times 10^5$).	107
5.4	Summary of the overall sound pressure level reduction $\Delta OASPL$ in TBL-TE noise for proposed novel TE treatments over moderate Reynolds numbers ($3.2\text{--}8 \times 10^5$).	107
6.1	Summary of the parameters that relate the near-wake flow characteristics to the TBL-TE noise generation.	130
7.1	TE-noise-dominant frequency range f_{TE} for the forced-transitioned reference blade.	163
8.1	Corrected angles of attack for wind turbine airfoils S1–S5.	184
8.2	The maximum L/D and the corresponding angle of attack for airfoils S1 to S5	186
8.3	Boundary layer parameters towards the suction-side for S1 and S5	187
8.4	Boundary layer parameters towards the pressure-side for S1 and S5	188

Nomenclature

The majority of the abbreviations, symbols and mathematical operators used in this thesis are listed below. Although some symbols have been used for multiple purposes, they should be unambiguous according to their context.

Abbreviations

NSF Noise scaling function

OAPWL Overall sound power level

OASPL Overall sound pressure level

SPL Sound pressure level

3D Three-dimensional

APE Acoustic perturbation equation

BEMT Blade element momentum theory

BG Background

BPM Brooks, Pope and Marcolini

CAA Computational aeroacoustics

CAD Computer-aided design

CBF Conventional beamforming

CFD Computational fluid dynamics

CSD Cross-spectral density

DLR German Aerospace Center

DNC Direct noise computation

DNS Direct numerical simulation

FMM Fast multipole method

FWH Ffowcs-Williams and Hawkings

IAG Institute of Aerodynamics and Gas Dynamics (University of Stuttgart)

LBL-TE Laminar-transitional boundary layer trailing-edge

LBM	Lattice-Boltzmann method
LE	Leading edge
LES	Large-eddy simulation
LWT	UNSW Large Wind Tunnel
MPP	Micro-perforated panel
NASA	National Aeronautics and Space Administration (US)
OGV	Outlet guide vane
PABF	Phase-averaged beamforming
PIV	Particle image velocimetry
PSD	Power spectral density
PWL	Sound power level
RANS	Reynolds averaged Navier-Stokes
RMS	Root-mean-square
RPM	Rotations per minute
SGS	Subgrid-scale
T-S	Tollmien-Schlichting
TBL-TE	Turbulent boundary layer trailing-edge
TE	Trailing edge
UAT	UNSW Anechoic Wind Tunnel
UFL	University of Florida
VT	Virginia Polytechnic Institute and State University
XCOR	Cross-correlation coefficient

Roman Symbols

C	Cross-spectral matrix
h	Steering vector
p	A set of sound pressure signals
w	Tapering function

\mathbf{x}	Observer location
\mathcal{L}	Acoustically weighted airfoil response function
\bar{r}	Nondimensional radial location of blade segments
\overline{U}_c	Mean convection velocity
A_P	Permeable area of the flat-plate extension
$A_{atm,1/3}$	Atmospheric correction in third-octave band
A_{FP}	Area of porous region on the flat-plate extension
A_{ref}	Wing area of airfoil model
AR	Micro-tube aspect ratio
b	Thickness of trailing edge
c	Airfoil chord
c_0	Speed of sound
C_d	Drag coefficient
C_l	Lift coefficient
C_m	Pitching moment coefficient
D	Noise directivity function
D_0	Diameter of porous specimen
d_0	Pore diameter
D_H	Width of the UAT test section
f	Frequency
F_d	Drag
F_l	Lift
F_s	Sampling frequency
$f_{1/3}$	Center frequency of third-octave bands
g	Steering vector component
h	Half of serration amplitude
h_0	Porous specimen thickness

h_b	Thickness of the bottom panel in PA/PF structures
h_m	Thickness of the air gap/foam in PA/PF structures
h_r	Rotor hub height
h_t	Thickness of the top panel in PA/PF structures
I	Number of data segments for phase-averaged beamforming
I_{TN}	Noise intensity factor
I_{uu}	Turbulence intensity
k	Wavenumber
L	Airfoil span
L/D	Lift -to-drag ratio
L'_c	Acoustic spanwise coherence length
l_m	Measured airfoil span
L_s	Simulated airfoil span
l_s	Distance between the noise source and shear layer in the vertical direction
L_t	Length of tapering function
l_y	Spanwise correlation length
L_{den}	Annual day-evening-night A-weighted equivalent noise level
M_∞	Mach number
M_l	Local Mach number of blade segments
M_p	Acoustic mass of micro-perforated panel
M_z	Pitching moment
N_b	Number of blades
p	Pressure signal
p'	Predicted far-field sound pressure
p'_{rms}	RMS of surface pressure fluctuations
P_{qq}	PSD of mass flow rate
Q	Vortex criterion

q_∞	Dynamic pressure
q_m	Mass flow rate
r_e	Distance from noise source to observer
R_p	Acoustic resistance of micro-perforated panel
r_p	Complex sound reflection coefficient
R_t	Rotor radius
$R_{pp,\tau=0}$	Spatial correlation of surface pressure fluctuations
R_{pp}	Space-time correlation of surface pressure fluctuations
R_{uu}	Auto correlation fuction of fluctuating velocity
$R_{vv,\tau=0}$	Spatial correlation of vertical velocity fluctuations
Re_c	Reynolds number based on chord
SPL_a	Corrected sound pressure level
SPL_m	Measured sound pressure level
SPL_s	Simulated sound pressure level
$SPL_{1/3}$	Sound pressure level in third-octave bands
St_b	Strouhal numbers based on trailing-edge thickness
St_c	Strouhal number based on chord
St_{δ^*}	Strouhal number based on displacement thickness
U	Mean streamwise velocity
u	Instantaneous streamwise velocity
u'	Fluctuating streamwise velocity
U_∞	Freestream velocity
u_θ	Instantaneous angular velocity component about the airfoil TE
U_c	Convection velocity
U_i	Incoming wind speed
U_r	Linear velocity of blade segments due to rotational movement
u_r	Instantaneous radial velocity component about the airfoil TE

v	Instantaneous vertical velocity
v'	Fluctuating vertical velocity
v_i	Induced velocity of blade segments
V_T	Total volume of porous material
V_v	Volume of void-space in porous material
x	Spatial variable
x_{sh}	Shifted distance of the beamforming result due to the convection effect
X_{TSR}	Tip-speed ratio
Y	Beamforming output
y	Spatial variable
Z	Complex acoustic impedance
z	Spatial variable

Greek Symbols

α	Angle of attack
α_c	Corrected angle of attack
α_g	Geometric angle of attack
α_p	Sound absorption coefficient
$\alpha_{L/D,max}$	L/D peak angle of attack
α_{pi}	Pitch angle
δ^*	Boundary layer displacement thickness
δ	Boundary layer thickness
δ_{ILS}	Turbulence integral length scale
Γ	Gamma function
γ	Coherence function
λ	Serration wavelength
λ_2	Vortex criterion
ξ	Spatial separation

μ	Kinetic viscosity
ω	Angular frequency
ω_r	Rotational angular velocity
ϕ	Porosity
ϕ_{qq}	Wall pressure spectrum
ρ	Air density
σ	Solidity for blade segments
τ	Temporal separation
τ_{ij}	Stress tensor
θ	Boundary layer momentum thickness
θ_i	Desired phase angle for rotor blades
H_s	Boundary layer shape factor

Operators

$[:]^H$	Hermitian transpose
$[:]^T$	Matrix transpose
\circ	Hadamard product
$\mathcal{F}[:]$	One-sided fast Fourier transform
$\lfloor : \rfloor$	Rounding to the nearest integer
$E[:]$	Expected value

Subscripts

$[:]_{\text{UAT}}$	Operating condition in anechoic wind tunnel
$[:]_{\text{WT}}$	Wind turbine operating condition
$[:]_{\text{SGS}}$	Subgrid-scale

Chapter 1

Introduction

1.1 Background

Due to the expanding transportation network and increasing demand for the deployment of renewable energy, increasing numbers of aircraft and wind turbines have been operating near populated areas [1, 150]. The associated noise pollution, which can have adverse effects on human health [74], has become a notable concern for communities living near airports and wind farms. In comparison to other environmental noise sources (such as road noise and rail noise), annoyance due to wind turbine and aircraft noise was found to be more severe at the same annual day-evening-night A-weighted equivalent noise level L_{den} [98]. Therefore, wind turbine and aircraft noise regulations have become increasingly strict, posing a significant challenge for the design of relevant noise reduction technologies.

Airfoil self-noise is a leading contributor to environmental noise as it is a major component of aero-engine fan rotor noise [116], fan outlet guide vane (OGV) noise [116] and wind turbine noise [148, 174]. It originates from the interaction between an airfoil (wing or blade) and the turbulence produced in its own boundary layer and near wake. Brooks et al. [31] summarised five theoretical generation mechanisms of airfoil self-noise and the corresponding flow conditions are shown in Figure 1.1. A brief description of each mechanism is presented as follows:

- **Turbulent boundary layer trailing-edge (TBL-TE) noise**

When the Reynolds number based on chord, Re_c , is sufficiently large ($> 3 \times 10^6$) for an airfoil application (such as industrial-scale wind turbine blades and aero-engine fan blades at prevalent operating conditions), the boundary layer near the trailing edge (TE) is fully developed and turbulent. Within this boundary layer, eddies of various scales and energy levels interact with the airfoil surface, generating broadband acoustic waves. As the turbulent eddies propagate to the airfoil TE,

an impedance discontinuity at the sharp edge scatters the acoustic waves, forming TBL-TE noise with a broadband nature (see Figure 1.1a for the corresponding flow condition).

- **Laminar-transitional boundary layer trailing-edge (LBL-TE) noise**

Laminar-transitional boundary layer trailing-edge noise is often produced when the boundary layer remains in laminar or transitional regimes over at least one side of an airfoil, which may occur for applications that operate at low-to-moderate Reynolds numbers (such as micro wind turbines and unmanned aerial vehicles) or scenarios when the wind turbine blades or aero-engine fan blades operate at off-design conditions. Such noise originates from an aeroacoustic feedback loop between the Tollmien-Schlichting instability waves in the upstream boundary layer and vortex-shedding noise produced at the TE [31]. In this feedback loop, the acoustic waves generated at the trailing edge propagate upstream, encountering and amplifying the Tollmien-Schlichting (T-S) waves that originate from flow instabilities in the upstream boundary layer. Meanwhile, the amplified T-S waves will intensify the near-wake vortex shedding, thus efficiently promoting the emission of high-amplitude quasi-tonal noise (see Figure 1.1b for the corresponding flow condition).

- **Bluntness vortex-shedding noise**

A blunt TE can improve the structural strength and lift-to-drag ratio of an airfoil [182], but its bluntness can promote the formation of intense vortex-shedding in the wake (see Figure 1.1c) when the ratio between the bluntness height and the boundary layer displacement thickness $b/\delta^* > 0.3$ [24]. This can cause periodic pressure fluctuations related to the shedding frequency near the airfoil TE and the emission of bluntness vortex-shedding noise with a tonal nature. Rotor blades and wing designs are likely to have small bluntness relative to their boundary layer thickness [31], therefore such self-noise mechanism is usually less prominent.

- **Stall noise**

When the airfoil exceeds the critical angle of attack where maximum lift is produced, large-scale flow separations occur in the suction-side boundary layer (see Figure 1.1d). The non-recoverable separation can produce low-frequency stall noise,

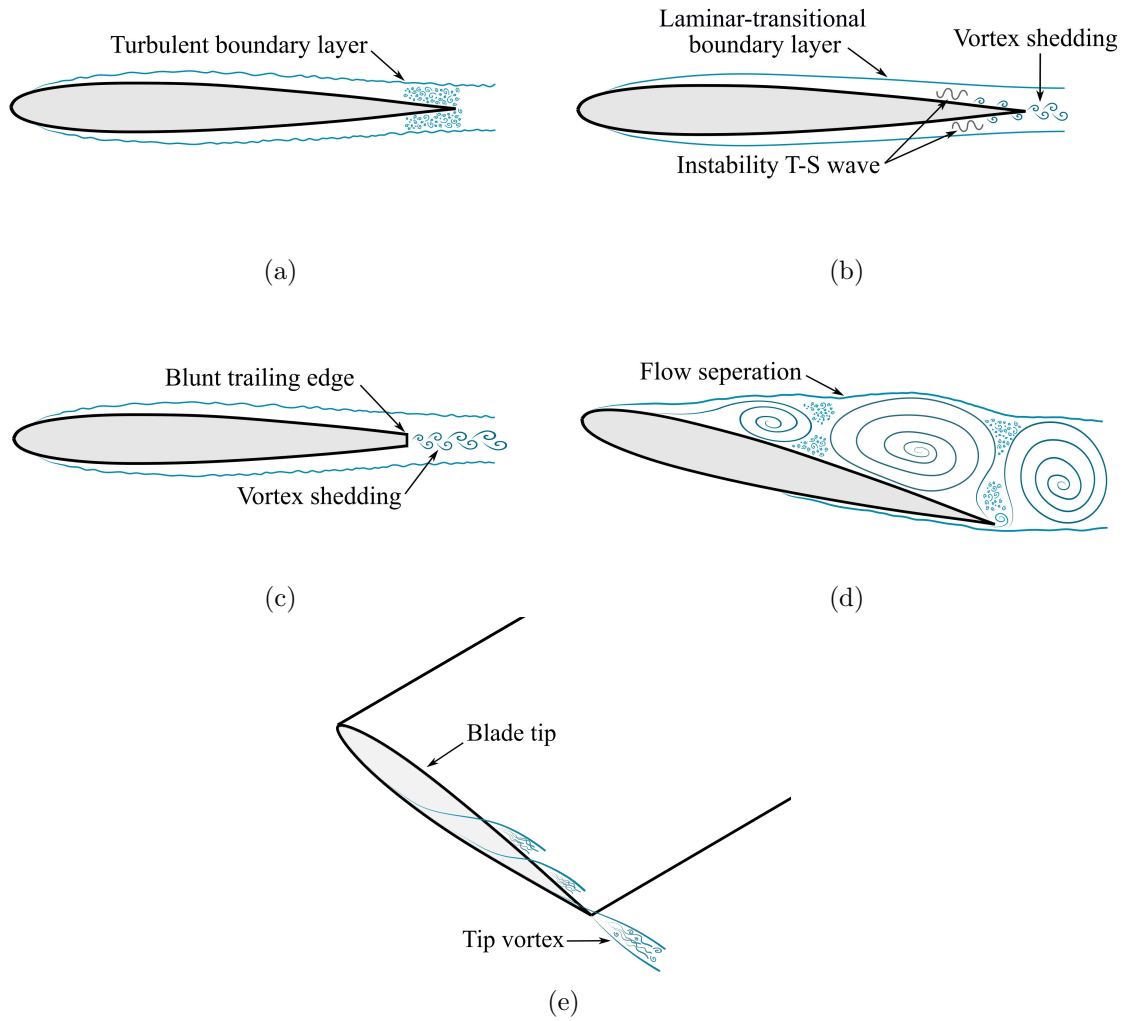


Figure 1.1: Schematics of flow conditions that induce the airfoil self-noise: (a) TBL-TE noise; (b) LBL-TE noise; (c) bluntness vortex-shedding TE noise; (d) stall noise; (e) tip vortex-formation noise.

which is similar to the flow-induced noise of a bluff body [31]. For state-of-the-art airfoil applications, the aerodynamic design of their blades or wings can effectively prevent stall under prevalent operating conditions.

- **Tip vortex-formation noise**

As the locally separated flow passes over the blade tip, vortices with a thick viscous turbulent core will interact with the TE of blade tip region (see Figure 1.1e), emitting tip vortex-formation noise. This noise mechanism can occur for thick blade tips, where the tip vortex is allowed to develop efficiently. However, as confirmed in field measurements [148, 174], this noise mechanism is not prominent for state-of-the-art wind turbine blade tips, likely due to their sharp tip geometries.

In this thesis, investigations focus on TBL-TE noise and LBL-TE noise, as they are the dominant noise mechanisms for high-Reynolds-number [116, 148, 174] and low-to-moderate-Reynolds-number [24, 25] applications, respectively. Without further explanation, TE noise refers to these two self-noise mechanisms in the rest of this thesis.

Inspired by owl's silent flight and unique wing features, many passive TE treatments (such as serrated, brush and porous TEs) have been developed and proven to be effective in airfoil TE noise control. Porous TEs and novel TE serrations, due to their superior potential in TE noise attenuation, have received much attention. However, past studies on these TE treatments were performed individually using different methods at different operating conditions and facilities. It is difficult to conclude which type of TE treatment is more efficient in TE noise control. Moreover, the physical mechanisms associated with their noise reduction have not been well understood. Their effects on the airfoil LBL-TE noise and rotor TE noise have also not been reported in detail.

This thesis presents a systematic study on developing novel porous treatments for airfoil and rotor TE noise control, which includes: 1) acoustic characterisation of novel porous structures; 2) aeroacoustic and flow measurements for the airfoil with novel porous TE; 3) numerical investigations on noise generation mechanisms for the airfoil with novel porous TE and 4) aeroacoustic measurements for the rotor blades with novel porous TE. In addition, the aeroacoustic performance of novel porous TE on the airfoil and rotor TE noise has been compared with that of novel serrated TEs. Furthermore, a prediction model for wind turbine noise has been developed and validated. This model can potentially be used to predict the noise reduction performance of TE treatments on full-scale wind turbines.

1.2 Aims and Objectives

The primary aim of this thesis are to develop quiet airfoils and rotors using novel porous and serrated TE treatments while deepening our understanding of the physical mechanisms controlling noise reduction. The secondary aim is to develop a high-accuracy prediction method for wind turbine noise. To achieve these aims, the specific objectives of this thesis are:

1. Experimentally characterise the acoustic properties of porous materials to evaluate their feasibility for TE noise control;
2. Experimentally evaluate the noise reduction performance of novel porous, serrated and porous-serrated TE treatments;
3. Experimentally and numerically investigate the flow characteristics that are related to the noise reduction by the novel TE treatments;
4. Apply novel porous and serrated TE treatments to rotor blades and experimentally evaluate their feasibility in rotor TE noise control;
5. Develop a noise scaling model to accurately predict the noise performance of a full-scale wind turbine using wind tunnel measurement data.

1.3 Thesis Structure

This thesis is structured in accordance with the aims and objectives presented in Sec. 1.2.

The contents for each chapter are summarised as shown in Figure 1.2.

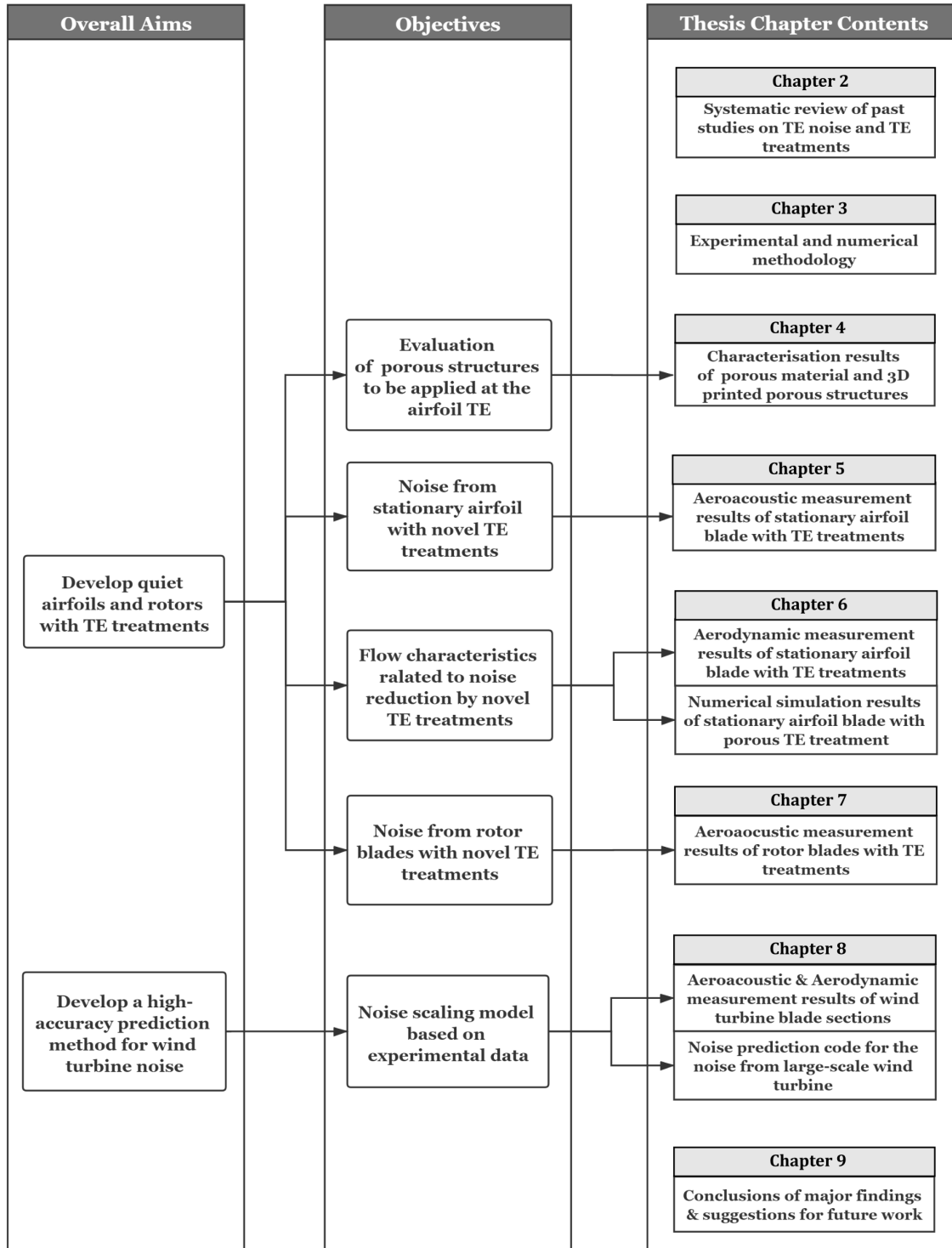


Figure 1.2: Thesis structure and the summarised contents for each chapter.

1.4 Publications

During this PhD project, the following papers were published:

- Jiang, C., Moreau, D., Fischer, J. and Doolan, C.J., 2021. Additively Manufactured Sound-Absorbing Porous Structures for Airfoil Trailing-Edge Noise Control. *Journal of Aerospace Engineering*.
- Jiang, C., Fischer, J.R., Moreau, D. and Doolan, C.J., 2019. Experimental Investigation of Novel Porous-serrated Treatments on Airfoil Trailing Edge Noise Reduction. In *25th AIAA/CEAS Aeroacoustics Conference* (p. 2435).
- Jiang, C., Moreau, D., Yauwenas, Y., Fischer, J.R., Doolan, C.J., Gao, J., Jiang, W., McKay, R. and Kingan, M., 2018. Control of rotor trailing edge noise using porous additively manufactured blades. In *2018 AIAA/CEAS Aeroacoustics Conference* (p. 3792).
- Jiang, C., Moreau, D. and Doolan, D., 2017. Acoustic absorption of porous materials produced by additive manufacturing with varying geometries. In *Proceedings of ACOUSTICS*.
- Echeverria, C.A., Pahlevani, F., Handoko, W., Jiang, C., Doolan, C. and Sahajwalla, V., 2019. Engineered hybrid fibre reinforced composites for sound absorption building applications. *Resources, Conservation and Recycling*, 143, pp.1-14.
- Delhomme, F., Hajimohammadi, A., Almeida, A., Jiang, C., Moreau, D., Gan, Y., Wang, X. and Castel, A., 2020. Physical properties of Australian hurd used as aggregate for hemp concrete. *Materials Today Communications*, 24, p.100986.
- Doolan, C., Moreau, D., Awasthi, M. and Jiang, C., 2018, November. The UNSW anechoic wind tunnel. In *Proceedings of ACOUSTICS* (Vol. 7, No. 9).

Chapter 2

Literature Review

2.1 Overview

In line with the primary thesis aims (Sec. 1.2), this chapter systematically reviews past studies on TE noise and its control from in terms of its theoretical, experimental and numerical aspects. First, a review on the generation mechanisms, characteristics and prediction methods of TE noise is presented in Sec. 2.2. Then, the current research status on the noise reduction performance and mechanisms of sawtooth-serrated, porous and novel TE treatments for airfoils and rotors is presented in Sec. 2.3. Finally, research gaps are identified and summarised in Sec. 2.4.

2.2 Airfoil Trailing-Edge Noise

As described in Sec. 1.1, this thesis focuses on the TE treatments for reducing the TBL-TE noise and LBL-TE noise. In order to gain an in-depth understanding of the generation mechanisms, characteristics and prediction methods of these two self-noise sources, a systematic review of the relevant theoretical, experimental and numerical work will be presented.

2.2.1 Turbulent Boundary Layer Trailing-Edge Noise

Turbulent boundary layer trailing-edge (TBL-TE) noise has been extensively studied since the late 1950s, when Powell [154] published the first paper on edge noise. In this study, a dimensional analysis on TBL-TE noise was performed based on Lighthill's acoustic analogy theory [117], suggesting that dipole edge noise is the predominant noise source in low Mach number flow and the noise intensity is scaled with the fourth to fifth power of freestream velocity, U_∞^{4-5} . Later in 1970, Ffowcs Williams and Hall [190] performed an analytical study on the noise generated by the interaction between the turbulent flow and a rigid half plane, in which the well-known dependence of radiated noise intensity on the fifth power of freestream velocity U_∞^5 was proposed. During the 1970s, several semi-analytical theories on TBL-TE noise were proposed by Crighton et al. [52], Chase [37, 38], Chandiramani [36], Howe [90], Amiet [6] and Tam et al. [180]. Howe [91] comprehensively reviewed early semi-analytical theories (until 1978) and categorised them into: theories based on 1) Lighthill's acoustic analogy [117] (such as Refs. [52, 90, 190]); 2) linearised hydroacoustic equations (such as Refs. [6, 36, 37, 38]) and 3) ad-hoc models (such as Ref. [180]). It was concluded that all these theoretical models are essentially equivalent, leading to the same velocity dependence U_∞^5 of the radiated noise intensity, dependencies on the turbulent length scales and static noise directivity. Based on these models, Howe [91] proposed a unified theory of TBL-TE noise, which incorporates the effects of the Kutta condition and Doppler amplification. In a more recent review by Howe [93], the effects of finite TE thickness were investigated analytically based on an extension of diffraction theories [36, 37], which accounts for modifications of the turbulence convected past variable-geometry edges. Among these theoretical models, only Amiet's model [6]

introduced the effect of finite chord length, hence possessing great value for practical applications. In Amiet's model [6], the far-field noise spectra ϕ_{pp} can be expressed as

$$\phi_{pp}(\mathbf{x}, \omega) = (c^2 L) D(\mathbf{x}, \omega) |\mathcal{L}(\omega)|^2 l_y(\omega) \phi_{qq}(\omega), \quad (2.1)$$

where \mathbf{x} denotes the observer location, ω is the angular frequency, c is the airfoil chord, L is the airfoil span, $D(\mathbf{x}, \omega)$ is a dipole radiation function, $\mathcal{L}(\omega)$ is the acoustically weighted airfoil response function, $l_y(\omega)$ is the spanwise correlation length and ϕ_{qq} is the wall pressure spectrum. According to Amiet's theory [6], the far-field noise spectrum is proportional to the spanwise correlation length and wall pressure spectrum. The latter can be predicted from the boundary layer velocity field using TNO-Blake model [25, 152]

$$\phi_{qq}(\omega) = \frac{4\pi\rho^2}{\Lambda_{p|z}} \int_0^\delta \Lambda_{v|y}(y) U_c(y) \phi_{vv}(\omega/U_c(y), k_z = 0) \left[\frac{\partial U(y)}{\partial y} \right]^2 \frac{\overline{v'^2}(y)}{U_c(y)} e^{-2|k|y} dy, \quad (2.2)$$

where y is the vertical location in the TE boundary layer, ρ is the air density, $\Lambda_{p|z}$ is the spanwise correlation length, $\Lambda_{v|y}$ is the vertical integral length scale, U_c is the local convection velocity and ϕ_{vv} is the dimensionless wavenumber spectral density of vertical velocity fluctuations v' . Later theoretical studies by Howe [94] and Roger et al. [162] both considered the leading-edge scattering effect for an airfoil with a finite chord. The former work extended Amiet's theory [6] based on the vanishing Mach number Green's function tailored to a finite-chord flat plate. The latter work derived and integrated a leading-edge back-scattering correction into the Amiet's model [6]. Both studies suggested that this leading-edge scattering effect can be significant at low frequencies where the airfoil chord is acoustically compact. This brief review of theoretical works on TBL-TE noise is considered sufficient for this thesis, the reader is referred to Refs. [91, 93] for more detailed reviews.

Experimentally, early measurements by Fink [65] on an airfoil-like plate model confirmed the fifth power velocity dependence proposed by Ffowcs Williams and Hall [190]. Brooks and Hodgson [28] performed the first comprehensive investigation of TBL-TE noise of a NACA 0012 airfoil, where the surface pressure spectra measured near the TE were related to the far-field noise by using evanescent wave theories [36, 38, 91] on TBL-TE noise. Afterwards, Brooks, Pope and Marcolini [30, 31] published the most comprehensive data

set of the self-noise for NACA 0012 airfoils, and developed the well-known semi-empirical model (the so-called BPM model) based on this data set. The BPM model provides useful formulations to relate the TE boundary layer parameters to the TBL-TE noise, which can effectively predict the peak Strouhal number and level of the noise spectra. The comparison [31] between BPM prediction results and experimental data [175] for a cambered helicopter blade section show a reasonable agreement, illustrating the versatility of the BPM model. This semi-empirical model was later incorporated into “NAFNoise” code [138], a widely used engineering tool for wind turbine noise prediction. In recent years, with increasing concern of the noise from low-Mach-number high-Reynolds-number airfoil applications (such as wind turbine noise), numerous experimental investigations have been performed on airfoil TBL-TE noise, where the noise data were measured using individual microphones [136, 137, 161] (background noise corrected), pairs of microphones [20, 21, 134] (based on the coherent power output method used in Refs. [28, 30, 31]), hot-wire sensors [87, 88] (based on the coherent particle velocity method), elliptical acoustic mirrors [83, 84, 85] and microphone arrays [56, 57, 96, 131, 146] (based on the acoustic beamforming method). A recent review by Doolan and Moreau [58] compared the TBL-TE noise data of NACA 0012 airfoils measured from different facilities (NASA [28, 31], DLR [83, 84, 85], VT [56], UFL [21] and IAG [88]) over the last 40 years. The noise spectra at Reynolds numbers based on chord between 1 and 1.3×10^6 collapse well and are in reasonably good agreement with BPM model predictions. However, larger errors are present for BPM predictions at higher Reynolds numbers (1.5 to 3×10^6) and the data from different facilities start to show large discrepancies (up to over 10 dB) in the peak 1/3 octave sound pressure level (scaled based on BPM model), which is likely caused by different boundary layer tripping methods, measurement techniques and background noise scattering effects of different facilities. Since the BPM model is developed based on the experimental data measured over Reynolds numbers from 6.9×10^4 to 1.47×10^6 , predictions for higher Reynolds numbers ($Re_c > 1.47 \times 10^6$) rely on extrapolated equations. In order to accurately predict the TBL-TE noise from high-Reynolds-number applications (such as large-scale industrial wind turbines), further experimental investigations are needed to extend the BPM model. Moreover, the cross-facility comparisons highlighted the importance of computational investigations, in which the extraneous noise sources and effects

of facility scattering can be eliminated.

With the rapid development of computing power and numerical techniques, computational investigations of TBL-TE noise have become increasingly feasible. Early numerical investigation can be referred to the work by Wang and Moin [189], where an incompressible large-eddy simulation (LES) is adopted to compute the unsteady flow over a Blake airfoil. The far-field noise spectra and near-field source-term characteristics were determined using the Lighthill equation derived by Ffowcs-Williams and Hall [190]. Oberai et al. [144] later employed an unstructured mesh and incompressible LES simulation to compute the low-Mach-number turbulent flow over a NACA 4412 airfoil, and used Lighthill's analogy [117, 118] to investigate the edge scattering effects and noise directivity. More recently, direct noise computations (DNC) were performed by Le Garrec et al. [108], Gloerfelt et al. [73] and Marsden et al. [129], where the far-field noise is directly calculated from the resolved compressible flow field instead of acoustic analogies. Direct numerical simulations (DNS) have also been employed to investigate TBL-TE noise in work by Sandberg, Jones and Sandham [168, 169]. The acoustic pressure obtained by DNS was compared with acoustic analogies and Amiet's theory [6], suggesting Amiet's model can predict the noise generated from turbulent flow past a flat-plate TE with reasonable accuracy, despite numerous assumptions and simplifications. Winkler et al. [191, 192] used an incompressible LES simulation to compute the flow field around a NACA 6512-63 airfoil, and calculated the far-field noise using Amiet's theory [6], Ffowcs-Williams and Hall's theory [190] and Curle's acoustic analogy [53]. Predictions from Ffowcs-Williams and Hall's model [190] showed the closest comparisons with experimental data. In addition, the effects of different boundary layer tripping devices were also investigated. Ewert et al. [61] applied a hybrid method to investigate the noise generated by turbulent flow past a NACA0012 airfoil, where the flow field is solved by Reynolds averaged Navier-Stokes (RANS) simulation and the acoustic pressure is computed by a computational aeroacoustics (CAA) approach based on the acoustic perturbation equations (APE) with stochastic sound sources generated using the random particle-mesh approach. Comparisons between the simulated acoustic results and experimental data suggested that good prediction quality can be achieved by this fast hybrid RANS/CAA approach with calibrated RPM parameters. In recent work by Wolf et al. [193, 194], compressible LES simulations and Ffowcs-Williams

and Hawkings (FWH) acoustic analogy [63] were employed to investigate the noise from NACA 0012 airfoils, where surface and volume integrations in the FWH equation were accelerated using a fast multipole method (FMM). Far-field acoustic predictions are in good agreement with experimental data from Brooks et al. [31]. Moreover, it was found that the mean flow convection can significantly affect the noise directivity at medium and high frequencies (Helmholtz number $kc \geq 3.68$, Strouhal number $St_c \geq 5.09$) even for low-Mach-number ($M_\infty = 0.115$) flow. The quadrupole sources are negligible for low-Mach-number ($M_\infty \leq 0.115$) flow, while can present significant effects at medium and high frequencies ($kc \geq 4.91$, $St_c \geq 1.95$) for moderate-Mach-number ($M_\infty = 0.4$) flow.

2.2.2 Laminar-Transitional Boundary Layer Trailing-Edge Noise

Laminar-transitional boundary layer trailing-edge (LBL-TE) noise has a character consisting of a broadband hump superimposed with several discrete high-amplitude tones [7]. It usually occurs at Reynolds numbers (4×10^4 to 2×10^6) and angles of attack (0° to 12°) within a certain envelope [10, 122]. Previous studies on this self-noise source mainly focus on its generation mechanism and the prediction of the frequencies of the discrete tones. Paterson et al. [153] performed the first comprehensive investigation on the LBL-TE noise of NACA 0012 and NACA 0018 airfoils at various Reynolds numbers (4.4×10^5 to 2.2×10^6) and angles of attack (-6° to 16°). The frequency of primary tones with respect to freestream velocity were found to form a “ladder structure” [7, 143, 181]. As the velocity increases gradually, the frequency of the primary tone first slowly increases with a dependency on freestream velocity $U_\infty^{0.8}$. After a certain velocity, the primary tone will suddenly jump to a higher frequency, forming another “step” gradually increasing with $U_\infty^{0.8}$. The average primary-tone frequency shows a dependency on freestream velocity of $U_\infty^{1.5}$, which was also confirmed later in the BPM model [31]. Tam [181] derived a model to describe the evolution frequency of the tones based on the velocity dependency of $U_\infty^{0.8}$, and proposed that the discrete tones are generated due to a self-excited feedback loop between the origin of vortex shedding at airfoil TE and the acoustic waves produced by the amplified vortex-shedding oscillation in the downstream wake. After that, several experi-

mental [7, 8, 9, 31, 39, 41, 124, 130, 142, 143, 157], numerical [55, 97, 103, 104, 105, 168] and theoretical [7, 106, 130, 143] studies have been performed in order to understand the noise generation mechanism and predict the evolution of the high-amplitude tones. It is believed that the high-amplitude tonal noise is produced by an aeroacoustic feedback loop. Several aeroacoustic feedback loop models have been proposed in past studies. Three typical ones are: 1) Model A [7, 39, 106]: feedback loop between the upstream-radiating acoustic waves generated at the TE and the instability T-S wave at its origin; 2) Model B [55, 97, 104, 105, 157, 168]: feedback loops between the acoustic waves generated in the wake and the instability T-S wave at its inception position on the pressure side (or both the pressure and suction sides); 3) Model C [181]: feedback loop between the airfoil TE and the acoustic waves emitted from dipole noise sources in the wake (as illustrated in Fig.1 of Ref. [42]). In addition, a number of studies [39, 41, 55, 104, 105, 122, 130, 143, 157, 168] linked tonal noise production to the existence of a laminar separation bubble near the TE. The dominant tone is commonly attributed to the TE scattering of T-S instability waves that originate upstream and are amplified by inflectional mean velocity profiles in the separated shear layer. Although there is no general consensus on the generation mechanism of such self-noise source, it can be concluded from previous studies that the noise generation is highly related to the boundary layer instabilities and the vortex shedding in the wake. Therefore, the control strategy for the LBL-TE noise should focus on suppressing these flow characteristics.

2.3 Trailing-Edge Treatments for Noise Reduction

It has long been recognised that owls can fly silently. In a recent experimental study by Sarradj et al. [173], the flyover noise from a common kestrel, a Harris's hawk and a barn owl was quantified. The noise spectra, which were scaled to account for the flight speed, indicated that the barn owl was substantially 3 to 8 dB quieter than the other two bird species at frequencies above 1.6 kHz. Later, the aerodynamic noise from the wings of five species of birds was measured by Geyer et al. [70] in an aeroacoustic wind tunnel. The acoustic results (scaled using Mach number and lift coefficient) suggested that the wings

of two owl species were significantly (10 to 20 dB) quieter than that of other birds in flow, further confirming the owls' silent flight is due to their wing features instead of lower flight speed. It is believed that the owl's wing has three distinctive physical features that relate to its silent flight [18, 75, 100, 119]: 1) a downy upper wing surface with velvety texture; 2) comb-like stiff feathers at the leading edge of the wing; 3) a permeable and flexible fringe at the TE of the wing and primary feathers. These alleged silent wing features have led to many low-noise TE designs (such as TE serrations and porous TEs) and extensive research to understand the physical mechanisms responsible for noise reduction.

2.3.1 Effects of Trailing-Edge Sawtooth-Serrations on Turbulent Boundary Layer Trailing-Edge Noise

Trailing-edge sawtooth-serrated treatment, as a promising strategy for TBL-TE noise control, has received much attention since the 1990s. The structure of typical TE sawtooth serrations is shown in Figure 2.1, where $2h$ and λ are the root-to-tip amplitude and wavelength of the serrations, respectively. In this thesis, these two parameters are adopted to describe the geometry of the serrated TEs.

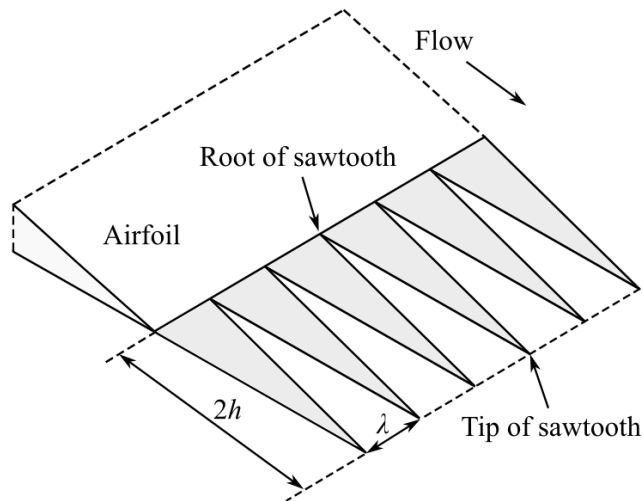


Figure 2.1: Sketch of the geometries of TE sawtooth serrations.

In 1991, Howe [92] proposed the first analytical model for the aerodynamic noise of a semi-infinite plate with TE sawtooth serrations at zero angle of attack in low-Mach-number flow. Due to the complexity of this problem, a tailored Green's function based on the slender-wing approximation and frozen turbulence assumption were adopted in Howe's

model. According to this model, the maximum reduction in far-field sound pressure level by the sawtooth serrations is proportional to $10 \log[1 + (4h/\lambda)^2]$ when the serration is sharp enough ($\lambda/h < 1$) and the frequency is sufficiently high ($\omega h/U_\infty \gg 1$). This suggested that sharper serrations with a smaller wavelength-to-amplitude ratio λ/h can achieve greater noise reduction. However, it was found in later experimental work by Dassen et al. [54], Gruber et al. [78] and Moreau et al. [133] that Howe's model overpredicts the noise reduction by TE sawtooth serrations. Recently, Lyu et al. [125] proposed a new analytical model for the noise prediction of TE serrations based on Amiet's TE noise theory [6]. In this model, Amiet's theory was generalised for the application to TE sawtooth serrations, and its solutions were validated by the finite element method. The second-order solutions of Lyu et al.'s model [125] can provide more realistic predictions of the noise reduction by TE serrations compared with Howe's model [92]. It was suggested that the noise reduction by TE sawtooth serrations is due to the destructive interference of the scattered surface pressure induced by the serrated geometries. Nevertheless, since the effects of serrated geometries on the hydrodynamic flow field cannot be described by current analytical models, experimental and numerical investigations are essential for understanding the noise reduction mechanism.

Indeed, numerous experimental studies have been conducted on the noise generation of serrated TEs over the last three decades. In 1996, Dassen et al. [54] measured the noise from a series of airfoils and flat plates with serrated TEs ($\lambda/h = 0.2$) in an anechoic wind tunnel. The TE noise levels (over 1 to 6 kHz) of airfoils and flat plates were found to be reduced by the serrated TEs by up to 8 dB and 10 dB, respectively. The experimental data were compared with the predictions using Howe's model [92], first reporting the overprediction by Howe's model. After more than one decade, Gruber et al. [76, 77, 78, 79] performed a comprehensive study on the TBL-TE noise of a NACA 6512 airfoil with thirty-six different TE sawtooth-serration geometries ($0.1 \leq \lambda/h \leq 6$) at various Reynolds numbers ($2.1 \times 10^5 \leq Re_c \leq 8.3 \times 10^5$) and geometric angles of attack ($0^\circ \leq \alpha_g \leq 15^\circ$). The noise reduction dependency on $10 \log[1 + (4h/\lambda)^2]$ predicted by Howe [92] showed a poor match with experimental data. Instead, two more critical parameters: non-dimensional frequency $f\delta/U_\infty$ and non-dimensional serration amplitude h/δ were proposed, where δ is the boundary layer thickness near the straight TE. A noise increase of up to 7.2 dB was

observed at high frequencies where the non-dimensional frequency $f\delta/U_\infty > 1$. When the serration amplitude was small relative to the TE boundary layer thickness ($h/\delta < 0.25$), no significant noise reduction was observed as the acoustic scattering efficiency of serrations becomes similar to that of a straight TE. It was suggested that the noise reduction by TE serrations is mainly due to reductions in the convection velocity and the coherence of surface pressure fluctuations along the TE. Later, Moreau and Doolan [133] compared the TBL-TE noise from a flat plate with two TE sawtooth-serration geometries. Contrary to Howe's theory, the wide serrations with a larger wavelength-to-amplitude ratio ($\lambda/h = 0.6$) achieved a better (0.5 dB more) noise reduction compared to the narrow serrations ($\lambda/h = 0.2$). It was suggested that the effects of serrated geometries on the hydrodynamic field at the source location may play an important role in noise reduction. The assumption that the turbulent flow is not affected by the presence of serrations in Howe's theory is likely invalid, hence explaining the large discrepancies between the predictions and experimental data. Since then, more attention has been paid to the flow characteristics around the serrated TEs in more recent experimental studies. The hydrodynamic field in the vicinity of TE serrations has been investigated using hot-wire anemometry [43, 121, 187], laser doppler anemometry [121], stereoscopic particle image velocimetry (PIV) [110, 111, 112, 113, 114] and tomographic PIV [12, 110]. Important findings from these recent studies are summarised as follows: 1) streamwise vortices along the serrated TEs were observed [12, 43, 113, 187]; 2) the interaction between the streamwise vortices and turbulent boundary layer can redistribute the momentum transport and turbulent shear stress hence affect the acoustic scattering efficiency of the TE [43]; 3) the strength of the streamwise vortices is related to the local flow misalignment which is sensitive to the serration flap angle [113, 187]; 4) the high-frequency noise increase reported by Gruber et al. [76, 77, 78, 79] may be due to intense turbulent flow near the pressure-side serration edges [113, 114]; 5) serrations can cause significant reductions in lift coefficient at low angles of attack and reduce the turbulent energy in the wake [121].

Numerically, Jones and Sandberg [101, 102, 167] first employed DNS to investigate the noise from airfoils with sawtooth-serrated TEs. In these studies, the immersed boundary method was adopted to simulate the flow around the complex serrated geometries without the need for complex grid generation. Trailing-edge serrations were found to effectively

reduce the far-field noise level by 6 to 10 dB with only minor effects on the noise directivity. The Reynolds stress amplitude, spanwise coherence and turbulent spectra upstream of the extended serrations were not significantly altered by the serrated geometries, hence the noise reduction is mainly due to the changes in the scattering process. It was also suggested that the noise reduction could potentially relate to the hydrodynamic changes in the vicinity of serrated geometries, where the streamwise-oriented turbulent structures gradually develop into spanwise-dominant regimes along the serrations, eventually forming horse-shoe vortices in the wake region between two serration tips. Arina et al. [11] used compressible LES to simulate the near-field flow of a NACA 65-1210 airfoil with TE sawtooth-serrations and the FWH acoustic analogy to calculate the far-field acoustic pressure. The predicted far-field noise level and directivity of the baseline airfoil were in good agreement with experimental data. Serrations were found to effectively reduce the TBL-TE noise at low-to-moderate frequencies ($f < 4$ kHz) but increase the noise at high frequencies (as reported by Gruber et al. [77, 78, 79]). High streamwise vorticity appeared along the serration edges (as observed in Refs. [12, 43, 113, 187]) and the integral length scale in the near wake was significantly reduced by serrated geometries. More recently, Sanjose et al. [170] adopted Lattice-Boltzmann method (LBM) to perform DNS-resolution simulations on a controlled diffusion airfoil with TE sawtooth-serrations. Both the aerodynamic performance and far-field noise were effectively predicted, showing a good agreement with experimental data.

2.3.2 Effects of Porous Trailing-Edge Treatments on Turbulent Boundary Layer Trailing-Edge Noise

In recent years, the use of porous TEs for TBL-TE noise reduction has gained much attention. Due to the complexity of the physical properties of porous material, it is difficult to describe its actual physical geometries in analytical modelling. Porous structures are usually simplified to a perforated flat plate in analytical studies on the acoustic scattering problem of porous or poroelastic TEs. The physical geometries of porous geometries are described by the porosity and pore radius of the plate. In 2013, Jaworski and Peake [99] performed an analytical study on the acoustic scattering of a semi-infinite poroelastic edge

when a turbulent eddy passes over it. This problem was solved using the Wiener-Hopf technique, and the far-field acoustic power scattered from a porous TE was identified to scale with freestream velocity U_∞^6 . The numerical results indicated that the rigid-porous TE can achieve a noise reduction over lower frequencies. Later, a more realistic problem of the acoustic scattering by a finite rigid plate with a poroelastic TE was solved by Ayton [15] based on a Wiener-Hopf factorisation process. In this study, the effects of finite chordlength were taken into account. It was concluded that poroelastic TEs could be efficient in TE noise control, but the interaction between the scattered acoustic fields of the rigid leading edge and poroelastic TE may increase the scattered far-field noise. In a more recent study by Kisil and Ayton [107], the effects of a porous TE extension with a finite chord on TE noise scattering was investigated analytically. In accordance with the work of Jaworski et al. [99], porous TE extensions were found to significantly reduce the low-frequency noise, while the interference of the impermeable-permeable junction may lead to a slight noise increase at high frequencies (as observed in the experimental study by Geyer et al. [71]). However, these analytical studies for the porous TEs with simplified geometries have not yet been experimentally validated, and the effects of the unavoidable flow perturbations due to the permeability of the porous structures are difficult to investigate analytically.

Several experimental studies on porous TEs have examined their effects on the TBL-TE noise of an airfoil [34, 35, 68, 69, 71, 86, 172]. Geyer, Sarradj and Fritzsche [68, 69, 172] characterised the flow resistivity of sixteen types of porous materials and performed a comprehensive investigation of fully porous SD 7003 airfoils made of these materials. In these studies, the far-field noise, aerodynamic performance and boundary layer parameters of the porous airfoils were measured using a microphone array, a six-component force balance and a single hot-wire probe, respectively, in an anechoic wind tunnel. Measurements were performed at various Reynolds numbers ($4 \times 10^5 \leq Re_c \leq 8 \times 10^5$) and geometric angles of attack ($-16^\circ \leq \alpha_g \leq 20^\circ$). Porous airfoils were found to reduce the TBL-TE noise by up to more than 10 dB at low-to-moderate frequencies ($St_c < 100$). However, a noise increase was observed at high frequencies, presumably due to the surface roughness of the porous material. The noise reduction by porous airfoils is largely related to the material flow resistivity, but no general dependency or scaling law was established. Moreover, the

porous materials led to a reduction in lift and an increase in drag, and the aerodynamic performance of porous airfoils gradually deteriorated with a decreasing flow resistivity. Later, Geyer and Sarradj [71] extended their work to a series of airfoils with a portion of their TE region made of porous materials. The chordwise extent (normalised by the airfoil chord) of the porous TE region varied from 0.05 to 1 (fully porous), and five types of porous materials with a different flow resistivity were examined in this study. A larger porous region led to a higher noise reduction without considering its aerodynamic disadvantage. When scaling the noise spectra with the measured lift, porous materials with a low flow resistivity were found to be not feasible for airfoil TE noise control due to their penalty in aerodynamic performance. Partially porous airfoils, even with only a small TE region made of high-flow-resistivity materials, could effectively control the TBL-TE noise. Fluctuating velocity data revealed that a decrease of flow resistivity or an increase of chordwise porous extent could lead to an increase in the boundary layer thickness, wake deficit and turbulence intensity. Herr et al. [86] measured the acoustic and aerodynamic performance of a NACA0012-derivative airfoil with a series of porous metal TEs with different micro-structures and flow resistivities. A maximum broadband noise reduction of up to 6 dB was achieved by porous TEs over low-to-moderate frequencies ($f < 10$ kHz) without significantly compromising the aerodynamic performance. Higher noise reduction was obtained using materials with a higher functional-layer flow resistivity. Moreover, a high-frequency noise increase (as reported in Refs. [68, 69, 71]) was observed for the porous metal TEs with a relatively large spanwise pore size ($> 160 \mu\text{m}$). More recently, Carpio et al. [34, 35] measured the hydrodynamic field around four porous metal-foam TEs (attached to a NACA 0018 airfoil) and the far-field noise scattered by them using a time-resolved planar PIV system and a microphone array, respectively. A broadband noise reduction of up to 10 dB was achieved over low frequencies ($f < 1.6$ kHz) by the metal foam edge with a higher permeability (lower flow resistivity), which is in accordance with previous experimental data. In contrast to the porous TEs examined in Refs. [68, 69, 71], these metal-foam TEs can lead to a reduction of turbulence intensity in the boundary layer near the TE [34, 35]. Additionally, the convection velocity and Reynolds shear stress magnitude in the TE boundary layer were also reduced. It was concluded that the low-frequency noise reduction is attributed to these changes in the TE boundary layer and

the attenuated acoustic impedance jump at the edge due to flow permeation through the porous metal foam. Unfortunately, the high-frequency noise increase was again observed and believed to be due to roughness-generated noise.

Numerically, only a handful of studies [23, 62, 163, 164] have investigated the noise generation of an airfoil with a porous TE. All these studies are based on a hybrid two-step CFD/CAA procedure, where the turbulence statistics are first obtained by the RANS [62, 163, 164] or the zonal LES [23] simulations and then used as the input for the CAA step to compute the acoustic field. The effect of porous material was modelled by a volume-average model based on a linear-friction Darcy term and a non-linear Forchheimer term, in which the physical properties of the porous material are described by porosity, permeability and Forchheimer coefficient. In the more recent studies [23, 164], the measured acoustic spectra [86] of both the solid and porous airfoils can be accurately (error within ± 3 dB) reproduced over the lower frequencies ($f < 6.3$ kHz) where noise reduction was achieved by the porous TE. However, the high-frequency noise increase was not predicted by these numerical studies. This could result from the lack of details in describing the porous material or the limited accuracy of the CFD simulations.

2.3.3 Effects of Novel Trailing-Edge Treatments on Turbulent Boundary Layer Trailing-Edge Noise

During recent years, many researchers have investigated the effects of novel TE geometries on TBL-TE noise. Analytically, Azarpeyvand et al. [17] extended Howe's model [92] and derived the analytical expression of far-field acoustic spectra for novel periodic geometries (slitted, slitted-sawtooth and sawtooth-sinusoidal serrations). These complex geometries can significantly affect the interference between the acoustic waves scattered from the edge, thus reducing the far-field noise level. Among these novel geometries, slitted-sawtooth serrations were found to be most efficient in TBL-TE noise control, which has also been confirmed experimentally [80]. Ayton [16] recently proposed a method based on the Wiener-Hopf technique for analytically solving the far-field acoustic spectrum of the TBL-TE noise scattered from arbitrary but periodically serrated TEs. Two critical noise reduction mechanisms were proposed for serrated TEs: 1) the destructive interfer-

ence (over low-to-moderate frequencies) of acoustic fields scattered from the serration root and tip, which can be maximised by square-wave geometry; 2) the acoustic energy redistribution (over high frequencies) from low cut-on modes to high cut-off modes, which is only effective for non-flat geometries. This study provided some useful insights into the optimal geometry design for TBL-TE noise control. However, the accuracy of analytical modeling is still limited by the fact that the effects of complex geometries on the turbulent flow cannot be modelled analytically.

Several experimental studies [80, 83, 84, 110, 115] have examined the noise reduction capability of TE extensions with novel geometries. It was found that the TBL-TE noise can be effectively reduced by TE brushes [64, 83, 84] by up to 10 dB (broadband reduction), slits [80] by up to 5 dB (reduction in overall sound power level *OAPWL*), perforated serrations [80] by up to 1 dB (*OAPWL* reduction), randomly distributed serrations [80] by up to 3 dB (*OAPWL* reduction), slitted serrations [80, 110] by up to 8 dB (broadband reduction) and hybrid-slitted serrations [115] by up to 8 dB (broadband reduction). Chong et al. [45] investigated the self-noise generation of a NACA 0012 airfoil with three-dimensional cut-in serrations of different serration amplitudes ($2h = 10$ or 20 mm) and wavelength-to-amplitude ratios ($\lambda/h = 0.49$ – 1.87). Serrations with such 3D geometry can achieve a broadband noise reduction of up to 6.5 dB but also promote high-amplitude narrow-band noise due to the bluntness of the cut-in serration root. Smaller serration angle and large serration amplitude ($2h/\delta \geq 1$) were found to be beneficial for TBL-TE noise reduction. In follow-up studies by Vathylakis et al. [186] and Chong et al. [40], novel TE treatments combining the cut-in serration and porous material, namely porous-serrated treatments, were investigated. The use of porous material in between the cut-in serrations can completely suppress the narrow-band noise increase due to the blunt serration roots and achieve a further 1.5 dB broadband noise reduction (compared to the cut-in serrations) without compromising the aerodynamic performance. More recently, inspired by the downy canopy on owl's flight feathers and the great potential of canopy structures [47] in attenuating surface pressure fluctuations (by up to 30 dB), Clark et al. [48] proposed a series of 3D finlet add-ons for TBL-TE noise control. In this study, 3D finlet add-ons were attached onto the airfoil surface near the TE. Broadband noise reductions of up to 10 dB can be achieved by these add-ons over high frequencies with minute aerodynamic penalty

(a slight increase in drag).

Numerically, in addition to sawtooth-serrated and porous TEs, only a few studies [13, 14, 183, 184] investigated flat-plate TE extensions with novel-serrated geometries (slitted-sawtooth serrations [184], combed-sawtooth serrations [14, 183] and curved serrations [13]). In these studies, the flow field and far-field noise were simulated using the compressible LBM and FWH acoustic analogy [63], respectively. In addition to these novel serrated TEs, the airfoil with straight and sawtooth-serrated TEs were also simulated, and their far-field noise spectra predicted by the FWH analogy were in good agreements with the experimental data measured in Ref. [112]. Simulation results indicated that both the curved and combed-sawtooth serrations are more efficient in TBL-TE noise control compared to conventional sawtooth serrations, however, their actual noise reduction capabilities have not yet been confirmed experimentally in the literature.

2.3.4 Effects of Trailing-Edge Treatments on Laminar-Transitional Boundary Layer Trailing-Edge Noise

The noise generated by the interaction between a laminar-transitional boundary layer and a treated TE, such as a serrated TE, has been rarely studied. Chong et al. [42, 44] experimentally investigated the effects of cut-in sawtooth serrations on the LBL-TE noise. It was found that the tonal noise level can be significantly reduced by such TE treatment when the serration angle and amplitude is sufficiently large. Near-wall flow characteristics obtained using a hot-wire probe and hot-film arrays indicated that the cut-in serrations promote bypass transition to suppress flow separation, which reduces the two-dimensionality of the T-S wave and sequentially restrains the amplification process in the acoustic feedback loop. More recently, Moreau and Doolan [132] measured the far-field noise and near-wake velocity fluctuations of a sharp-edge flat plate with sawtooth-serrated TE extensions at low Reynolds numbers. Contrary to the cut-in serrations examined in Refs. [42, 44], excess tonal noise was observed for the serrated extension with a small serration angle. Near-wake velocity data indicated that such geometry could induce intensive vortices at its serration tips, hence promoting the generation of high-amplitude tonal noise.

For the porous and novel TE treatments, previous studies have mainly focused on the

reduction of TBL-TE noise; the effects of these treatments on LBL-TE noise has not yet been reported in open literature. Since the latter self-noise mechanism can be the dominant noise source for airfoil applications operating at relatively low Reynolds numbers [132] (e.g., wind turbine blades operating at off-design conditions), more attention should be paid to LBL-TE noise when developing low-noise TE treatments.

2.3.5 Rotor Trailing-Edge Treatments

Numerous studies on TE treatments for stationary airfoils have been reviewed. Surprisingly, little information about rotor TE treatments for self noise control has been reported publicly. Oerlemans et al. [147] measured the noise from a reference two-blade wind turbine model, a wind turbine model with acoustically optimised profiles and a wind turbine model with TE sawtooth serrations using a microphone array in an anechoic wind tunnel. Results showed that a broadband noise reduction of 2 to 3 dB can be achieved with TE serrations. Later, Oerlemans et al. [149] extended their work to a 94m-diameter wind turbine consisting of a standard (baseline) blade, a shape-optimised blade and a blade with TE sawtooth serrations. For the most prominent operating conditions (wind speeds from 6 to 10 m/s), the noise reduction with the serrated treatment was found to increase with increasing wind speed, and an averaged A-weighted overall noise reduction of 3.2 dB was reported. More recently, Oerlemans et al. [145] reported limited experimental results (A-weighted overall noise levels) for wind turbines with a porous TE device and TE combed-sawtooth serrations. The porous treatment reduced the A-weighted overall noise level by approximately 2 dB without compromising the turbine output level. The combed-sawtooth serrations were found to be a more promising design compared to the sawtooth serrations, achieving a further noise reduction of approximately 2 dB at high wind speed. Unfortunately, no details of these two promising designs were included (except for a photo of the combed-sawtooth serrations).

2.4 Summary and Research Gaps

To better explain the research objectives, methodology and theoretical basis of this thesis, this chapter first systematically reviewed the state of knowledge on airfoil TE noise from

the theoretical, experimental and numerical perspectives. Summarised from past theoretical studies, the intensity of TBL-TE noise is related to the following characteristics: 1) surface pressure fluctuations (such as surface pressure spectrum in Ref. [6]); 2) length scale of coherent turbulent structures (such as spanwise correlation length in Ref. [6]); 3) turbulence convection velocity [6, 25, 152, 162]. These findings will be used as the theoretical basis for the analysis of the noise reduction mechanisms for porous and serrated TE treatments in Chapter 6. Experimentally, the dependency of TE noise intensity on U_∞^5 and the semi-empirical BPM model have been validated by numerous studies. In Chapter 8, they will be employed as the theoretical basis and guidance for developing the noise scaling model for wind turbine noise prediction. Numerically, various techniques (such as DNS, DNC and LES combined with FWH) have been employed to investigate the TBL-TE noise in past studies. The method of using compressible LES for flow modelling and FWH acoustic analogy for noise prediction has the advantages of relatively low computational cost (compared to DNS) and high noise prediction accuracy. Therefore, it will be employed to investigate the noise generation mechanism of an airfoil with porous TE treatment in Chapter 6. In terms of the LBL-TE noise, past studies mainly focus on its generation mechanism. Although no general consensus has been established, it can be concluded that the production of such self-noise is strongly related to the boundary layer instabilities and vortex shedding in the wake. This finding will be used to explain how the flow characteristics are related to the LBL-TE noise reduction by treated TEs in Chapter 6.

In order to identify the research gaps, a significant number of studies on TE treatments for airfoils and rotors have also been reviewed. Most of these studies have focused on the control of TBL-TE noise. TE sawtooth serrations, as the most common TE treatment, have received much attention during the last three decades. Analytical studies suggest that the noise reduction by TE sawtooth serrations is solely due to the destructive interference induced by the serrated geometries in the acoustic scattering process. However, experimental and numerical studies have indicated that the serrated geometries can significantly alter the turbulent flow structure and redistribute the momentum transport and turbulent shear stress, thus reducing the noise scattered from the edge. These findings indicate that both the source strength and scattering process need to be considered when

investigating the noise reduction mechanisms of TE treatments.

For porous TE treatments, both analytical, experimental and numerical studies have reported that significant noise reductions can be achieved over low frequencies. It was suggested that the low-frequency noise reduction may be due to: 1) reduced turbulence intensity, Reynolds shear stress and convection velocity in the boundary layer; 2) reduced acoustic impedance jump at the TE due to the flow permeation through the porous material. However, a broadband noise increase over high frequencies has been observed for most porous TE treatments in experiments. This noise increase may result from the roughness noise induced by the porous geometries, but no direct evidence has been reported in past studies. Due to the complexity of the physical properties of porous material, existing analytical and numerical studies rely on simplified geometries or models of porous media to describe the porous structures. Consequently, the high-frequency noise increase has not yet been detected in analytical and numerical studies. Moreover, the porous materials in previous experimental and numerical studies are only characterised by the flow resistivity (permeability) and porosity. Since many porous materials inherently have a good sound absorption capability, the sound absorption may also play a role in noise reduction by attenuating the noise scattering process. Prior to this thesis, no literature has been found to relate the sound absorption to the TE noise reduction.

Several novel TE treatments, including the brushes, slits, slitted serrations, porous-serrated TE and 3D finlet add-on, have shown great potential in TBL-TE noise control. The noise reduction performance of these treatments was determined by either comparing to an airfoil with straight edge, an airfoil with a flat-plate extension or an airfoil with TE sawtooth serrations, and measurements were performed using different boundary layer tripping methods and measurement techniques at different facilities and operating conditions. All these differences could potentially lead to a biased comparison, therefore it is of great importance to examine the novel TE treatments using the identical experimental setup and reference to provide a fair comparison of their noise reduction capability. Moreover, no literature has been found to evaluate the TE noise performance of rotors with novel serrated and porous treatments, nor report the effects of novel serrated, porous and porous-serrated TE treatments on LBL-TE noise.

In this thesis, the following research gaps are addressed:

1. The potential effect of the sound absorption of porous structures on TE noise generation is experimentally investigated;
2. The mechanisms of the noise reduction by porous TE treatments and the associated high-frequency noise increase are numerically investigated;
3. The noise reduction performance of a series of novel serrated, porous and porous-serrated TEs (see Table 3.4 for their geometries) on the LBL-TE noise and TBL-TE noise are experimentally evaluated using the identical measurement setup;
4. The flow characteristics around a series of novel serrated, porous and porous-serrated TEs are related to their TBL-TE noise reductions;
5. The aeroacoustic performance of rotor blades with porous, extended-serrated and cut-in-serrated TEs are experimentally evaluated.

Chapter 3

Methodology

3.1 Overview

This chapter details the experimental techniques and computational methodology employed to investigate the noise generation of airfoils and rotors with trailing-edge (TE) treatments, and the experimental techniques used for developing a noise prediction model for industrial-scale wind turbines based on university-scale wind tunnel data. It is structured as follows: first, Sec. 3.2 describes the characterisation method and geometries of the porous structures to be applied in airfoil TE noise control. Next, Sec. 3.3 details the facility, experimental setup and measurement techniques used in two experimental campaigns in the UNSW Anechoic Wind Tunnel, in which the effects of porous and serrated edge treatments on TE noise generation have been investigated. Afterwards, details of the measurements performed using the UNSW Rotor Rig are described in Sec. 3.4, where the aeroacoustic performance of rotors with treated TEs have been evaluated. Finally, the computational methodology employed to study the noise generation mechanisms of the airfoil with a porous TE is detailed in Sec. 3.5.

3.2 Acoustic Characterisation of the 3D Printed Porous Structures

Porous structures have been characterised in terms of acoustic absorption for their application in airfoil TE noise control. The sound absorption of traditional porous material is usually proportional to its thickness. However, the airfoil TE region is too thin for traditional porous material to be efficient as a sound absorber. Inspired by the micro-perforated panel (MPP) theory proposed by Maa [126, 127, 128], two types of porous structures that can achieve good sound absorption with a limited thickness have been additively manufactured (3D printed) and characterised in two measurement campaigns: MC Campaign 1 and MC Campaign 2.

3.2.1 Test Specimens

In both MC Campaign 1 and 2, 3D printed porous specimens are made of the material Visijet M3 supplied by 3D Systems Inc.®. This material has a liquid density of 1.02 g/cm^3 at 80°C , a tensile strength of 42.4 MPa , a tensile modulus of 1463 MPa and a flexural strength of 49 MPa . A high-definition professional 3D printer Projet 3500 HDMax is employed for specimen fabrication. All specimens were printed with a layer resolution of $16 \text{ }\mu\text{m}$ and an accuracy of $0.025\text{-}0.05 \text{ mm}$ per 25.4 mm of part dimension.

Figure 3.1 shows the structure of test specimens in MC Campaign 1. The geometries of these specimens are characterised by pore diameter d_0 , thickness h_0 , pore aspect ratio $AR = d_0/h_0$ and porosity $\phi = V_v/V_T$, where V_v is the volume of void-space and V_T is the total volume of material. The acoustic properties of ten porous specimens and three reference specimens were measured, where the reference specimens are used to evaluate the effectiveness of the porous specimens. All cylinder specimens have a diameter of $D_0 = 29 \text{ mm}$. For the ten porous specimens P1 to P10, the porosity ϕ ranges from 5.35 to 11.53%; pore diameter d_0 ranges from 0.6 mm to 1 mm and thickness h_0 ranges from 5 mm to 10 mm. Reference specimen R1 is a 3D printed solid cylinder with a diameter $D_0 = 29 \text{ mm}$ and thickness $h_0 = 10 \text{ mm}$. Specimens 40PPI, 20PPI and 10PPI are aluminium foams with a pore density of 40, 20 and 10 pores per inch, respectively. According to

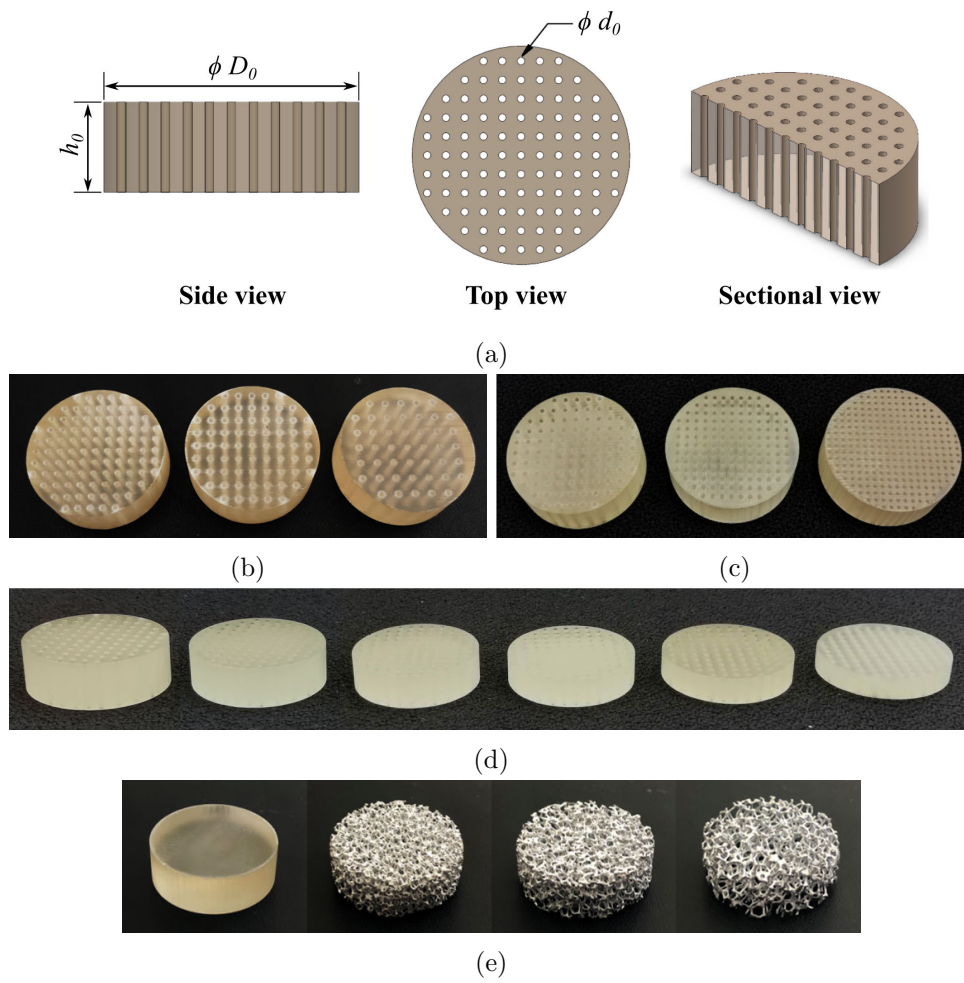


Figure 3.1: Geometries of the 3D printed micro-tube specimens and reference specimens: (a) schematic of micro-tube structures; photos of specimens with (b) different porosity ϕ , (c) different pore diameter d_0 and (d) different thickness h_0 ; (e) photos of reference specimens (from left to right): SR (3D printed solid resin with $h_0 = 10$ mm), 40PPI, 20PPI and 10PPI (aluminium foam with $\phi = 92$ –94%).

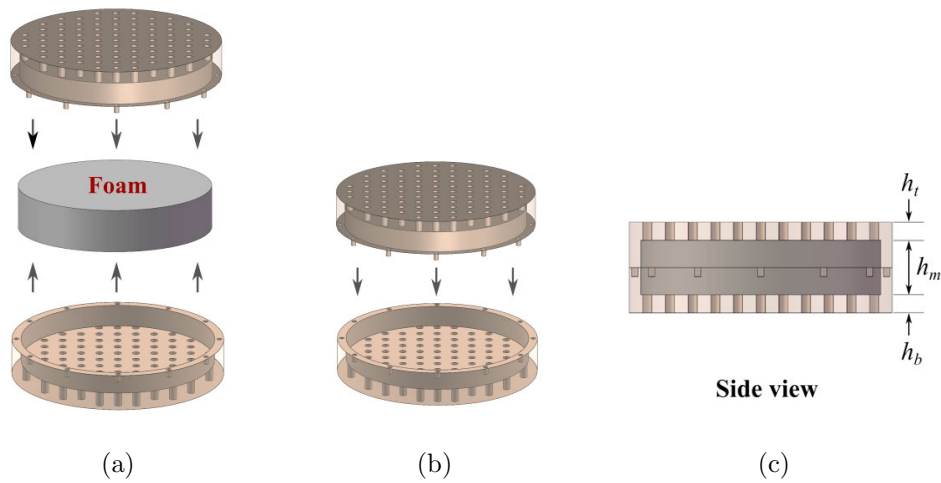


Figure 3.2: Geometries of the 3D printed micro-perforated housings: (a) with melamine resin foam (Basotect® foam) infill; (b) with an air gap; (c) schematic of the assembled specimen and its dimensions.

Table 3.1: Geometric parameters of micro-tube specimens, reference specimen and porous aluminium specimens in MC Campaign 1.

Specimen	No. of Holes	Pore Diameter d_0 (mm)	Porosity ϕ (%)	Thickness h_0 (mm)	Aspect Ratio AR
P1	97	1	11.53	10	10.0
P2	69	1	8.20	10	10.0
P3	45	1	5.35	10	10.0
P4	146	0.8	11.11	10	12.5
P5	269	0.6	11.51	10	16.7
P6	97	1	11.53	9	9.0
P7	97	1	11.53	8	8.0
P8	97	1	11.53	7	7.0
P9	97	1	11.53	6	6.0
P10	97	1	11.53	5	5.0
SR	0	0	0	10	N/A
40PPI	N/A	N/A	92–94	10	N/A
20PPI	N/A	N/A	92–94	10	N/A
10PPI	N/A	N/A	92–94	10	N/A

Table 3.2: Geometric parameters of micro-perforated housings with an air gap or acoustic foam infill in MC Campaign 2.

Specimen	Pore Diameter d_0 (mm)	Porosity ϕ (%)	h_t (mm)	h_m (mm)	h_b (mm)	Gap Media
PA1	1	11.53	1	8	1	Air
PA2	1	11.53	2	6	2	Air
PA3	1	11.53	3	4	3	Air
PA4	1	11.53	4	2	4	Air
PF1	1	11.53	1	8	1	Foam
PF2	1	11.53	2	6	2	Foam
PF3	1	11.53	3	4	3	Foam
PF4	1	11.53	4	2	4	Foam
F10 ^a	N/A	>99	0	10	0	Foam

^a F10 is a 10 mm-thick Basotech[®] foam without the micro-perforated housing.

the manufacturer, all porous aluminium specimens have a porosity of 92–94 %. Detailed geometric parameters of the test specimens in MC Campaign 1 are listed in Table 3.1.

In MC Campaign 2, a novel structure consisting of a micro-perforated housing (geometries based on specimen P1) and acoustic foam (Basotech[®] foam) infill is additively manufactured and characterised. Figure 3.2 shows the structure of test specimens in MC Campaign 2. All specimens have a diameter D_0 of 29 mm and total thickness h_0 of 10 mm.

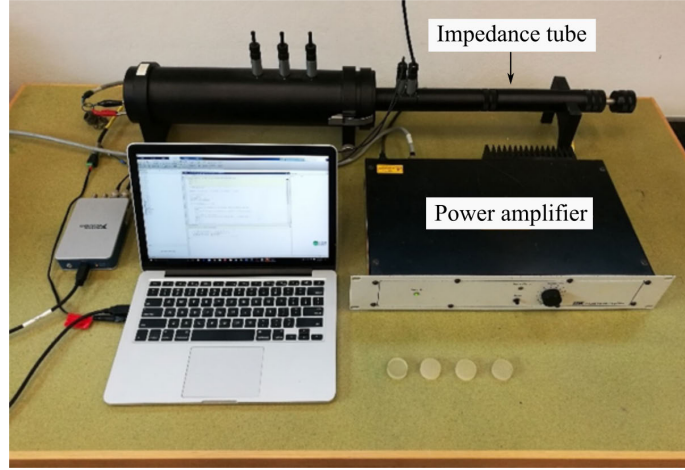
The pore diameter d_0 and porosity ϕ of the micro-perforated housing part are identical to those of specimen P1 in MC Campaign 1. For specimens PA1–PA4, thickness of the top micro-perforated panel h_t is identical to that of the bottom micro-perforated panel h_b , varying from 1–4 mm. In between these two panels, an air gap is present with a thickness h_m varying from 2–8 mm. For specimens PF1–PF4, their 3D printed geometries are identical to those of PA1–PA4, whereas the air gap is replaced by a cylindrical Basotect[®] foam (melamine resin foam). Note that the top and bottom panels are connected through pins as shown in Figure 3.2. Detailed geometric parameters of test specimens in MC Campaign 2 are listed in Table 3.2.

3.2.2 Measurement Setup and Theoretical Background

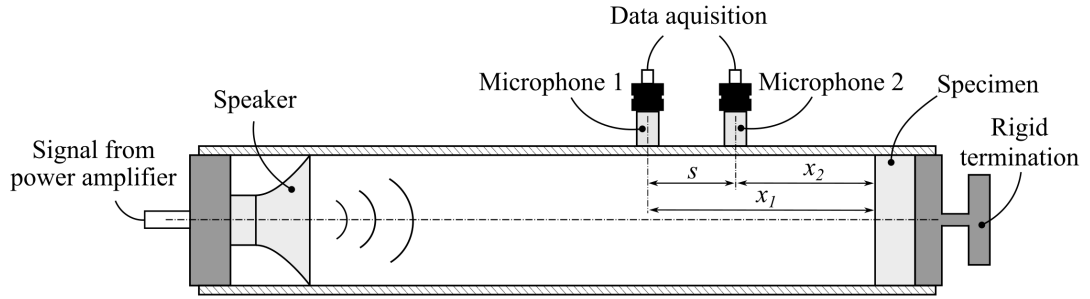
A two-microphone impedance tube B&K type 4206 was used to characterise the acoustic properties of the porous specimens proposed in this thesis. As shown in Figure 3.3a, it consists of a solid anodised aluminium tube with a diameter of 29 mm (on the right) and a loudspeaker (at the left end). The specimen was held at a rigid termination at the right end of the tube. A B&K LDS PA25E power amplifier drove the loudspeaker to act as a sound source. Sound pressures were measured by two GRAS[®] type 40 PH 1/4 inch free-field microphones positioned separately on the top of the tube. A laptop and a 24 bit NI 9234 CompactDAQ were used to generate the noise source signal and collect data. The test specimen was fixed at the right end of the impedance tube as shown in Figure 3.3b, where the distances from the test specimen front face to the furthest and nearest microphones are denoted as x_1 (0.17 m) and x_2 (0.15 m), respectively, and the distance between two microphones is denoted as $s = x_1 - x_2$ (0.02 m).

Acoustic characterisation by the impedance tube is based on the transfer function method [46]. It uses the transfer function between the signals measured by two microphones at different locations and the transfer function between these two locations for incident and reflected waves to calculate the acoustic properties of the test specimen. The transfer functions for the incident wave H_I and for the reflected wave H_R can be determined by

$$H_I = \frac{p_{2I}}{p_{1I}} = e^{-jk_0(x_1-x_2)} = e^{-jk_0s} \quad (3.1)$$



(a)



(b)

Figure 3.3: Acoustic characterisation setup:(a) measurement setup in-situ;(b) Schematic of impedance tube.

$$H_R = \frac{p_{2R}}{p_{1R}} = e^{-jk_0(x_1-x_2)} = e^{jk_0s}, \quad (3.2)$$

where p_{iI} and p_{iR} are the incident and reflected sound pressure at the position of microphone i , s is the distance between the two microphones and k_0 is the wave number $k_0 = 2\pi f/c_0$. H_I and H_R only vary when microphone distance s changes. The transfer function between the signals measured from microphones 1 and 2 can be determined as

$$H_{12} = \frac{p_2}{p_1} = \frac{e^{jk_0x_2} + r_p e^{-jk_0x_2}}{e^{jk_0x_1} + r_p e^{-jk_0x_1}} \quad (3.3)$$

where r_p is the complex sound reflection coefficient, and p_1 and p_2 are the sound pressure measured by microphone 1 and 2. Manipulating Eq. (3.3), the complex sound reflection coefficient r_p , complex acoustic impedance Z and sound absorption coefficient α_p can then be obtained by

$$r_p = \frac{H_{12} - H_I}{H_R - H_{12}} e^{2jk_0x_1}, \quad (3.4)$$

$$Z = \frac{1 + r_p}{1 - r_p} \rho c, \quad (3.5)$$

$$\alpha_p = 1 - |r_p|^2. \quad (3.6)$$

3.2.3 Maa's Model of Micro-Perforated Panel

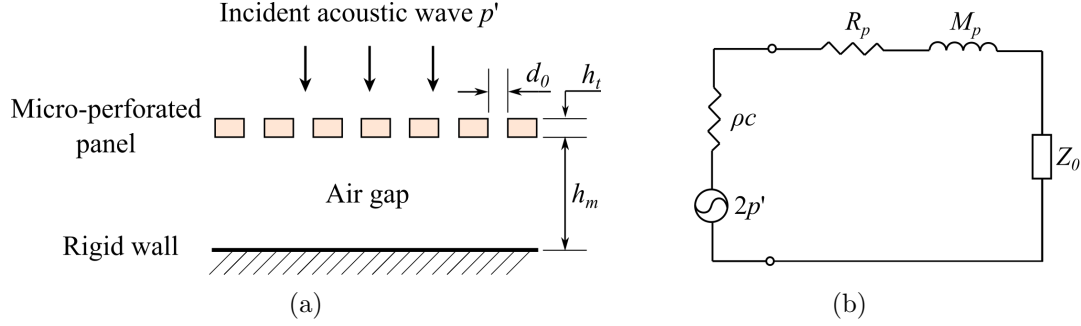


Figure 3.4: Schematics of (a) micro-perforated resonant absorber (micro-perforated panel with an air gap) and (b) its equivalent circuit.

In MC Campaign 2, the analytical model of a micro-perforated panel proposed by Maa [126] is used to predict the sound absorption of the top micro-perforated panel and air gap, which corresponds to regions of thickness h_t and h_m as shown in Figure 3.2c. In order to attain broadband high acoustic absorption, a perforated panel should match the characteristic acoustic resistance of air while retaining low acoustic mass. Since the acoustic resistance is inversely proportional to the perforation diameter, an ordinary perforated panel with large-size perforations can not provide enough acoustic resistance to achieve efficient acoustic absorption. However, when the perforations are reduced to sub-millimeter size ($d_0 < 1$ mm), sufficient acoustic resistance can be provided for efficient sound absorption.

Figure 3.4 shows the structure of a micro-perforated panel absorber and its equivalent circuit. In Maa's model, the micro-perforated panel are treated as the parallel connection of a large number of micro-tubes. According to the solutions obtained by Rayleigh [158] for the acoustic wave in small cylindrical tube and the simplified derivation by Crandall [51], the acoustic impedance of a single micro-tube Z_1 can be approximated (error $< 6\%$) by [126, 127, 128]

$$Z_1 = \frac{32\rho\mu h_t}{d_0^2} \sqrt{1 + \frac{k_p^2}{32}} + j\omega\rho h_t \left(1 + \frac{1}{\sqrt{9 + k_p^2/2}} \right), \quad (3.7)$$

where ρ is the air density, μ is the kinetic viscosity, d_0 is the perforation diameter, h_t is the perforation height (panel thickness), $\omega = 2\pi f$ is the angular frequency and $k_p = d_0\sqrt{\omega/4\mu}$. Considering the end effects induced by sound radiation from the micro-tube end and friction loss of the flow through micro-tube, acoustic impedance Z_1 can be corrected to

$$Z_1 = \frac{32\rho\mu h_t}{d_0^2} \sqrt{1 + \frac{k_p^2}{32} + \frac{\sqrt{2}k_p d_0}{8 h_t}} + j\omega\rho h_t \left(1 + \frac{1}{\sqrt{9 + k_p^2/2}} + 0.85 \frac{d_0}{h_t}\right). \quad (3.8)$$

Assuming the interference of the micro-tubes are negligible, the total impedance from the micro-perforated panel Z_p can be obtained by dividing porosity of the panel ϕ , which is given by

$$Z_p = \frac{Z_1}{\phi}. \quad (3.9)$$

According to the equivalent circuit as shown in Figure 3.4b, the total acoustic impedance of the micro-perforated resonant absorber (micro-perforated panel with an air gap) Z_{total} is given by

$$Z_{total} = Z_p + Z_0. \quad (3.10)$$

The acoustic impedance of the air gap Z_0 is determined by

$$Z_0 = -j\rho c \cot\left(\frac{\omega h_m}{c}\right), \quad (3.11)$$

where c is sound of speed and h_m is thickness of the air gap. The acoustic absorption of the micro-perforated resonant absorber α_p can then be determined by

$$\alpha_p = \frac{4R_p\rho c}{(R_p + \rho c)^2 + (\omega M_p - \rho c \cot(\omega h_m/c))^2}, \quad (3.12)$$

where R_p and M_p are the acoustic resistance and acoustic mass of the micro-perforated panel determined from Eqs. (3.8) and (3.9), given by

$$R_p = \frac{32\rho\mu h_t}{\phi d_0^2} \sqrt{1 + \frac{k_p^2}{32} + \frac{\sqrt{2}k_p d_0}{8 h_t}}, \quad (3.13)$$

$$M_p = \frac{\rho h_t}{\phi} \left(1 + \frac{1}{\sqrt{9 + k_p^2/2}} + 0.85 \frac{d_0}{h_t}\right). \quad (3.14)$$

3.3 Anechoic Wind Tunnel Measurements

Two experimental campaigns were conducted in the UNSW Anechoic Wind Tunnel for the purpose of 1) investigating airfoil low-noise TE treatments and 2) predicting wind turbine noise using data obtained from a university-scale lab. A summary of experimental measurements taken in the UAT is presented in Table 3.3.

Table 3.3: Summary of UAT measurements

Campaign name	Airfoil profile	Measurements
UAT Campaign 1	NACA0012	Microphone array, hot-wire near-wake velocity
UAT Campaign 2	Cambered wind turbine airfoil	Microphone array, aerodynamic force, pitot tube near-wake velocity

3.3.1 Facility

The UNSW Anechoic Wind Tunnel (UAT) is an open-jet wind tunnel with a $0.455\text{ m} \times 0.455\text{ m}$ test-section that is surrounded by a $3\text{ m} \times 3.2\text{ m} \times 2.15\text{ m}$ anechoic chamber. The tunnel is driven by a centrifugal fan that draws air into the test chamber through a $1.07\text{ m} \times 1.07\text{ m}$ honeycomb, five turbulence reduction screens and a 5.5:1 area ratio contraction section. The air then flows into the anechoic chamber through the inlet as shown in Figure 3.5. The airfoil model is mounted immediately downstream of the inlet between two end-plates. The maximum freestream velocity of this facility is approximately 60 m/s. The acoustic absorbing walls in the test chamber are made from 250 mm thick, acoustic grade Basotect[®] foam, which leads to a quasi-anechoic environment inside the chamber for frequencies above approximately 250 Hz. An acoustically lined U-bend diffuser-muffler system, placed between the fan and the chamber, serves to expand the flow and shield the test-section from the fan noise. The freestream, test-section velocity is monitored using the difference between the settling chamber and test-section pressure. The uncertainty in the velocity measurement is 0.02 m/s at freestream velocity of 30 m/s.

The level of background noise is a critical characteristic for the quality of acoustic measurements obtained in a wind tunnel. The background noise of the UAT at freestream velocities of 10 to 50 m/s (every 2 m/s) was characterised by a GRAS[®] type 40 PH 1/4

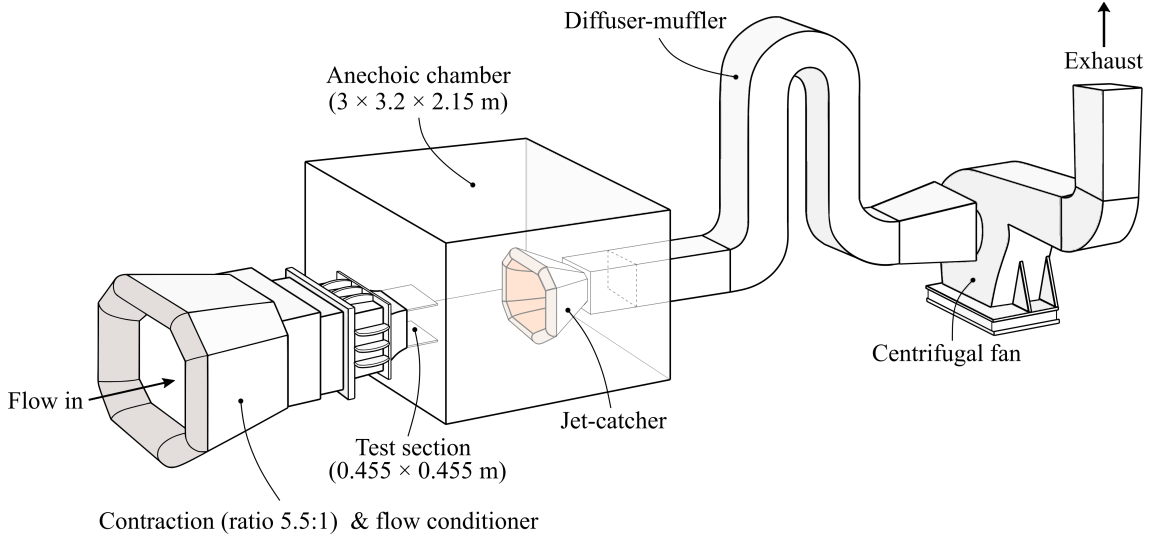
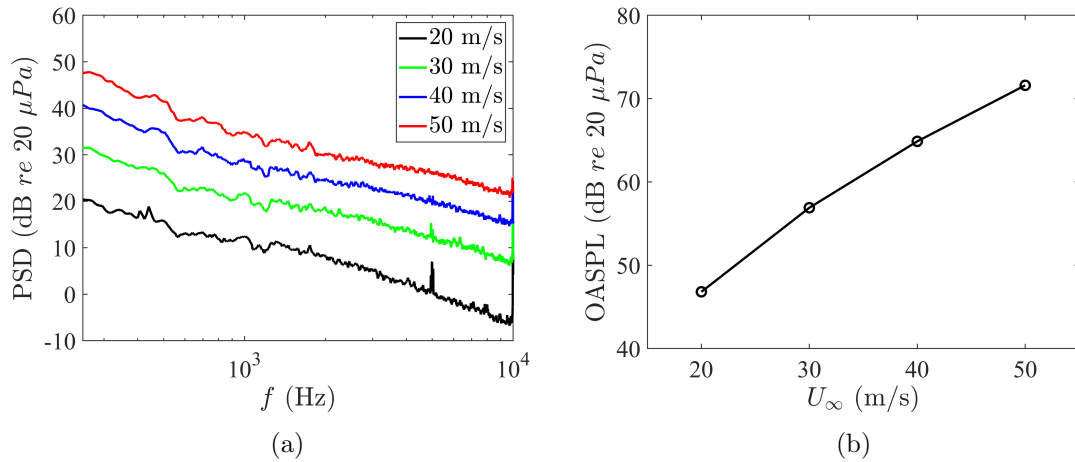


Figure 3.5: Schematic of the UNSW Anechoic Wind Tunnel

inch microphone placed 800 mm away from center line of the test section pointing to the flow perpendicularly. Figure 3.6 shows the measured power spectral density (PSD) and overall sound pressure level (OASPL) of the background noise at freestream velocities of 20, 30, 40 and 50 m/s. All background noise spectra show a low noise level and a approximately ‘linear’ (in logarithmic scale) frequency characteristics.

Figure 3.6: Background noise measured in UAT at $U_{\infty} = 20, 30, 40$ and 50 m/s: (a) power spectral density (PSD); (b) overall sound pressure level (OASPL) over 250 to 10000 Hz.

The turbulence intensity and flow uniformity of the UAT were characterised using a Dantec Dynamics[®] miniature hot-wire probe and a 4-hole TFI[®] Cobra 382 type pressure probe. All flow characterisations were conducted at freestream velocity $U_{\infty} = 30$ m/s. Figure 3.7 presents the turbulence intensity measured by the hot-wire and Cobra probe along the center-line of the jet core at streamwise location $x/D_H = 0 - 1.4$ ($x/D_H = 0$ is at

the contraction outlet plane, and positive x stands for downstream locations), where D_H is the width of the test section ($D_H = 0.455$ m). The results obtained with the hot-wire and Cobra probe show good consistency, and the turbulence intensity $I_{uu} = \sqrt{u'^2}/U$ (u' is the fluctuating streamwise velocity and U is the local mean velocity) along the jet core center-line varies from 0.22 % to 0.62 %. The test model is usually installed at a downstream location x/D_H between 0 and 0.6, where I_{uu} maintains steady and low (around 0.25 % at $U_\infty = 30$ m/s).

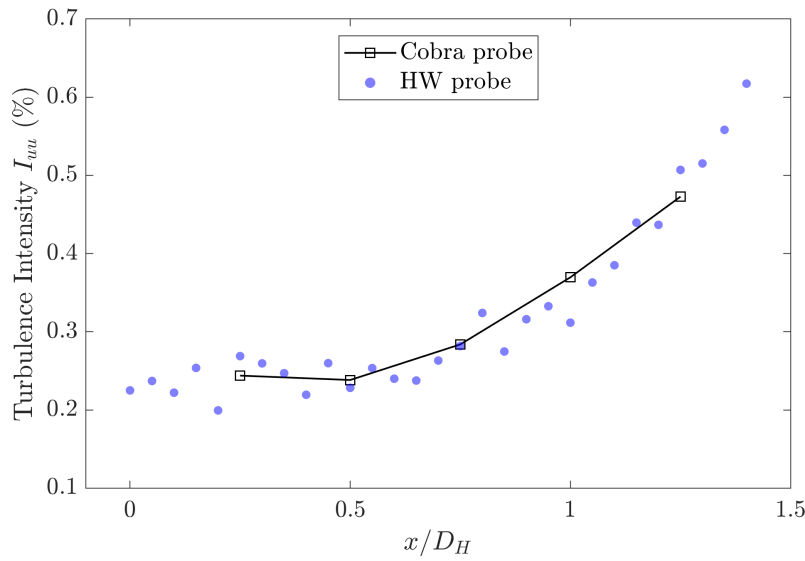


Figure 3.7: Turbulence intensity measured by hot-wire and Cobra probe along the jet core center-line.

Figure 3.8 shows the mean velocity profiles across the mid-plane of the contraction outlet at downstream location $x/D_H = 0.25, 0.5, 1$ and 1.5 in y and z directions. The flow in the jet potential core is highly uniform between $-0.4 D_H$ to $0.4 D_H$ on the cross-lines in y and z directions at all cross-stream planes.

Figure 3.9 shows the turbulence intensity I_{uu} results obtained from the same dataset acquired with the hot-wire probe. For cross-lines in y and z directions on the planes at $x/D_H = 0.25$ and 0.5 , the distribution of I_{uu} in the jet core region ($|y| < 0.15D_H$ and $|z| < 0.15D_H$) is highly uniform and is maintained at a low level. The turbulence intensity increases rapidly near the edges of the contraction outlet, indicating the presence of the turbulent shear layer around the jet potential core. The size of the low turbulence region keeps reducing on the planes further downstream ($x/D_H = 1$ and 1.5) due to the development of the shear layer. All flow measurements were conducted at the region where

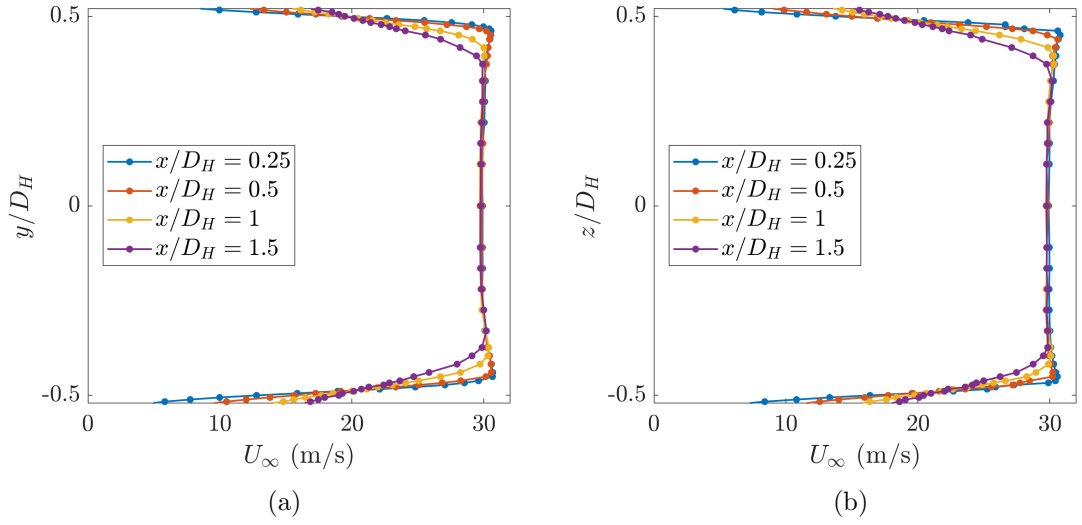


Figure 3.8: The hot-wire measurement results of the mean velocity profiles across the mid-plane of the contraction outlet at various downstream locations in (a) the y-direction and (b) the z-direction at $U_\infty = 30$ m/s.

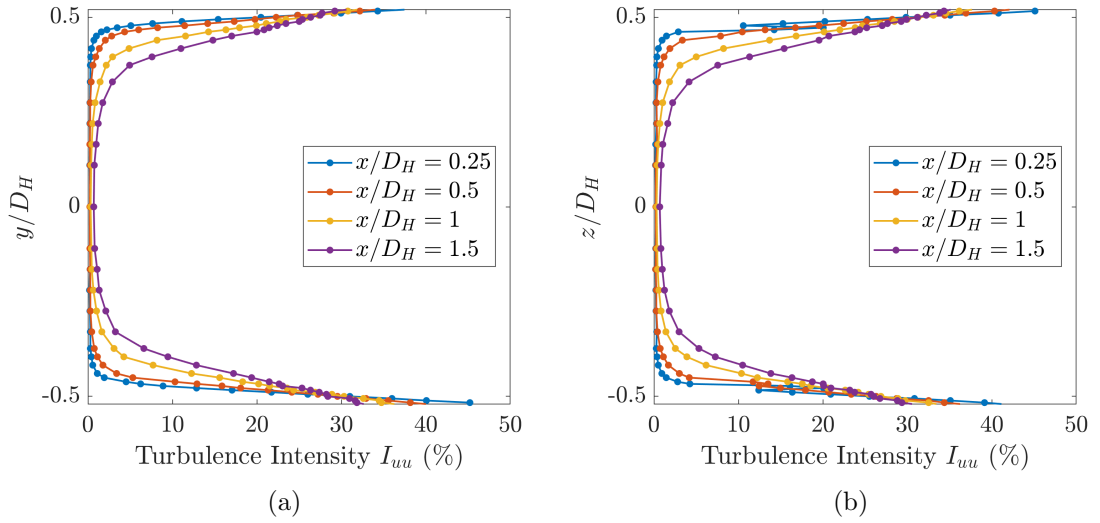


Figure 3.9: The hot-wire measurement results of the turbulence intensity I_{uu} across the mid-plane of the contraction outlet at various downstream locations in (a) the y-direction and (b) the z-direction at 30 m/s.

the flow is highly uniform and has low turbulence level ($x < 0.7D_H$, $|y| < 0.15D_H$ and $|z| < 0.15D_H$).

Figures 3.10 and 3.11 present the mean velocity and turbulence intensity I_{uu} results obtained using the Cobra probe on the cross-stream planes at $x/D_H = 0.25$ and 0.5 in a form of colormaps. This aims to evaluate the effects of the contraction geometries on the flow uniformity. The results have shown that the mean velocity and turbulence intensity are preserved uniformly over a large region ($|y| < 0.3D_H$ and $|z| < 0.3D_H$) on both planes,

indicating the flow uniformity in the jet potential core is not significantly affected by the octagonal geometry of the contraction outlet.

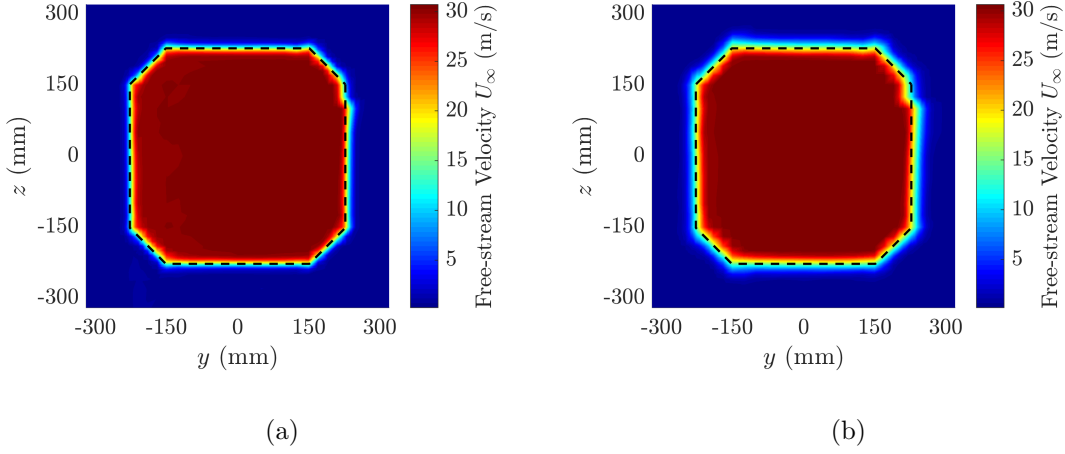


Figure 3.10: Colormaps of the mean velocity ($U_\infty = 30$ m/s) measured by Cobra probe on the cross-stream planes at (a) $x/D_H = 0.25$ and (b) 0.5. Boundary of the test-section inlet is marked by the dashed black line.

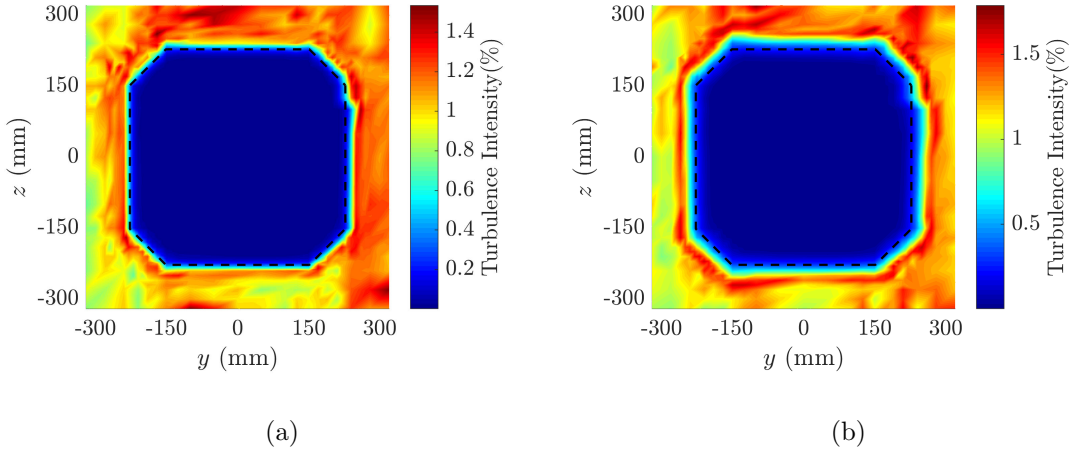


Figure 3.11: Colormaps of the turbulence intensity ($U_\infty = 30$ m/s) measured by Cobra probe on the cross-stream planes at (a) $x/D_H = 0.25$ and (b) 0.5. Boundary of the test-section inlet is marked by the dashed black line.

3.3.2 Test Models and Setup

UAT Campaign 1

The airfoil model used in UAT Campaign 1 is composed of a main aluminium body and an additively manufactured resin flat-plate extension (see Figure 3.12a). The main body

has a NACA0012 profile with a span of 0.455 m, a theoretical chord of 0.2 m and an actual chord of 0.19 m (due to truncated TE). The extension plate has a total length of 0.05 m (0.04 m for the flat-plate region which extends the chord) and a thickness of 1 mm. Unless otherwise specified, the overall chord length of the airfoil model, 0.24 m, will be used as the reference chord length for UAT Campaign 1.

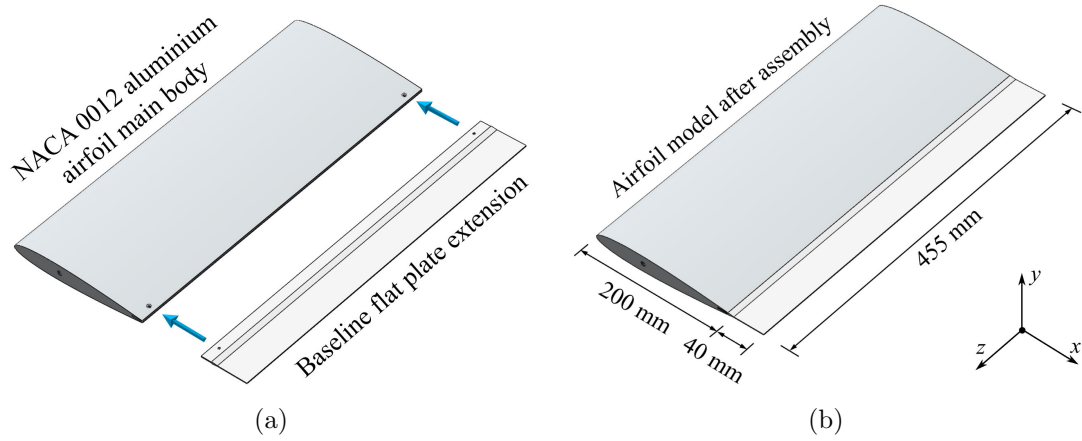

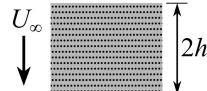
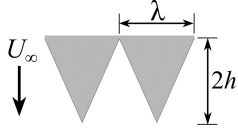
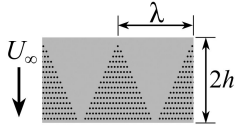
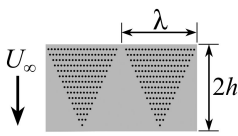
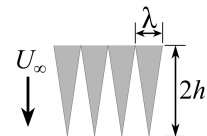


Figure 3.12: CAD drawings of the airfoil model. (a) Model before assembly; (b) Model after assembly (dimensions included).

A total of 12 TE extension designs, including one baseline flat-plate extension, have been investigated. The geometrical parameters for these extensions are summarised in Table 3.4. This experimental campaign focuses on characterising the acoustic performance and near wake flow of porous, novel serrated, combined porous-serrated and serrated-porous flat-plate TEs. The flat-plate extension on the baseline model serves as a reference to keep the maximum chord, hence the maximum chord-based Reynolds number Re_c , identical for all cases. Xfoil predictions of the lift coefficients for the baseline model and a bare NACA0012 airfoil of 200 mm chord only show a difference of up to approximately 5% at the same flow speed and angle of attack. This indicates the effects of the thin flat-plate extension on aerodynamic lift generation is not significant. For extensions that have porous structures, their porous regions consist of a series of uniformly-spaced cylindrical through-holes with 0.8 mm diameter on the flat-plate and share the same porosity ϕ (defined as the ratio of permeable area A_P to the area of porous region on the flat-plate extension A_{FP} , i.e., $\phi = A_P/A_{FP}$) of 0.13, which was optimally determined on the basis of acoustic absorption measurements in Chapter 4. For extensions that have sawtooth-serrated structures, they have different values for λ and λ/h (the definitions of λ and h are summarised in Table 3.4),

and their geometries are based on two basic sawtooth-serrated cases (NS and WS). For extensions NS, NSP, NPS, CS, CSP, SS and SSP, they share the same λ and λ/h values, and the comparison between these cases can provide insight to evaluate the effects of novel serrations and novel poro-serrated structures on TE noise reduction/generation.

Table 3.4: Geometries for TE extensions tested in this study. The direction of free stream velocity U_∞ is also shown in the sketch (from top to bottom).

Sketches	Descriptions	Abbr.
	Baseline TE: unserrated, nonporous reference flat-plate extension, amplitude $2h=40$ mm, thickness $b=1$ mm	BL
	Porous TE: unserrated, porous flat-plate extension, amplitude $2h=40$ mm, porosity $\phi=0.13$, hole diameter $d_0=0.8$ mm, $b=1$ mm	P
	Wide-serrated TE: wide-sawtooth-serrated flat-plate extension, $2h=40$ mm, wave length $\lambda=36$ mm, $\lambda/h=1.8$, $b=1$ mm	WS
	Wide-serrated-porous TE: wide serrations (tips pointing in the freestream velocity direction) combined with porous serrations. $2h=40$ mm, $\lambda=36$ mm, $\lambda/h=1.8$, $\phi=0.13$, $d_0=0.8$ mm, $b=1$ mm	WSP
	Wide-porous-serrated TE: porous serrations (tips pointing in the freestream velocity direction) combined with wide serrations. $2h=40$ mm, $\lambda=36$ mm, $\lambda/h=1.8$, $\phi=0.13$, $d_0=0.8$ mm, $b=1$ mm	WPS
	Narrow-serrated TE: narrow-sawtooth-serrated flat-plate extension, $2h=40$ mm, $\lambda=12$ mm, $\lambda/h=0.6$, $b=1$ mm	NS

	<p>Narrow-serrated-porous TE: narrow serrations (tips pointing in the freestream velocity direction) combined with porous serrations. $2h=40$ mm, $\lambda=12$ mm, $\lambda/h=0.6$, $\phi=0.13$, $d_0=0.8$ mm, $b=1$ mm</p>	NSP
	<p>Narrow-porous-serrated TE: porous serrations (tips pointing in the freestream velocity direction) combined with narrow serrations. $2h=40$ mm, $\lambda=12$ mm, $\lambda/h=0.6$, $\phi=0.13$, $d_0=0.8$ mm, $b=1$ mm</p>	NPS
	<p>Curved-serrated TE: curved-sawtooth-serrated flat-plate extension, $2h=40$ mm, $\lambda=12$ mm, $\lambda/h=0.6$, $b=1$ mm</p>	CS
	<p>Curved-serrated-porous TE: curved serrations (tips pointing in the freestream velocity direction) combined with porous serrations. $2h=40$ mm, $\lambda=12$ mm, $\lambda/h=0.6$, $\phi=0.13$, $d_0=0.8$ mm, $b=1$ mm</p>	CSP
	<p>Slitted-serrated TE: slitted-sawtooth-serrated flat-plate extension $2h=40$ mm, $\lambda=12$ mm, $\lambda/h=0.6$, $b=1$ mm</p>	SS
	<p>Slitted-serrated-porous TE: slitted serrations (tips pointing in the freestream velocity direction) combined with porous serrations. $2h=40$ mm, $\lambda=12$ mm, $\lambda/h=0.6$, $\phi=0.13$, $d_0=0.8$ mm, $b=1$ mm</p>	SSP

Measurements of the airfoil model were taken under two boundary layer conditions: 1) natural boundary layer transition for the investigation of laminar-transitional boundary layer trailing-edge (LBL-TE) noise (UAT Campaign 1a); 2) forced boundary layer transition for the investigation of turbulent boundary layer trailing-edge (TBL-TE) noise (UAT Campaign 1b). Note that the forced boundary layer transition was achieved by installing a 0.4 mm thick zig-zag Glasflügel turbulator at 10% chord on both sides of the

airfoil model. In **UAT Campaign 1a**, the acoustic and flow measurements of the 12 TE extensions attached to the natural-transitioned airfoil were taken at freestream velocities from 12 m/s to 20 m/s corresponding to Reynolds numbers of 1.9×10^5 to 3.2×10^5 . In **UAT Campaign 1b**, the extensions BL, P, NS, CS, NSP and CSP were tested on the forced-transitioned airfoil at freestream velocities from 20 m/s to 50 m/s corresponding to Reynolds numbers of 3.2×10^5 to 8×10^5 . For all measurements in UAT Campaign 1, the airfoil model was set at a geometric angle of attack of 4° , which corresponds to an effective angle of attack of 1.9° after the open-jet correction using Eq. (3.29).

Figure 3.13 shows the acoustic measurement setup for UAT Campaign 1. The airfoil

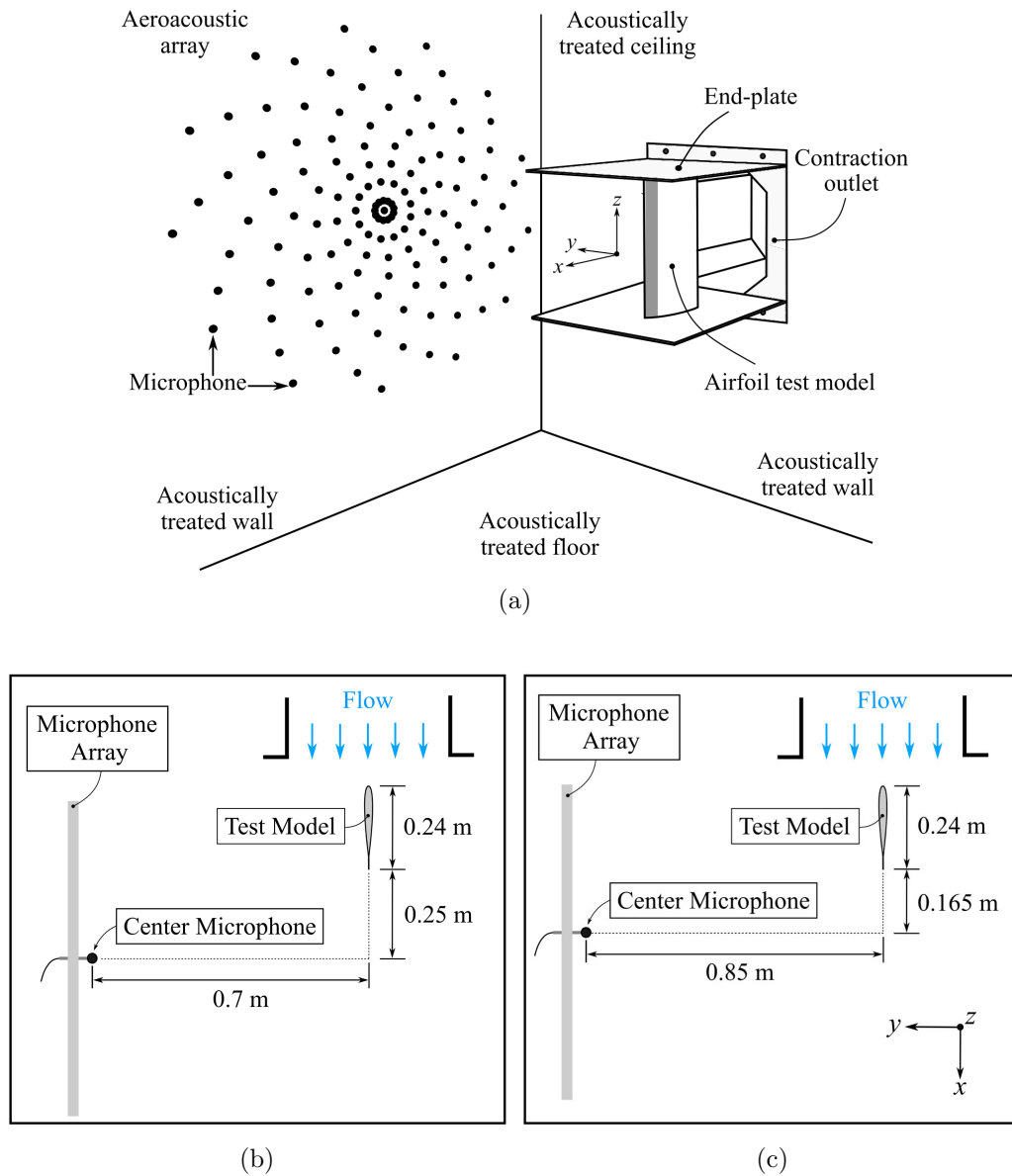


Figure 3.13: Schematics of the acoustic measurement setup for UAT Campaign 1: (a) perspective view; top view for (b) UAT Campaign 1a and (c) UAT Campaign 1b.

with TE extension was mounted between two end-plates. A 64-microphone phased array was installed on the pressure-side of the airfoil to measure the far-field sound. The microphones in the array were arranged in an optimised spiral fashion to have the smallest beamwidth possible at the largest aperture possible [155]. The location of the array centre relative to the airfoil TE (set at zero geometric angle of attack) in UAT Campaign 1a and 1b are shown in Figures 3.13b and 3.13c, respectively. The array utilised GRAS[®] type 40 PH 1/4 inch microphones which have a flat response (within ± 2 dB) up to 20 kHz. A wind-screen was installed on each array microphone to shield them from extraneous noise which might be present due to recirculation within the anechoic chamber. The acoustic pressure from the microphones was acquired using a National Instrument[®] PXI platform with 24-bit resolution at a sampling rate of 2^{16} Hz for 32 s.

Hot-wire anemometry was used to perform the near wake survey of streamwise velocity of the novel TE extensions. In **UAT Campaign 1a**, three Dantec Dynamics miniature hot-wire probes were used for measuring the mean and fluctuating velocity 1 mm ($0.004c$) downstream of the TE of natural-transitioned airfoil model (see Figure 3.14). Probes were held in a 3D printed aerodynamic probe holder which was mounted to a Dantec[®] traverse (positional uncertainty of $6.25 \mu m$) through an extruded aluminium aerodynamic traverse arm. The three probes were oriented parallel to the free stream velocity and positioned at 1 mm downstream of the TE at multiple span-wise locations, where the z coordinates for

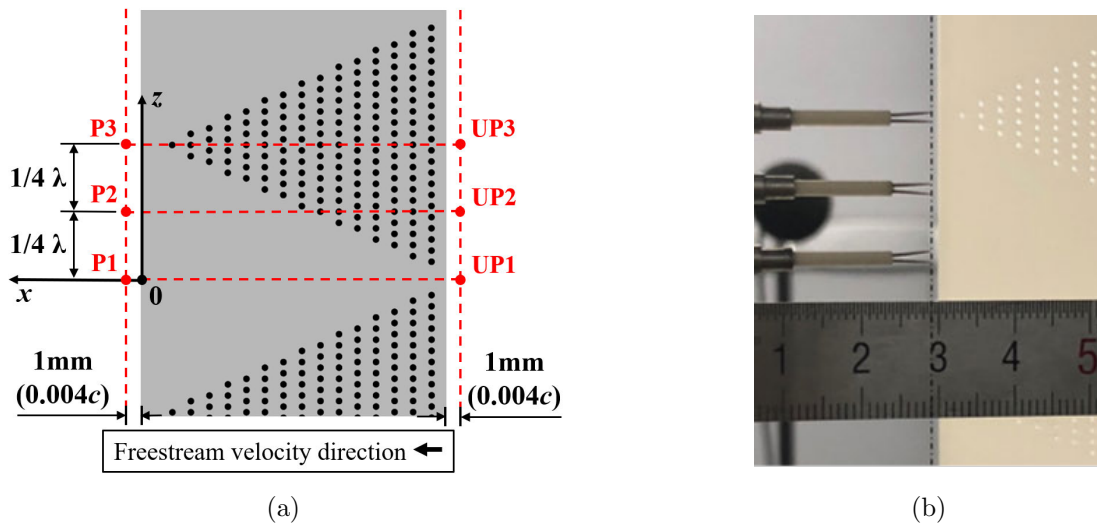


Figure 3.14: Flow measurement setup of UAT Campaign 1a: (a) Schematic of the measurement locations for hot-wire probes (y axis is positive out-of-plane); (b) Positions of hot-wire probes *in-situ*.

positions P1, P2 and P3 are 0 , $1/4 \lambda$ and $1/2 \lambda$, respectively. Note that positions P1 and P3 point towards streamlines along solid and porous geometries respectively, and position P2 is at the midpoint of the line connecting P1 and P3. These three positions are $1/4 \lambda$ apart from each other. For serrated geometries, P1 and P3 correspond to the positions downstream of the tip and gap of the serration. The flow measurements were taken at a freestream velocity $U_\infty = 18 \text{ m/s}$, and the hot-wire probes were traversed along the y -axis (positive out-of-plane in Figure 3.14a) from -50 to 50 mm . In addition, the boundary layer profiles at 1 mm upstream of the TE extensions (locations UP1, UP2 and UP3 as shown in Figure 3.14a) on the suction side were also measured along the y -axis from 0.6 to 50 mm . Each velocity record was sampled at $51,200 \text{ Hz}$ for 32 s .

In **UAT Campaign 1b**, a Dantec Dynamics miniature hot-wire probe was used for the measurement of mean and fluctuating velocity. The movement of this probe was achieved using the same traversing system as UAT Campaign 1a. Flow measurements were performed in a streamwise-normal plane 2 mm ($0.008c$) downstream of the TE of forced-transitioned airfoil model (see Figure 3.15). The velocity data were acquired at 325

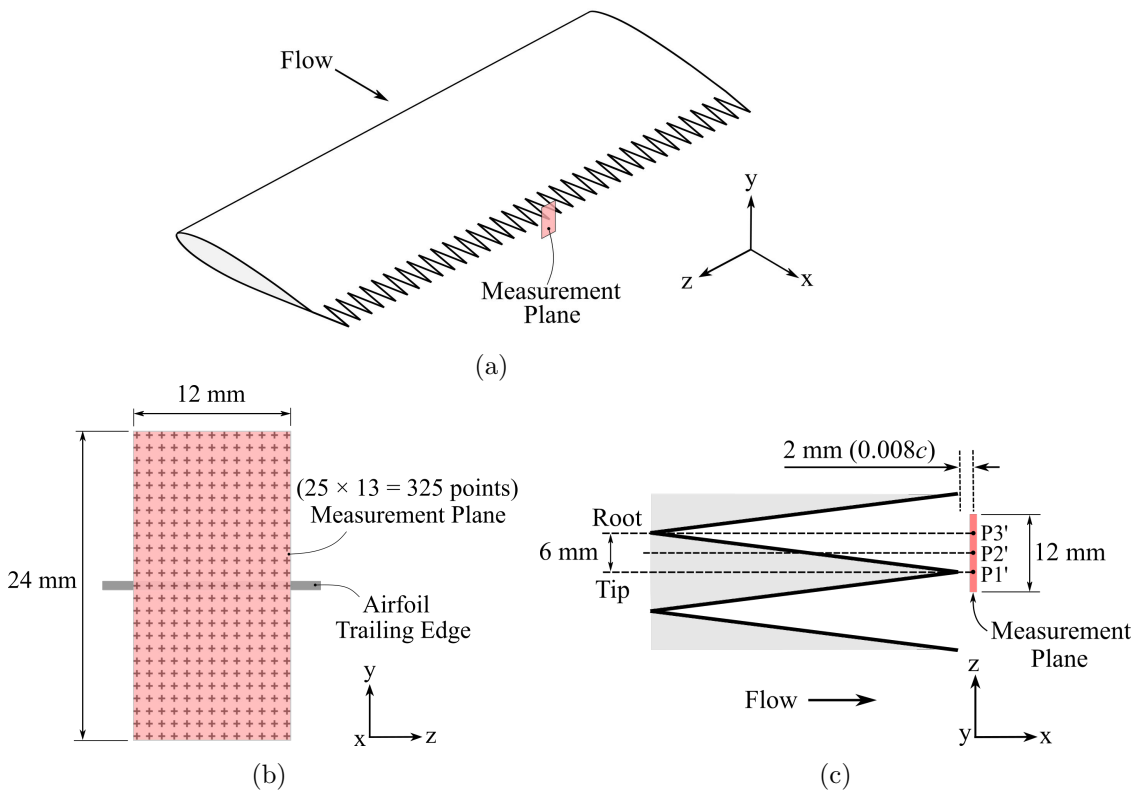


Figure 3.15: Location of the flow measurement points for UAT Campaign 1b: (a) perspective view; (b) view normal to x axis; (c) view normal to y axis.

points in a rectangular region with a spanwise width of 12 mm (λ) and vertical length of 24 mm (see Figure 3.15b). This measurement region covers the root and tip positions in spanwise direction (see Figure 3.15c), and the entire near-wake profile in vertical direction. The spanwise location of positions P1', P2' and P3' corresponds to that of positions P1, P2 and P3 in UAT Campaign 1a (as shown in Figure 3.14a). The measurement points are 1 mm apart from each other, and each data record was sampled at 51,200 Hz for 16 s. The details of the hot-wire anemometry system and its characteristics will be described in Sec. 3.3.4.

UAT Campaign 2

For a typical large-scale industrial wind turbine, the tip region of the blades contributes the most to its aerodynamic noise generation as the TE noise level is proportional to U_∞^5 and the tip region has higher linear velocity. In order to accurately predict the noise performance of a large-scale industrial wind turbine in a most cost-effective way, 5 aluminium wind turbine airfoils scaled from the tip sections of a real-life wind turbine were produced according to the 3D CAD model provided by Goldwind[®] (see Figure 3.16), and tested in this campaign. The geometric parameters for these sections are presented in Table 3.5. All airfoil models were scaled to have a chord length of 200 mm, a span of 455 mm and an identical profile to the midspan profile of the corresponding wind turbine section. Note that the boundary layer on each airfoil was tripped at 10% chord location on both sides using a 0.4 mm thick zig-zag turbulator tape.

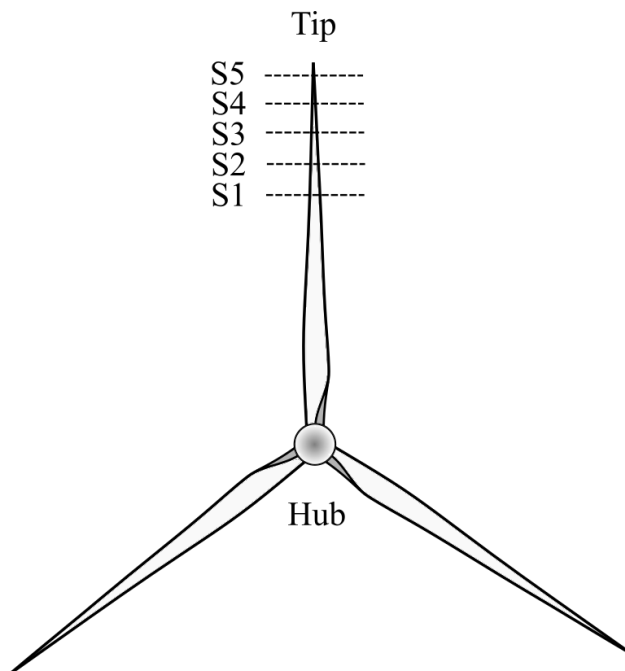


Figure 3.16: Schematic of the wind turbine and the locations of test model profile.

Table 3.5: Geometric parameters for cambered airfoil models

Wind turbine section	Start spanwise location (mm)	End spanwise location (mm)	Test model spanwise location (mm)	Test model designation
1	40495	48370	44432	S1
2	48370	55000	51685	S2
3	55000	57100	56050	S3
4	57100	60700	58900	S4
5	60700	65200	62950	S5

Figure 3.17 shows the structure and assembly of the airfoil model. It consists of a 12 mm circular spar which runs along the entire span and was bolted to the bottom turn- tables using M8 size bolts as shown in Figure 3.17c below. To provide further structural support, another M8 size bolt and a M6 both were used to pin the airfoil section to the bottom turn-table which was connected to the force balance. Top turn-table was also attached to the airfoil model through bolt connection.

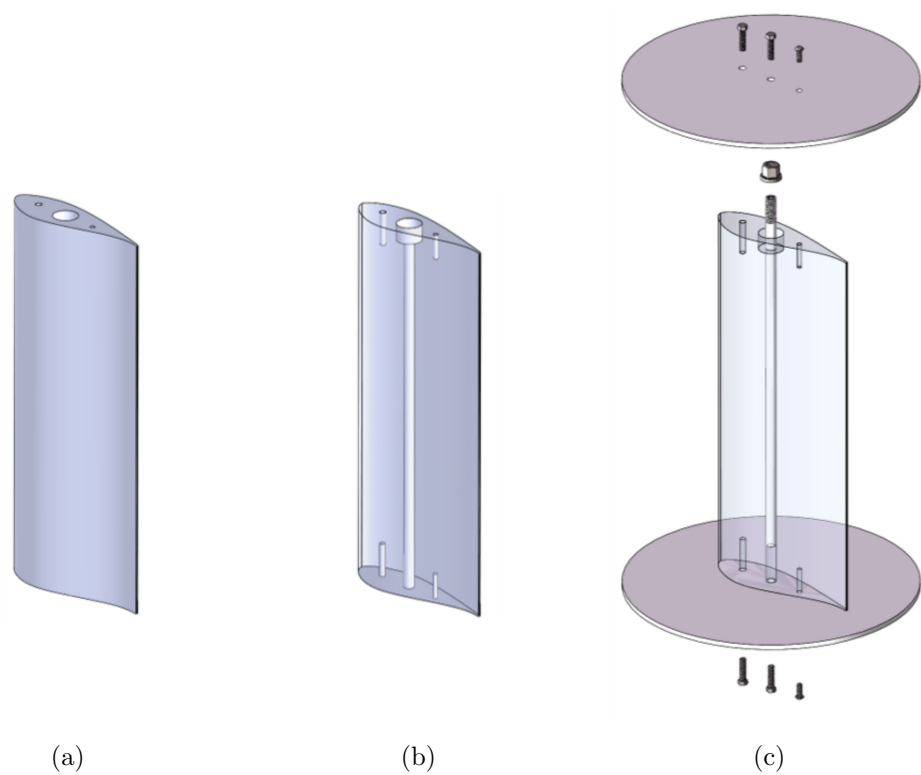


Figure 3.17: CAD drawings of wind turbine airfoil model (a) S1 (b) transparent S1 (c) S1 Assembly exploded view

The acoustic and aerodynamic force measurement setup for UAT Campaign 2 is shown in Figure 3.18. The airfoil was mounted onto two turn-tables where the bottom table was directly attached to a six component force balance. The balance was installed onto the top of a rotary table which can be used to adjust the geometric angle of attack of the airfoil. The entire balance assembly was bolted to a platform which was connected to a rigid frame at the floor of the anechoic chamber, thereby ensuring the structural integrity of the setup. Also shown in Figure 3.18a are the end-plates with a 352 mm bore to install the 350 mm diameter turn-tables. The end-plates were bolted to the contraction outlet as well as the supporting beams to ensure the plates were flush with the turn-tables. The 1 mm gap between the end-plates and the turn-tables isolates the force-balance from any contact with the end-plates so that the aerodynamic moments and loads on the airfoil were directly transmitted to the balance. Acoustic data were taken with the same 64-microphone array as in UAT Campaign 1 with identical configuration except the relative location of the array center to the airfoil TE has changed (as shown in Figure 3.18b)

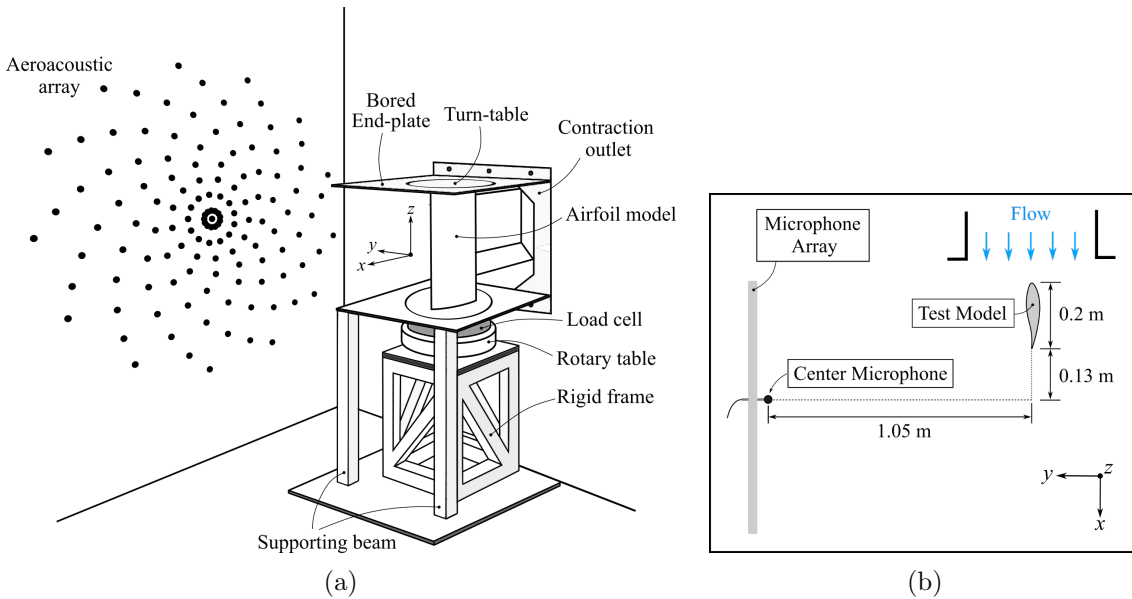


Figure 3.18: Schematics of the acoustic and aerodynamic force measurements setup for UAT Campaign 2: (a) perspective view; (b) top view.

The near-wake profile of the wind turbine airfoil was measured using a pitot probe with 0.3 mm internal diameter mounted on the same Dantec Dynamic[®] traverse system as UAT Campaign 1. The static pressure was measured near the test section using a PVC tube mounted outside the flow region, and the total pressure was acquired from a Scanivalve[®] DSA 2317 pressure scanner connected to the pitot probe through a PVC

tube. The pressure scanner has a range of 2488.4 Pa and an uncertainty of ± 1.24 Pa. As shown in Figure 3.19, the pitot probe was positioned 1 mm downstream of the TE midspan and traverses along the vertical direction to obtain the near-wake profile.

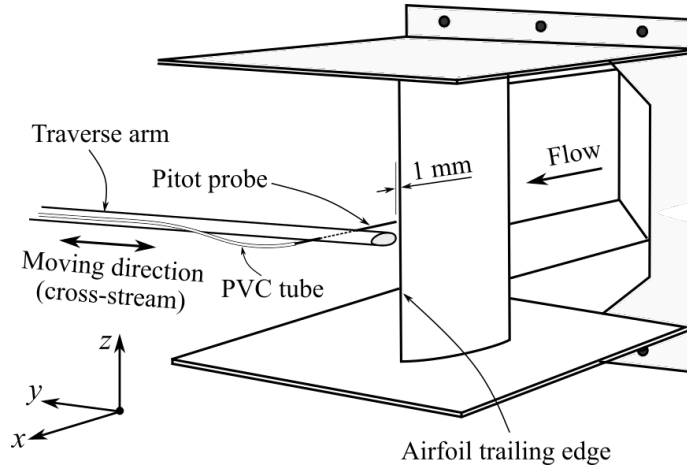


Figure 3.19: Schematic of the boundary layer measurement setup for UAT Campaign 2.

3.3.3 Acoustic Beamforming

Beamforming Principle

Beamforming is a spatial filtering process technique that is capable of extracting the noise source location and magnitude and is widely used in aeroacoustic applications. Conventional beamforming relies on the far-field acoustic signals captured at discrete positions from the microphone array, which can be post-processed to estimate the direction of the incoming signal based on the time delay between the microphones, or phase difference in the frequency domain. The phase differences between the microphone signals from the array can be evaluated by the cross-spectral matrix. For a set of sound pressure signals $\mathbf{p}(\omega)$ taken from an n -channel microphone array, the corresponding cross-spectral matrix \mathbf{C}_m is defined as

$$\mathbf{C}_m(\omega) = E[\mathbf{p}(\omega), \mathbf{p}(\omega)^H] = \begin{bmatrix} S(x_1, x_1) & S(x_1, x_2) & \cdots & S(x_1, x_n) \\ S(x_2, x_1) & S(x_2, x_2) & \cdots & S(x_2, x_n) \\ \vdots & \vdots & \ddots & \vdots \\ S(x_n, x_1) & S(x_n, x_2) & \cdots & S(x_n, x_n) \end{bmatrix}, \quad (3.15)$$

$$\mathbf{p}(\omega) = [p(x_1, \omega), p(x_2, \omega), \dots, p(x_{n-1}, \omega), p(x_n, \omega)]^T, \quad (3.16)$$

where x_n represents the n th microphone position, ω is the angular frequency ($\omega = 2\pi f$), $[\cdot]^T$ denotes the matrix transpose operator, $E[\cdot]$ represents the expected value, H represents Hermitian transpose and $S(x_{n_1}, x_{n_2})$ represents the cross-power spectral density of the signals from microphones n_1 and n_2 . The cross-spectral densities are Fourier transformed from the time-series far-field acoustic pressure using a Hann window function with 50% overlap. The phase differences between microphones are taken into account as a steering vector for a specific grid point on the scanning plane. As the noise source is assumed to be monopolar in conventional beamforming, the steering vector is based on the free-field Green's function for a monopole. For grid point m , its steering vector can be determined by

$$\mathbf{h}_m = [g_1, g_2, \dots, g_n]^T, \quad (3.17)$$

where g_n represents steering vector component for microphone n , which is defined as:

$$g_n = \frac{r_{mn}}{r_{m0}} \exp(j\omega\tau_{mn}), \quad (3.18)$$

where r_{mn} is the distance between the m th grid point and the n th microphone, r_{m0} represents the distance between the m th grid point and the reference microphone, and τ_{mn} is the propagation time from the m th steering location grid point to the n th microphone. The reference microphone is chosen as the center microphone of the array. The conventional beamforming output for the m th scanning grid point is then obtained by:

$$Y(\mathbf{h}_m) = \frac{\mathbf{h}_m^T C_m(\omega) \mathbf{h}_m}{n^2}. \quad (3.19)$$

The beamforming output can be further improved by removing the diagonal terms in the cross-spectral matrix. This helps removing the microphone self-noise to obtain a higher signal-to-noise ratio of the beamforming output, which can be determined by

$$Y(\mathbf{h}_m) = \frac{\mathbf{h}_m^T (C_m(\omega))_{diag=0} \mathbf{h}_m}{n^2 - n}. \quad (3.20)$$

Conventional beamforming has good frequency resolution when applied to stationary noise sources such as TE noise from a stationary airfoil and has been further extended to advanced algorithms, such as deconvolution algorithms DAMAS [29] and CLEAN-SC [177]. For the purpose of this thesis, conventional beamforming [141] has been proven to be adequate and is used to process the microphone data taken from the microphone array introduced in Sec. 3.3.2. Moreover, due to the convection effect on the acoustic wave propagation, the acoustic ray path from the noise source in the flow will be refracted towards the upstream direction when encountering the shear layer. Consequently, the source position obtained using the beamforming algorithm will be shifted into the downstream direction. This convection effect is corrected using Mach number correction method [151]. The shifted distance of the noise source x_{sh} is obtained by solving the convected wave equation using the velocity potential and a Prandtl–Glauert transformation [195], which can be simply expressed as

$$x_{sh} = M_{\infty} l_s , \quad (3.21)$$

where M_{∞} is the freestream Mach number and l_s is the distance between the source and shear layer in the vertical direction. This correction model has been proven to be valid for low Mach number flows ($M_{\infty} \leq 0.3$), which is adequate for the measurements in this thesis.

Source Region Integration

Airfoil TE noise is generated from distributed sources along the entire TE span. Therefore, to obtain the sound pressure level spectra of the entire TE, the beamforming output has to be integrated over a specific region. The noise spectra were integrated using the procedure introduced by [27]. First, the coordinates of grid points in the scanning plane are defined as $(x, y) = (x_0 + a\Delta x, y_0 + b\Delta y)$, where Δx and Δy are grid spacing and a and b are integers. The integration region is defined by x from $x_0 + a_1\Delta x$ to $x_0 + a_2\Delta x$ and y from $y_0 + b_1\Delta y$ to $y_0 + b_2\Delta y$. In this section, let $Y_{a,b}$ represent $Y(\mathbf{h}_m)$ in Eq. (3.20). The integrated output Y_T for this region can then be determined by the following equations

$$Y_T = \sum_{a=a_1}^{a_2} \sum_{b=b_1}^{b_2} [Y_{a,b} R_{a,b}] , \quad (3.22)$$

$$R_{a,b} = \left[\sum_{a=a'_1}^{a'_2} \sum_{b=b'_1}^{b'_2} Q_{a',b'} \right]_{a,b}, \quad (3.23)$$

$$Q_{a',b'} = \left[\frac{\mathbf{h}^T (\mathbf{G}'_{a,b})_{diag=0} \mathbf{h}}{n^2 - n} \right]_{a',b'}, \quad (3.24)$$

$$\mathbf{G}'_{a,b} = \begin{bmatrix} (g_1^* g_1)^{-1} & (g_1^* g_2)^{-1} & \cdots & (g_1^* g_n)^{-1} \\ & (g_2^* g_2)^{-1} & & \vdots \\ & & \ddots & \vdots \\ & & & (g_n^* g_n)^{-1} \end{bmatrix}_{a,b}, \quad (3.25)$$

where $R_{a,b}$ is a factor that accounts for the beampattern characteristics of the integrated region, and $Q_{a',b'}$ accounts for the influence from the remaining grid points inside the integration region when calculating the characteristic factor $R_{a,b}$ for grid point (a,b) . The synthesised cross-spectral matrix $\mathbf{G}'_{a,b}$ uses the inverses of steering vectors of location (a,b) to account for the beamforming characteristics.

3.3.4 Hot-wire Anemometry

As mentioned in Secs. 3.3.1 and 3.3.2, hot-wire anemometry is used for the flow characterisation of the UAT and the near wake survey of the NACA0012 airfoil with TE extension. A hot-wire is a thin platinum (or platinum alloys) wire that is kept at a constant temperature by placing it in one arm of a Wheatstone bridge. When air flows over the wire, the temperature of the wire will tend to reduce and unbalance the bridge as the moving air convects the heat. Using a constant-current power supply, the Wheatstone bridge can re-balance itself faster than the changes caused by heat transfer from the smallest eddies in the flow. This means that the temperature of the wire can virtually kept constant. As the heat loss from the wire is proportional to the voltage of the bridge, the velocity at the wire location can be related to this voltage. The hot-wire probe employed is the Dantec Dynamics[®] miniature hot-wire probe that has a $5 \mu m$ wire made from platinum. The probe was controlled by an IFA300 Constant Temperature Anemometer (CTA) system, which maintains the wire temperature at $275^\circ C$. Each velocity data set was acquired at a sampling rate of 51,200 Hz (for 32 s and 16 s in UAT Campaign 1a and 1b, respectively) using a National Instrument[®] PXI platform that was connected to the IFA300 CTA sys-

tem. The velocity spectra were Fourier transformed from the time-series velocity data using a Hann window function with 50% overlap.

3.3.5 Aerodynamic Force Measurement

The forces and moments on the airfoil blades were measured using a six component, JR-3[®] force balance which has a measurement range of 400 N. The accuracy of the force balance along the normal and axial directions is ± 1 N, while along the pitching moment axis the accuracy is ± 0.125 N.m. As described previously in Sec. 3.3.2, the entire airfoil/turntable assembly rotates with the balance, the longitudinal and lateral forces sensed by the force balance yield a direct measure of the axial and normal forces on the airfoil, respectively. These are then converted to lift and drag forces using the geometric angle of attack. The rotational axis about which the balance measures the moments is located at 40% chord location with respect to the airfoil. As the pitching moment at the quarter-chord is required for the open-jet correction, the measured pitching moment is transferred to the quarter-chord location using the measured lift and drag forces. The definition of the lift coefficient C_l , drag coefficient C_d and pitching moment coefficient C_m is given in Eqs. (3.26)–(3.28) as follows

$$C_l = F_l / (q_\infty A_{ref}) \quad (3.26)$$

$$C_d = F_d / (q_\infty A_{ref}) \quad (3.27)$$

$$C_m = M_z / (q_\infty A_{ref} c) \quad (3.28)$$

,where F_l , F_d , and M_z are the lift, the drag, and the pitching moment obtained from the force balance measurements, q_∞ is the dynamic pressure, c is the chord-length of the airfoil model and A_{ref} is the reference area which is taken to be the wing area of the airfoil model: $A_{ref} = \text{span} \times \text{chord} = 0.455 \text{ m} \times 0.2 \text{ m}$.

3.3.6 Aerodynamic Corrections

The wake and the solid blockages in an open-jet type wind-tunnel are negligible since the flow is free to expand [72]. However, the presence of an airfoil section in an open-jet curves the flow streamlines so that a correction to the angle of attack, drag, and pitching

moment is required in order to compare the results to the unbounded freestream case. The corrections proposed by Barlow et al. [22] were used to correct the aerodynamic data for the open-jet boundary interference. The corrected angle of attack (α_c) is given by

$$\alpha_c = \alpha_g - [0.25(c/D_H)C_l + \pi/24(c/D_H)^2C_l](57.3) \quad (3.29)$$

where, α_g is the geometric angle of attack, c is the airfoil chord, D_H is the height of the open-jet which is equal to the airfoil span in the present work, and C_l is the measured lift coefficient as defined in Eq. (3.26). The drag measurement in the present work was corrected for open-jet boundary interference using the following formulation given by Barlow et al. [22]

$$C_{d,c} = C_{d,u} - \sqrt{3}\sigma/\pi C_l^2 \quad (3.30)$$

where, $C_{d,c}$ is the corrected drag coefficient, $C_{d,u}$ is the uncorrected drag coefficient obtained from the force balance measurement using Eq. (3.27), and C_l is the lift coefficient from the balance measurement. The pitching moment was measured about the 40% chord location and was then transferred to the quarter-chord location using the measured lift and drag. The corrected quarter-chord pitching moment according to Barlow et al. [22] is given by

$$C_{m_{1/4},c} = C_{m_{1/4},u} - \pi^2/96(c/D_H)^2C_l \quad (3.31)$$

where, $C_{m_{1/4},c}$ is the corrected, quarter-chord pitching moment coefficient and $C_{m_{1/4},u}$ is the uncorrected moment coefficient about the quarter-chord obtained from the force balance measurement using Eq. (3.28). As before, c and D_H are the airfoil chord length and open-jet height, respectively.

3.4 Rotor Rig Measurements

The acoustic performance of rotor blades with porous and serrated TEs have been characterised using the UNSW Rotor Rig and a 64-channel microphone array. Acoustic measurements were taken at operating conditions of RPM = 800 and 900 and pitch angle = 0°, 5° and 10° for the blades with natural-transition and forced-transition boundary layers. Conventional and two phase-averaged beamforming methods were used to localise the

noise sources and evaluate the TE noise levels. The following sections detail the facility, test models, measurement setup and phased-averaged beamforming methods used in this experimental campaign.

3.4.1 Facility

The UNSW Rotor Rig consists of a 3kW direct-drive motor, three rotor blades of 1.04 m diameter, a semi-ellipsoidal nose cone (filled with Basotect[®] acoustic foam) installed on the rotor hub, and a supporting tower station. The rig is installed in a regular octagonal wooden test-section with a width between the flat edges of 3.05 m, an edge length of 1.26 m and a cross-sectional area of 7.7 m². The tunnel is an interchangeable section of the UNSW Large Wind Tunnel (LWT), which can be assembled into the LWT circuit to extend the measurement capability for various inflow conditions. However, to permit acoustic beamforming measurements of the blade rotational plane, the tunnel test-section

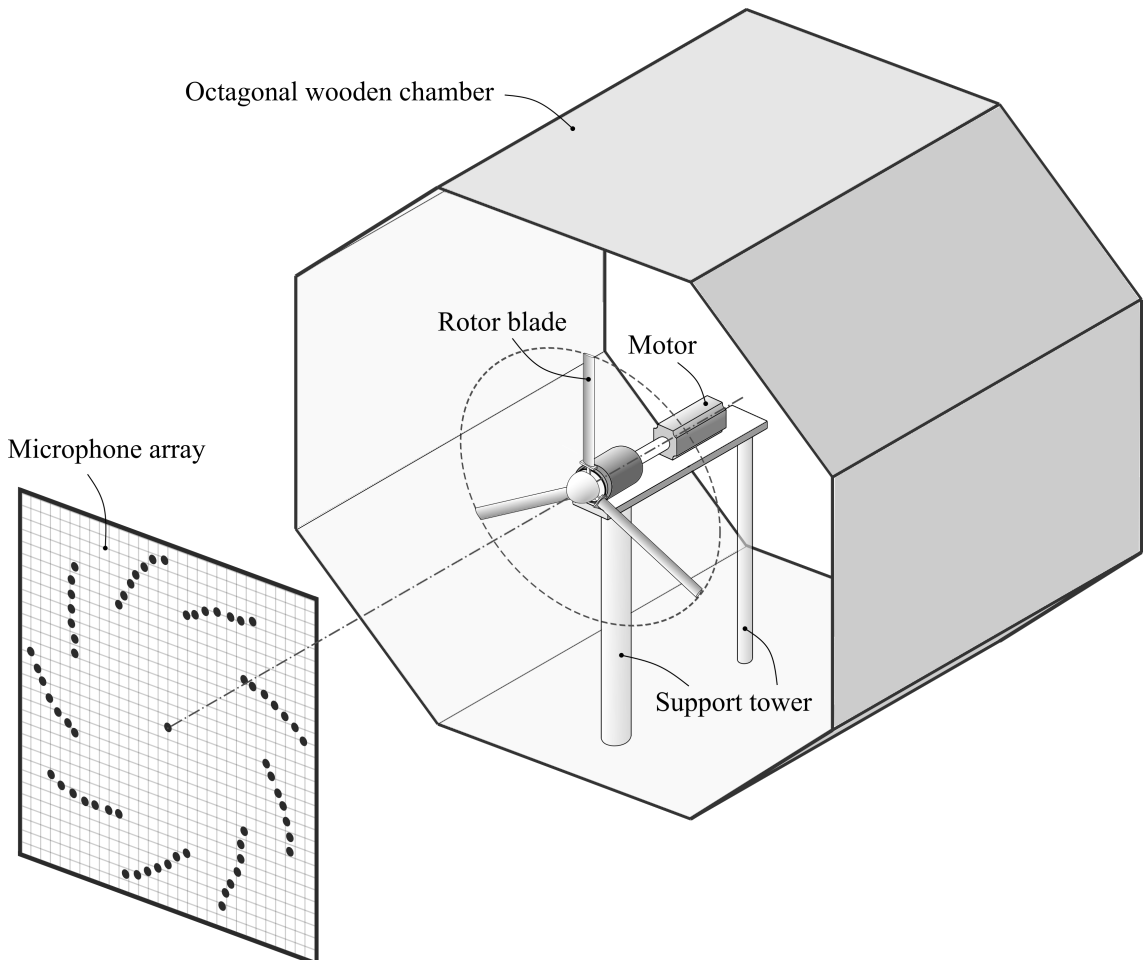


Figure 3.20: Schematic of the UNSW Rotor Rig.

is disassembled from the LWT with a microphone array placed in front of the rotor (see Figure 3.20). As a result, all measurements were performed at zero inflow speed. The direct-drive motor has a rated power of 3 kW, which allows a maximum RPM of 900 for the test models investigated in this thesis.

3.4.2 Rotor Blade Models and Test Setup

The rotor model has a hub height of 1.42 m and a rotor diameter of 1.04 m as shown in Figure 3.21. The axial distance between the TE of rotor blades and the supporting tower is 0.07 m. The blades have a constant-chord along the span, and rotate clockwise when looking towards the rotor from the microphone array. In order to evaluate the acoustic performance of the porous TE treatment and compare its noise reduction performance with that of traditional saw-tooth-serrated TE treatments [45, 149] for rotor applications, four sets of rotor blades were designed and manufactured; reference (Ref), porous (P), cut-serrated (CutS) and extended-serrated (ExtS) blades have been tested in this experimental campaign (see Figure 3.22). Blade models were produced by 3D printing using a white resin material C-UV 9400, and the reference blade model has a NACA0012 profile and a chord of 0.07 m. Table 3.6 summarises the detailed geometrical parameters of the other three test models. The geometries of the porous region in blade P were determined by the

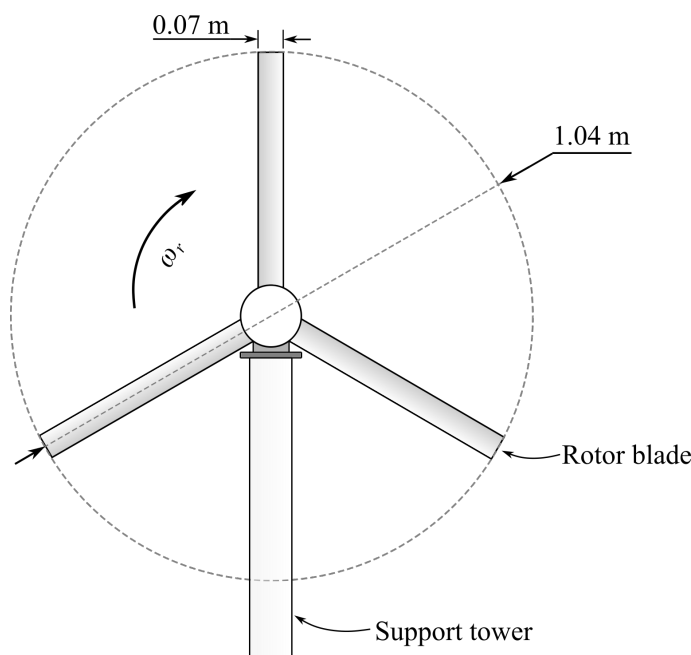


Figure 3.21: Schematic of rotor geometries (view from the microphone array).

acoustic characterisation procedure described in Sec. 3.2 and designed according to the geometrical parameters of impedance tube specimen P4 (see Figure 3.23). The serrated regions of blades ExtS and CutS have the same amplitude as the porous region in blade P, and identical wavelength-to-amplitude ratio λ/h to that of the TE extension NS tested in UAT Campaign 1 (details in Sec. 3.3.2 and Table 3.4).

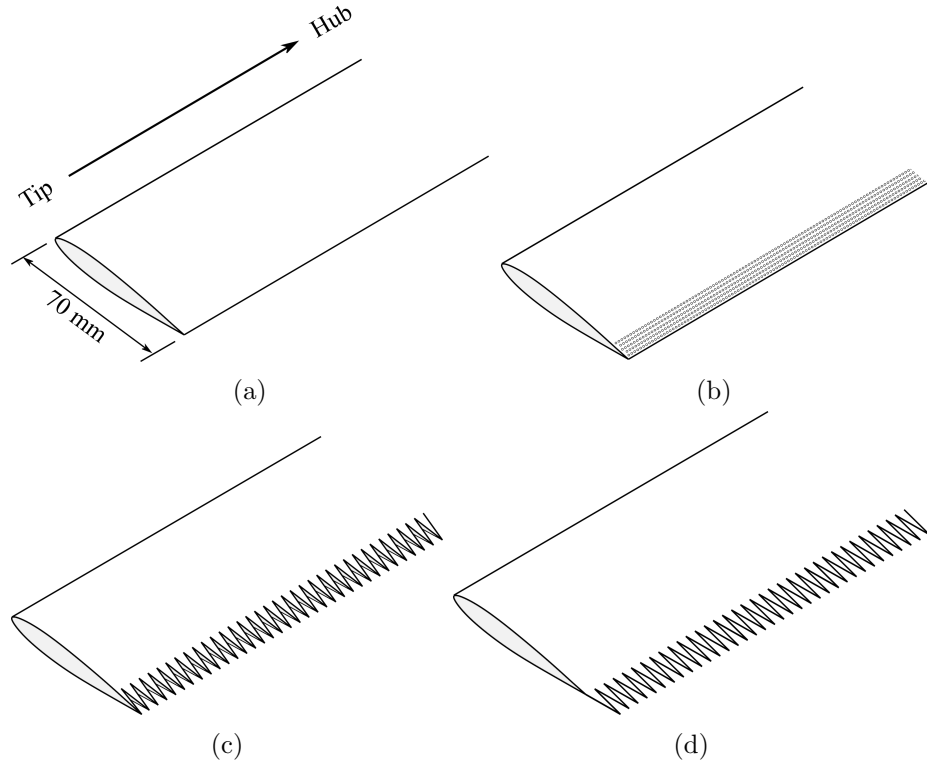


Figure 3.22: Schematic of rotor blade models: (a) Reference NACA0012 blade (Ref); blades with (b) porous TE (P), (c) cut-serrated TE (CutS) and (d) extended-serrated TE (ExtS).

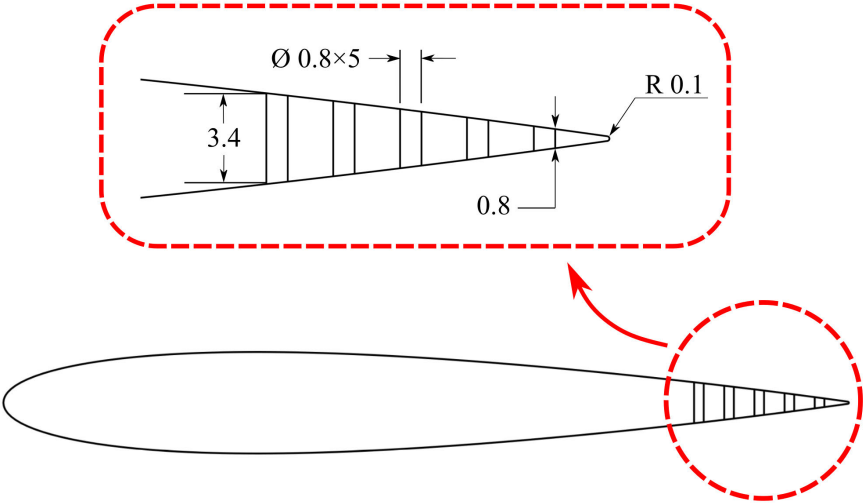
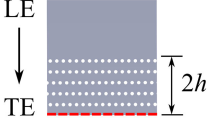
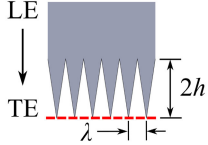
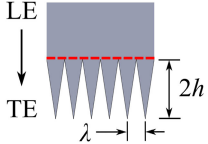


Figure 3.23: Transparent drawing of the porous region in rotor blade P.

Table 3.6: Geometries of rotor blades with porous, cut-serrated and extended-serrated TEs.

Sketches	Descriptions	Abbr.
	Porous TE: streamwise length of porous region $2h=14$ mm, porosity $\phi=0.13$, hole diameter $r=0.8$ mm	P
	Cut-serrated TE: sawtooth serrations are geometrically cut into the airfoil TE, amplitude $2h=14$ mm, wavelength $\lambda=4.2$ mm, $\lambda/h=0.6$	CutS
	Extended-serrated TE: sawtooth serrations are geometrically extended out of the airfoil TE as a serrated flat-plate extension, amplitude $2h=14$ mm, wavelength $\lambda=4.2$ mm, $\lambda/h=0.6$, extension thickness $b = 1$ mm	ExtS

Note: --- indicates the TE location of the reference blade.

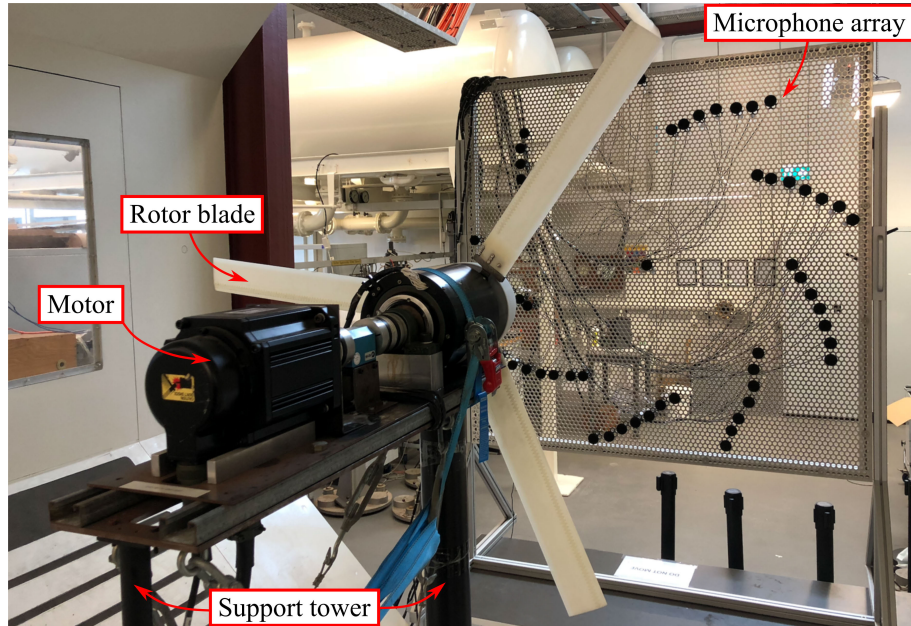


Figure 3.24: Aeroacoustic measurement setup for the rotor blades in-situ.

The acoustic measurement setup for the rotor blades is shown in Figures 3.20 and 3.24. Far-field acoustic data were taken using a 64-channel microphone array located 1.665 m away from the rotor rotational plane. The microphones were arranged in a spiral pattern on a 1.5×1.5 m perforated aluminium frame, in which the center microphone was aligned with the rotor rotational axis. The array utilizes GRAS[®] type 40 PH 1/4 inch

microphones which have a flat response (within ± 2 dB) up to 20 kHz. The microphone data were acquired using a National Instrument[®] PXI platform with 24-bit resolution at a sampling rate of 2^{16} Hz. For each set of blades, the following two scenarios are considered: 1) allowing natural transition of the boundary layer to evaluate the effects of TE treatments on the LBL-TE noise; 2) forcing the boundary layer to turbulence to evaluate the TBL-TE noise. In scenario 2, the forced boundary layer transition was achieved by installing a zig-zag turbulator at 10% chord on both sides of the blade. The data for each scenario were acquired at RPM of 800 and 900, and pitch angles of 0° , 5° and 10° for a sampling time of 32 s.

3.4.3 Phase-Averaged Beamforming

For rotational noise sources, conventional beamforming (as introduced in Sec. 3.3.3) can only localise and quantify the noise sources averaged over the entire revolution. The noise level in the acoustic map is not representative of the instantaneous source strength. Therefore, phase-averaged beamforming (PABF) methods are adopted to evaluate the strength and location of the noise sources at a particular phase angle of interest. The following sections detail the two phase-averaged beamforming methods [156, 198] used in this study.

PABF Method 1

The conventional beamforming algorithm calculates the cross-spectral matrix over the entire time record, while phase-averaged beamforming averages small segments of data around the desired phase angle θ_i to de-rotate the results. Data taken between phase angles $[\theta_i - \Delta\theta, \theta_i + \Delta\theta]$ were used to calculate the sound contributions from the rotation plane (as illustrated in Figure 3.25).

When the rotor blade passes through the phase angles of interest $[\theta_i - \Delta\theta, \theta_i + \Delta\theta]$, the propagation time of the acoustic pressure wave emitted from each scanning grid point differs for each array microphone due to the variance in propagation distance. PABF Method 1 [156] calculates the delayed and summed pressure record in the time domain at each scanning grid point according to the propagation delay between each grid point m

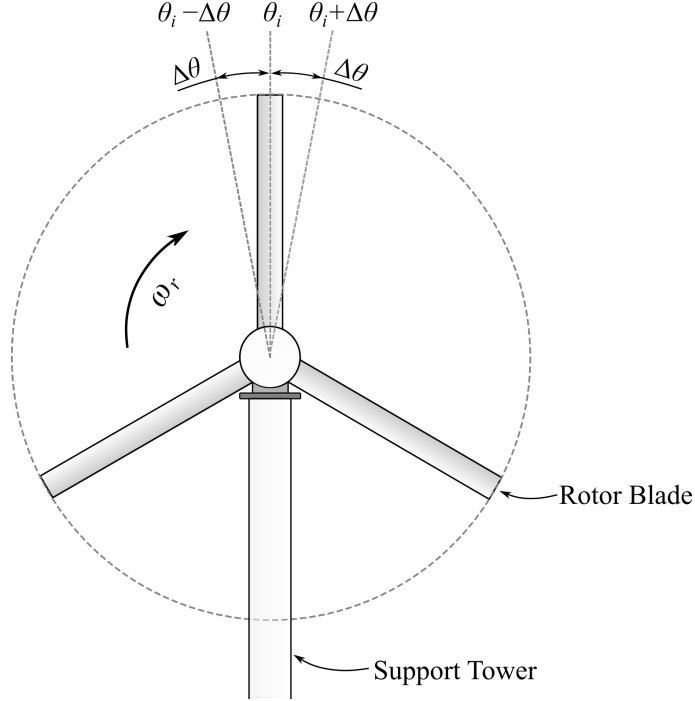


Figure 3.25: Schematic of the data segment used to perform the phase-averaged beamforming for the rotor at desired phase angle.

and microphone n using

$$\overline{p_m}(t_i) = \frac{1}{\sqrt{N \sum_{n=1}^N (r_{m,1}/r_{m,n})^2}} \sum_{n=1}^N p_n(t_i - t_{m,n}), \quad (3.32)$$

$$t_i = t(\theta(t) = \theta_i) + [-\Delta\theta, \Delta\theta]/\omega_r, \quad (3.33)$$

$$t_{m,n} = r_{m,n}/c, \quad (3.34)$$

where $\overline{p_m}(t_i)$ is the delayed and summed pressure at grid point m corresponding to the i -th time record when $\theta(t) \in [\theta_i - \Delta\theta, \theta_i + \Delta\theta]$, $p_n(t)$ is the pressure record of microphone n , $r_{m,n}$ is the distance between microphone n and the scan grid point m , c is the speed of sound, $t_{m,n}$ is the sound propagation time from grid point m to microphone n , N is the number of microphones on the array, and ω_r is the rotational angular velocity. The terms in the front of the pressure record summation in Eq. (3.32) correspond to the amplitude corrections in conventional beamforming, which is equivalent to the amplitude corrections of the "formulation 4" steering vectors described in [171].

The output power spectrum of the delayed and summed pressure at each grid point

m is then estimated using Welch's method by

$$Y_m(f) = \frac{2}{IF_s \sum_{l=1}^{L_t} w(l)^2} \sum_{i=1}^I |\mathcal{F}\{\mathbf{w} \circ \overline{p_m(t_i)}\}|^2, \quad (3.35)$$

where F_s is the sampling frequency, I is the number of data segments (around the angle of interest θ_i) over the entire pressure record, \mathbf{w} is the tapering function (a Hann window in this study), w is the tapering function component, L_t is the length of tapering function, \mathcal{F} stands for one-sided fast Fourier transform, and \circ denotes the Hadamard product.

PABF Method 2

As the cross-spectral matrix is not utilised in PABF Method 1, the coherence between the acoustic signals from different array microphones is not taken into account properly. PABF Method 2 is an improvement on PABF Method 1 and calculates the cross-spectral matrix for each scanning grid point using the delayed acoustic pressure record over the desired angle range $[\theta_i - \Delta\theta, \theta_i + \Delta\theta]$, and then performs conventional beamforming for each cross-spectral matrix to obtain the acoustic map output for each scanning grid point.

For the scanning grid point m , the cross-spectral matrix \mathbf{C}_m is calculated using the delayed acoustic pressure record $p_n(t_i - t_{m,n})$ as defined in Eqs. (3.32)–(3.34). The matrix element C_{m,n_1,n_2} ($n_1, n_2 \in [1, 2, 3, \dots, N]$) for microphones n_1 and n_2 is determined by

$$C_{m,n_1,n_2} = \frac{2}{IF_s \sum_{l=1}^{L_t} w(l)^2} \sum_{i=1}^I (\mathcal{F}\{\mathbf{w} \circ p_{n_1}(t_i - t_{m,n_1})\})^H (\mathcal{F}\{\mathbf{w} \circ p_{n_2}(t_i - t_{m,n_2})\}), \quad (3.36)$$

where H denotes Hermitian transpose, and the definitions of I , F_s , \mathbf{w} , w , L_t , t_i , $t_{m,n}$, c , \circ and \mathcal{F} remain the same as described previously for PABF Method 1 Equations (3.32)–(3.35). Conventional frequency-domain beamforming is then performed using the cross-spectral matrix calculated from Eq. (3.36) for each scanning grid point.

In this study, the delay of pressure record for grid point m and microphone n is realised by shifting an integer number of samples, $K_{m,n}$, determined by the sound propagation delay $t_{m,n}$:

$$K_{m,n} = \lfloor F_s t_{m,n} \rfloor, \quad (3.37)$$

where $\lfloor \cdot \rfloor$ denotes the operation of rounding to the nearest integer. The rounding of $K_{m,n}$

will inevitably create a residual time $t_{res,m,n}$ that can be defined as

$$t_{res,m,n} = t_{m,n} - K_{m,n}/F_s . \quad (3.38)$$

The residual time can be corrected by adjusting the forward propagation function, applying a frequency-domain phase shifting in steering vectors. The modified forward propagation function can be written as

$$a_{m,n}(f) = \frac{r_{m,0}}{r_{m,n}} e^{-2\pi f t_{res,m,n}} . \quad (3.39)$$

The “formulation 4” steering vector described in [171] is then determined by

$$\mathbf{h}_m(f) = [h_{m,1}(f), h_{m,2}(f), h_{m,3}(f), \dots, h_{m,n}(f)]^T , \quad (3.40)$$

$$h_{m,n}(f) = \frac{1}{\sqrt{N}} \frac{a_{m,n}(f)}{\|\mathbf{a}_m(f)\|} , \quad (3.41)$$

$$\mathbf{a}_m(f) = [a_{m,1}(f), a_{m,2}(f), a_{m,3}(f), \dots, a_{m,n}(f)]^T , \quad (3.42)$$

where $[\cdot]^T$ denotes the matrix transpose operator and N is the number of microphones in the array. The output of power spectral density at scanning grid point m is then determined by

$$Y_m(f) = \mathbf{h}_m(f)^H \mathbf{C}_m \mathbf{h}_m(f) . \quad (3.43)$$

In this study, phase-averaged beamforming was performed on data blocks where each block corresponds to an angular movement of 5° ($\Delta\theta = 2.5^\circ$). For the sampling rate of 2^{16} Hz, the numbers of samples per block were rounded to be 68 and 61 for the RPM of 800 and 900, respectively. When performing the fast Fourier transform, the samples in each block were zero-padded to a length of 256 after applying a Hann window, providing a frequency resolution of 256 Hz.

3.5 Numerical Simulation Methodology

Compressible Large-Eddy Simulation (LES) was performed to investigate the flow characteristics and aeroacoustic performance of a NACA 0012 airfoil with a porous TE. This

section describes the numerical techniques of flow simulation and acoustic prediction applied in this study. The governing equations, subgrid-scale turbulence model, boundary conditions and computational grid, in addition to the FWH acoustic analogy are detailed.

3.5.1 Governing Equations

The governing equations employed in the LES simulation are obtained by filtering the time-dependent Navier-Stokes equations. The eddies with scales smaller than the filter width or computational grid spacing are effectively filtered out by applying a spatial filter. As a result, the filtered equations govern the dynamics of the large eddies. A spatially filtered variable (denoted by overbar) is defined by

$$\bar{\phi}(x) = \int_D \phi(x') G(x, x') dx' , \quad (3.44)$$

where D represents the fluid domain and $G(x, x')$ is the filter function. The spatial filtering function and spatially filtered variable are defined as

$$G(x, x') = \begin{cases} 1/V, x' \in v \\ 0, x' \text{ otherwise} \end{cases} , \quad (3.45)$$

$$\bar{\phi}(x) = \frac{1}{V} \int_v \phi(x') dx' , x' \in v , \quad (3.46)$$

where V is the volume of a computational cell and v is the fluid domain within the cell. In LES for compressible flows, the Favre (density-weighted) filtering is introduced to avoid modeling the subgrid scales of the continuity equation, which is defined as

$$\tilde{\phi} = \frac{\overline{\rho\phi}}{\bar{\rho}} \quad (3.47)$$

where the Favre-filtered variable is denoted by tilde. Applying the spatial and Favre filtering operations, the continuity and momentum equations yield:

$$\frac{\partial \bar{\rho}}{\partial t} + \frac{\partial(\bar{\rho} \tilde{u}_i)}{\partial x_i} = 0 \quad (3.48)$$

$$\frac{\partial(\bar{\rho} \tilde{u}_i)}{\partial t} + \frac{\partial(\bar{\rho} \tilde{u}_i \tilde{u}_j)}{\partial x_j} = \frac{\partial(\bar{\rho} \tilde{\sigma}_{ij})}{\partial x_j} - \frac{\partial \bar{p}}{\partial x_i} - \frac{\partial \tau_{ij}^{SGS}}{\partial x_j} \quad (3.49)$$

where τ_{ij}^{SGS} is the subgrid-scale stress, and σ_{ij} is the stress tensor due to molecular viscosity defined by

$$\sigma_{ij} = \left[\mu \left(\frac{\partial \bar{u}_i}{\partial x_j} + \frac{\partial \bar{u}_j}{\partial x_i} \right) \right] - \frac{2}{3} \mu \delta_{ij} \frac{\partial \bar{u}_k}{\partial x_k}. \quad (3.50)$$

In Eq.(3.50), μ is the dynamic viscosity (also called coefficient of molecular viscosity) determined by three coefficient Sutherland's law:

$$\mu = \mu_0 \left(\frac{T}{T_0} \right)^{(3/2)} \frac{T_0 + C_0}{T + C_0} \quad (3.51)$$

where $\mu_0 = 1.76^{-5} \text{ kg/m}^{-1}\text{s}^{-1}$, $T_0 = 271.11 \text{ K}$ and $C_0 = 110.56 \text{ K}$.

The filtered energy equation can be expressed as:

$$\frac{\partial(\bar{\rho}\tilde{h}_s)}{\partial t} + \frac{\partial(\bar{\rho}\tilde{u}_i\tilde{h}_s)}{\partial x_i} - \frac{\partial\bar{p}}{\partial t} - \tilde{u}_j \frac{\partial\bar{p}}{\partial x_i} - \frac{\partial}{\partial x_i} \left(\kappa_c \frac{\partial\tilde{T}}{\partial x_i} \right) = \frac{\partial}{\partial x_j} \left[\underbrace{\bar{\rho}(\tilde{u}_i\tilde{h}_s - \tilde{u}_i\tilde{h}_s)}_{\text{subgrid enthalpy flux}} \right] \quad (3.52)$$

where κ_c and h_s are the thermal conductivity and sensible enthalpy, respectively. The subgrid enthalpy flux term in Eq. (3.52) will be detailed in the next section.

3.5.2 Subgrid-Scale Models

To close the filtered LES equations, a subgrid-scale (SGS) model proposed by Smagorinsky [178] is employed to simulate the effects of the unresolved flow on resolved flow. The compressible form of the SGS stress tensor is defined as:

$$\tau_{ij}^{SGS} = \widetilde{\bar{\rho}u_i u_j} - \bar{\rho}\tilde{u}_i\tilde{u}_j, \quad (3.53)$$

The SGS stress tensor term can be split into its isotropic and deviatoric parts

$$\tau_{ij}^{SGS} = \underbrace{\tau_{ij}^{SGS} - \frac{1}{3}\tau_{kk}\delta_{ij}}_{\text{deviatoric}} + \underbrace{\frac{1}{3}\tau_{kk}\delta_{ij}}_{\text{isotropic}}, \quad (3.54)$$

where the deviatoric part is modeled using Boussinesq hypothesis [89]:

$$\tau_{ij}^{SGS} - \frac{1}{3}\tau_{kk}\delta_{ij} = -2\mu_{SGS}(\widetilde{S_{ij}} - \frac{1}{3}\widetilde{S_{kk}}\delta_{ij}). \quad (3.55)$$

In Eq (3.55), μ_{SGS} is the SGS turbulent viscosity, S_{ij} is the strain-rate tensor for the resolved scale defined by

$$S_{ij} = \frac{1}{2} \left(\frac{\partial u_i}{\partial x_j} + \frac{\partial u_j}{\partial x_i} \right). \quad (3.56)$$

The compressible subgrid enthalpy flux term in Eq.(3.52) is approximated using the gradient hypothesis:

$$\rho(\widetilde{u_i h_s} - \widetilde{u_i} \widetilde{h_s}) = -\frac{\mu_{SGS} C_p}{Pr_{SGS}} \frac{\partial \widetilde{T}}{\partial x_j}, \quad (3.57)$$

where Pr_{SGS} is a subgrid Prandtl number set to 0.85 for simulations in this thesis. The SGS turbulence viscosity is modeled by

$$\mu_{SGS} = \rho L_s^2 |\widetilde{S}| \quad (3.58)$$

where $|\widetilde{S}| = \sqrt{2\widetilde{S_{ij}}\widetilde{S_{ij}}}$, and L_s is the SGS mixing length determined by

$$L_s = \min(\kappa d_w, C_s \Delta) \quad (3.59)$$

where κ is the von Kármán constant, d_w is the distance to the closest wall, Δ is the local grid scale computed according to the computational cell volume V using $\Delta = V^{1/3}$, and C_s is the Smagorinsky constant which is computed using a dynamic procedure [120] based on the Germano identity [67].

The governing equations of the compressible LES simulation were solved using an ANSYS FLUENT 19.2 finite-volume solver. The iterative process of pressure–velocity coupling was computed using the SIMPLEC method [185]. The temporal discretisation scheme is advanced using a second-order implicit method and the convection term is discretised using a second-order central-differencing scheme. The size of time step was set to 2×10^{-5} s, which corresponds to a Nyquist frequency of 25 kHz. The convergence criteria were set to a scaled residual of 5×10^{-4} at each time step for each directional component of the velocity and governing equations of continuity and energy. Convergence was typically achieved in less than 50 iterations for each time step. The simulation for each case ran for a total of 5000 time steps (0.1 s in physical time) after simulation has become quasi-static. Computations were performed on the Gadi cluster of the Australian National Computational Infrastructure (NCI) on four computation nodes, which consists

of 192 Intel Xeon Platinum 8274 3.2 GHz processor cores with 700 GB physical memory.

3.5.3 Computational Grid and Boundary Conditions

Two scenarios were simulated: a turbulent boundary layer convecting over 1) a NACA 0012 reference airfoil (LES Case 1) and 2) a NACA 0012 airfoil with a porous TE (LES Case 2) at an angle of attack of 5° and freestream velocity of 50 m/s. The airfoil profile, chord length and TE geometries in LES Case 1 and Case 2 are identical with those of blades Ref and P (as described in Sec 3.4.2), respectively. See Figures 3.22, 3.23 and Table 3.6 for details of the geometries. The spanwise width in these simulations $L_s = 0.13c$, and periodic boundary conditions were applied in the spanwise direction. A no-slip wall condition was applied to the surface of the airfoil models. To generate the turbulent boundary layer, a uniform flow suction over the region $-0.86 < x/c < -0.815$ and flow blowing over the region $-0.815 < x/c < -0.77$ were implemented over $0.1 < z/c < 0.9$. Note that $x/c = 0$ and $z/c = 0.5$ denote the airfoil TE and mid-span, respectively. The velocity magnitude of these jets were constant, identical and set to $U_{blowing} = U_{suction} = 0.03U_\infty$. This boundary layer tripping method has been successfully implemented in the compressible LES simulation by Wolf and Lele [193]. Moreover, a surface (as shown in Figure 3.26b) was chosen to perform FWH acoustic analogy for far-field sound pressure predictions.

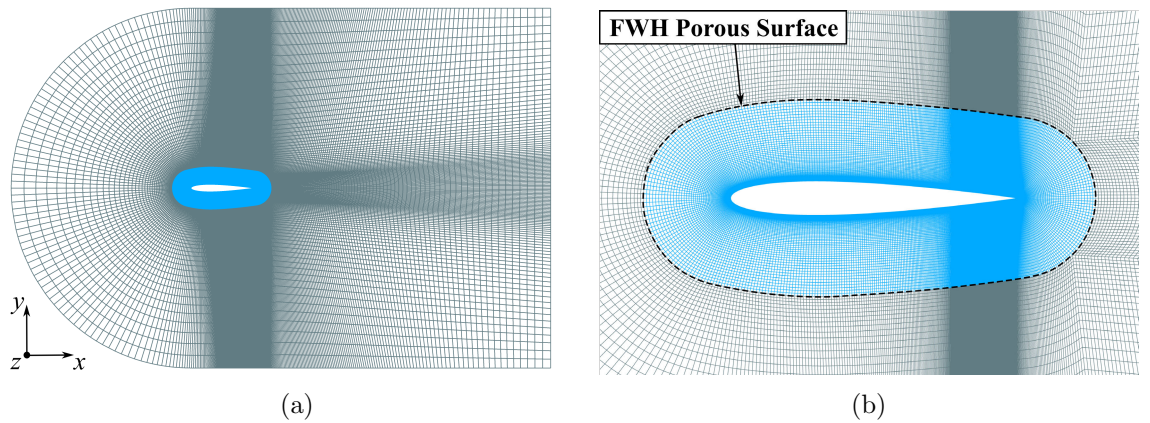


Figure 3.26: Computational grids looked from spanwise direction: (a) full view; (b) near-field detailed view and FWH porous surface.

Computational grids were created using the O-grid blocking scheme. The total number of cells for LES Case 1 and Case 2 are 6.1×10^7 and 6.7×10^7 , respectively. Both cases share an identical grid topology and structure except the grids inside the pores near the

airfoil TE (as shown in Figure 3.27). The size of the streamwise elements is reduced in the region near airfoil TE to capture the contributions of smaller eddies to TE noise generation. In the TE region ($-0.2 < x/c < 0$), the maximum grid spacing in terms of wall units $\Delta x^+ \approx 11$ (streamwise direction), $\Delta z^+ \approx 12$ (spanwise direction), which complies with the requirements for a high resolution LES simulation according to the criteria in [188]. The y^+ value on the surface of the airfoil wall is less than 1.6.

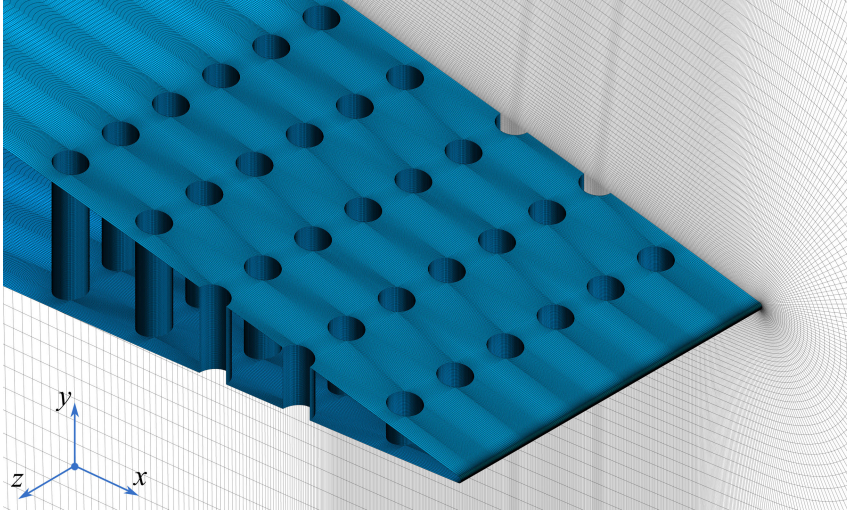


Figure 3.27: Detailed view of computational grids for the TE porous region in LES Case 2.

3.5.4 Grid Convergence Study

A grid convergence study was undertaken to estimate the discretisation errors and determine the grid spacing convergence using the method proposed by Roache [160]. According to Richardson extrapolation [159], the discrete solution f of a parameter or a function can be expressed as [160]

$$f = f_{exact} + a_1 d + a_2 d^2 + a_3 d^3 + \dots \quad (3.60)$$

where a_i are the coefficients of the Taylor series expansion that are independent to any discretisation, d is the grid spacing and f_{exact} is the exact solution when the grid spacing approaches zero. For the second-order discretisation method used in this study, $a_1 = 0$. Dropping the high-order term, the exact solution can be estimated by

$$f_{exact} \cong f_1 + \frac{f_1 - f_2}{r^2 - 1} \quad (3.61)$$

where f_1 and f_2 are the discrete solutions for fine and coarse meshes, and r is the refinement ratio $r = d_1/d_2 > 1$.

The discretisation error for each grid refinement can be reported using a standardised parameter Grid Convergence Index (GCI), which is defined as [160]

$$\text{GCI}_{i,j} = F_s \left| \frac{f_i - f_j}{1 - r^p} \right| \quad (3.62)$$

where $\text{GCI}_{i,j}$ is the GCI for the fine mesh, f_i and f_j are the discrete solutions for the fine and coarse meshes, p is the order of algorithm accuracy ($p = 2$ in this study) and F_s is a safety factor which is recommended to be set to 3 [160]. The grid spacing convergence for LES Case 2 (the airfoil with porous TE) was examined using three meshes M_1 , M_2 and M_3 , corresponding to the coarse, medium and fine meshes, respectively. The grid refinement was performed globally with the aforementioned y^+ value maintained in all three meshes. The refinement ratio was estimated as $r = (N_{i+1}/N_i)^{1/3}$, where N_i is the number of cells for mesh M_i . The number of cells for the three meshes was adjusted to have a constant refinement ratio of 2.

Four parameters C_l , $\overline{C_{f,TE}}$, U_{PR3} and $p_{rms,PR3}$ were used to assess the grid convergence and the discretisation errors in mean and unsteady flow statistics. The parameter C_l is the time-averaged lift coefficient that can represent the overall aerodynamic performance of the airfoil with porous TE. The parameter $\overline{C_{f,TE}}$ is the time-averaged skin friction coefficient spatially averaged over the surface of the TE porous region ($x/c = -0.2-0$), which can be used to evaluate the capability of the LES in resolving near-wall turbulence [188]. The spatial discretisation errors in the dynamics of flow through the pores were demonstrated using U_{PR3} and $p_{rms,PR3}$, where U_{PR3} is time-averaged velocity at the jet core within the pore PR3 (as defined in Figure 6.39) and $p_{rms,PR3}$ is the maximum value of the root-mean-square of surface pressure fluctuations at the wall of pore PR3. Table 3.7 summarises the results of the grid convergence study for LES Case 2, where $\text{GCI}_{2,1}$ and $\text{GCI}_{3,2}$ are the grid convergence indices for coarse-to-medium and medium-to-fine refinements, respectively, and ϵ is the discretisation error of the discrete solution for the fine mesh M_3 relative to the exact solution estimated using Eq. (3.61). A reduction in GCI for successive grid refinements is observed for all parameters including the flow statistics for the highly unsteady flow through the pores, and the discretisation errors for the fine mesh

are small ($< 4.1\%$). The fine mesh was considered to be adequate to capture the major flow features in the TE porous region to investigate the noise reduction mechanism, and therefore was used to obtain the LES results.

Table 3.7: The results of the grid convergence study for LES Case 2.

	GCI _{2,1}	GCI _{3,2}	ϵ
C_l	6.77 %	2.24 %	0.74 %
$\overline{C}_{f,TE}$	46.37 %	10.48 %	3.38 %
U_{PR3}	35.4 %	12.61 %	4.03 %
$p_{rms,PR3}$	36.12 %	4.84 %	1.64 %

3.5.5 FWH Analogy

The far-field acoustic pressures for the numerical simulations were predicted using Ffowcs Williams and Hawkings (FWH) acoustic analogy formulation [63]. It is an inhomogeneous wave equation derived by manipulating the continuity equation and the Navier-Stokes equations. The FWH equations were applied to a static FWH surface for acoustic predictions. The wave equation for this scenario can be written as:

$$\frac{1}{a_0^2} \frac{\partial^2 p'}{\partial t^2} - \nabla^2 p' = \frac{\partial^2}{\partial x_i \partial x_j} \{T_{ij} H(f)\} - \frac{\partial}{\partial x_i} \{[P_{ij} n_i + \rho u_i u_n] \delta(f)\} + \frac{\partial}{\partial t} \{\rho u_n \delta(f)\} \quad (3.63)$$

where u_i are the components of local fluid velocity, u_n is the component normal to the FWH surface (denoted by $f = 0$), n_i are the components of the unit normal vector to the exterior of the FWH surface (denoted by $f > 0$), a_0 is the far-field speed of sound, $\delta(f)$ is the Dirac delta function, $H(f)$ is the Heaviside function and p' is the sound pressure in the far field. The Lighthill stress tensor T_{ij} is defined as:

$$T_{ij} = \rho u_i u_j + P_{ij} - a_0^2 (\rho - \rho_0) \delta_{ij} \quad (3.64)$$

where P_{ij} is the compressive stress tensor for stokes flow, defined as

$$P_{ij} = p \delta_{ij} - \mu \left(\frac{\partial u_i}{\partial x_j} + \frac{\partial u_j}{\partial x_i} - \frac{2}{3} \frac{\partial u_k}{\partial x_k} \delta_{ij} \right). \quad (3.65)$$

Note that the subscript 0 denotes free-stream quantities. Under the assumptions of the free-space flow and the absence of obstacles between the sound sources and the receivers, the wave equation (3.63) can be integrated analytically to obtain the far-field acoustic pressure prediction. The complete solution consists of surface integrals and volume integrals. Both monopole, dipole and quadrupole sources contribute to the surface integrals, while the volume integrals only represent quadrupole sources in the region exterior to FWH surface. For simulations in this thesis, the flow Mach number is low ($M_\infty = 0.147$) and the FWH surface encloses the source region (as shown in Figure 3.26b). The contribution of volume integrals becomes negligible hence is dropped from the calculation. The predicted acoustic pressure at a far-field observer can be calculated using Eqs.(3.66)–(3.69).

$$p'(\mathbf{x}, t) = p'_1(\mathbf{x}, t) + p'_2(\mathbf{x}, t) , \quad (3.66)$$

$$p'_1(\mathbf{x}, t) = \frac{1}{4\pi} \int_{f=0} \left[\frac{\rho_0 U_n (r \dot{M}_r + c(M_r - M^2))}{r^2 (1 - M_r)^3} \right]_{ret} dS \\ + \frac{1}{4\pi} \int_{f=0} \left[\frac{\rho_0 (U_{\dot{n}} + \dot{U}_n)}{r(1 - M_r)^2} \right]_{ret} dS , \quad (3.67)$$

$$p'_2(\mathbf{x}, t) = \frac{1}{4\pi a_0} \int_{f=0} \left[\frac{\dot{L}_r}{r(1 - M_r)^2} \right]_{ret} dS \\ + \frac{1}{4\pi} \int_{f=0} \left[\frac{L_r - L_M}{r^2 (1 - M_r)^2} \right]_{ret} dS \\ + \frac{1}{4\pi a_0} \int_{f=0} \left[\frac{L_r (r \dot{M}_r + a_0 (M_r - M^2))}{r^2 (1 - M_r)^3} \right]_{ret} dS , \quad (3.68)$$

where

$$U_n = U_i n_i, \quad U_{\dot{n}} = U_i \dot{n}_i, \quad \dot{U}_n = \dot{U}_i n_i , \\ M_r = M_i r_i, \quad \dot{M}_r = \dot{M}_i r_i , \\ L_M = L_i M_i, \quad L_r = L_i r_i, \quad \dot{L}_r = \dot{L}_i r_i , \\ U_i = \rho u_i / \rho , \\ L_i = P_{ij} n_j + \rho u_i u_n . \quad (3.69)$$

In Eqs.(3.67)–(3.69), the dot over a variable stands for the variable source–time differentiation, M_i is the component of the local Mach number vector of the source, r_i is the component of the unit vector in the radiation direction, r is the distance between the source and observer, and $[\cdot]_{ret}$ denotes the quantity evaluated at retarded time $\tau = t - r/a_0$.

3.6 Uncertainty of Statistical Quantities

The stochastic data sets obtained from experimental (microphone, hot-wire) measurements and numerical (LES) simulations are analysed using several statistical quantities, including mean, root-mean-square (RMS), cross-correlation coefficient (XCOR), power spectral density (PSD) and cross-spectral density (CSD) estimations. As each data set is sampled over a certain time interval t_s and could contain self-correlated data, these statistical quantities can only be estimated within a certain level of confidence interval. An averaging procedure, which can lead to statistical errors, is used in the estimation of these quantities. The following will present the equations used to calculate the statistical uncertainty with a confidence level of 95%, and summarise the typical uncertainty level for the statistical quantities presented in Chapters 3–8.

According to Glegg and Devenport [72], assuming errors are normally distributed, the uncertainty interval (at 95% confidence level) for mean, RMS and XCOR estimators can be calculated by (nonlinear and/or correlation terms neglected)

1. Mean estimator \bar{a}

$$\bar{a} = \frac{1}{N_{tot}} \sum_{n=1}^{N_{tot}} a_n , \quad (3.70)$$

$$\delta[\bar{a}] = \frac{2\sqrt{\sum_{n=1}^{N_{tot}} (a_n - \bar{a})^2}}{N_{tot}} , \quad (3.71)$$

where $\delta[\cdot]$ denotes the uncertainty estimation, a_n is the discrete data sample and N_{tot} is the total number of samples for data set a .

2. Root-mean-square (RMS) estimator $\sqrt{a'^2}$

$$\sqrt{a'^2} = \sqrt{\frac{1}{N_{tot}} \sum_{n=1}^{N_{tot}} (a_n - \bar{a})^2} , \quad (3.72)$$

$$\delta[\sqrt{a'^2}] = \frac{\sqrt{2}\sqrt{a'^2}}{\sqrt{N_{tot}}} . \quad (3.73)$$

3. Cross-correlation coefficient (XCOR) estimator ρ_{ab}

$$\rho_{ab} = \frac{\overline{a'b'}}{\sqrt{a'^2}\sqrt{b'^2}} , \quad (3.74)$$

$$a' = a_n - \bar{a} , \quad b' = b_n - \bar{b} , \quad n \in [1, 2, \dots, N_{tot}] , \quad (3.75)$$

$$\delta[\rho_{ab}] = \frac{2}{\sqrt{N_{tot}}} (1 - \rho_{ab}^2) , \quad (3.76)$$

where a and b are two independent data sets.

For spectral quantities PSD and CSD, their statistical uncertainties are estimated based on the effective number of independently performed spectral averages N_{rec} , which can be determined by

$$N_{rec} = \text{int} \left[\frac{N_{tot}/N_0 - 1}{1 - \Lambda_o} \right] + 1 , \quad (3.77)$$

where N_0 is the number of samples in each data record for fast Fourier transform, Λ_o is the overlap ratio and $\text{int}[\cdot]$ denotes the integer part of the result. The uncertainty interval (at 95% confidence level) for PSD and CSD estimators can be calculated by [72]

1. Power spectral density (PSD) estimator G_{aa}

$$\delta[G_{aa}] = \frac{2G_{aa}}{\sqrt{N_{rec}}} . \quad (3.78)$$

2. Cross-spectral density (CSD) estimator G_{ab}

$$\delta[|G_{ab}|] = \frac{2\sqrt{G_{aa}G_{bb}}}{\sqrt{N_{rec}}} . \quad (3.79)$$

Table 3.8 summarises the parameters used to calculate the uncertainty of statistical quantities in Chapters 3–8, and typical statistical uncertainty results calculated using Eqs. 3.70–3.79.

Table 3.8: Statistical parameters and uncertainties for quantities presented in Chapters 3–8 (Exp.: Experimental; Num.: Numerical; HW: Hot-wire; Mic.: Microphone; F_s : sampling frequency).

Section	Data type	Method	Quantity	Quantity type	F_s (Hz)	N_{tot}	Window	Λ_o	N_{rec}	Uncertainty (%)
3.3.1	Exp.	HW	Mean velocity	Mean	51200	409600	-	-	-	0.0009 ¹
3.3.1	Exp.	HW	Velocity fluctuation	RMS	51200	409600	-	-	-	0.22
3.3.1	Exp.	Mic.	Noise spectrum	PSD	65536	2097152	Hann	0.5	511	8.85
4.2	Exp.	Mic.	PSD in transfer function	PSD	51200	512000	Hann	0.5	79	22.50
4.2	Exp.	Mic.	CSD in transfer function	CSD	51200	512000	Hann	0.5	79	22.50 ²
5.2	Exp.	Mic.	Cross spectral matrix	CSD	65536	2097152	Hann	0.5	511	12.26 ³
5.3	Exp.	Mic.	Cross spectral matrix	CSD	65536	2097152	Hann	0.5	511	11.15 ⁴
6.2.1	Exp.	HW	Mean velocity	Mean	51200	1638400	-	-	-	0.039 ⁵
6.2.2	Exp.	HW	Velocity fluctuation	RMS	51200	1638400	-	-	-	0.11
6.2.2	Exp.	HW	Velocity spectrum	PSD	51200	1638400	Hann	0.5	255	12.52
6.3.1	Exp.	HW	Mean velocity	Mean	51200	819200	-	-	-	0.024 ⁶
6.3.2	Exp.	HW	Velocity fluctuation	RMS	51200	819200	-	-	-	0.16
6.4.1	Exp.	Mic.	Noise spectrum	PSD	65536	2097152	Hann	0.5	511	8.85
6.4.2	Num.	LES	Correlation function	XCOR	50000	5000	-	-	-	4.24 ⁷
6.4.2	Num.	LES	Mean mass flow rate	Mean	50000	5000	-	-	-	1.13 ⁸
6.4.2	Num.	LES	Velocity fluctuation	RMS	50000	5000	-	-	-	2.00
6.4.2	Num.	LES	Surface pressure fluctuation	RMS	50000	5000	-	-	-	2.00
7.2	Exp.	Mic.	Cross spectral matrix	CSD	65536	2097152	Hann	0.5	511	29.40 ⁹
8.3	Exp.	Mic.	Cross spectral matrix	CSD	65536	2097152	Hann	0.5	511	21.01 ¹⁰

Example uncertainties for

¹ velocity data measured at the core of UAT test section, $x/D_H=0.5$ and $U_\infty = 30$ m/s;

² CSD results for specimen P4 at 5 kHz;

³ CSD results between the center microphone and its closest microphone at 5 kHz for the baseline airfoil in UAT Campaign 1a;

⁴ CSD results between the center microphone and its closest microphone at 5 kHz for the baseline airfoil in UAT Campaign 1b;

⁵ velocity data measured at 1 mm downstream of the baseline airfoil TE in UAT Campaign 1a;

⁶ velocity data measured at 1 mm downstream of the baseline airfoil TE in UAT Campaign 1b;

⁷ spatial and space-time correlation coefficients of 0.5;

⁸ mass flow rate data for pore PR3;

⁹ CSD results between two microphones close to the rotor blade tip at 5 kHz for the reference rotor at 900 RPM and 5° pitch angle;

¹⁰ CSD results between the center microphone and its closest microphone at 5 kHz for the S5 airfoil in UAT Campaign 2.

Chapter 4

Acoustic Characterisation of Porous Structures

4.1 Overview

This chapter experimentally characterises the sound absorption coefficient of porous structures to be applied in airfoil trailing-edge noise control. Inspired by the micro-perforated panel theory proposed by Maa [126, 127, 128] (its principle and formulations have been described in Sec. 3.2.3), a series of porous specimens with micro-tube pores have been fabricated by additive manufacturing. The acoustic absorption of the micro-tube structures with various geometric parameters has been measured using a two-microphone impedance tube in MC Campaign 1 as described in Sec. 3.2. The geometric design criteria for such a structure to achieve maximum sound absorption over a certain frequency range will be discussed. Moreover, in order to achieve broadband acoustic absorption, two novel composite structures: 1) micro-perforated housing with an air gap and 2) micro-perforated housing with acoustic foam infill have been additively manufactured and characterised in MC Campaign 2 (details in Sec. 3.2). The advantages of such structures over traditional porous acoustic absorbers and the method of tuning their peak sound absorption frequency will be discussed in detail.

4.2 Acoustic Absorption of Micro-Tube Porous Structures

This section presents the acoustic characterisation results of MC Campaign 1. The acoustic absorption of ten 3D printed micro-tube porous specimens and three porous aluminium specimens (detailed geometric parameters are summarised in Table 3.1) has been characterised using a two-microphone impedance tube. The effects of important geometric parameters of micro-tube porous structures on the acoustic absorption will be analysed through a parametric study.

4.2.1 Effects of Porosity

Figure 4.1a presents the sound absorption coefficient of micro-tube specimen P1, reference specimen SR and porous aluminium specimens 40PPI, 20PPI and 10PPI. Compared with the non-porous ($\phi = 0$) 3D-printed Visijet M3 material (SR) and highly porous ($\phi = 92\text{--}94\%$) aluminium foams (10PPI, 20PPI and 40PPI) that have been previously applied as trailing-edge treatment [2], the proposed micro-tube structure P1 ($\phi = 11.53\%$) shows significantly greater potential for sound absorption over high frequencies (3.2–6.4 kHz). This indicates that the porosity can lead to effective sound absorption ($\alpha_p > 0.25$) only for materials with a specific porous structure. Figure 4.1b compares the sound absorption coefficient of specimens P1, P2, P3 and SR. The micro-tube specimens P1, P2 and P3 have a identical pore diameter d_0 but different porosity ϕ due to a different number of pores. At frequencies lower than 3.2 kHz, all specimens have similar sound absorption coefficients which are relatively low (< 0.1) and could be considered inefficient for sound absorption. For frequencies higher than 3.2 kHz, the sound absorption coefficient of the micro-tube specimens is significantly greater than that of solid reference specimen SR, indicating that the effective sound absorption over 3.2–6.4 kHz is due to the micro-tube porous structures. Furthermore, the acoustic absorption spectra of specimens P1–P3 show a peak amplitude varying from 0.56–0.90 at frequencies ranging from 5–6 kHz. The peak frequency and amplitude of the absorption coefficient shows a tendency to decrease with decreasing porosity. Therefore, for noise control over a specific frequency range, a potential

strategy of shifting the peak sound absorption coefficient is to optimally adjust the porosity distribution.

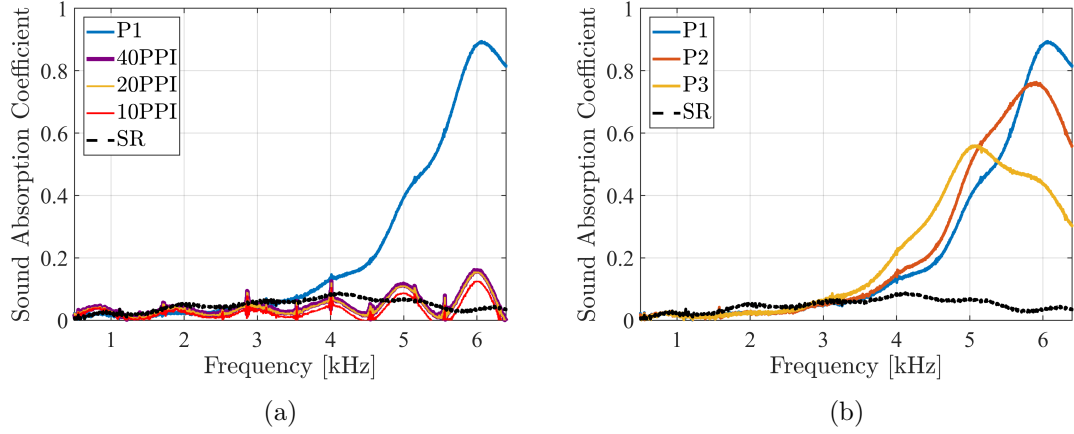


Figure 4.1: Sound absorption coefficient of (a) specimen P1 compared with solid reference specimen SR and porous aluminium specimens 40PPI, 20PPI and 10PPI; (b) specimens with identical thickness h_0 , pore diameter d_0 but different porosity ϕ : P1 ($\phi=11.53\%$), P2 ($\phi=8.20\%$) and P3 ($\phi=5.35\%$) compared with specimen SR.

4.2.2 Effects of Aspect Ratio

Figure 4.2a shows the acoustic absorption performance of specimens P1, P4, P5 and reference specimen SR. The porous specimens have a comparable porosity ϕ (11.53, 11.11 and 11.51% for P1, P4 and P5, respectively) and identical thickness h_0 but different pore diameters d_0 (1, 0.8 and 0.6 mm for specimens P1, P4 and P5, respectively). As shown in Figure 4.2a, the frequency characteristics of their sound absorption coefficients are similar and hence reasonably independent of pore diameter d_0 . It can be seen that their peak sound absorption coefficients are also similar, only varying within a small range from 0.85–0.9.

Figure 4.2b compares the sound absorption coefficient of specimens with an identical porosity ϕ , pore diameter d_0 but different thickness h_0 . It is noticeable that the shape of their acoustic absorption spectra is similar. However, their peak amplitudes vary significantly from 0.11 to 0.90, indicating a strong dependency of sound absorption amplitude on the geometry of the micro-tubes inside these porous specimens. For a certain cylinder-shape micro-tube, its geometry can be described by the aspect ratio $AR = d_0/h_0$. Figure 4.3 shows the variation of peak sound absorption coefficients with aspect ratio. First, the

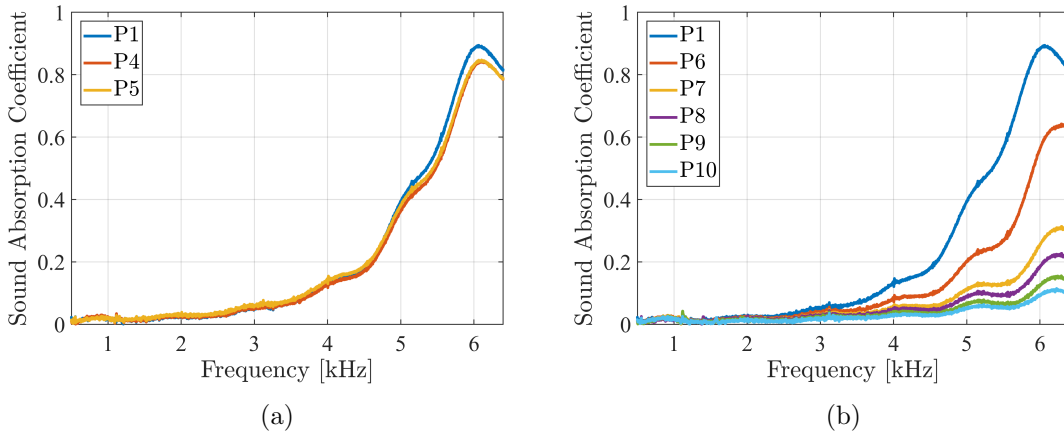


Figure 4.2: Sound absorption coefficients of micro-tube specimens with same porosity ($\phi = 11.5\%$): (a) specimens with same thickness h_0 but different pore diameter d_0 ; (b) specimens with same pore diameter d_0 but different thickness h_0 .

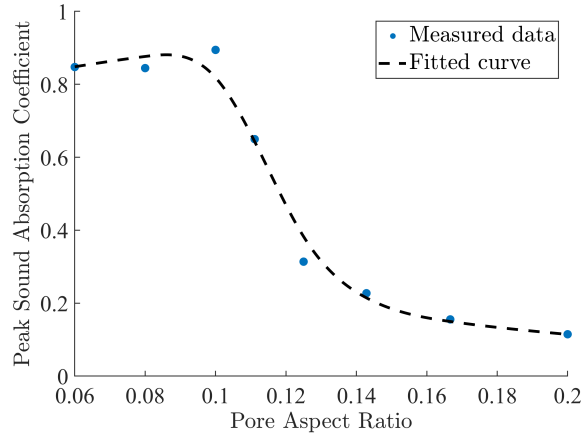


Figure 4.3: Relationship between pore aspect ratio and peak sound absorption coefficient (all specimens have a similar porosity within 11.1–11.5%).

peak absorption coefficient increases with aspect ratio from $AR = 0.06$ to 0.1 and peaks at around $AR = 0.1$ with the value of $\alpha_p = 0.90$. As the aspect ratio keeps increasing from 0.1 to 0.16 , α_p quickly decreases to around 0.2 . Finally, it gently approaches an asymptotic value of 0.1 as the aspect ratio increases further. Since porosity is the most sensitive parameter affecting acoustic absorption of the micro-tube structure, it can be concluded that the maximum acoustic absorption performance of such acoustic absorber with a certain porosity may be achieved by optimal design of the pore aspect ratio. Summarising the results of Figures 4.1–4.3 for the proposed 3D printed micro-tube structures with a porosity of 11.53% , the pore aspect ratio should be less than 0.14 to be effective in normal-incident sound absorption ($\alpha_p > 0.25$).

In general, it can be deduced that for porous structures with a certain porosity, an

optimal aspect ratio to achieve maximum sound absorption and a maximum aspect ratio for effective sound absorption ($\alpha_p > 0.25$) exist. To optimally design the geometry of micro-tube structures for sound absorption over a certain frequency range, porosity and pore aspect ratio are the two crucial parameters that need to be determined.

4.3 Acoustic Absorption of Micro-Perforated Housings with Air Gap and Foam Infill

This section presents the acoustic characterisation results of MC Campaign 2. The acoustic absorption of eight novel micro-perforated absorbers (geometries are described in Figure 3.2 and Table 3.2) have been characterised using a two-microphone impedance tube. Experimental data will be compared with Maa's analytical model [126] of a micro-perforated absorber, and improvements in sound absorption with the proposed novel structure will be demonstrated.

Figure 4.4 shows the sound absorption coefficient of specimens PA1–PA4 and predictions using Maa's model. Note that predictions are only performed on the composite of the top micro-perforated panel and the air gap (the bottom micro-perforated panel is excluded) due to the limitations in Maa's model. As shown in Figures 4.4a–4.4c, when the bottom panel is relatively thin ($h_b \leq 3$ mm), the acoustic absorption of the novel absorber is dominated by its top composite (top panel + air gap), showing good agreement with the model predictions over lower frequencies (< 4.2 kHz). The discrepancies at higher frequencies (> 4.2 kHz) are likely due to the extra sound absorption from the bottom micro-perforated panel. However, Maa's model fails to predict the peak frequency of the acoustic absorption spectrum for specimen PA4 as shown in Figure 4.4d. This may be due to the the relatively large increase in acoustic resistance at lower frequencies [126] caused by the sufficiently thick ($h_b = 4$ mm) bottom panel, resulting in a shift in peak frequency from 5.6 to 4.7 kHz.

Figure 4.5 compares the sound absorption coefficient of the micro-perforated housings with an acoustic foam infill (specimens RF1–RF4) and an air gap (specimens RA1–RA4). The acoustic foam infill significantly increases the bandwidth of sound absorption, giving rise to broadband sound absorption with a limited specimen thickness (10 mm). The

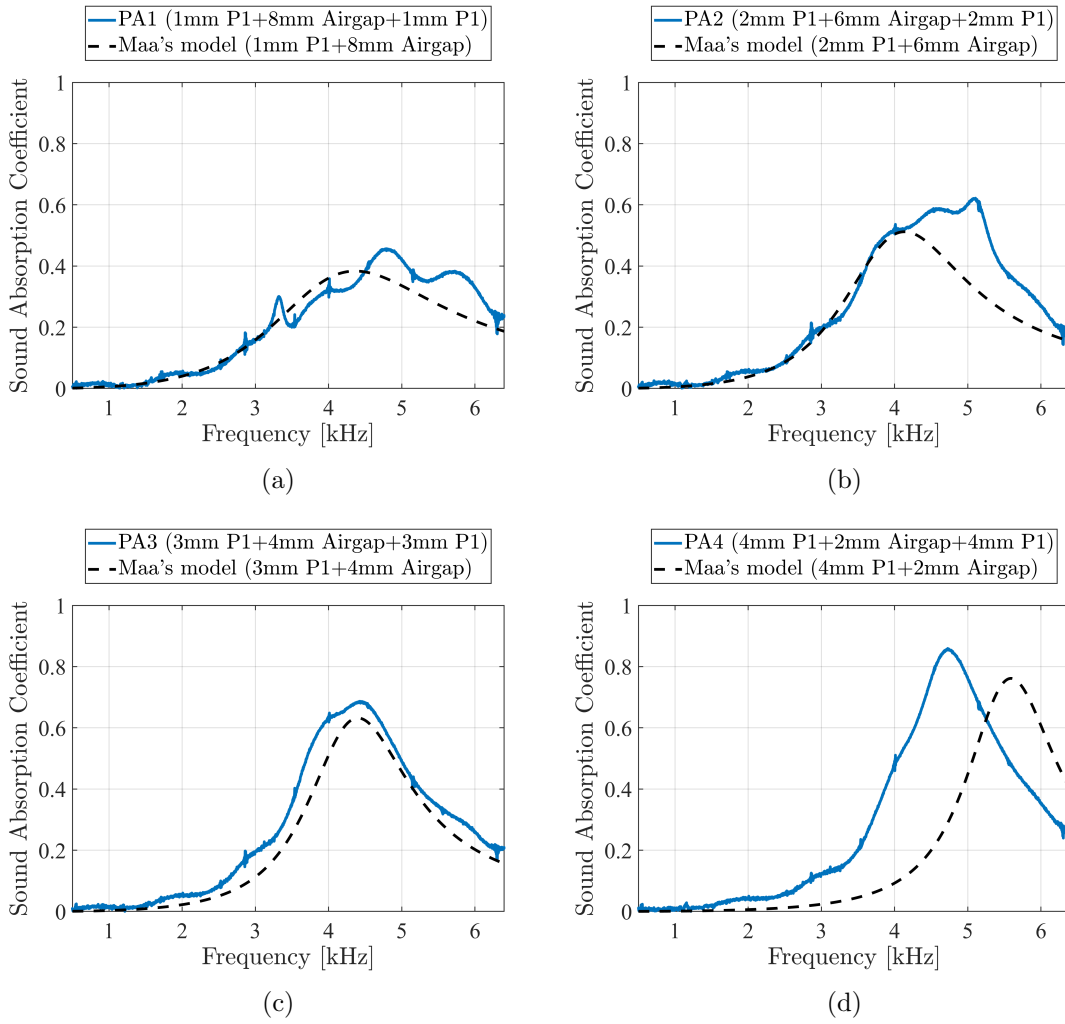


Figure 4.4: Sound absorption coefficient of specimens (a) PA1, (b) PA2, (c) PA3 and (d) PA4 compared with predictions using Maa's model (bottom micro-perforated panel excluded).

amplitude of the broadband increase in sound absorption coefficient increases with the thickness of acoustic foam infill, while the spectral shape is not significantly altered by the acoustic foam infill due to the broadband nature of the sound absorption coefficient. In Figure 4.6, the sound absorption coefficient of specimens PF1–PF4 is compared with that of a 10 mm thick acoustic foam. The peak sound absorption coefficient of the acoustic foam (specimen F10) is increased from 0.5 to 0.8–0.9 by the micro-perforated housings with an acoustic foam infill (specimens PF1–PF4). The proposed novel structure provides an approach of achieving efficient broadband sound absorption over a desired frequency range with a limited specimen thickness. When the bottom panel thickness is small with respect to the specimen total thickness, the geometric parameters of the micro-perforations can be optimally designed using Maa's model to achieve efficient broadband sound absorption

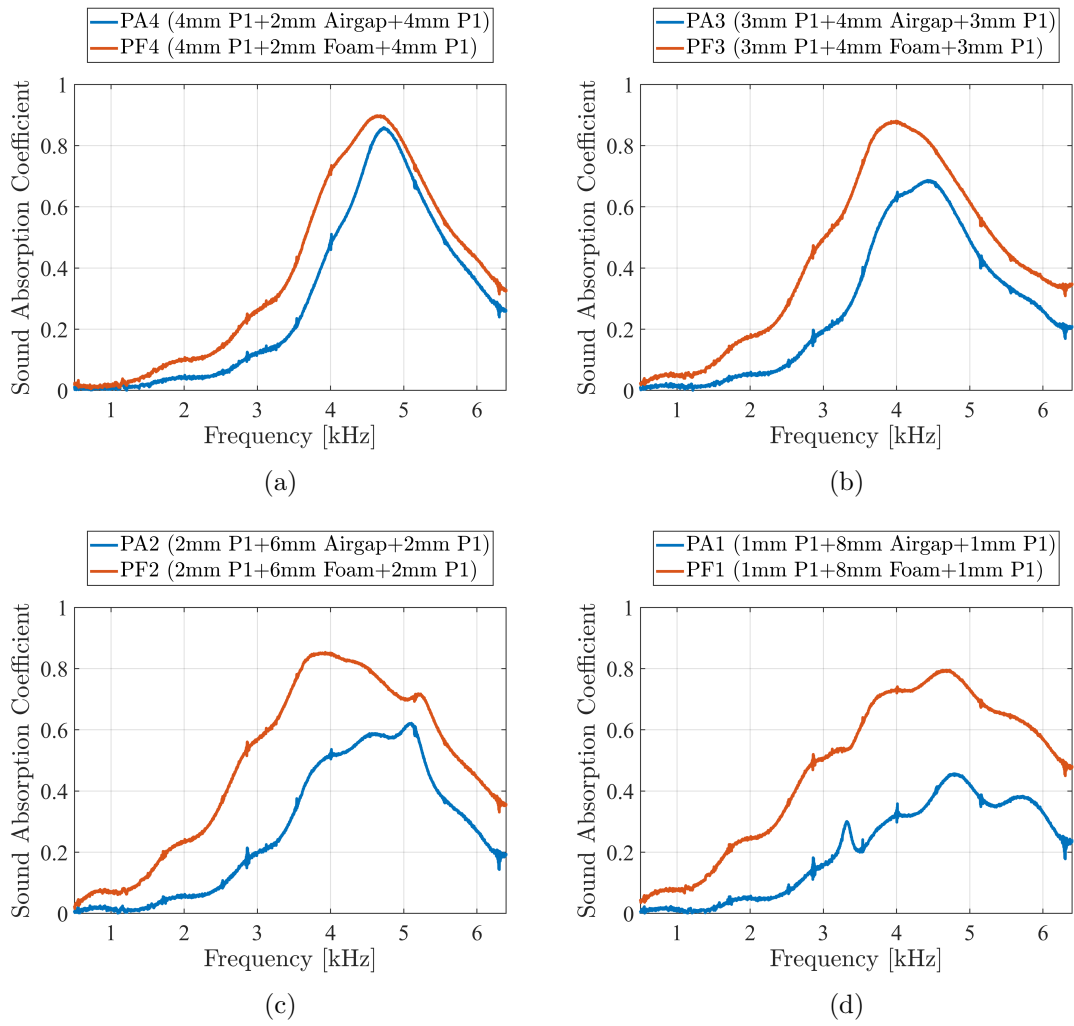


Figure 4.5: Sound absorption coefficient of specimens (a) PF1, (b) PF2, (c) PF3 and (d) PF4 compared with that of specimens PA1–PA4.

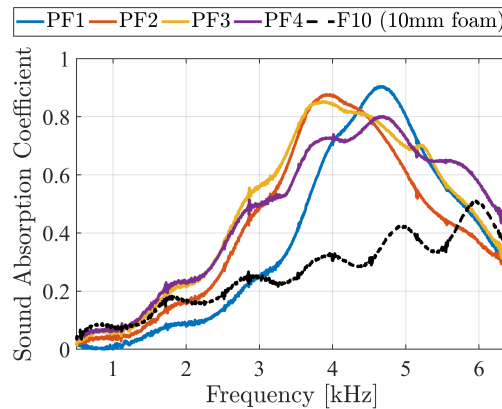


Figure 4.6: Sound absorption coefficient of specimens PF1–PF4 compared with that of a Basotect[®] foam with 10 mm thickness (F10).

over a certain frequency range of interest.

4.4 Summary

The feasibility of using additive manufacturing to fabricate micro-tube structures for acoustic absorption has been investigated in this chapter. In MC Campaign 1, a series of such 3D printed structures has been fabricated and their sound absorption performance has been measured using an impedance tube. The results have shown that a peak sound absorption coefficient of 0.90 can be achieved by the test specimens, and they are examined to have good sound absorption performance over higher frequencies ranging from 3.2–6.4 kHz. Based on the experimental data obtained in this work, it can be concluded that the frequency characteristics of the acoustic absorption spectra for micro-tube structures are related to their porosity. Furthermore, for such structures to achieve maximum sound absorption over a desired frequency range, the following geometric design criteria have been established: 1) the peak frequency of the sound absorption coefficient can be shifted to lower frequencies by decreasing the porosity; 2) for micro-tube structures with a certain porosity, the amplitude of their sound absorption coefficient is strongly related to the pore aspect ratio, and a maximum sound absorption coefficient can be achieved by selecting an optimal pore aspect ratio. The porous structure based on specimen P4 has been applied in airfoil trailing-edge noise control, which will be further discussed in Chapters 5, 6 and 7.

In addition, novel sound-absorbing structures consisting of a micro-perforated housing with an air gap (PA structure) and a Basotect[®] foam infill (PF structure) have been proposed and characterised in MC Campaign 2. The frequency characteristics of sound absorption for the PA structures can be predicted by Maa's analytical model when the thickness of bottom the perforated panel is small ($h_b/h_0 \leq 0.3$) relative to the total specimen thickness. Moreover, extra sound absorption due to the bottom micro-perforated panel of the PA structures has been observed over higher frequencies ranging from 4.2–6.4 kHz. For PF structures, their foam infill can increase the peak sound absorption coefficient and sound absorption bandwidth without altering the frequency characteristics. Comparison between the PF structures and a Basotect[®] foam with identical thickness suggests that PF structures can significantly increase the peak sound absorption and shift the peak frequency to that of the corresponding PA structures. Therefore, PF structures

can provide efficient broadband sound absorption with a limited specimen thickness, where the peak sound absorption can be tuned to the desired frequency range by optimally designing the micro-perforated geometries based on Maa's model.

Chapter 5

Airfoil Trailing Edge Noise Reduction Using Porous and Serrated Edge Treatments

5.1 Overview

This chapter experimentally investigates the trailing-edge (TE) noise performance of a NACA 0012 airfoil with one reference and eleven novel serrated, porous, porous-serrated and serrated-porous flat-plate TE extensions (as defined in Table 3.4). The porous geometries have been designed according to the acoustic characterisation results presented in Chapter 4. The two experimental campaigns UAT Campaign 1a and UAT Campaign 1b (as described in Sec. 3.3.2) have been conducted to evaluate the laminar-transitional boundary layer trailing-edge (LBL-TE) noise and turbulent boundary layer trailing-edge (TBL-TE) noise of the proposed TE extensions, respectively.

In UAT Campaign 1a, acoustic measurements have been performed on a natural-transitioned NACA 0012 airfoil with treated TE extensions at a geometric angle of attack $\alpha_g = 4^\circ$ and freestream velocities $U_\infty = 12\text{--}20\text{ m/s}$ ($Re_c = 1.9\text{--}3.2 \times 10^5$). In UAT Campaign 1b, acoustic measurements have been performed on a forced-transitioned NACA 0012 airfoil with treated TE extensions at a geometric angle of attack $\alpha_g = 4^\circ$ and freestream velocity $U_\infty = 20\text{--}50\text{ m/s}$ ($Re_c = 3.2\text{--}8 \times 10^5$). The acoustic results of UAT Campaign 1a and UAT Campaign 1b will be presented in Secs. 5.2 and 5.3, respectively. The noise reduction performance of the treated TE extensions will be analysed in different frequency regions categorised by their dominant noise mechanism.

5.2 Laminar-Transitional Boundary Layer Trailing-Edge Noise

This section presents the acoustic results of UAT Campaign 1a as described in Section 3.3.2. In this experimental campaign, the effects of 11 treated flat-plate TE extensions on LBL-TE noise have been characterised. These extensions are attached to the TE of a NACA 0012 airfoil model during the measurements (as shown in Figure 3.12), and their geometries have been summarised in Table 3.4. Acoustic measurements were performed at freestream velocities from 12 to 20 m/s ($Re_c = 1.9\text{--}3.2 \times 10^5$), where the instability tonal noise is expected to be the dominant noise source [10, 55, 123].

Conventional beamforming [141] is used to estimate the location and strength of the noise sources. The formulations of this beamforming algorithm have been presented in Section 3.3.3. Figure 5.1 shows sample beamforming sound maps at 2520 Hz for extensions BL, NS, CS and CSP. All maps are shown using a 10 dB dynamic range. The dominant noise sources are located at the airfoil TE, and extensions NS, CS and CSP are shown to significantly reduce the TE noise level by 10 dB, 10 dB and 4 dB compared to the baseline (BL) case, respectively.

To obtain the spectral information for the noise radiated from the airfoil TE with high signal-to-noise ratio, the sound pressure levels in the beamforming maps are integrated over the TE region using the source integration method [27] as described in Section 3.3.3. The positions of the array microphones, airfoil model and TE integration region are shown in Figure 5.2, in which the black circles represent the microphones, green rectangle is the airfoil model and red rectangle is the integration region (flow direction is from left to right).

In the Reynolds number range ($1.9\text{--}3.2 \times 10^5$) for UAT Campaign 1a, the generation mechanism for airfoil TE noise is rather complicated. Three major noise sources are expected to be observed [31]: the LBL-TE noise (so called instability tonal noise in [7, 39, 106, 157]), the broadband noise due to the harmonics of Tollmien–Schlichting (T-S) waves and the bluntness vortex-shedding noise. Figure 5.3a presents the integrated narrow-band noise spectrum for the baseline case at a freestream velocity $U_\infty = 18$ m/s

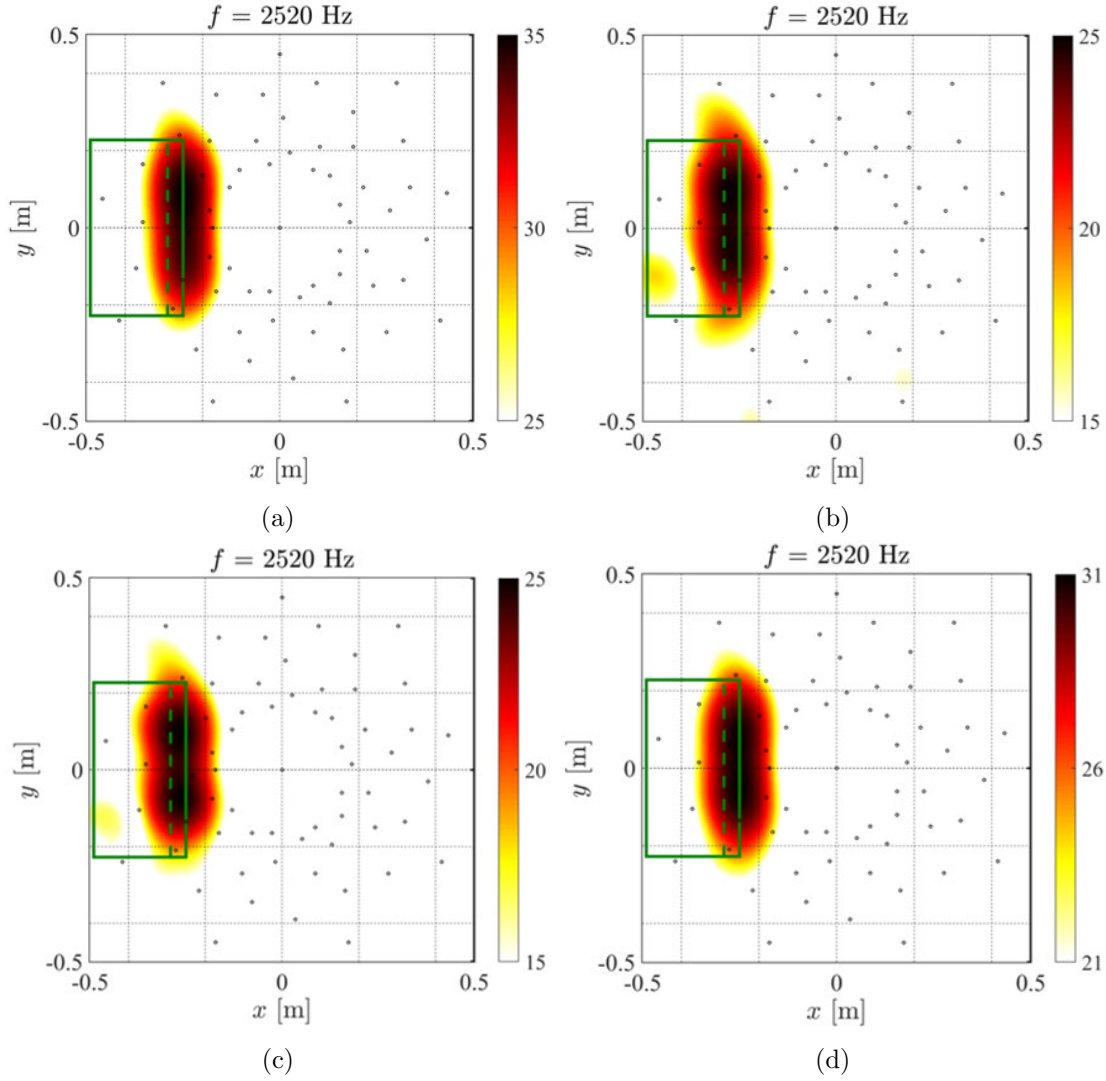


Figure 5.1: Beamforming sound maps for the natural-transitioned NACA 0012 airfoil with extensions (a) BL, (b) NS, (c) CS and (d) CSP at freestream velocity $U_\infty = 18$ m/s and frequency $f = 2520$ Hz (color bar scale in dB). Flow comes from left to right. Green rectangle is the position of airfoil model, and green dash-line is the leading edge of flat-plate extension (x and y correspond to horizontal (streamwise) and vertical coordinates).

($Re_c = 2.9 \times 10^5$), showing the appearance of the aforementioned noise sources. A broadband hump with multiple equally-spaced discrete tones is observed at frequencies ranging from 0.4 kHz to 0.9 kHz, which is likely LBL-TE noise. At higher frequencies around 3 kHz, a significant hump is observed possibly produced by trailing-edge bluntness vortex-shedding. A comparison between measured acoustic data and predictions of the peak frequency of LBL-TE noise and bluntness vortex-shedding noise from the classic BPM empirical model [31] further supports the observation (see Figure 5.3b). Even though BPM model over-predicts the noise levels for LBL-TE and bluntness vortex-shedding, their peak frequencies f_{LBL} and f_b are found to be in good agreement with peak fre-

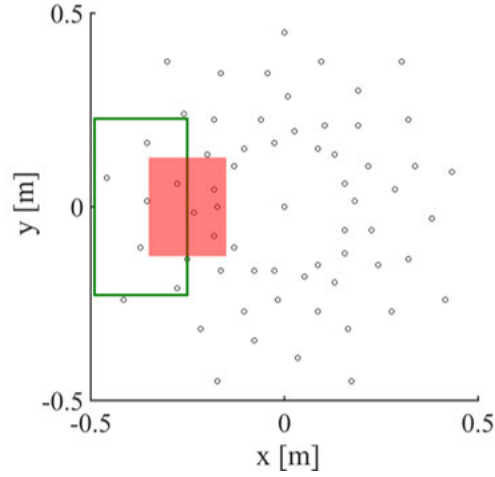


Figure 5.2: Schematic of the positions of array microphones (black circles), airfoil model (green rectangle) and TE integration region (red rectangle) for UAT Campaign 1a.

quencies of the low- and high-frequency hump, respectively. A noise level correction of $[10 \log_{10}(0.232 f_{LBL})]$ dB [39] is applied in the LBL-TE noise prediction to allow direct comparison with the experimental data. To be noticed, as the noise spectra (shown in Figure 5.3a) of the baseline extension and background collapse together at higher frequencies (3.5 kHz to 10 kHz), airfoil noise data in this frequency range are masked by tunnel background noise. Since the level of masked high-frequency noise is much lower compared with that of instability tonal noise (more than 30 dB lower than the peak tonal noise), their contribution to overall sound pressure level (between 0.25 kHz and 10 kHz) is negligible.

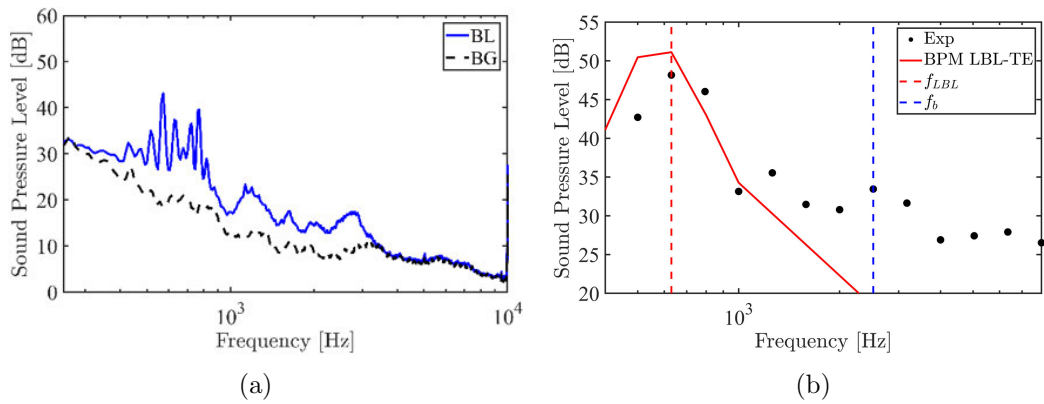


Figure 5.3: Acoustic data for baseline (BL) case at $U_\infty = 18$ m/s. (a) Integrated narrow-band noise spectrum of baseline case (BL) compared to background noise (BG); (b) integrated 1/3 octave band noise spectrum of baseline case (Exp) compared to BPM predictions (BPM LBL-TE: level-corrected BPM prediction of LBL-TE noise; f_{LBL} : peak frequency of LBL-TE noise; f_b : peak frequency of bluntness vortex-shedding noise.)

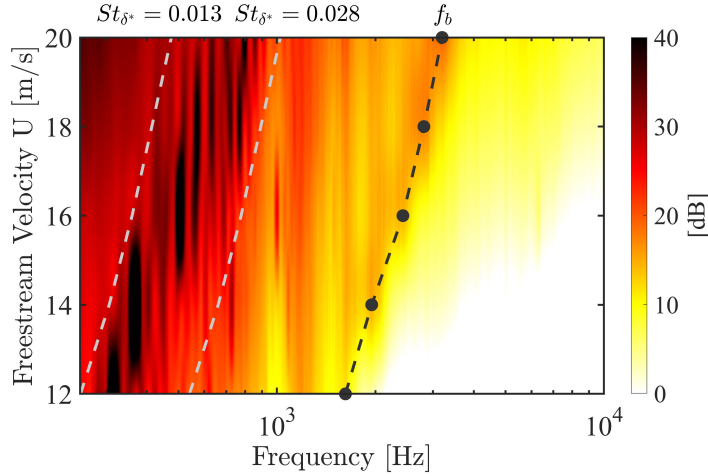


Figure 5.4: Colormap of narrow-band noise spectra for the natural-transitioned NACA 0012 airfoil with baseline flat-plate extension (St_{δ^*} - Strouhal number based on displacement thickness δ^* ; f_b - peak frequency of bluntness vortex-shedding noise).

Figure 5.4 presents narrow-band (8 Hz bandwidth) noise spectra (integrated over the TE region as shown in Figure 5.2) for the airfoil model with extension BL, plotted as a colormap of frequency versus freestream velocity. The discrete tones embedded within the broadband humps below 1 kHz are likely produced by the acoustic feedback loop and the most amplified T-S waves in the boundary layer [42]. They are found to occur at St_{δ^*} of between 0.013 and 0.028, where St_{δ^*} is the Strouhal number based on the displacement thickness δ^* on the pressure side at the TE. As discussed in Sec. 6.2.1, the boundary layer displacement thickness δ^* has been estimated by XFOIL for acoustic scaling. Table 5.1 summarises the peak frequency f_b of the high-frequency humps and corresponding Strouhal numbers St_b based on TE thickness b for the baseline case at freestream velocity $U_\infty =$

Table 5.1: Peak frequencies f_b and Strouhal numbers St_b of bluntness vortex-shedding noise for airfoil with baseline flat-plate extensions at freestream velocities ranging from 12 m/s to 20 m/s.

U_∞ (m/s)	Bluntness Noise Peak Frequency f_b for BL Extension (Hz)	Bluntness Noise Peak St_b for BL Extension	Bluntness Noise Peak St_b in Ref. [186]
12	1620	0.14	0.12 - 0.22
14	1949	0.14	
16	2428	0.15	
18	2814	0.16	
20	3200	0.16	

12–20 m/s. The peaks of bluntness vortex-shedding noise occur at Strouhal numbers St_b of between 0.14 and 0.16. This agrees with the findings in Ref. [186] which has reported that the bluntness vortex-shedding noise for a NACA 0012 airfoil occurs at St_b of between 0.12 and 0.22.

Figure 5.5 shows the noise attenuation achieved with serrated extensions (NS, CS, WS and SS) at frequencies ranging from 0.25–10 kHz and freestream velocities of between 12 and 20 m/s. The noise attenuation ΔSPL is plotted as a colormap as a function of frequency f and freestream velocity U_∞ , in which ΔSPL is defined as:

$$\Delta SPL = SPL_{BL} - SPL_{Treated} , \quad (5.1)$$

where SPL_{BL} and $SPL_{Treated}$ are the sound pressure levels at the TE region of the airfoil with baseline and treated TEs, respectively. Based on the noise spectra of baseline extension BL, noise attenuation maps can be categorised into the following four frequency regions by St_{δ^*} and St_b :

- Frequency region for instability tonal noise (R1): $0.013 < St_{\delta^*} < 0.028$;
- Frequency region for broadband noise (R2): $St_{\delta^*} > 0.028 \cap St_b < 0.115$;
- Frequency region for bluntness vortex shedding noise (R3): $0.115 < St_b < 0.175$;
- High-frequency region (R4): $St_b > 0.175 \cap f < 10 \text{ kHz}$.

All serrated extensions are efficient in reducing bluntness vortex-shedding noise that occurs over region R3. For classic straight-saw-tooth extensions NS ($\lambda/h = 0.6$) and WS ($\lambda/h = 1.8$), the noise levels in frequency regions R1 and R2 are significantly reduced at lower freestream velocities $U_\infty = 12\text{--}16 \text{ m/s}$ (see Figures 5.5a and 5.5b). At higher flow speeds $U_\infty = 18\text{--}20 \text{ m/s}$, NS and WS introduce more tones over regions R1 and R2, however, the frequencies of the tones differ from those of the baseline extension. For curved-saw-tooth extension CS ($\lambda/h = 0.6$), the noise levels are consistently attenuated over frequency regions R1, R2 and R3 throughout the entire freestream velocity range (Figure 5.5c). On the contrary, the slitted-saw-tooth extension SS ($\lambda/h = 0.6$) fails to suppress the boundary-layer instability noise and produces more undesirable tonal noise over frequency regions R1 and R2 (Figure 5.5d). It is noted that the noise levels for

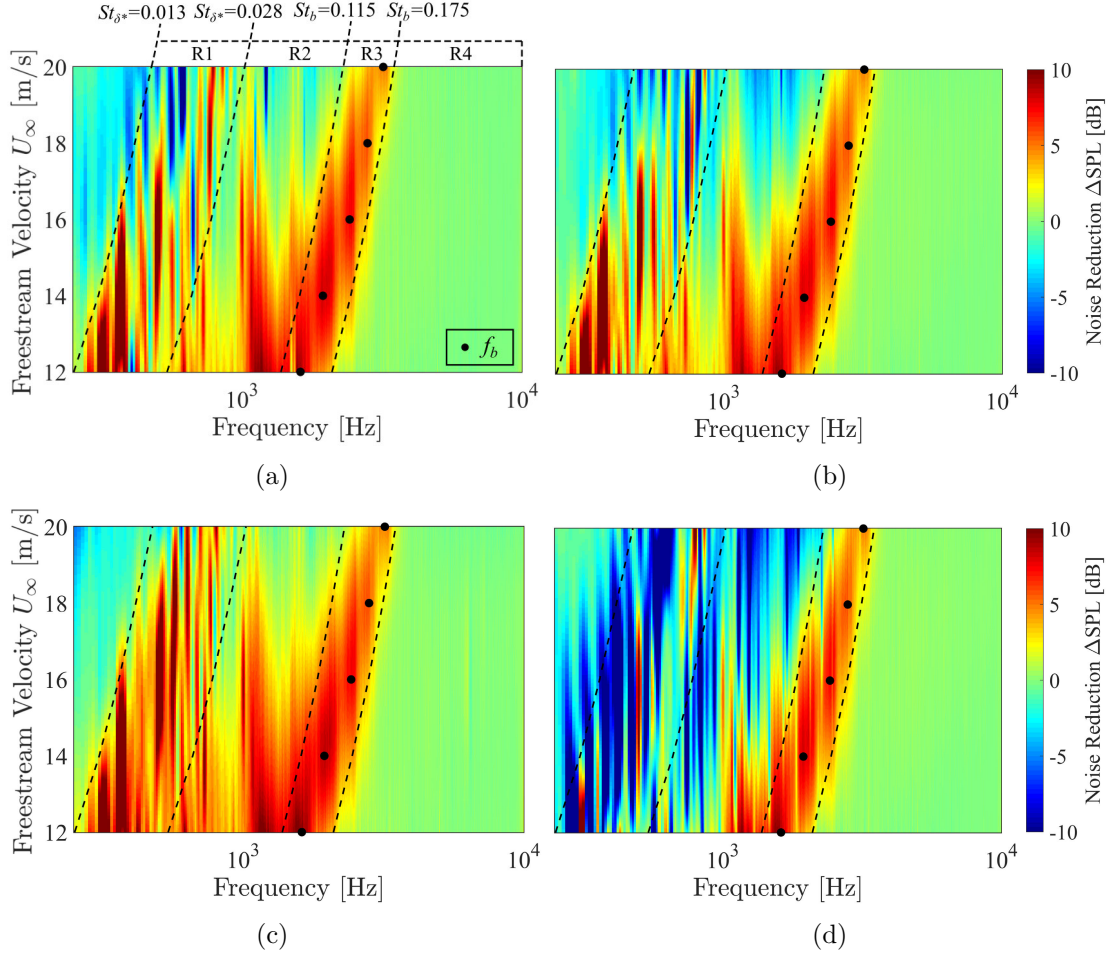


Figure 5.5: Colormaps of narrow-band noise attenuation ΔSPL for (a) narrow-serrated (NS), (b) wide-serrated (WS), (c) curved-serrated (CS) and (d) slitted-serrated (SS) extensions (St_{δ^*} - Strouhal number based on displacement thickness δ^* ; St_b - Strouhal number based on TE thickness b ; f_b - peak frequency of bluntness vortex-shedding noise).

serrated and baseline extensions are equivalent in high-frequency region R4, where the measured noise signal is masked by wind tunnel background noise.

Figure 5.6 shows the noise attenuation maps for extensions with porous structures (P, CSP, NSP, NPS, WSP and WPS). As all these extensions have the same straight blunt TE across the span, they are not as efficient as serrated extensions in reducing bluntness vortex-shedding noise over frequency region R3. For all-porous extension P, the porosity facilitates a reduction in the broadband TE noise in region R2 but fails to achieve noise attenuation in high-frequency region R4. In addition, multiple tonal noise increases are observed for the all-porous extension but not for serrated-porous extensions (Figures 5.6b, 5.6d and 5.6f). This indicated that the uniformly-spaced pores (P) may enhance the acoustic feedback loop or change frequency characteristics of the instability tonal noise, while the serrated-porous extensions (CSP, NSP and WSP) may have destructive

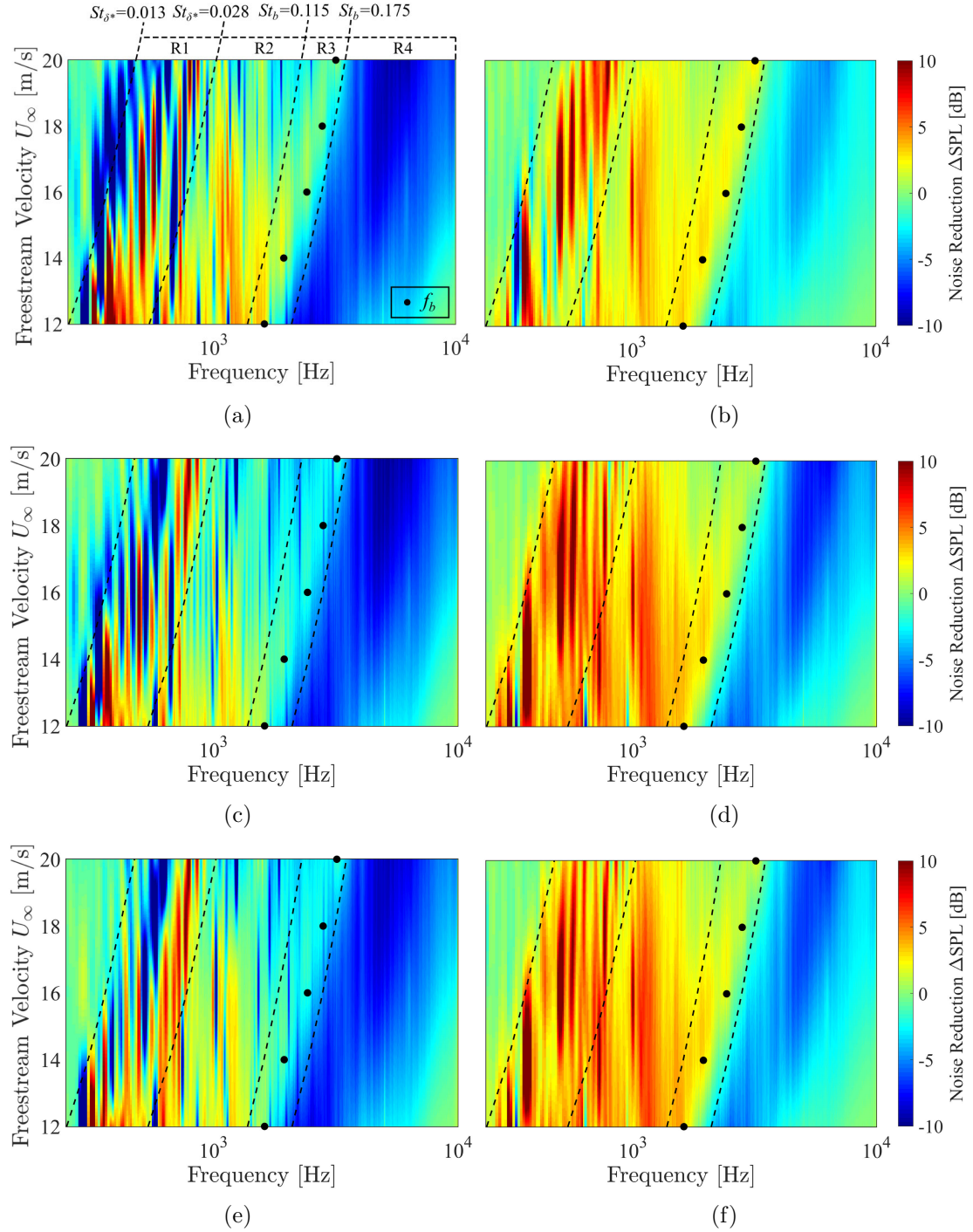


Figure 5.6: Colormaps of narrow-band noise attenuation ΔSPL for (a) porous (P), (b) curved-serrated-porous (CSP), (c) narrow-porous-serrated (NPS), (d) narrow-serrated-porous (NSP), (e) wide-porous-serrated (WPS) and (f) wide-serrated-porous (WSP) extensions (St_{δ^*} - Strouhal number based on displacement thickness δ^* ; St_b - Strouhal number based on TE thickness b ; f_b - peak frequency of bluntness vortex-shedding noise).

effects on the separation bubbles hence suppressing the acoustic feedback loop. For porous-serrated extensions NPS and WPS (Figures 5.6c and 5.6e), their acoustic performance is similar to that of extension P in all frequency regions R1–R4. This indicates that the

porous structures play a decisive role in aerodynamic noise production for porous-serrated TEs. In contrast, the aerodynamic noise production of serrated-porous extensions CSP, NSP and WSP (Figures 5.6b, 5.6d and 5.6f) is more likely to be dominated by the serrated geometries. Noticeable noise reduction is achieved with all serrated-porous extensions over regions R1, R2 and R3. Interestingly, although the serrated geometries of NSP ($\lambda/h = 0.6$) and WSP ($\lambda/h = 1.8$) are identical with those of NS ($\lambda/h = 0.6$) and WS ($\lambda/h = 1.8$), the tonal noise induced by NS and WS at higher flow speeds is not observed for NSP and WSP. This suggests that the porous geometries in the voids between the serrations have the potential to suppress the tonal noise induced by serrated TEs. However, compared to extension CS, the addition porous geometries of CSP fails to further reduce the noise levels in regions R1 and R2. This indicates the curved TE geometries may have more destructive effects on the laminar separation bubbles and the subsequent acoustic feedback loop than the serrated-porous geometries. Furthermore, for all extensions that have porous structures, a significant broadband noise increase is observed in high-frequency region R4. Table 5.2 lists the porosity ϕ (defined as the ratio of permeable area A_P to the total area of flat-plate A_{FP} , i.e., $\phi = A_P/A_{FP}$) for porous and serrated-porous extensions. The high-frequency broadband noise levels for extensions CSP, NSP and WSP increase with an increase in porosity ϕ , suggesting that the broadband noise increase may arise from the discontinuities in the porous geometries, i.e. pore edges and permeability. For porous-serrated extensions (NPS and WPS), their high-frequency broadband noise levels are higher than those for serrated-porous extensions (NSP and WSP). Although they have identical overall porosity, the local porosity of the former ones decreases along the streamwise direction, while that of the latter ones gradually increases. This indicates the excessive high-frequency broadband noise is more likely to be attributed to the upstream porous geometries as the porous-serrated extensions have the highest porosity upstream and higher noise levels. This point can be further supported by the observation that the noise performances of extensions with similar upstream porosity (NPS, WPS and P) are comparable in R4.

Figure 5.7 compares the overall noise attenuation $\Delta OASPL$ over 0.25 to 10 kHz of extensions CS, NS, WS, CSP, NSP, WSP and P at Reynolds numbers ranging from 1.9 to

Table 5.2: Geometric parameters of porous and serrated-porous extensions

Extension	Pore diameter r (mm)	Pore number n_p	Permeable surface area A_P (mm^2)	Flat-plate surface area A_{FP} (mm^2)	porosity ϕ $= A_P/A_{FP}$
CSP	0.8	585	1164	18200	0.03
NSP	0.8	1060	2109	18200	0.06
WSP	0.8	1138	2264	18200	0.06
P	0.8	2433	4840	18200	0.13

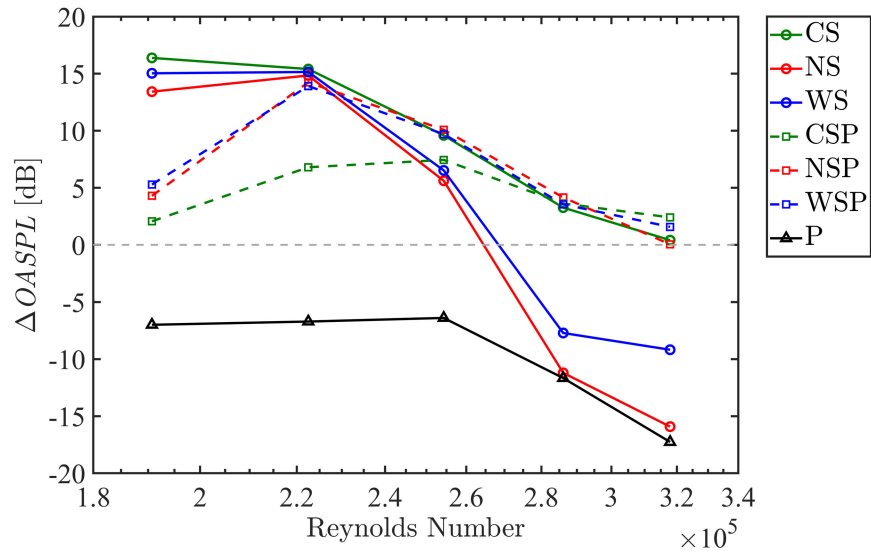


Figure 5.7: The noise attenuation in overall sound pressure level $\Delta OASPL$ (log scale on x axis) over frequencies ranging from 0.25 kHz to 10 kHz for extensions CS, NS, WS, CSP, NSP, WSP and P at Reynolds number ranging from 1.9×10^5 to 3.2×10^5

3.2×10^5 . The overall noise attenuation $\Delta OASPL$ is defined as:

$$\Delta OASPL = OASPL_{BL} - OASPL_{Treated}, \quad (5.2)$$

where $OASPL_{BL}$ and $OASPL_{Treated}$ are the overall sound pressure levels of the baseline and treated TE extensions, respectively. For most cases discussed here, $\Delta OASPL$ shows the trend of decreasing with increasing Reynolds number. All-porous extension P fails to achieve overall noise reduction. In contrast, its presence leads to increases in $OASPL$ of up to 17.3 dB at low-to-moderate Reynolds numbers ($1.9\text{--}3.2 \times 10^5$). Traditional straight-sawtooth extensions NS and WS can achieve an attenuation in $OASPL$ of up to 15 dB at lower Reynolds numbers ($1.9\text{--}2.7 \times 10^5$), while causing significant noise increases of up to

15.9 dB at higher Reynolds numbers ($2.7\text{--}3.2\times 10^5$) due to the extra instability tonal noise produced by straight-sawtooth serrations. Curved-serrated extension CS can effectively attenuate TE noise over the entire Reynolds number range ($1.9\text{--}3.2\times 10^5$) with a maximum reduction in *OASPL* of 16.4 dB. For serrated-porous extensions, their porous structures help to suppress instability tonal noise and therefore consistently achieve a reduction in *OASPL* of up to 14.2 dB over the entire Reynolds number range ($1.9\text{--}3.2\times 10^5$).

5.3 Turbulent Boundary Layer Trailing-Edge Noise

This section presents the acoustic results of UAT Campaign 1b as described in Section 3.3.2. Trailing-edge extensions BL, P, NS, CS, NSP and CSP have been tested on a forced-transition airfoil model in this experimental campaign. These extensions have been selected because of their ability to attenuate LBL-TE noise (as presented in Sec. 5.2). In UAT Campaign 1b, the effects of these extensions on the TBL-TE noise has been characterised by a 64-channel microphone array. Acoustic measurements are performed at freestream velocities from 20 to 50 m/s ($Re_c = 3.2\text{--}8\times 10^5$), and a 0.4 mm thick zig-zag turbulator tape is installed on both side of the airfoil model at 10% chord to generate a turbulent boundary layer at the model TE. Details of the measurement setup have been described in Section 3.3.2.

In this campaign, the beamforming sound maps are processed using the same method as in UAT Campaign 1a (see Section 3.3.2 for details). Figure 5.8 shows sample beamforming sound maps at 2520 Hz for extensions BL, P, NS, CS, NSP and CSP. All maps are shown using a 6 dB dynamic range. The most dominant noise source is located at the airfoil TE, and extensions P, NS, CS, NSP and CSP are shown to reduce the TE noise level at 2520 Hz by 0.8, 2.1, 3.2, 2.7 and 2.1 dB, respectively. Note that the discrepancies in leading-edge (LE) junction noise level are due to the change in dynamic range.

To obtain the TE noise spectra with high signal-to-noise ratio, the sound pressure levels in the beamforming maps are integrated using the same source integration method as in UAT Campaign 1a (see Section 3.3.3 for the details of this method). The TE integration region is marked as a red rectangle in Figure 5.9. Figure 5.10 presents the narrow-band noise spectra integrated over the TE region of the airfoil model with baseline extension

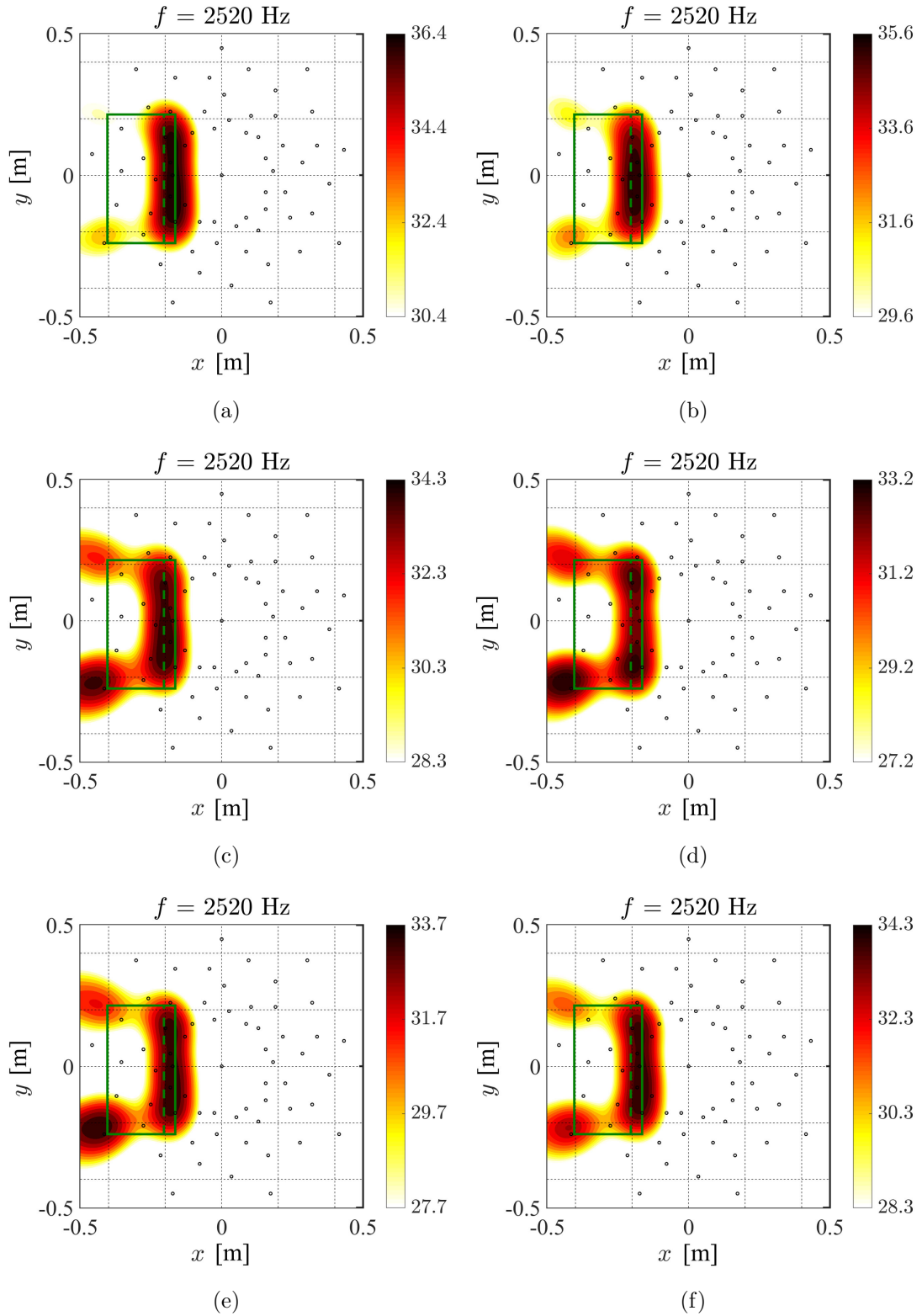


Figure 5.8: Beamforming sound maps for the forced-transitioned airfoil with extensions (a) BL, (b) P, (c) NS, (d) CS, (e) NSP and (f) CSP at freestream velocity $U_\infty = 36$ m/s and frequency $f = 2520$ Hz (color bar scale in dB). Flow comes from left to right. Green rectangle is the position of airfoil model, and green dash-line is the leading edge of flat-plate extension (x and y correspond to horizontal (streamwise) and vertical coordinates).

and background noise (without airfoil model) at $U_\infty = 36$ m/s. The signal-to-noise ratio is consistently larger than 5 dB over 5 kHz to 8 kHz. However, for frequencies higher than 8 kHz, the TE noise is masked by the background noise of the UAT. The narrow-band peak observed at around 5 kHz is most likely due to the TE bluntness, since this peak has a Strouhal number based on TE thickness $St_b=0.139$, which is in accordance to the St_b range for bluntness vortex-shedding noise as shown in Table 5.1.

Figure 5.11 presents a comparison of the integrated spectra for LE and TE regions (as shown in Figure 5.9) at $U_\infty = 36$ m/s. Note that the area of the LE and TE integration regions are identical. Here, f_{TE} is the critical frequency for TE noise dominance, which is defined as the frequency above which the noise level of the TE region is higher ($\Delta SPL > 1.5$ dB) than that of the LE region. Limited by the size of the microphone array, the location of dominant noise sources at low frequencies ($f < f_{TE}$) is difficult to identify due to the large beamwidth in sound map results. As a result, the LE and TE regions show a comparable noise level over this frequency range. At higher frequencies ($f > f_{TE}$), the TE region shows a significantly higher noise level (up to ~ 20 dB) compared to that of the LE region, indicating the TE noise is dominant over this frequency range. Therefore, the frequency range $f > f_{TE}$ is selected for TE noise comparison in UAT Campaign 1b. As discussed previously, the noise spectra above 8 kHz are masked by the UAT background noise.

Figure 5.12a presents narrow-band (8 Hz) noise spectra integrated over the TE region

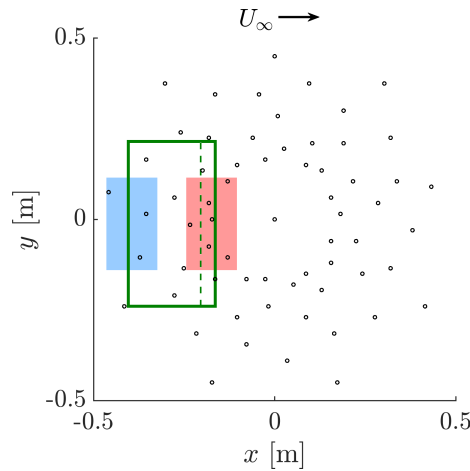


Figure 5.9: Schematic of the positions of array microphones (black circles), airfoil model (green rectangle) and the integration regions of leading edge (blue rectangle) and TE (red rectangle) for UAT Campaign 1b.

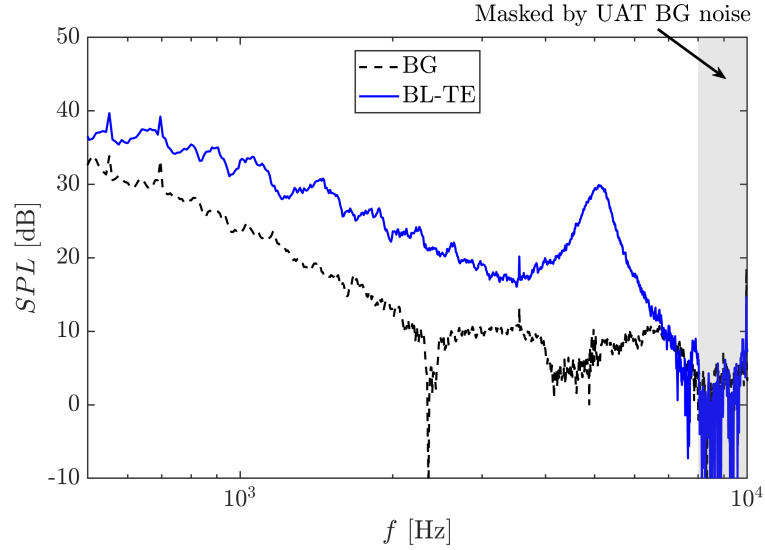


Figure 5.10: Noise spectra integrated over the TE region for airfoil with baseline extension (BL-TE) and background noise without airfoil model (BG) at freestream velocity of 36 m/s.

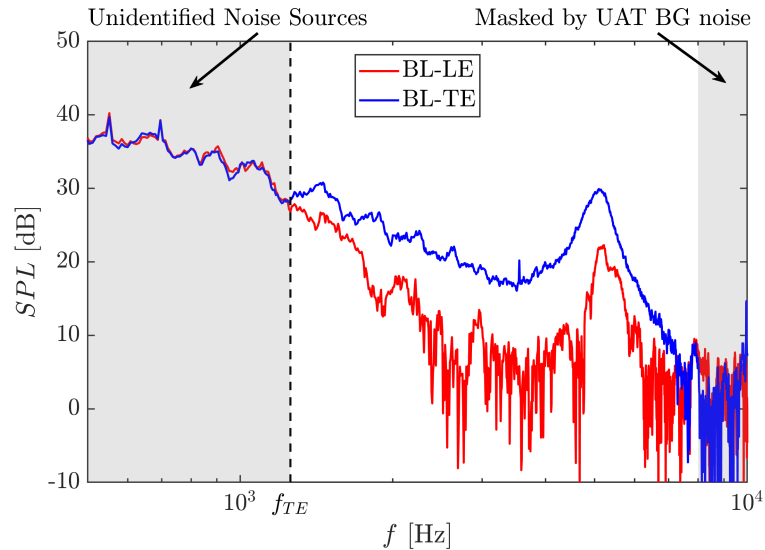


Figure 5.11: Noise spectra integrated over the leading-edge (BL-LE) and trailing-edge (BL-TE) regions for the airfoil model with baseline extension at freestream velocity of 36 m/s (f_{TE} - critical frequency for TE noise dominance).

(as shown in Figure 5.9) for the airfoil model with extension BL at freestream velocities from 20 to 50 m/s. The sound pressure levels are plotted as a colormap of frequency versus freestream velocity. No tonal noise is observed for the baseline case, and the fitted curve of discrete frequencies f_{TE} at various freestream velocities (from 20 to 50 m/s with an increment of 2 m/s) is presented as a grey dotted curve. The noise spectral data over frequencies above f_{TE} are of interest for TE noise comparison. Similar to the naturally-transition airfoil model tested in UAT Campaign 1a, high-frequency humps arising from

the TE bluntness vortex-shedding are also observed. The peaks of TE bluntness noise (marked as grey dots) occur at Strouhal numbers St_b (based on TE thickness b) of between 0.12 and 0.151, which are in accordance with the Strouhal number range reported in Ref. [186]. Figure 5.12b shows the BPM TBL-TE noise predictions based on the boundary layer displacement thickness estimated using XFOIL. Note that the predicted noise spectra have been adjusted to the narrow-band level with a bandwidth of 8 Hz. The measured TBL-TE noise levels are found to be comparable to the BPM predictions, and the discrepancies in peak frequency may be due to errors in the XFOIL estimation.

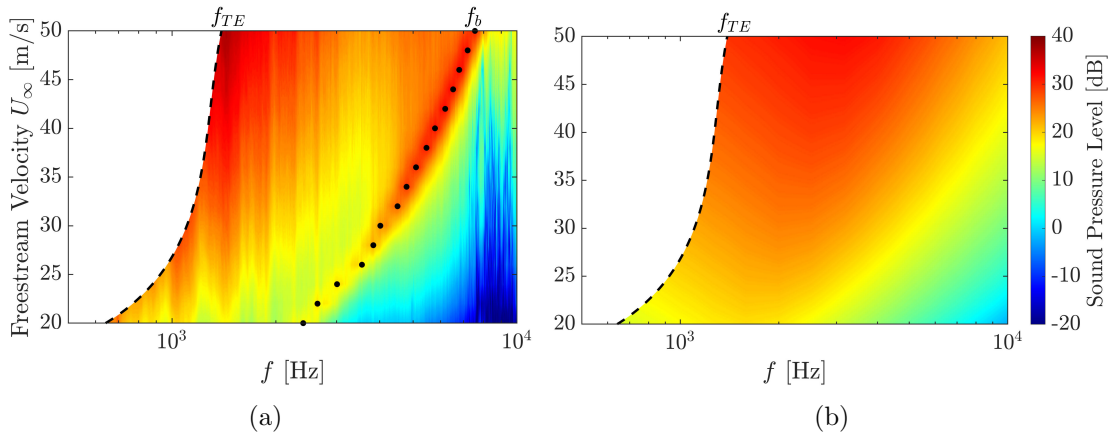


Figure 5.12: Colormaps of narrow-band noise spectra for (a) the forced-transitioned NACA 0012 airfoil with baseline flat-plate extension (f_{TE} - critical frequency for TE noise dominance; f_b - peak frequency of bluntness vortex-shedding noise) and (b) the BPM predictions of TBL-TE noise.

In Figure 5.13, the noise attenuation performance of extensions NS, CS, NSP, CSP and P at frequencies from 0.5–10 kHz and freestream velocities of between 20 and 50 m/s ($Re_c = 3.2\text{--}8 \times 10^5$), is presented. Noise attenuation levels ΔSPL (defined in Eq. 5.1) are plotted as colormaps of frequency versus freestream velocity. Based on the frequency characteristics of the noise spectra, the noise attenuation maps can be categorised into the following three frequency regions (as illustrated in Figure 5.13a):

- Frequency region for TBL-TE noise (R1'): $f > f_{TE} \cap St_b \leq 0.11$;
- Frequency region for TE bluntness vortex-shedding noise (R2'): $0.11 < St_b < 0.16$;
- High-frequency region (R3'): $St_b \geq 0.16 \cap f < 10 \text{ kHz}$.

The serrated extensions NS and CS are equally effective in reducing bluntness vortex-shedding noise that occurs over frequency region R2' (see Figures 5.13a and 5.13b). The

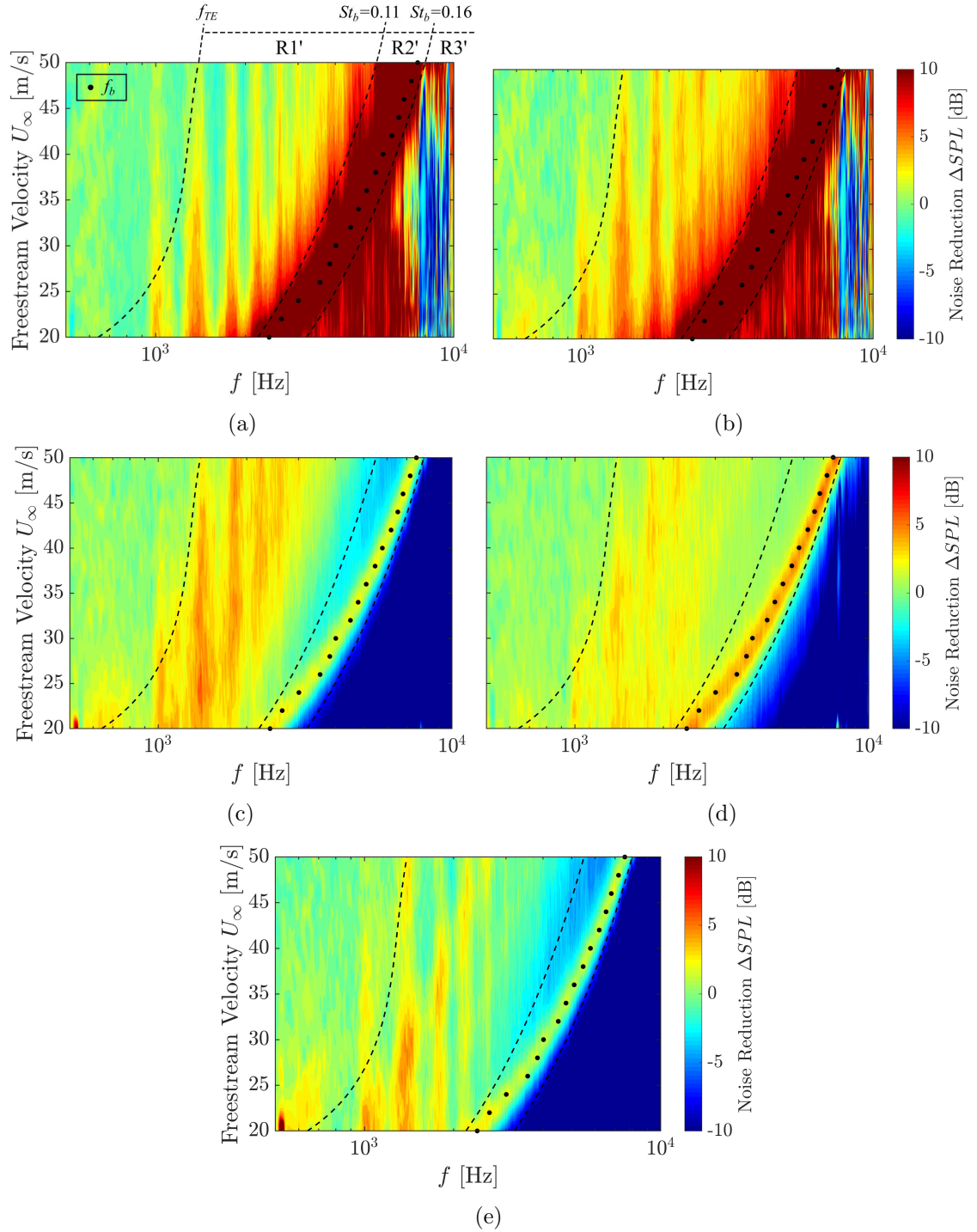


Figure 5.13: Colormaps of narrow-band noise attenuation ΔSPL for extensions (a) NS, (b) CS, (c) NSP, (d) CSP and (e) P (f_{TE} - critical frequency for TE noise dominance; St_b - Strouhal number based on TE thickness b ; f_b - peak frequency of bluntness vortex-shedding noise).

curved-serrated extension CS shows greater capability in the attenuation of broadband TBL-TE noise over frequency region $R1'$, compared to the classic saw-tooth-serrated extension NS with identical λ/h value. At frequencies above 8 kHz, the sound pressure levels emitted from the TE region of cases NS and CS are relatively low, and therefore, are masked by the background noise of the UAT. As a result, the noise attenuation maps for extensions NS and CS are incoherent above 8 kHz.

The extensions with porous structures P, NSP and CSP can also achieve noticeable reductions in TBL-TE noise, especially over lower frequencies in region $R1'$ (see Figures 5.13c–5.13e). The broadband reduction observed over $R1'$ is consistent with the analytical study [99] on a semi-infinite poroelastic edge, where numerical simulations indicate that the rigid, porous TE is efficient in reducing broadband noise at low frequency but inefficient at high frequency. However, extensions P, NSP and CSP are not as efficient as the serrated extensions in reducing bluntness vortex-shedding noise over region $R2'$. This is likely due to their straight blunt TE across the span (as shown in Figure 3.14b), giving rise to more correlated vortex-shedding structures behind the blunt TE. It was reported that porous TEs can significantly suppress bluntness vortex-shedding noise [2, 3]. The inconsistent observations may be due to the use of metal foams in Refs. [2, 3]. The irregular channels within metal foams may inhibit the generation of spanwise-coherent vortex shedding. In high frequency region $R3'$, a significant broadband noise increase is observed for all porous extensions P, NSP and CSP. This broadband noise increase compromises the noise attenuation over higher frequencies in region $R1'$ and frequency region $R2'$ to some extent. Similar to the observations in UAT Campaign 1a, the level of excessive high-frequency broadband noise produced by the porous extensions increases with an increase in porosity ϕ (see Table 5.2 for geometric parameters), further indicating that the high-frequency broadband noise is directly related to the porous geometries. It is worth noting that this high-frequency broadband noise (so-called ‘roughness’ noise) has also been reported in previous studies [68, 86, 165, 172] on porous TEs. Suppression of this high-frequency broadband noise is important for the application of porous structures in low-noise TE designs.

Figure 5.14 compares the overall noise attenuation $\Delta OASPL$ (defined in Eq. 5.2) over different frequency regions for forced-transitioned airfoil model with TE extensions P, NS,

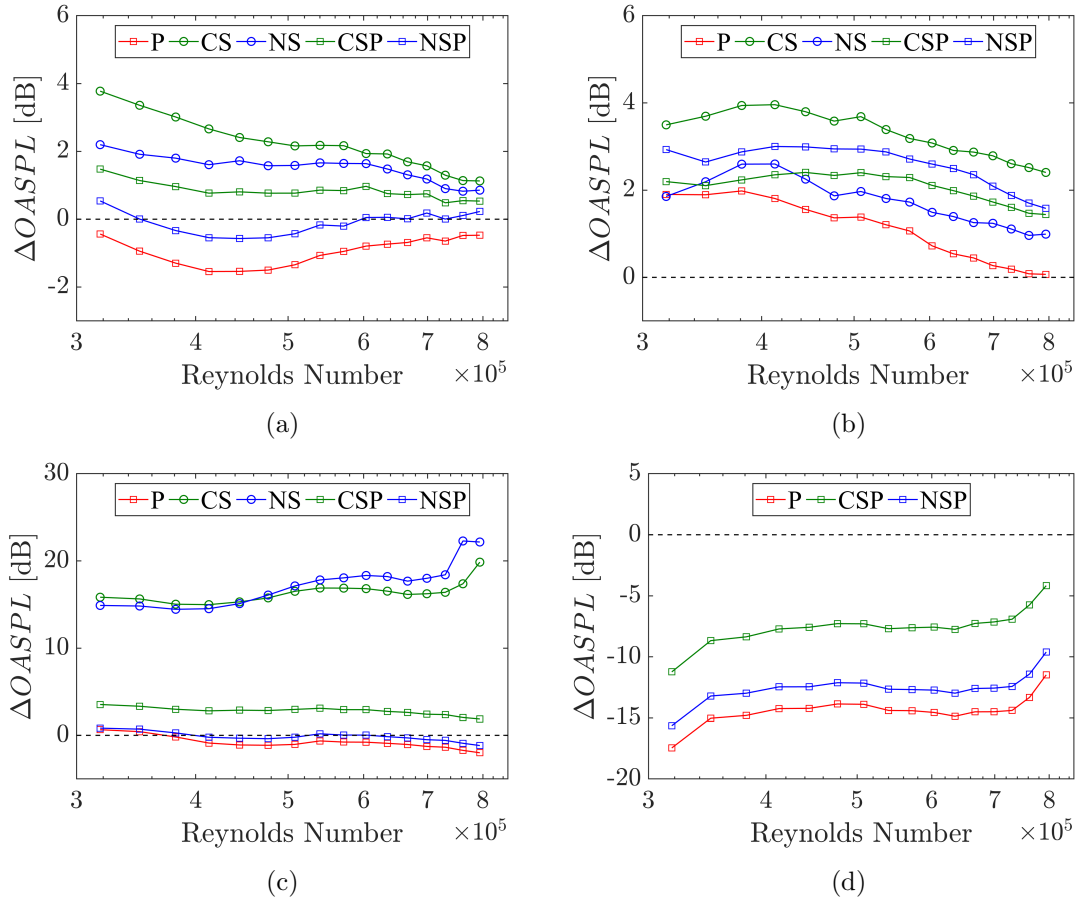


Figure 5.14: The noise attenuation in overall sound pressure level $\Delta OASPL$ (log scale on x axis) for extensions P, NS, CS, NSP and CSP at Reynolds numbers from 3.2×10^5 to 8×10^5 over (a) frequencies from 0.5 kHz to 10 kHz and frequency regions (b) R1' (TE turbulence noise), (c) R2' (TE bluntness noise) and (d) R3' (high-frequency broadband noise increase).

CS, NSP and CSP at Reynolds numbers from 3.2×10^5 to 8×10^5 . Over the frequency range of 0.5–10 kHz (Figure 5.14a), extensions CS, NS and CSP consistently achieve an overall noise reduction (of up to 3.8, 2.2 and 1.5 dB, respectively) over the entire Reynolds number range (3.2 – 8×10^5), and $\Delta OASPL$ decreases with an increase in Reynolds number. Extensions NSP and P fail to reduce the overall sound pressure level due to the excessive high-frequency broadband noise originating from their porous geometries of large porosity ϕ . For frequency region R1' (Figure 5.14b), all extensions reduce the TE broadband turbulence noise consistently over the entire Reynolds number range (3.2 – 8×10^5), among which extension CS achieves a maximum overall noise reduction of 4.0 dB. Similar to the results over the entire frequency range of interest (0.5–10 kHz), the overall noise reduction in R1' shows a trend of decreasing as the Reynolds number increases, especially over higher Reynolds numbers (5 – 8×10^5). This suggests that these TE extension designs are

less effective in TE noise reduction for high-Reynolds-number applications. For frequency region R2' (Figure 5.14c), the serrated extensions NS and CS both significantly reduce the TE bluntness noise, achieving a maximum overall noise reduction of 22.3 dB and 19.9 dB, respectively. The overall reduction in bluntness noise for NS and CS is maintained at a high level (> 14.5 dB) over the entire Reynolds number range ($3.2\text{--}8 \times 10^5$), increasing gradually as the Reynolds number increases. For the extensions with porous structure, CSP is the only one that can effectively reduce the overall bluntness noise (of up to 3.5 dB), while extensions P and NSP show a minor increase of overall noise level at Reynolds numbers above 4×10^5 . Contrary to the serrated extensions, the overall bluntness noise reduction of porous extensions P, NSP and CSP decreases gradually with increasing Reynolds number. For high-frequency region R3' (Figure 5.14d), the porous extensions P, NSP and CSP show a significant increase in overall noise level due to the excessive high-frequency broadband noise originating from their porous structures. A higher increase of *OASPL* over region R3' has been observed for porous extensions with a higher porosity.

5.4 Summary

This chapter has presented the acoustic results of UAT Campaign 1a and UAT Campaign 1b. The performance of eleven novel TE designs in reducing LBL-TE noise at low-to-moderate Reynolds numbers ($1.9\text{--}3.2 \times 10^5$) has been assessed in UAT Campaign 1a. Based on the results of UAT Campaign 1a, the five most promising TE designs have been tested in UAT Campaign 1b to evaluate their ability in TBL-TE noise attenuation at moderate Reynolds numbers ($3.2\text{--}8 \times 10^5$). To better illustrate the acoustic performance, the proposed TE designs have been categorised into two sets: 1) TE serrations and 2) TE designs with porous geometries. The features of their performance with respect to LBL-TE noise and TBL-TE noise production are summarised as follows:

- **Laminar-transitional boundary layer trailing-edge noise**

1. TE serrations: traditional straight-sawtooth narrow serrations (NS, $\lambda/h=0.6$) and wide serrations (WS, $\lambda/h=1.8$) are effective in attenuating broadband noise, bluntness vortex-shedding noise and instability tonal noise produced by T-S wave amplification at low Reynolds number, while introducing more high-level tonal noise

at moderate Reynolds number ($2.9\text{--}3.2\times 10^5$). The curved serrations (CS, $\lambda/h=0.6$) dampen instability noise and achieve significant attenuation in broadband noise and bluntness vortex-shedding noise over the low-to-moderate Reynolds number range ($1.9\text{--}3.2\times 10^5$) examined in this study. The slitted-serrations (SS, $\lambda/h=0.6$) performed similarly in attenuating broadband noise and bluntness vortex-shedding noise but introduced multiple tones with extremely high levels over the low-to-moderate Reynolds number range ($1.9\text{--}3.2\times 10^5$).

2. TE designs with porous geometries: all TE extensions with porous geometries are designed to maintain a straight TE along the spanwise direction and therefore provide poor reduction of bluntness vortex-shedding noise. The all-porous extension (P) fails to reduce the overall noise levels due to numerous excessive tones and significant broadband noise increase at higher frequencies. High-frequency broadband noise has been found to increase with an increase in porosity. However, broadband noise at frequency region R2 is observed to be reduced with porous geometries, which agrees with findings in an analytical study [99]. The acoustic performance of porous-serrated extensions NPS ($\lambda/h=0.6$) and WPS ($\lambda/h=1.8$) is dominated by their porous geometries, therefore showing similar results to those of all-porous extension P. On the contrary, serrated-porous designs of narrow-serrated-porous (NSP, $\lambda/h=0.6$), wide-serrated-porous (WSP, $\lambda/h=1.8$) and curved-serrated-porous (CSP, $\lambda/h=0.6$) are found to reduce the overall sound pressure levels consistently over low-to-moderate Reynolds numbers ($1.9\text{--}3.2\times 10^5$), in spite of the high-frequency noise increase produced by their porous geometries. Slitted-serrated-porous extension (SSP, $\lambda/h=0.6$) possessed the drawbacks of both slitted-serrated geometries and porous geometries, causing large noise increases over the low-to-moderate Reynolds number range ($1.9\text{--}3.2\times 10^5$).

- **Turbulent boundary layer trailing-edge noise**

1. TE serrations: traditional straight-sawtooth narrow serrations NS and curved serrations CS are both effective in reducing the TBL-TE noise and bluntness vortex-shedding noise over moderate Reynolds numbers ($3.2\text{--}8\times 10^5$). Both serrations can significantly reduce the TE bluntness noise by a comparable level. However, CS

shows a greater capability in TBL-TE noise reduction.

2. TE designs with porous geometries: all porous TE extensions P, NSP and CSP are efficient in reducing the TBL-TE noise over moderate Reynolds numbers (3.2×10^5), especially at lower frequencies dominated by TBL-TE noise ($R1'$). Similar to the case of laminar-transitional boundary layer noise, the porous extensions have poor capabilities in TE bluntness noise reduction. Only CSP can achieve an overall noise reduction over the frequency region dominated by bluntness noise ($R2'$), while P and NSP fail to reduce the overall noise level in $R2'$ at Reynolds numbers above 4×10^5 . A high-frequency broadband noise increase has also been observed for extensions with porous geometries, compromising their noise attenuation at high frequency ($R2'$ and $R3'$). Extensions with a higher porosity yield a higher level of high-frequency broadband noise, further demonstrating that the high-frequency noise increase originates from the porous geometries.

Finally, the overall noise attenuation performance $\Delta OASPL$ of the TE extensions, in terms of LBL-TE noise and TBL-TE noise, is summarised in Tables 5.3 and 5.4, respectively.

Table 5.3: Summary of the overall sound pressure level reduction $\Delta OASPL$ in LBL-TE noise for proposed novel TE treatments over low-to-moderate Reynolds numbers ($1.9\text{--}3.2 \times 10^5$).

TE treatments (Abbr.)	Description	$\Delta OASPL$ over 0.25–10 kHz (dB)
CSP	Curved-serrated-porous	2.0 ~ 7.4
NSP	Narrow-serrated-porous	0 ~ 14.2
WSP	Wide-serrated-porous	1.6 ~ 13.9
CS	Curved-serrated	0.4 ~ 16.4
NS	Narrow-serrated	-15.9 ~ 14.8
WS	Wide-serrated	-9.2 ~ 15.0
SS	Slitted-serrated	-23.9 ~ -9
P	Porous	-17.3 ~ -7.0
NPS	Narrow-porous-serrated	-20.3 ~ -4.8
WPS	Wide-porous-serrated	-19.1 ~ -6.5
SSP	Slitted-serrated-porous	-25.2 ~ -13.8

Table 5.4: Summary of the overall sound pressure level reduction $\Delta OASPL$ in TBL-TE noise for proposed novel TE treatments over moderate Reynolds numbers ($3.2\text{--}8 \times 10^5$).

TE treatments	$\Delta OASPL$ over 0.5–10 kHz (dB)	$\Delta OASPL$ over frequency region*		
		R1' (dB)	R2' (dB)	R3' (dB)
CS	1.1 ~ 3.8	2.4 ~ 4.0	15.0 ~ 19.9	-
NS	0.8 ~ 2.2	1.0 ~ 2.6	14.5 ~ 22.3	-
CSP	0.5 ~ 1.5	1.4 ~ 2.4	1.9 ~ 3.1	-7.7 ~ -4.2
NSP	-0.6 ~ 0.5	1.6 ~ 3	-1.2 ~ 3.1	-13.0 ~ -9.6
P	-1.5 ~ -0.4	0.1 ~ 1.8	-2.0 ~ -0.6	-14.9 ~ -11.5

* frequency regions R1', R2' and R3' are dominated by TBL-TE noise, TE bluntness noise and ex respectively.

Note: frequency region R3' is only applicable for TE treatments with porous structures.

Chapter 6

Flow Characteristics Around Porous and Serrated Trailing Edges

6.1 Overview

Having presented the trailing-edge (TE) noise reduction of novel porous and serrated TE treatments in Chapter 5, attention now turns to the flow characteristics around the porous and serrated TEs. This chapter aims to relate the flow characteristics of the different edges to their noise generation to aid understanding of the noise reduction mechanisms.

In this chapter, results and discussions of the flow measurements obtained in UAT Campaign 1a and UAT Campaign 1b are first presented in Secs. 6.2 and 6.3, respectively. Details of the test models and measurement setup for these two experimental campaigns have been described in Sec. 3.3.2. In UAT Campaign 1a, the mean and fluctuating velocity has been measured in the near wake of the 11 treated TE extensions attached to a naturally-transitioned NACA 0012 airfoil at a geometric angle of attack $\alpha_g = 4^\circ$ and freestream velocity $U_\infty = 18 \text{ m/s}$ ($Re_c = 2.9 \times 10^5$). Both the mean and fluctuating velocity are shown to be significantly altered by the treated TE extensions. The noise reduction by these extensions likely be attributed to their effects on the hydrodynamic field near TE, as the fluctuating velocity data have a strong correlation with the far-field acoustic data. The velocity fluctuations in the near wake of these extensions are related to their noise reduction or increase. In UAT Campaign 1b, the mean and fluctuating velocity have been measured in a near-wake plane of four treated TE extensions attached to a forced-transitioned NACA 0012 airfoil at a geometric angle of attack $\alpha_g = 4^\circ$ and freestream velocity $U_\infty = 36 \text{ m/s}$ ($Re_c = 5.8 \times 10^5$). The turbulence intensity and tur-

bulence integral length scale in the near-wake plane are characterised and related to the intensity of turbulent boundary layer trailing-edge (TBL-TE) noise.

Furthermore, Sec. 6.4 will present the results and discussions of LES simulations on a forced-transitioned NACA 0012 reference airfoil (LES Case 1) and a forced-transitioned NACA 0012 airfoil with a porous TE (LES Case 2) at an angle of attack $\alpha_g = 5^\circ$ and freestream velocity $U_\infty = 50$ m/s. FWH acoustic analogy predictions are shown to accurately capture the frequency characteristics of the noise spectra measured in experiments. Finally, mechanisms of the TBL-TE noise reduction and the high-frequency broadband noise increase of the porous TE are discussed in detail.

6.2 Flow Measurements in a Laminar-transitional Flow Regime

In this section, the flow measurement results for UAT Campaign 1a are presented and analysed. Mean and fluctuating velocities are measured using three single hot-wire probes at 1 mm upstream of the TE extensions ($x/c = -0.171$) and 1 mm downstream the TE of these extensions in the near wake ($x/c = 0.004$). First, the upstream ($x/c = -0.171$) boundary layer profiles on the suction surface are presented to verify the influence of novel TE extensions on the upstream boundary layer. Next, the near-wake ($x/c = 0.004$) profiles of novel TE extensions are presented to demonstrate their effects on the mean hydrodynamic field in the vicinity of their TEs. Assuming the near-wake velocity profiles represent the TE boundary layer, the boundary layer displacement thickness at the TE of baseline and novel extensions is then estimated using the mean velocity data measured in the near wake ($x/c = 0.004$). Finally, in order to relate the flow characteristics to TE noise generation, velocity fluctuations in the near wake ($x/c = 0.004$) of the TE extensions are analysed.

6.2.1 Mean Velocity Results

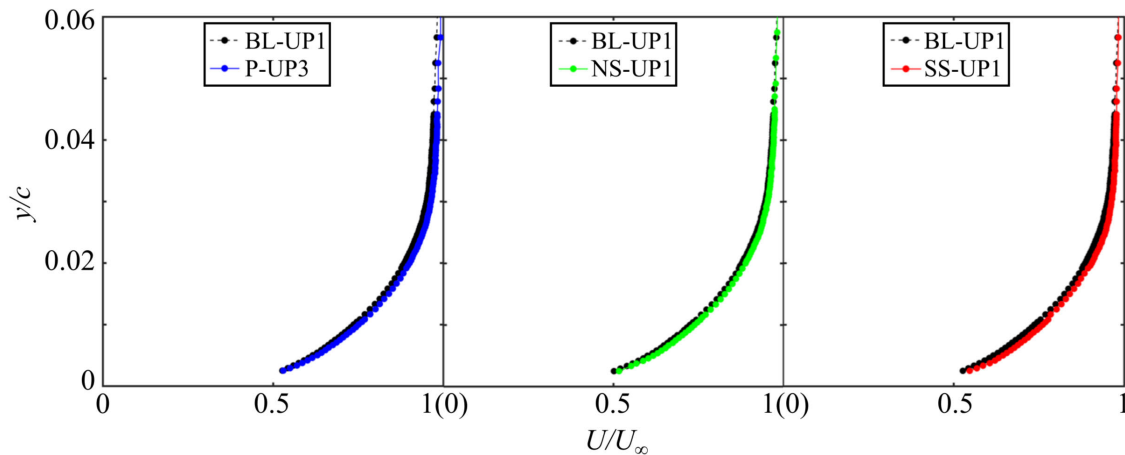


Figure 6.1: Mean velocity boundary-layer profiles measured at 1 mm upstream ($x/c = -0.171$) of baseline (BL-UP1), porous (P-UP3), narrow-serrated (NS-UP1) and slitted-serrated (SS-UP1) extensions. Note that UP1, UP2 and UP3 refer to the measurement positions as shown in Figure 3.14a.

Figure 6.1 compares the normalised mean velocity profiles measured at position UP1

of the baseline (BL), narrow-serrated (NS) and slitted-serrated (SS) TE extensions and position UP3 of porous (P) extension on the suction-side (probe is offset 0.6 mm above suction surface). The upstream mean velocity profiles for treated extensions show close agreement with that measured for the baseline extension, suggesting that the effects of TE treatments on the upstream boundary layer at this location are insignificant. This is also in agreement with previous experimental studies [12, 45, 112] on TE saw-tooth serrations.

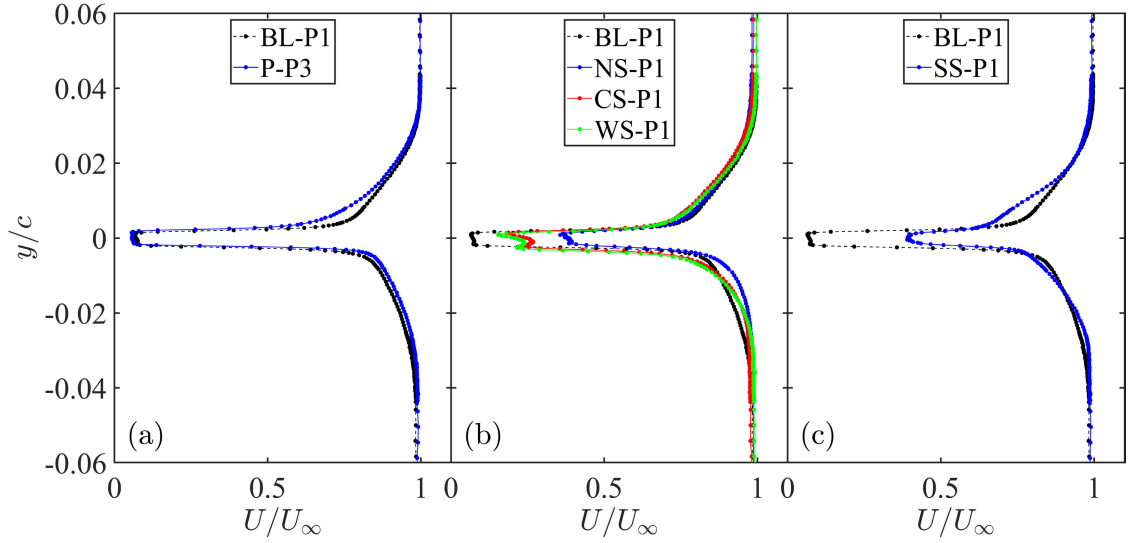


Figure 6.2: Near-wake (1mm downstream of TE, $x/c = 0.004$) mean velocity profile for baseline extension (BL-P1) compared with that for (a) porous extension (P-P3); (b) narrow-serrated (NS-P1), curved-serrated (CS-P1) and wide-serrated (WS-P1) extensions; (c) slitted-serrated extension (SS-P1). Note that P1, P2 and P3 refer to the measurement positions as shown in Figure 3.14a.

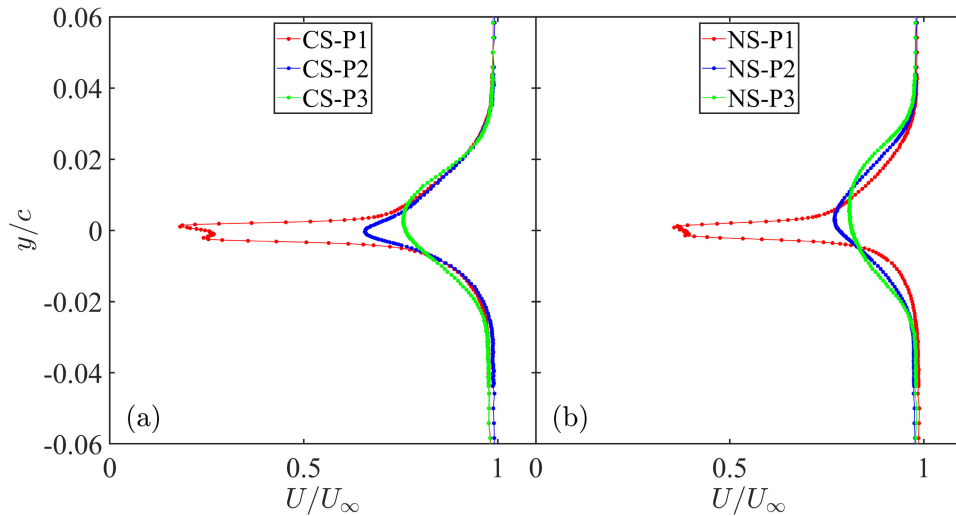


Figure 6.3: Wake ($x/c = 0.004$) mean velocity profile for (a) curved-serrated (CS) and narrow-serrated (NS) extensions at different spanwise positions P1, P2 and P3 as shown in Figure 3.14a.

Figure 6.2 compares the normalised mean velocity profiles measured at position P1 of baseline (BL), narrow-serrated (NS), curved-serrated (CS), wide-serrated (WS) and slitted-serrated (SS) extensions and position P3 of porous (P) extension. Note that the positive y axis corresponds to the suction-side of the extensions. Despite the fact that the geometries of extensions BL, NS, WS, CS and SS between positions UP1 and P1 are identical, their near-wake velocity profiles vary significantly. This indicates that the flow over the TE is altered by the spanwise-variant geometries of the treated extensions. For the serrated extensions NS, CS and WS, lower velocity deficits are observed in the vicinity of the TE ($-0.005 \leq y/c \leq 0.005$) and outer region of the pressure-side near wake ($y/c < -0.005$). The recovery of a velocity deficit may be induced by the edge geometries at adjacent spanwise locations. The near-wake profiles on the suction surface of extensions P and SS show a significantly higher velocity deficit in the outer region ($y/c > 0.005$). This may be caused by the flow perturbations travelling through permeable geometries from the pressure-side to suction-side. Figure 6.3 compares the wake profiles for serrated extensions CS and NS measured along serration tip (P1, $z/\lambda = 0$), midpoint (P2, $z/\lambda = 1/4$) and root (P3, $z/\lambda = 1/2$) at $x/c = 0.004$. For both extensions, the velocity deficit dip position gradually shifts to the suction-side as the spanwise measurement position changing from the serration tip to the root. Compared to CS, lower velocity deficits are observed at P2 and P3 of NS. This may be due to the presence of stronger jet flow through the serration gap [121] as the gap at the serration root of NS is wider than that of CS.

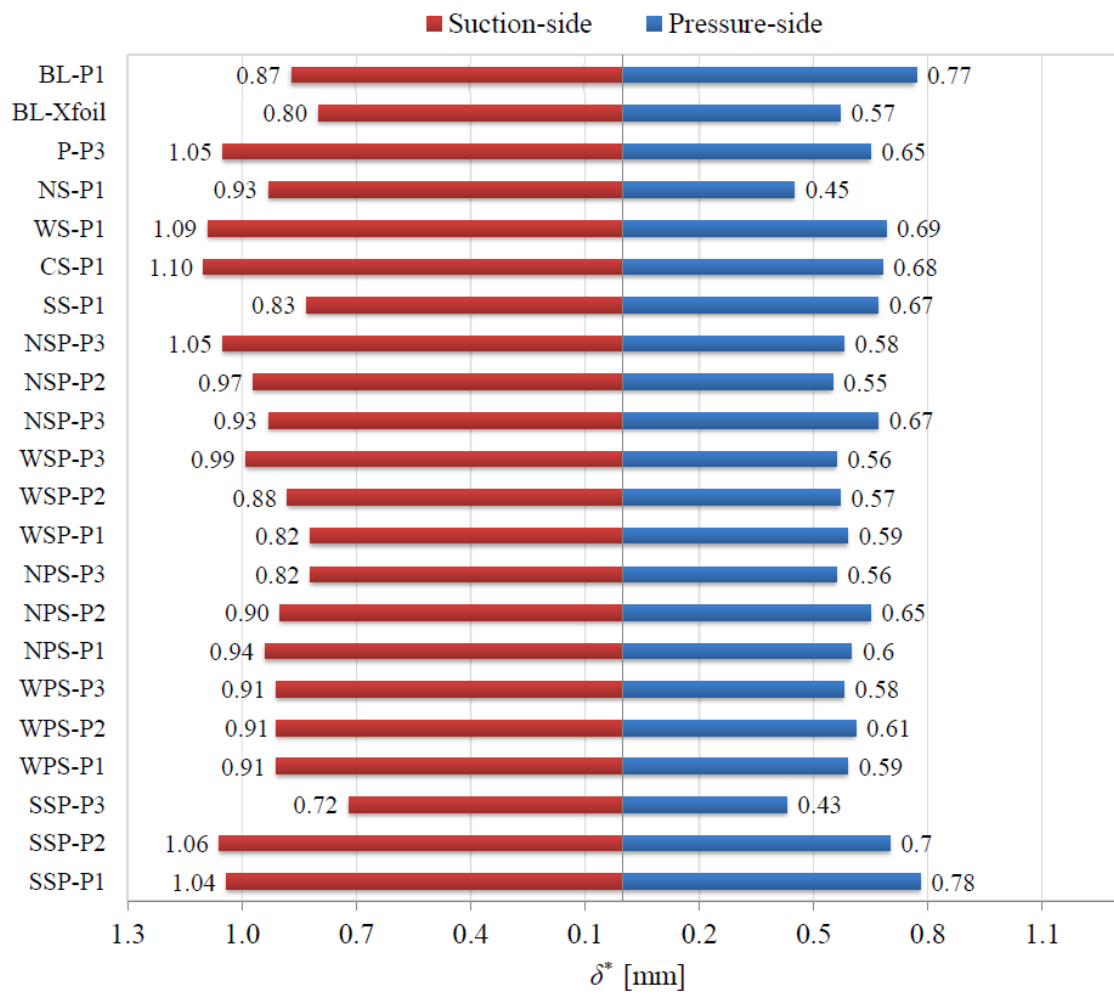


Figure 6.4: Trailing-edge boundary layer displacement thickness δ^* obtained from the near-wake measurements (at 1 mm downstream of TE, $x/c = 0.004$).

It is assumed that the near-wake velocity profile is a true representation of the boundary layer apart from a small inner region corresponding to the nascent shear layer. Figure 6.4 summarises the TE boundary layer displacement thickness δ^* of baseline and treated extensions, along with the XFOIL [59] estimations for the baseline case with natural boundary layer transition. As shown in Figure 3.14, the geometries upstream of measurement position P1 are solid, and they are identical for different TE extensions. If the effects of spanwise flow perturbations are assumed to be negligible, the boundary layer parameters measured at P1 should be very similar for different TE extensions. However, the displacement thickness measured at P1 for different cases deviates significantly (similar deviation has also been observed for position P3), further indicating that the presence of spanwise flow perturbations caused by different geometries can significantly affect the boundary layer parameters at the TE. Furthermore, XFOIL results show a good approximation to the experimental results for the baseline (BL). As the boundary layer parameters for the natural-transitioned cases are only measured at a freestream velocity of $U_\infty = 18 \text{ m/s}$ while acoustic data are measured at $U_\infty = 12 \text{ to } 20 \text{ m/s}$, the XFOIL predictions of displacement thickness are used in describing dimensionless quantities, such as Strouhal number, for the analysis of acoustic data at different freestream velocities in Sec.5.2.

6.2.2 Fluctuating Velocity Results

Figures 6.5–6.7 present spectral maps of fluctuating velocity (u'^2/Hz) measured in the vertical (y) direction in the near wake of baseline and treated TEs at $U_\infty = 18 \text{ m/s}$. Spectral maps are measured at 1 mm downstream ($x/c = 0.004$) of the TEs and presented with y axis in chord length normalised coordinates y/c ranging from -0.06 to 0.06. The center of the TE corresponds to $y/c = 0$, and the negative y axis corresponds to the near wake on the pressure-side of the TE.

Figure 6.5 shows fluctuating velocity spectral maps for extensions BL, NS, CS and SS at position P1 between 0.4 and 0.9 kHz (region R1), where LBL-TE noise is the dominant noise source. Baseline extension BL shows multiple high-energy peaks of velocity fluctuations at equally-spaced frequencies on the pressure-side (see Figure 6.5a). As the peaks are only shown in the near wake on the pressure-side, it is evident that the tonal noise measured in the far-field is likely due to the amplification of T-S waves over the pressure

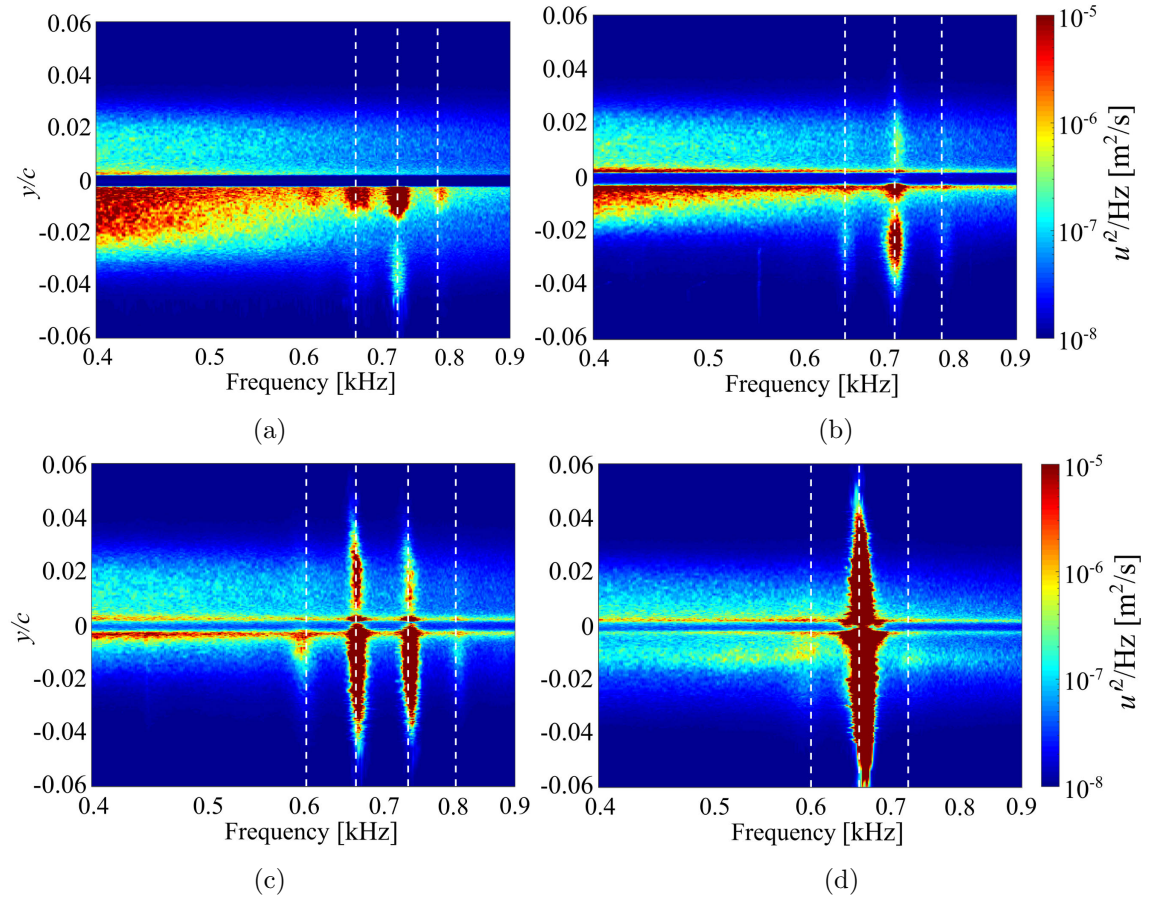


Figure 6.5: Velocity spectra maps (from 0.4 to 0.9 kHz, region R1) measured along vertical (y) direction in the near wake (at position P1, $x/c = 0.004$) of (a) baseline (BL), (b) curved-serrated (CS), (c) narrow-serrated (NS) and (d) slitted-serrated (SS) extensions (positive y axis corresponds to airfoil suction-side). Frequencies of the discrete tones of LBL-TE noise are marked by dashed white lines.

surface. Compared with the baseline case, extension CS shows lower fluctuating energy peaks, corresponding to a reduction in the levels of tonal noise measured in the far-field (Figure 5.5c). Extension NS is observed to enhance the equally-spaced fluctuating velocity peaks at slightly different frequencies, leading to the tonal noise increases observed in the acoustic measurement (Figure 5.5b). For extension SS, a significant peak in the fluctuating velocity is observed to occur at around 660 Hz in the near wake on the both pressure-side and suction-side, which explains why a large increase in tonal noise is observed at this frequency (Figure 5.5d).

Figure 6.6 presents fluctuating velocity spectral maps for extensions BL, NS, CS and SS at position P1 between 0.9 and 3 kHz (regions R2 and R3). Multiple equi-spaced energy peaks of velocity fluctuations are observed for extensions NS and SS, which correspond to the tonal noise increase observed in far-field noise measurements (Figures 5.5b and 5.5d).

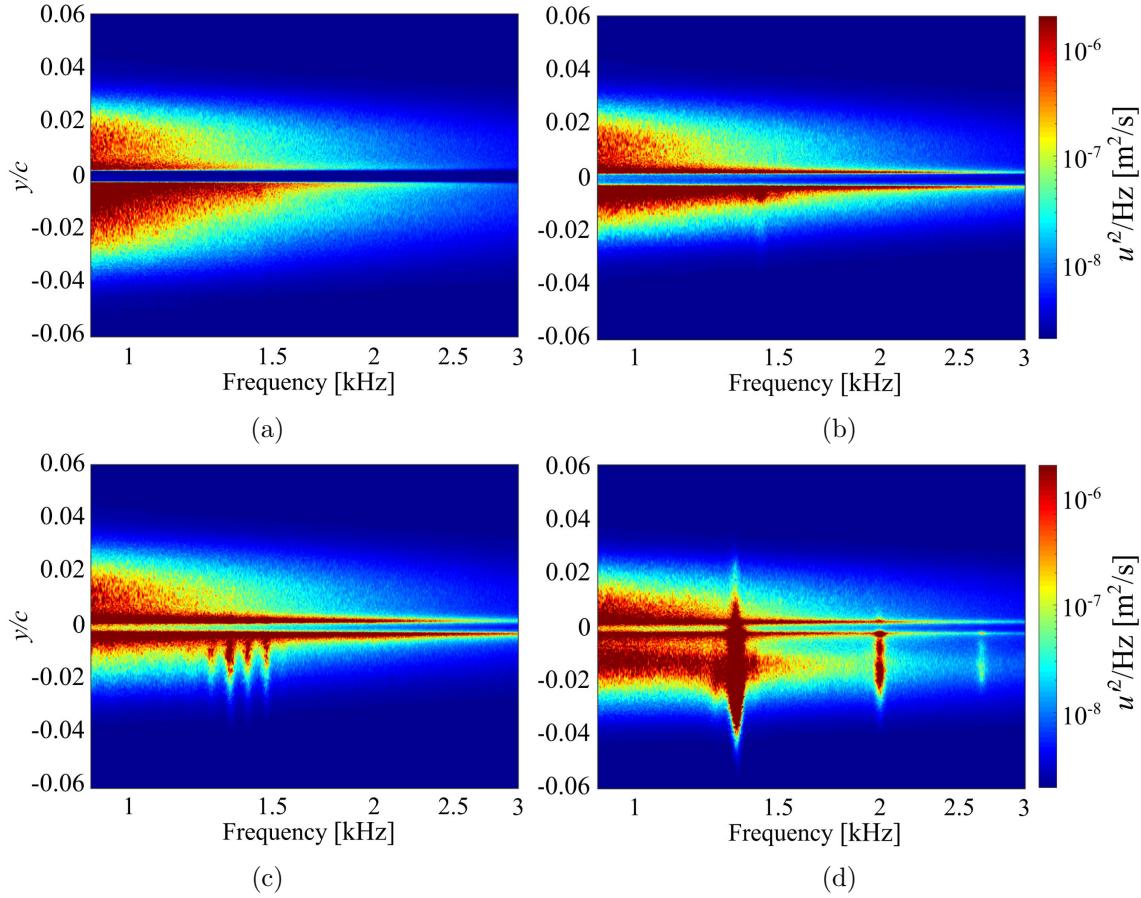


Figure 6.6: Velocity spectra maps (from 0.9 to 3 kHz, regions R2 and R3) measured along vertical (y) direction in the near wake (at position P1, $x/c = 0.004$) of (a) baseline (BL), (b) curved-serrated (CS), (c) narrow-serrated (NS) and (d) slitted-serrated (SS) extensions (positive y axis corresponds to airfoil suction-side).

However, no significant peaks are observed in the velocity spectral map for extension CS. In addition, the broadband energy levels of velocity fluctuations in the outer region ($y/c < -0.01$) of the pressure-side near wake of extension CS are significantly lower compared to extension BL. This agrees with the far-field acoustic measurement, which shows that curved serrations attenuate TE broadband noise and bluntness vortex-shedding noise without producing tonal noise over regions R2 and R3 (Figures 5.5c).

Figure 6.7 presents fluctuating velocity spectral maps for extensions BL and P between 3 kHz and 10 kHz (region R4). The energy of the velocity fluctuations is approximately identical in the near wake on the pressure-side but deviates on the suction-side. For extension P, higher levels of turbulent energy are measured in the near wake on suction-side, which may contribute to the broadband noise increase observed over high-frequency region R4. Note that the rise in the signal at high frequencies (8.5 to 10 kHz) is likely

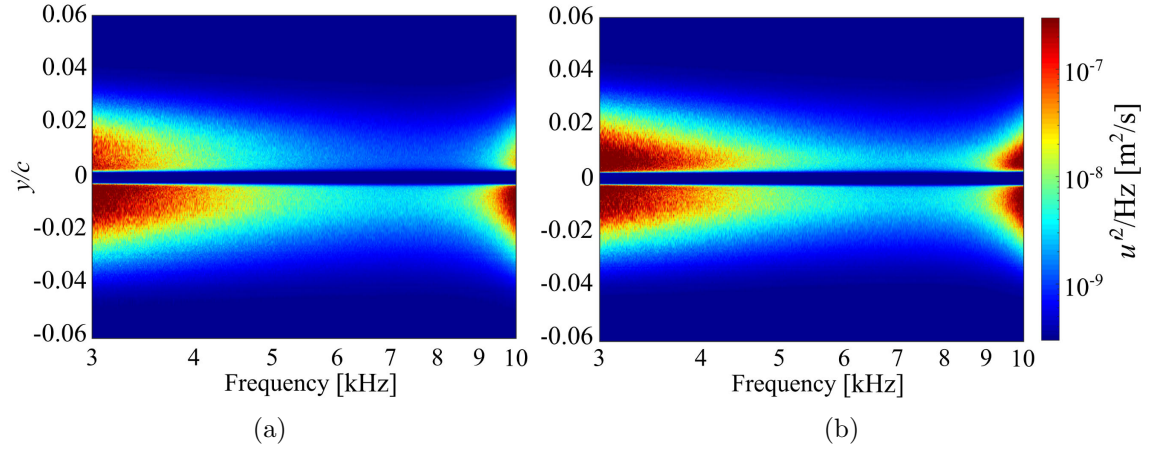


Figure 6.7: Velocity spectra maps (from 3 to 10 kHz, region R4) measured along vertical (y) direction in the near wake (1mm downstream) of (a) baseline (BL) extension at position P1 and (b) porous (P) extension at position P3 (positive y axis corresponds to airfoil suction-side).

due to the amplification effect of the electronic noise from constant-temperature hot-wire anemometry as reported in [66, 166].

Figure 6.8 shows the fluctuating velocity profiles for extensions BL, CS, NS, SS and P measured at $x/c = 0.004$ with the same y -axis range as spectral maps shown in Figures 6.5–6.7. Fluctuating velocity $\sqrt{u'^2}/U_\infty$ results are obtained by integrating the velocity power spectra over three frequency regions (as defined in Sec. 5.2) from: 1) 0.4 to 0.9 kHz (region R1, Figure 6.8a), 2) 0.9 to 3 kHz (regions R2 and R3, Figure 6.8b) and 3) 3 to 10 kHz (region R4, Figure 6.8c). For positions 1 mm downstream of TE (position P1 for BL, CS, NS and SS; position P3 for P), the velocity fluctuation on the pressure-side of serrated extensions NS and CS is consistently lower than that of baseline extension BL, which could contribute to the reduction in far-field noise levels of the LBL-TE broadband hump in R1 and its harmonics in R2. Slitted-serrated extension SS shows a significant increase in the turbulence levels on the suction-side over regions R1–R4 (Figures 6.8a–6.8c), and the velocity fluctuation slightly reduces on the pressure-side over regions R2–R4 (Figures 6.8b and 6.8c). In addition to the double-peak behaviour due to high velocity gradients in the near-wake inner region ($-0.05 < y/c < 0.05$), a third peak of the velocity fluctuation is observed on the suction-side at $y/c = 0.1$ – 0.2 over all frequency regions. This additional peak indicates the presence of intensive upward jet flow through the gap between slits. The turbulence levels for extension P are equivalent to those for extension BL on the pressure-side and consistently higher on the suction-side over regions R1–R4. The

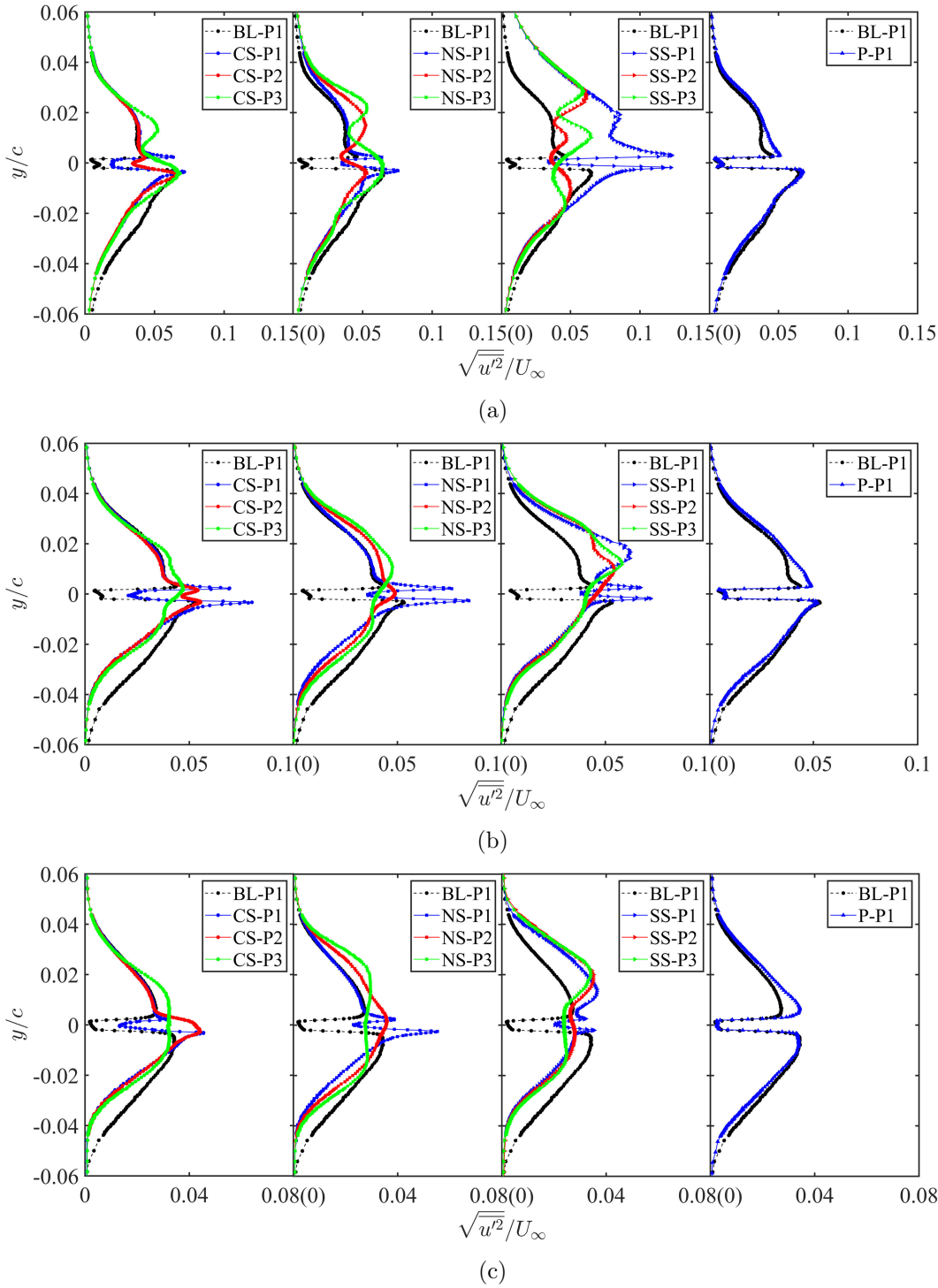


Figure 6.8: Fluctuating velocity $\sqrt{u'^2}/U_\infty$ integrated over (a) 0.4 to 0.9 kHz (region R1), (b) 0.9 to 3 kHz (R2 and R3), (c) 3 to 10 kHz (R4) measured along vertical (y) direction in the near wake ($x/c = 0.004$) of curved-serrated (CS-P1, -P2 and -P3), narrow-serrated (NS-P1, -P2 and -P3), slitted-serrated (SS-P1, -P2 and -P3) and all-porous (P-P3) extensions compared with that of baseline (BL-P1) extension (positive y axis corresponds to airfoil suction-side). Note that P1, P2 and P3 refer to the measurement positions as shown in Figure 3.14a.

increase in fluctuating velocity on the suction-side may result from additional turbulent eddies passing through the permeable porous geometries driven by the pressure difference between the pressure and suction surfaces. Although significant increases in broadband noise are observed over region R4 for extension P, the turbulence levels for extension P are not found to increase drastically, indicating that the velocity fluctuation in the near wake is not the only reason for the high-frequency broadband noise observed. For positions in the wake of serration midpoint (P2, $z/\lambda = 1/4$) and root (P3, $z/\lambda = 1/2$), the location of peak fluctuating velocity for both CS, NS and SS is shifted to suction-side. The shifted distance increases as the spanwise position changing from the serration tip to the root. Furthermore, the shifted distances for CS, NS and SS are found to be in ascending order, indicating the jet flow through the voids between serrated geometries of NS and SS is more intensive than that of CS. The significant changes in frequency and level of the LBL-TE tonal noise for NS and SS (as shown Figures 5.5 and 6.5) are likely attributed to the presence of stronger jet flow, altering the flow characteristics related to the T-S wave amplification and acoustic feedback loop.

6.3 Flow Measurements in a Turbulent Flow Regime

In this section, the flow measurement results for UAT Campaign 1b are presented and analysed. In the near-wake plane ($x/c = 0.008$), mean and fluctuating velocities in a rectangular region of 325 (13×25) points are measured to examine the contributions of spanwise-variant turbulent flow to TBL-TE noise production. The flow statistics related to TBL-TE noise generation are characterised for a baseline TE extension BL and four treated extensions P, NS, CS and CSP.

6.3.1 Mean Velocity Results

Figure 6.9 shows comparisons of the normalised mean velocity profiles measured at spanwise positions P1', P2' and P3' (as shown in Figure 3.15c) in the near-wake plane ($x/c = 0.008$) of baseline (BL), porous (P), narrow-serrated (NS), curved-serrated (CS) and curved-serrated-porous (CSP) extensions. Note that the positive y axis corresponds to the suction-side of the extensions, and positions P1', P2' and P3' correspond to the ser-

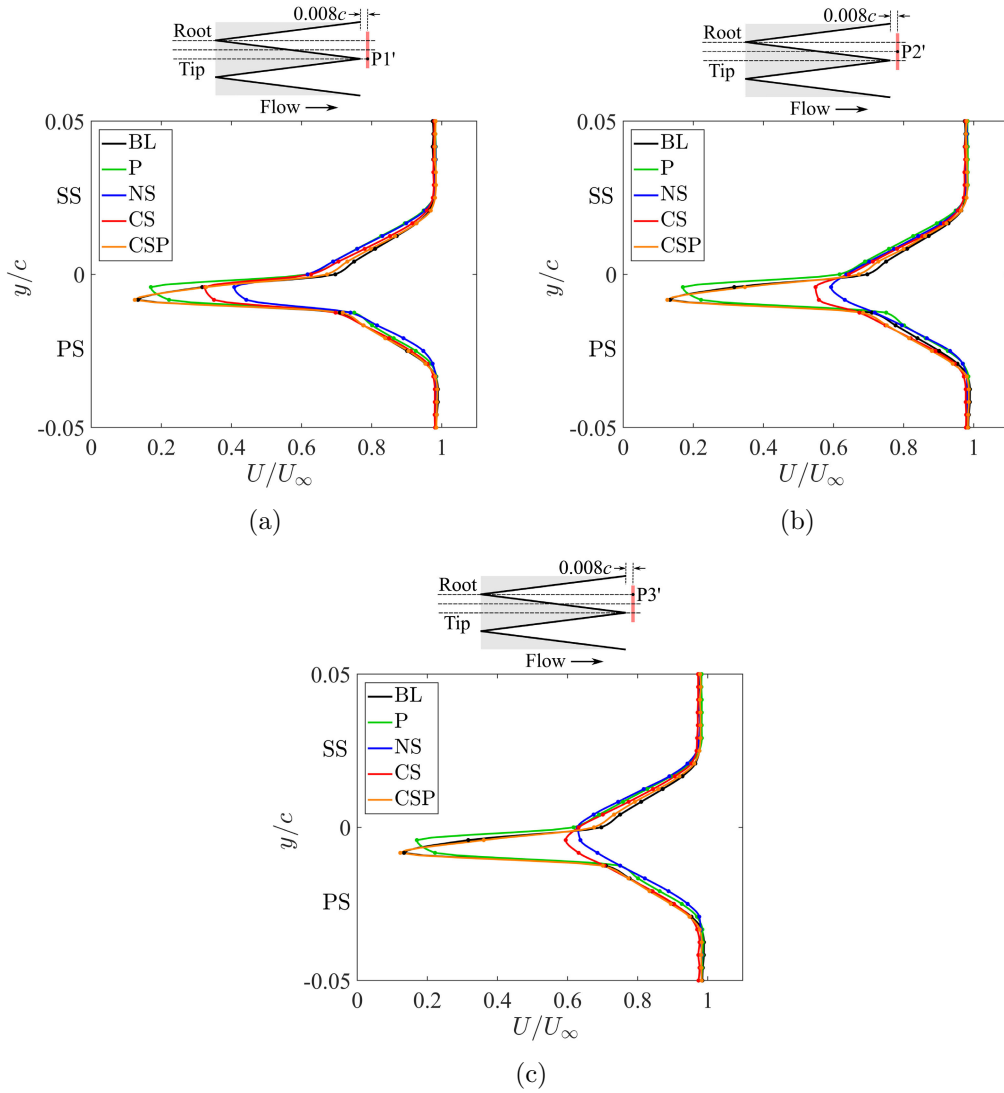


Figure 6.9: Normalised mean velocity U/U_∞ measured in the near wake ($x/c = 0.008$) at spanwise locations (a) $P1'$, (b) $P2'$ and (c) $P3'$. For extensions BL and P, only data measured at one position ($P1'$ for BL, $P3'$ for P) are presented as their geometries are uniformly distributed along the span.

ration tip ($z/\lambda = 0$), middle ($z/\lambda = 1/4$) and root ($z/\lambda = 1/2$) positions, respectively. Despite the fact that the geometries upstream of position $P1'$ are identical for most extensions (except extension P), the wake profiles of extensions NS and CS still show noticeable differences with extension BL. For extensions P, NS and CS, the velocity in the outer region ($y/c > 0$) of their wake profile on the suction surface is reduced. The flow deceleration is likely due to the turbulent flow passing through the pores for extension P, or through the void adjacent to the serration tip for extensions NS and CS. The velocity minimum in the near wake shifts towards suction-side for extensions P, NS and CS, further illustrating the presence of cross flow towards the suction surface. However, the mean

wake profiles of extension CSP at different spanwise locations are both similar to those of extension BL, and only a slightly higher velocity deficit is observed at positions P1', P2' and P3'. This indicates that the gradually varying (porosity increases towards downstream direction) porous geometry of CSP has a minor effect on the mean flow around TE. Moreover, extensions NS and CS show significantly lower velocity deficits in the inner region ($-0.015 < y/c < 0$) of their near wake, and the velocity deficits gradually decrease from the tip location (P1') towards the root location (P3'). This is because the distance from the model TE to the hot-wire probe increases as the probe moves from P1' to P3' and the flow past the TE has re-accelerated over a longer distance before reaching the hot-wire probe.

Figure 6.10 presents the contours of normalised mean velocity in the near-wake plane ($x/c = 0.008$) of extensions BL, P, NS, CS and CSP. The variation in mean velocity along the spanwise direction is unnoticeable for extensions BL, P and CSP. Similar to the wake profile results shown in Figure 6.9, the velocity in the near wake of CSP shows a comparable spatial distribution to that of BL. The near wake of extension P shows a larger region of low velocity ($U/U_\infty < 0.3$), which appears at a vertical (y) location closer to the suction surface. For serrated extensions, a more significant spanwise variation in velocity is observed in the near wake of extension NS, while extension CS shows a higher velocity deficit over a larger region in the vicinity of serration tip (P1').

6.3.2 Fluctuating Velocity Results

Figure 6.11 compares the turbulence intensity $\sqrt{u'^2}/U$ measured at spanwise positions P1', P2' and P3' in the near-wake plane ($x/c = 0.008$) of extensions BL, P, NS, CS and CSP. Due to the instrumentation noise observed above 8.5 kHz (as shown in Figure 6.7), the time-series velocity data have been low-pass filtered below 8.5 kHz for the analysis in this section. As shown in Figure 6.11, the highest turbulence intensity in the wake of extension P appears at a similar vertical (y) location to that of extension BL, while extension P increases the turbulence intensity in the suction-side wake but reduces it in the pressure-side wake. This further demonstrates the existence of turbulent flow permeation through the porous geometries of extension P from pressure to suction-side. In comparison, the turbulence intensity in the near wake of extension CSP is not significantly affected by

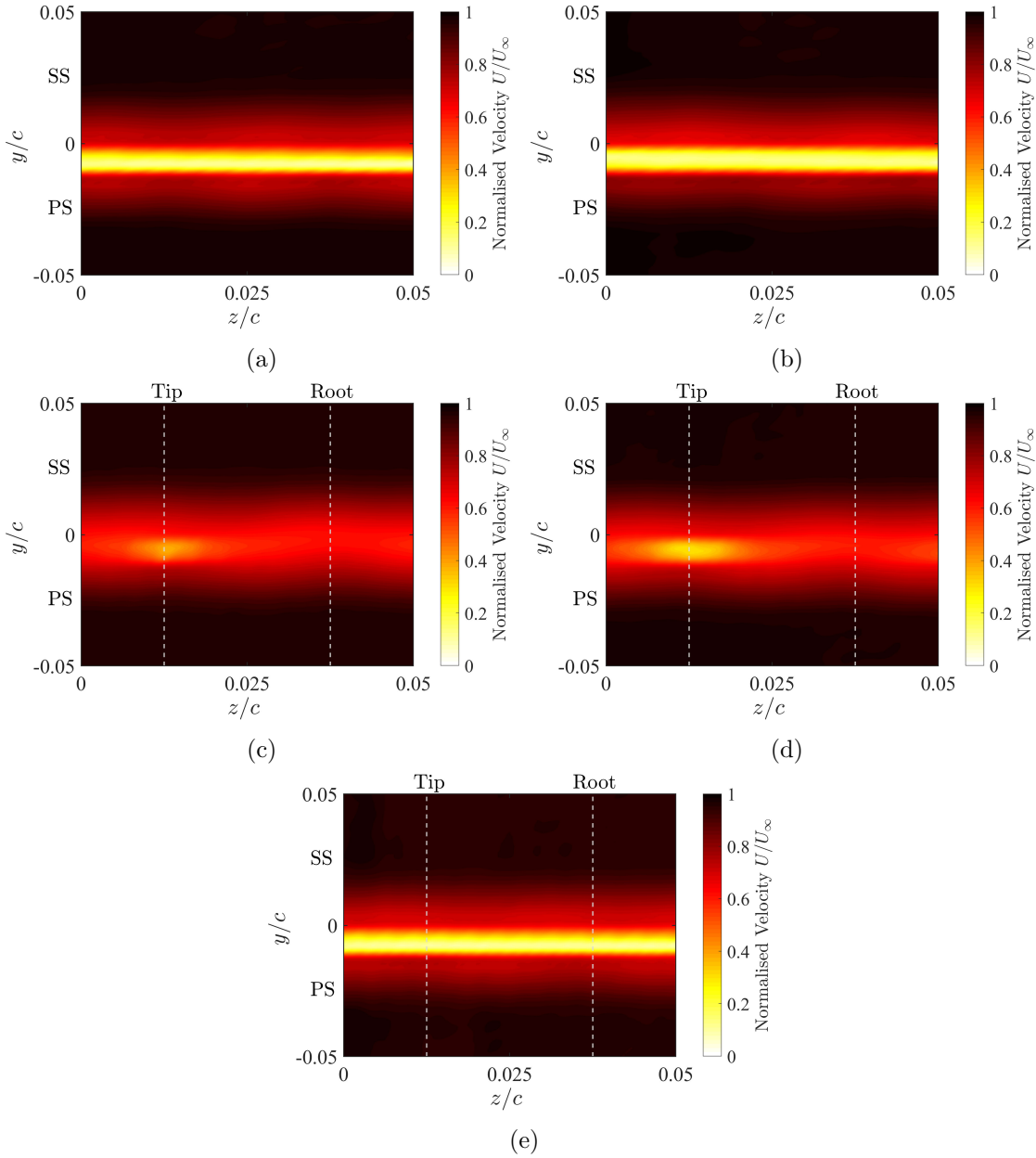


Figure 6.10: Contours of normalised mean velocity U/U_∞ measured in the near-wake plane ($x/c = 0.008$) for extensions (a) BL, (b) P, (c) NS, (d) CS and (e) CSP.

the gradually changed porous geometries, showing a comparable level and distribution to those of BL at spanwise locations P1', P2' and P3'. This may be because: 1) there is much less turbulent flow permeation due to the much lower porosity of CSP (see Table 5.2); 2) changes in turbulence intensity are too small to be captured by the coarse measurement points. For serrated extensions NS and CS, the turbulence intensity in the inner region of the wake ($-0.015 < y/c < 0$) is significantly increased at position P1' and reduced at positions P2' and P3'. Figure 6.12 presents the contours of turbulence intensity in the near-wake plane ($x/c = 0.008$). All extensions show a spatial distribution of turbulence

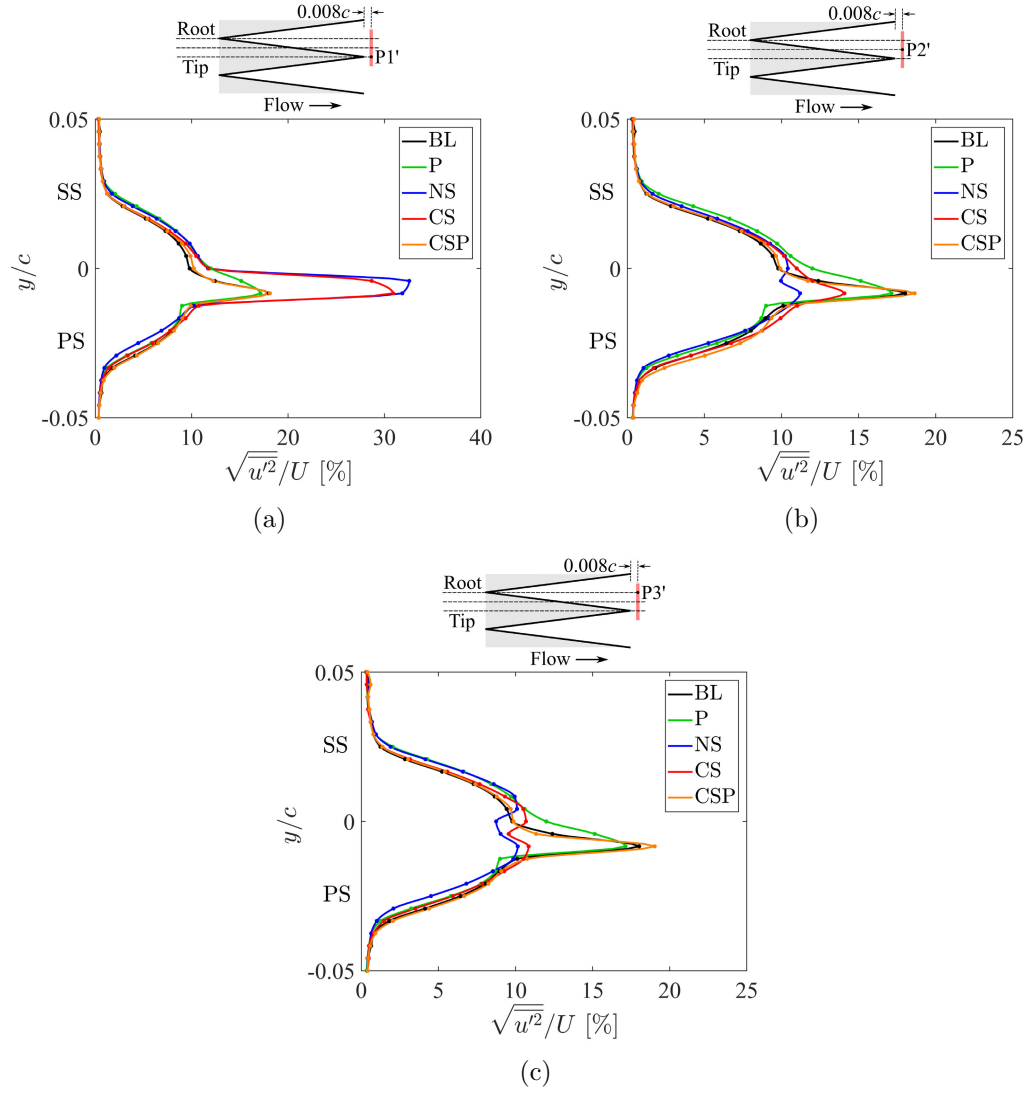


Figure 6.11: Turbulence intensity $\sqrt{u'^2}/U$ measured in the near wake ($x/c = 0.008$) at spanwise locations (a) P1', (b) P2' and (c) P3'. For extensions BL and P, only data measured at one position (P1' for BL, P3' for P) are presented as their geometries are uniformly distributed along the span.

intensity similar to that of normalised mean velocity (as shown in Figure 6.10), where the low velocity region corresponds to the high turbulence intensity region.

Turbulence integral length scale δ_{ILS} can be used as an indicator of the scales of turbulence in the near-wake plane ($x/c = 0.008$). Assuming frozen turbulence, δ_{ILS} can be calculated from the temporal correlation function R_{uu} of the streamwise velocity data:

$$R_{uu}(y, z, \tau) = E[u(y, z, t), u(y, z, t + \tau)], \quad (6.1)$$

where $u(y, z, t)$ stands for the instantaneous velocity measured by the hot-wire probe at

location (y, z) in the wake plane ($x/c = 0.008$) and E donotes the expectation operator.

The turbulence integral length scale δ_{ILS} can then be determined by [76]:

$$\delta_{ILS}(y, z) = U_c \tau_{1/2} , \quad (6.2)$$

where U_c is the convection velocity and $\tau_{1/2}$ is determined by:

$$\frac{R_{uu}(y, z, \tau_{1/2})}{R_{uu}(y, z, 0)} = 0.5 . \quad (6.3)$$

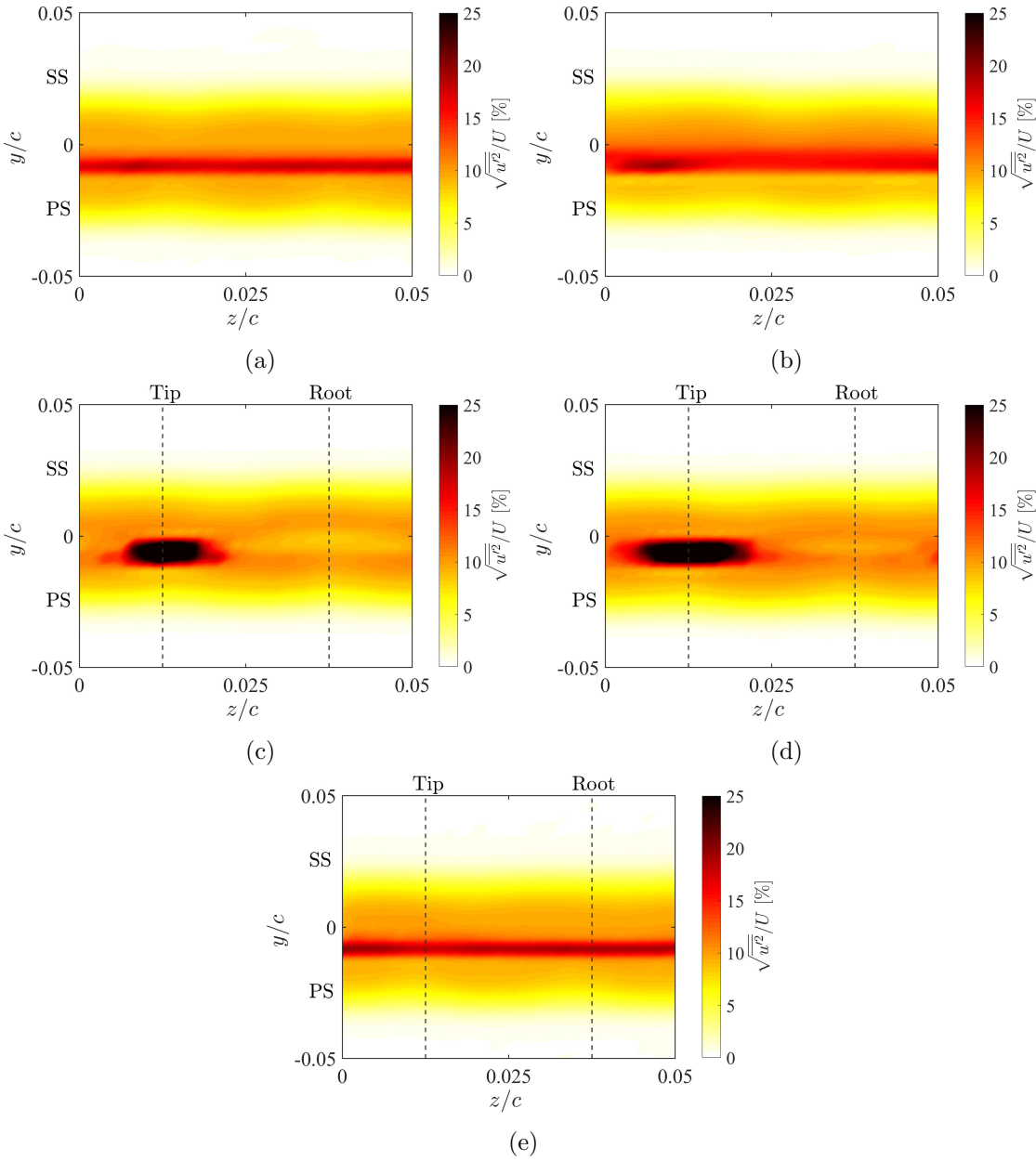


Figure 6.12: Turbulence intensity $\sqrt{u'^2}/U$ measured in the near-wake plane ($x/c = 0.008$) for extensions (a) BL, (b) P, (c) NS, (d) CS and (e) CSP.

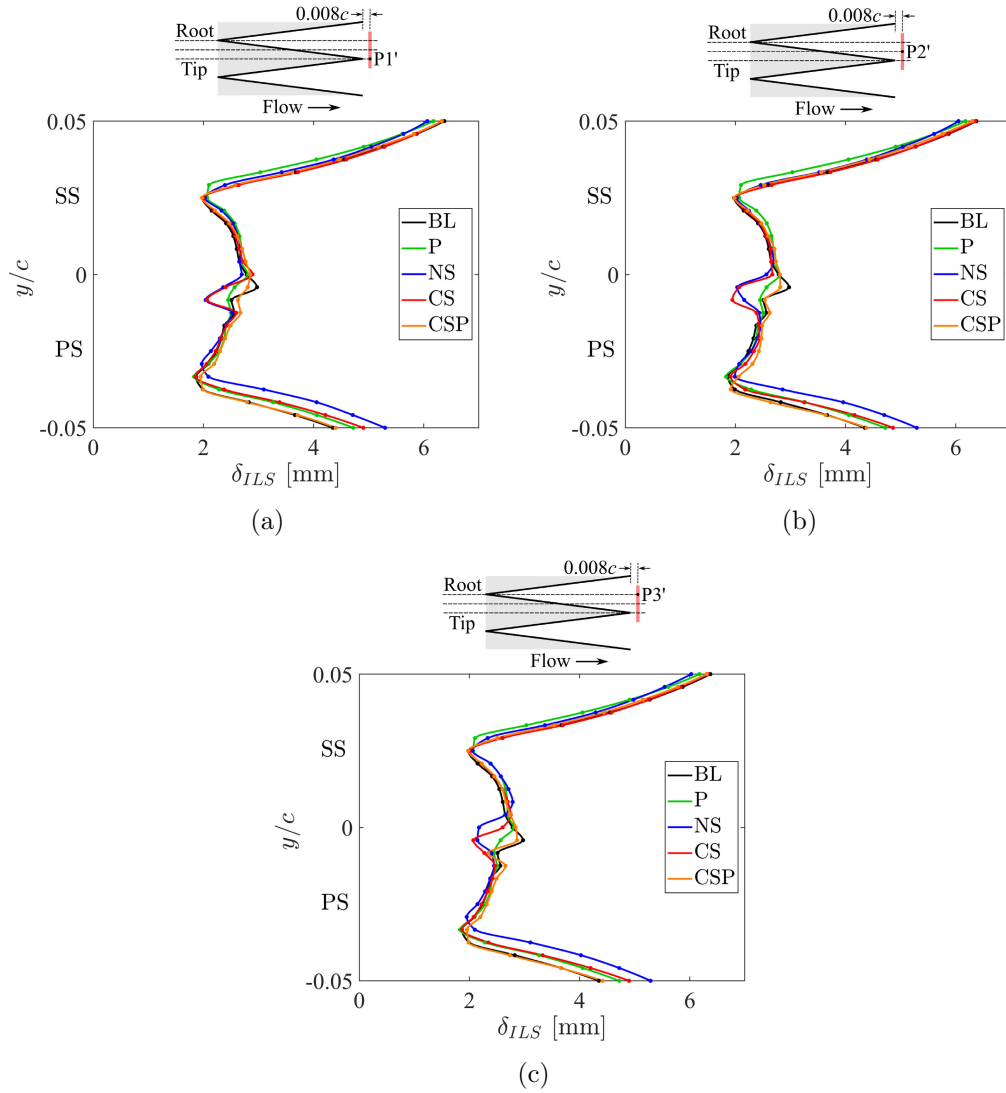


Figure 6.13: Turbulence integral length scale δ_{ILS} measured in the near wake ($x/c = 0.008$) at spanwise locations (a) P1', (b) P2' and (c) P3'. For extensions BL and P, only data measured at one position (P1' for BL, P3' for P) are presented as their geometries are uniformly distributed along the span.

In this study, the convection velocity of turbulent eddies is approximated by $U_c = 0.7U_\infty$ according to a previous study of a NACA 0012 airfoil with edge treatments [76, 79] and Howe's acoustic model of a serrated TE [92].

Figure 6.13 compares the turbulence integral length scale δ_{ILS} measured at spanwise positions P1', P2' and P3' in the near-wake plane ($x/c = 0.008$) of extensions BL, P, NS, CS and CSP. In the velocity deficit region of the near wake, where the flow develops from the upstream boundary layers, the scales of the turbulent eddies are significantly smaller than in the outer regions of the wake profiles. Compared to extension BL, a reduction of turbulence integral length scale of up to 32% in the vicinity of TE ($-0.015 <$

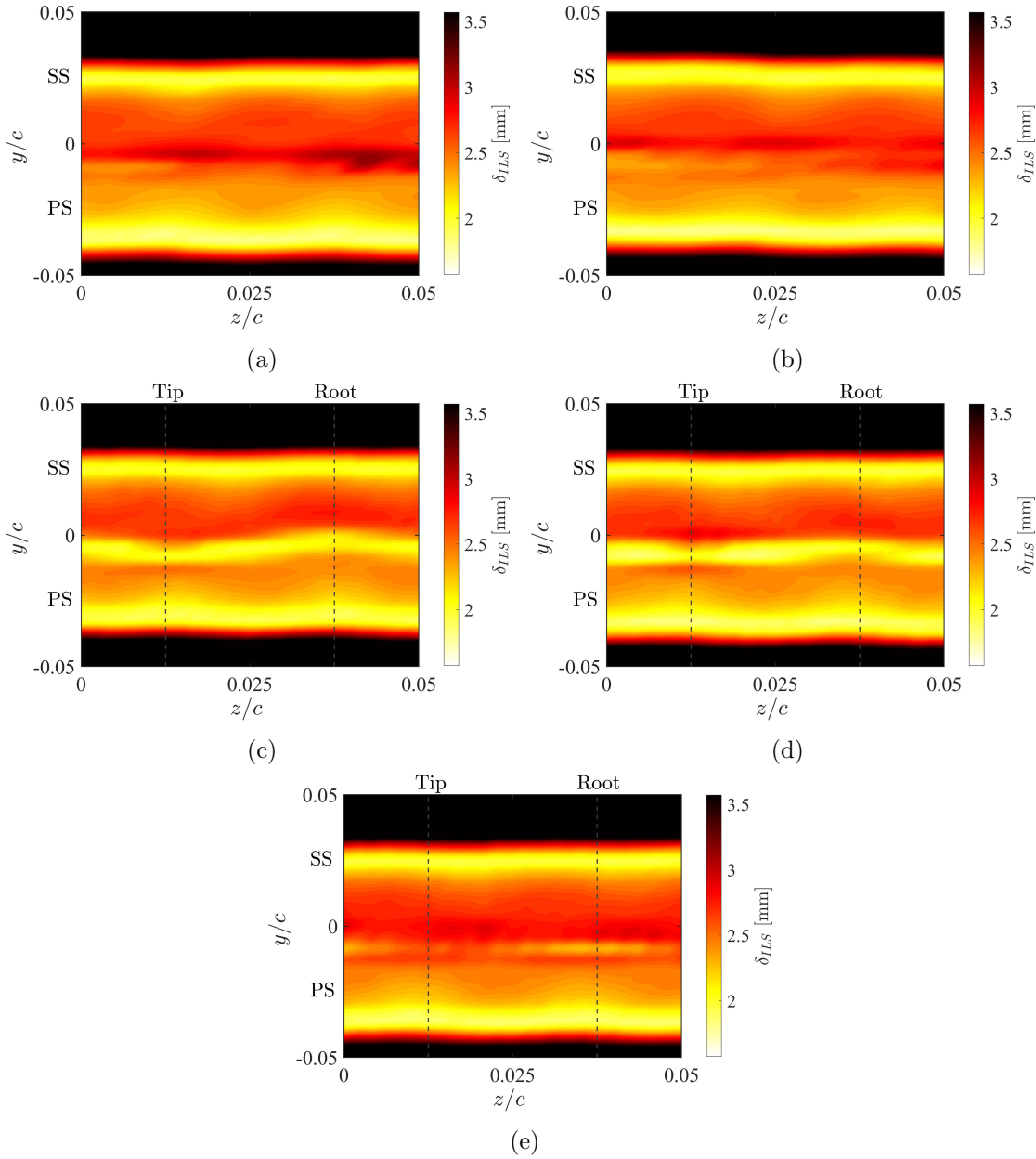


Figure 6.14: Contours of turbulence integral length scale δ_{ILS} measured in the near-wake plane ($x/c = 0.008$) for extensions (a) BL, (b) P, (c) NS, (d) CS and (e) CSP.

$y/c < 0$) is observed for all treated extensions at positions P1', P2' and P3'. Figure 6.14 presents contours of the turbulence integral length scale δ_{ILS} in the near-wake plane ($x/c = 0.008$). The turbulence length scales in the wake of extension P exhibit a similar spatial distribution to that of BL. However, the turbulence length scales are reduced by extensions NS, CS and CSP in the inner region ($-0.015 < y/c < 0$) of the near wake. Since the TE bluntness noise originates from vortex-shedding occurring behind the blunt edge geometry, a reduction of turbulence length scale near the edge of extensions NS, CS and CSP may contribute to their bluntness noise reduction (as shown in Figure 5.14c).

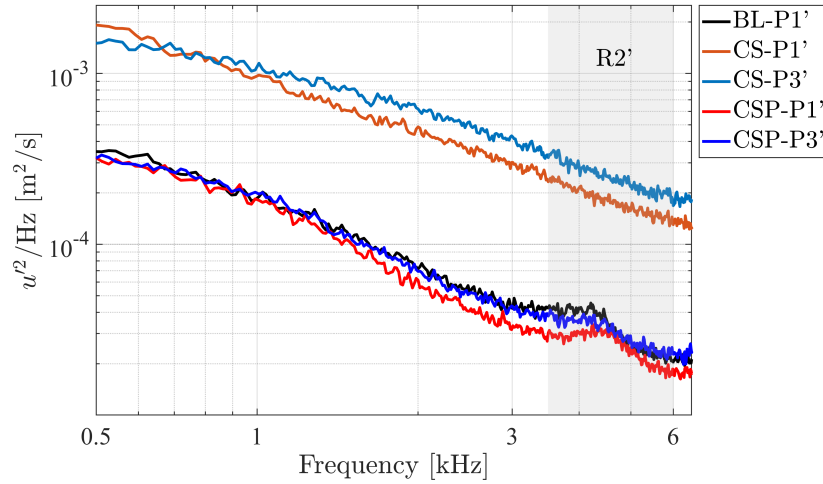


Figure 6.15: Velocity power spectra at the position of the highest velocity deficit. Frequency region R2' for bluffness vortex-shedding noise is marked in grey.

Figure 6.15 presents the velocity power spectra measured in the near-wake ($x/c = 0.008$) of BL, CS and CSP at the vertical location of the highest velocity deficit. For BL and CSP, a small hump is observed in the frequency region for bluffness vortex-shedding noise (R2'). The hump of CSP exhibits a slightly lower energy level compared to that of BL, which indicates that the bluffness noise reduction by CSP can also be attributed to the attenuation of vortex-shedding intensity. For CS, despite its significant bluffness noise reduction, it shows a much higher level of velocity fluctuation, and no energy increase is observed in R2'. The presence of bluffness vortex-shedding is not evidenced for serrated extensions.

6.3.3 TBL-TE noise Intensity Factor

In UAT Campaign 1b, flow measurements have been performed at a freestream velocity $U_\infty = 36 \text{ m/s}$ ($Re_c = 5.8 \times 10^6$). At this velocity, all treated extensions can effectively reduce the TBL-TE noise generated by the interaction between the airfoil TE and the turbulence past over it (see Figure 5.14b). This section aims to develop an approach to estimating the intensity of the TBL-TE noise source using the velocity data measured in the near-wake plane ($x/c = 0.008$). This approach is based on an analytical model proposed by Amiet [5] for the noise generated by the interaction of a turbulent stream and an airfoil. In this model, a simple expression for the far-field 1/3 octave-band sound pressure level $SPL_{1/3}$ is derived using the Von Karman model for the turbulence spectrum,

which is given as

$$SPL_{1/3} = 10 \log_{10} \left[\frac{L \delta_{ILS}}{2y^2} M_{\infty}^5 \frac{\overline{u'^2}}{U_{\infty}^2} \frac{\hat{K}_x^3}{(1 + \hat{K}_x^2)^{7/3}} \right] + 181.3, \quad (6.4)$$

where L is the airfoil span, y is the vertical location of the observer, M_{∞} is the freestream Mach number and \hat{K}_x is the dimensionless chordwise turbulence wavenumber. According to Eq. (6.4), the relationship between the velocity statistics and the far-field sound pressure level $SPL_{1/3}$ at a fixed location for an airfoil with a certain span is

$$SPL_{1/3} \propto \delta_{ILS} \cdot \left(\frac{\sqrt{\overline{u'^2}}}{U_{\infty}} \right)^2 \cdot M_{\infty}^5. \quad (6.5)$$

In a later study by Amiet [6], the model introduced above was extended to specifically apply to TBL-TE noise by taking the surface pressure spectrum upstream of the TE into account. As surface pressure data are not available in the current study, Eq. (6.5) is adopted to relate the velocity statistics to the intensity of the TBL-TE noise source. This is justified because: 1) TBL-TE noise and turbulence-interaction noise are both generated from the unsteady loading on the airfoil (TE or LE) due to the turbulent flow past over it; 2) the surface pressure spectrum at the airfoil TE is essentially produced by the turbulent flow past over the TE surface, and therefore its intensity can be related to the turbulence statistics in the near wake. In this study, a dimensionless noise intensity factor I_{TN} is proposed based on Eq. (6.5):

$$I_{TN} = \left(\frac{\delta_{ILS}}{c} \right) \left(\frac{\sqrt{\overline{u'^2}}}{U_{\infty}^2} \right) \left(\frac{U}{U_{\infty}} \right)^5, \quad (6.6)$$

where c is the airfoil chord. It is proposed that this noise intensity factor I_{TN} can provide some indication of the intensity of the TBL-TE noise source, although not to the absolute level, based on the properties of the near-wake flow.

Figure 6.16 presents contours of the noise intensity factor I_{TE} in the near-wake plane ($x/c = 0.008$). TBL-TE noise is found to be related only to the turbulence in the core region of the wake ($-0.035 < y/c < 0.025$), which develops from the upstream boundary layers at the TE. For extensions BL, P and CSP, contributions of the turbulence through the inner region of the wake core ($-0.015 < y/c < 0$) to noise generation are negligible,

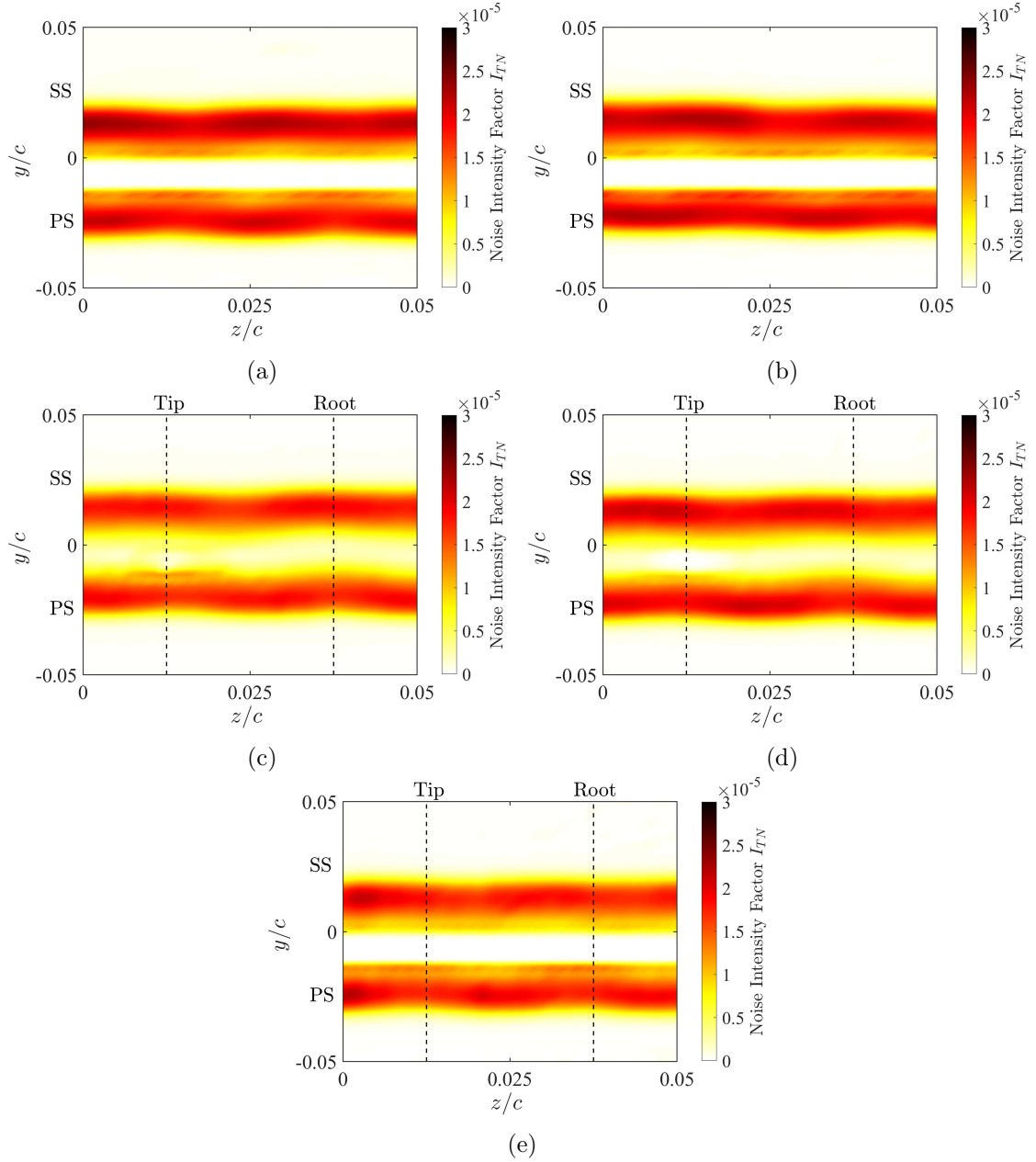


Figure 6.16: Contours of noise intensity factor I_{TN} measured in the near-wake plane ($x/c = 0.008$) for extensions (a) BL, (b) P, (c) NS, (d) CS and (e) CSP.

which is likely due to the high level of local velocity deficit. Extensions NS and CS show a higher noise intensity factor in the inner region of their wake core compared to that of other extensions. Both serrated extensions show a lower noise intensity factor in the vicinity of the serration tip. On the pressure-side of the serration tip, a high-noise-intensity region is observed at the location with the highest velocity deficit. This region is likely related to the vortex structures generated from the mixing layer at the serrated TE as reported in [12, 13].

To obtain the overall level of the individual terms in Eq. (6.6) over the measurement

plane in the near wake ($x/c = 0.008$), each term is integrated over measurement points where the turbulence intensity is larger than 1% and normalised by the number of integrated measurement points. This is because the regions with turbulence intensity less than 1% are in a freestream flow regime, therefore, their contribution to TBL-TE noise generation is negligible. Table 6.1 summarises these integrated parameters. Although some terms on the right-hand side of Eq. (6.6) are increased by extensions NS, CS and CSP, the integrated noise intensity factor I_{TN} of all treated extensions is still lower than that of extension BL, which is consistent with the acoustic results as shown in Figure 5.14b. When surface pressure fluctuation measurements are unavailable, the noise intensity factor I_{TN} provides an alternative approach to relate the near-wake flow characteristics to the intensity of TBL-TE noise.

Table 6.1: Summary of the parameters that relate the near-wake flow characteristics to the TBL-TE noise generation.

Test Model	BL	P	NS	CS	CSP
Integrated $\sqrt{u'^2}/U_\infty$	0.0515	0.0506	0.0563	0.0572	0.0503
Integrated δ_{ILS}/c	0.0102	0.0101	0.0098	0.0097	0.0103
Integrated U/U_∞	0.7651	0.7635	0.7941	0.7960	0.7506
Integrated $I_{TN} [\times 10^{-4}]$	0.1075	0.1065	0.0946	0.1002	0.0951

Note: values lower than baseline extension BL are marked in green; higher are in red.

6.4 Numerical Simulation of an Airfoil with Porous Trailing Edge

In this section, the results of Large Eddy Simulations (LES) and acoustic prediction using the FWH acoustic analogy for a forced-transitioned NACA 0012 reference airfoil (LES Case 1) and a forced-transitioned NACA 0012 airfoil with a porous TE (LES Case 2) are presented. The airfoil models in LES Case 1 and Case 2 have an identical profile and chord length. The porous TE geometries of LES Case 2 are identical to those of rotor blades P (see Figures 3.22, 3.23 and Table 3.6 for the details of porous geometries). In the LES simulations, both airfoil models are set at a freestream velocity of 50 m/s and angle of attack of 5° . The numerical method has been detailed in Sec. 3.5.

This section is structured as follows: first, the far-field acoustic results predicted using FWH acoustic analogy are verified by the comparison with experimental data, and used to analyse the noise directivity for reference and porous airfoils. Then, the Reynolds normal-stress and shear-stress are analysed in different frequency regions and related to the acoustic source intensity. Finally, the mechanisms for the noise reduction and increase by porous TE are investigated through a detailed analysis on the fluctuations of vertical velocity and wall surface pressure.

6.4.1 FWH Acoustic Analogy Results

The far-field acoustic results obtained from the FWH acoustic analogy are compared with the single-microphone measurement data of the forced-transitioned reference airfoil (Ref) and porous airfoil (Porous) in the UAT. The airfoil models for the wind tunnel measurements have the identical profile, chord length and TE geometries to those in LES Case 1 and Case 2 but a larger span of 455 mm. Forced boundary layer transition is achieved by installing a 0.4 mm zig-zag turbulator at 10% chord on both sides of the airfoil models. To maintain consistency with the simulations, wind tunnel measurements are performed at a freestream velocity of 50 m/s and a corrected angle of attack $\alpha_c = 5^\circ$, which corresponds to a geometric angle of attack $\alpha_g = 6.3^\circ$ due to the open-jet effects. The geometric angle of attack α_g is determined by the airfoil chord and geometries of the wind tunnel test section according to the open-jet correction method described in [31]:

$$\begin{aligned}\alpha_g &= \alpha_c \zeta, \\ \zeta &= (1 + 2\sigma)^2 + \sqrt{12\sigma}, \\ \sigma &= (\pi^2/48)(c/D_H)^2,\end{aligned}\tag{6.7}$$

where c is the airfoil chord and D_H is the vertical dimension of the test section. The microphone is positioned 1.05 m ($15c$) away from the airfoil TE in the vertical (y) direction. To account for the difference in airfoil span in experimental measurements and numerical simulations, the FWH acoustic results obtained from the simulated span L_s are corrected to the measured span L_m according to the method described in [19, 176]. The corrected sound pressure level SPL_a is calculated by:

$$SPL_a = SPL_s + SPL_c, \quad (6.8)$$

where SPL_s is the far-field sound pressure predicted by the FWH acoustic analogy using LES simulation data, and SPL_c is the span correction value which can be determined by

$$SPL_c = \begin{cases} 10 \log(N) & (L'_c/L_s \leq 1/\sqrt{\pi}) \\ 10 \log(\sqrt{\pi}N) + 10 \log(L'_c/L_s) & (1/\sqrt{\pi} < L'_c/L_s < N/\sqrt{\pi}) \\ 20 \log(N) & (L'_c/L_s \geq N/\sqrt{\pi}), \end{cases} \quad (6.9)$$

where $N = L_m/L_s$, and L'_c is the acoustic spanwise coherence length. In this study, L'_c is estimated from the spanwise coherence function of surface pressure γ at the airfoil TE. Assuming Gaussian distribution [19] of the spanwise coherence function γ , the acoustic spanwise coherence length L'_c can be obtained by data fitting from:

$$\gamma(\Delta z) = \exp\left(-\frac{\Delta z^2}{L_c'^2}\right), \quad (6.10)$$

where Δz is the distance between two separate points along the spanwise (z) direction at the airfoil TE. For both LES Case 1 and Case 2, the acoustic spanwise coherence length L'_c is smaller than $L_s/\sqrt{\pi}$ over the entire frequency range of interest (1–15 kHz). Therefore, the corrected sound pressure level SPL_a is calculated by: $SPL_a = SPL_s + 10 \log(L_m/L_s)$.

Figure 6.17a compares the 1/3 octave-band noise spectra of microphone measurement data and the FWH acoustic analogy results. Numerical predictions for both airfoils are in reasonably good agreement with experimental data, showing a prediction error of less than 5 dB over 2 to 8 kHz. The discrepancy below 2 kHz is likely due to the leading-edge junction noise and the masking effects of the wind tunnel background noise. At frequencies over 8 kHz, FWH predictions show significantly lower noise levels compared to the experimental data. This is likely due to the background noise (poor signal-to-noise ratio) at high frequencies in experiments and the limitation of the LES simulation. In LES simulations, the eddies smaller than the computational grid are simulated by the subgrid-scale (SGS) turbulence model. Since the SGS model is not capable of fully capturing the energy above the LES cut-off frequency, the acoustic energy associated with turbulent eddies smaller than the computational grid is not properly resolved in the FWH prediction results. Figure 6.17b presents the experimental and numerical results

of the noise reduction performance ΔSPL (as defined in Eq. 5.1) of the porous airfoil. FWH predictions of ΔSPL show an excellent agreement with the experimental data in terms of the spectral shape, accurately capturing the frequency regions of noise reduction and increase. However, wind tunnel measurement data show approximately 2–3 dB lower noise reductions over 2 to 5 kHz, which may be due to the masking effects of the UAT background noise.

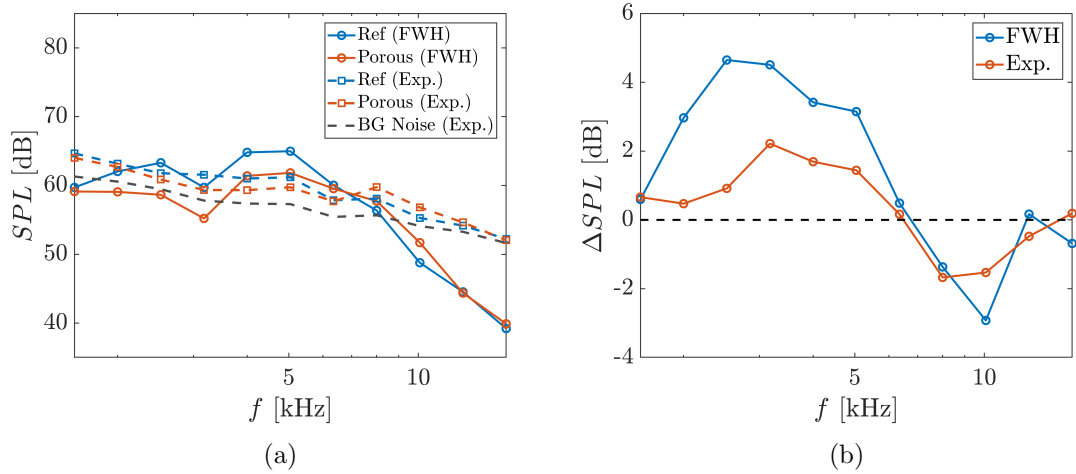


Figure 6.17: Comparison of the single-microphone measurement results (Exp.) and FWH acoustic analogy results (FWH): (a) sound pressure level SPL in 1/3 octave-bands; (b) noise reduction performance ΔSPL of the porous airfoil in 1/3 octave-bands.

Figure 6.18 shows the directivity pattern of the predicted acoustic pressure in 1/3 octave bands at observer locations $15c$ away from the airfoil TE in the midspan plane, where a position of 0° corresponds to the downstream of airfoil TE. At lower frequencies of 1.6 and 2 kHz, the airfoil noise source is emitted in a dipole form. At frequencies of 4 kHz ($c/\lambda = 0.82$) and 5 kHz ($c/\lambda = 1.03$) where highest noise levels are observed, the noise directivities resembles the typical “forward-looking” [82] directivity pattern that occurs when the wavelength is of the same order as the airfoil chord ($c/\lambda \sim 1$). The noise directivity pattern is not visibly altered by the porous airfoil at 1.6, 2 and 4 kHz. While at 5 kHz, the noise directivity pattern is significantly changed by the porous geometries, showing several additional lobes and lower magnitudes of acoustic pressure in the upstream positions of around 140° and 200° . At higher frequencies of 8 kHz and 10 kHz, the far-field acoustic pressures of the porous airfoil show a lower amplitude in the streamwise direction (positions of 180° and 0°) and a higher amplitude in other angular positions compared to the reference airfoil. This may be due to additional noise sources caused by the porous

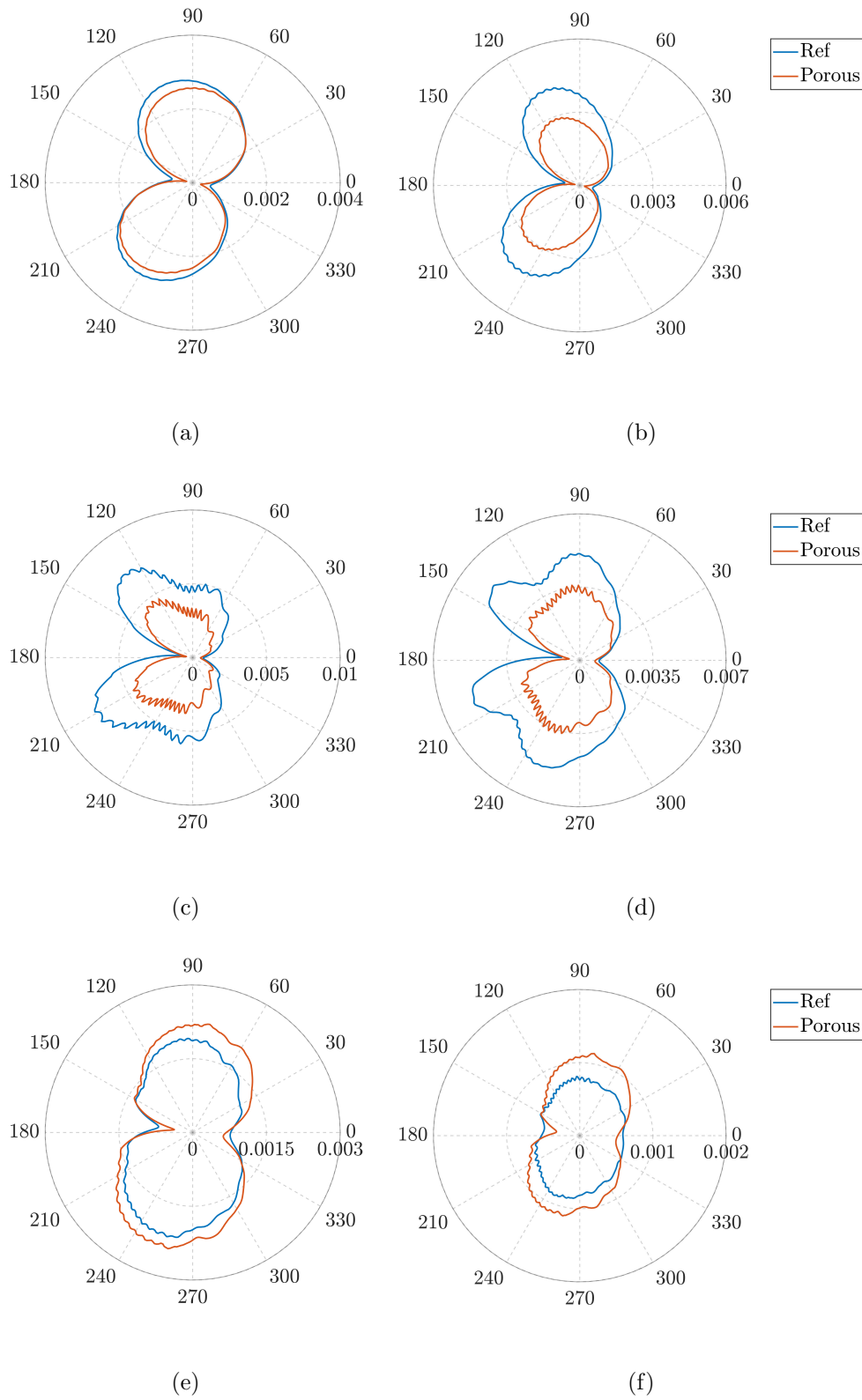


Figure 6.18: Directivity plot of the far-field 1/3 octave-band acoustic pressure $[\text{Pa}^2/\text{Hz}]$ for the reference airfoil (Ref) and airfoil with porous TE (Porous) at (a) 1.6 kHz, (b) 2 kHz, (c) 4 kHz, (d) 5 kHz, (e) 8 kHz and (f) 10 kHz.

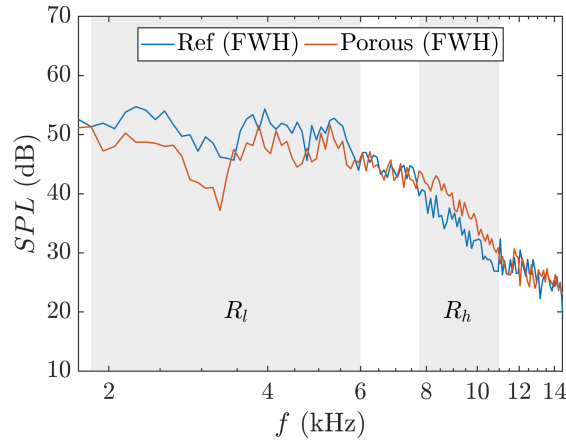


Figure 6.19: Narrow-band FWH acoustic analogy results. Frequency regions of interest are marked in grey (R_l : TE noise reduction region; R_h : high-frequency noise increase region).

geometries. For ease of analysing the flow characteristics related to the noise reduction and increase of the porous airfoil, two frequency regions R_l and R_h have been defined as shown in Figure 6.19: R_l is the frequency region where the TE noise level is reduced; R_h is the frequency region where a high-frequency noise increase is observed.

6.4.2 Flow Simulation Results

Figure 6.20 presents the distribution of the time-averaged pressure coefficient C_p along the midspan of the reference airfoil. Simulation results of the reference airfoil (LES Case 1) are compared with the Xfoil prediction for the experimental setup in the UAT. Excellent agreement is achieved except at locations near the artificial suction and blowing regions (numerical boundary layer tripping). The pressure coefficient results, along with the FWH acoustic analogy results, suggest that the wind tunnel measurement has been effectively modelled by the LES simulation.

Figure 6.21 shows the TE geometries of the porous airfoil. The cylindrical pores in the TE region have a diameter d_p of 0.8 mm. The spanwise spacing S_p and streamwise spacing L_p between the pores are 1.5 mm and 2.5 mm, respectively. As the pore pattern varies along the spanwise (z) direction, two representative spanwise locations PL1 (midspan: $z/c = 0$) and PL2 ($z/c = -0.011$) are chosen for analysing the spanwise variation of flow characteristics.

In Figure 6.22, the instantaneous flow structures over the reference and porous airfoil

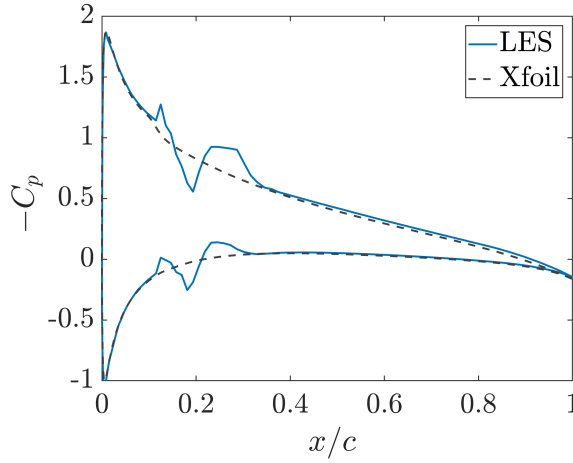


Figure 6.20: Distribution of pressure coefficient C_p over the reference airfoil compared with XFOIL prediction.

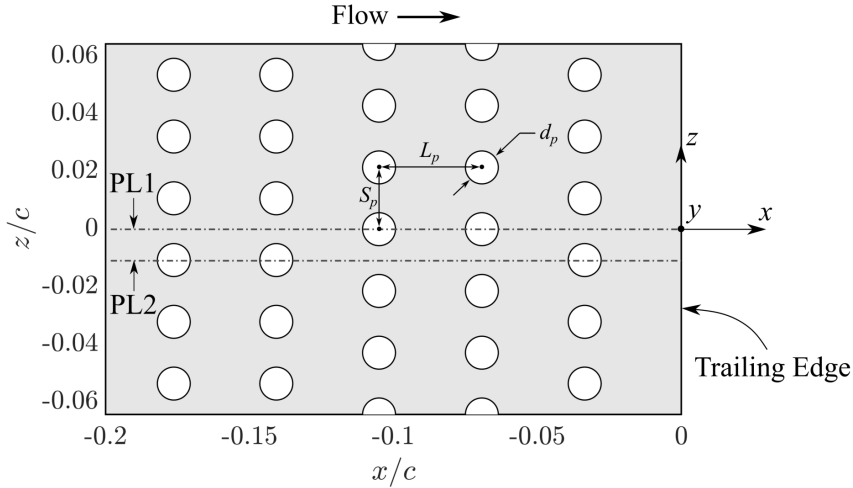


Figure 6.21: Sketch of the TE geometries of the porous airfoil (top view).

are presented. The boundary layer for both airfoils is well-developed and turbulent at the TE, showing a wide range of flow scales that could potentially contribute to aerodynamic noise generation. For the porous airfoil, high-vorticity turbulent flow is observed to travel through the porous geometries from the pressure surface to the suction surface. As a result, the vorticity near the airfoil TE is reduced on the pressure-side and increased on the suction-side.

The normalised streamwise Reynolds normal-stress $\overline{u'u'}/U_\infty^2$ of the porous airfoil in spanwise planes at PL1 ($z/c = 0$) and PL2 ($z/c = -0.011$) are compared with that of reference airfoil in the midspan plane in Figures 6.23, 6.24 and 6.25, which correspond to the unfiltered, low-frequency (R_l) and high-frequency (R_h) bandpass-filtered results,

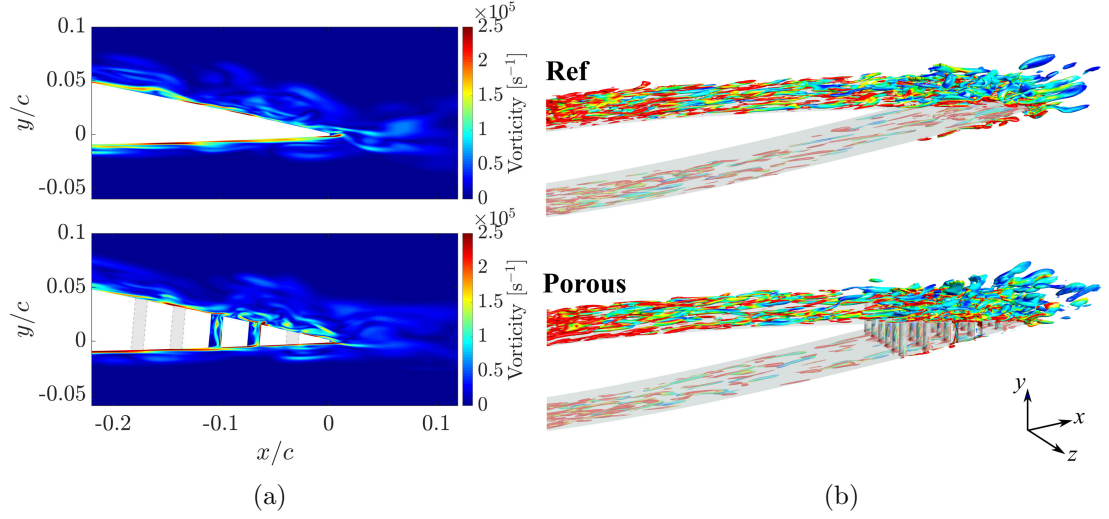


Figure 6.22: Instantaneous flow structures around the reference and porous airfoil TE: (a) vorticity in spanwise plane; (b) iso-surfaces of λ_2 criteria colored by vorticity.

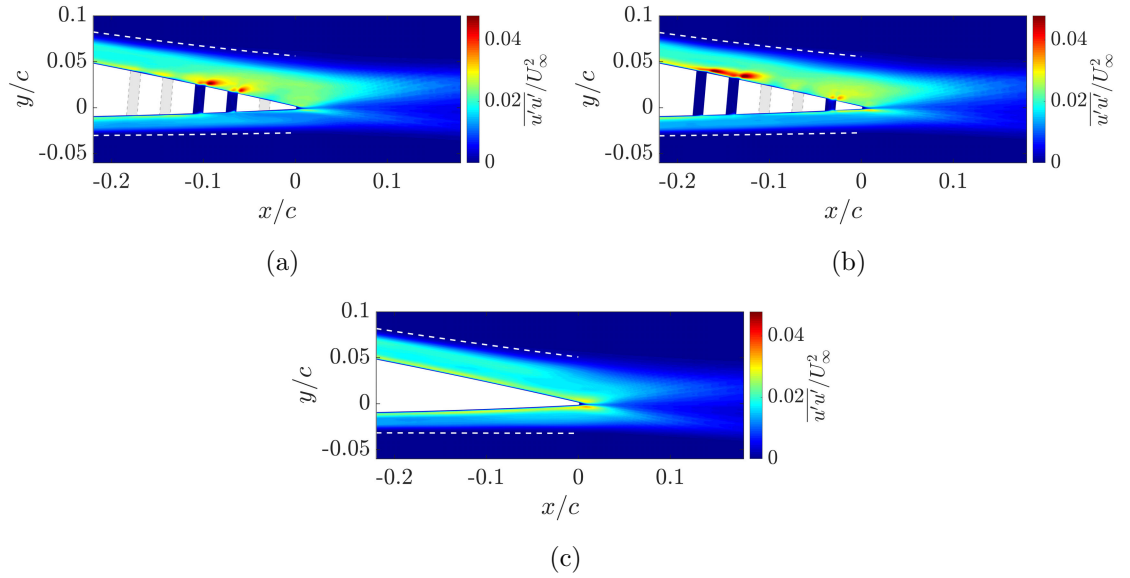


Figure 6.23: Contours of the normalised Reynolds normal-stress $\overline{u'u'}/U_\infty^2$ in spanwise planes at (a) PL1 and (b) PL2 of porous airfoil and (c) midspan plane of reference airfoil. Locations of $U = 0.99U_\infty$ are marked by white dashed lines.

respectively. For the unfiltered and low-frequency (R_l) results (Figures 6.23 and 6.24), the magnitude of $\overline{u'u'}/U_\infty^2$ in the TE boundary layer and wake is reduced by the porous TE on the pressure-side and increased on the suction-side compared to that of the reference airfoil. Immediately downstream of the pore wall on the suction-side, regions of high-amplitude streamwise velocity fluctuations are observed. For the high-frequency (R_h) bandpass-filtered results (Figure 6.25), the high-amplitude regions near the suction-side pore wall show a significantly higher magnitude of $\overline{u'u'}/U_\infty^2$ relative to that in the outer boundary

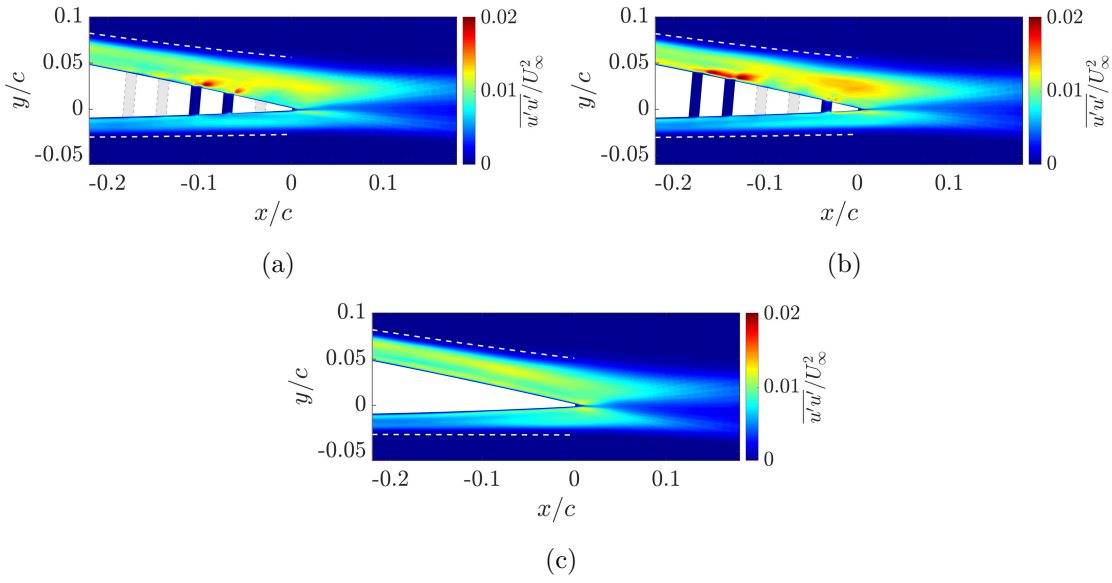


Figure 6.24: Contours of the normalised Reynolds normal-stress $\overline{u'u'}/U_\infty^2$ bandpass-filtered within R_l in spanwise planes at (a) PL1 and (b) PL2 of porous airfoil and (c) midspan plane of reference airfoil. Locations of $U = 0.99U_\infty$ are marked by white dashed lines.

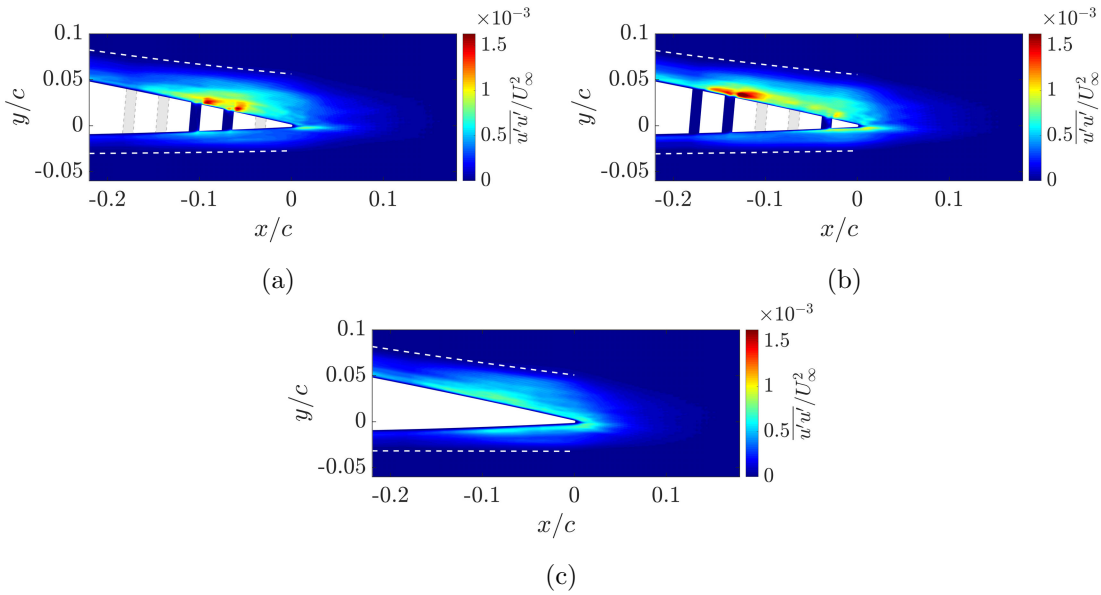


Figure 6.25: Contours of the normalised Reynolds normal-stress $\overline{u'u'}/U_\infty^2$ bandpass-filtered within R_h in spanwise planes at (a) PL1 and (b) PL2 of porous airfoil and (c) midspan plane of reference airfoil. Locations of $U = 0.99U_\infty$ are marked by white dashed lines.

layer and the vicinity of airfoil TE. This indicates that the eddies passing through the pores may have become the more prominent turbulent structures over frequency region R_h .

Figures 6.26, 6.27 and 6.28 present the unfiltered, low-frequency (R_l) and high-frequency (R_h) bandpass-filtered results of the normalised vertical Reynolds normal-stress $\overline{v'v'}/U_\infty^2$ of the porous airfoil in spanwise planes at PL1 ($z/c = 0$) and PL2 ($z/c = -0.011$) com-

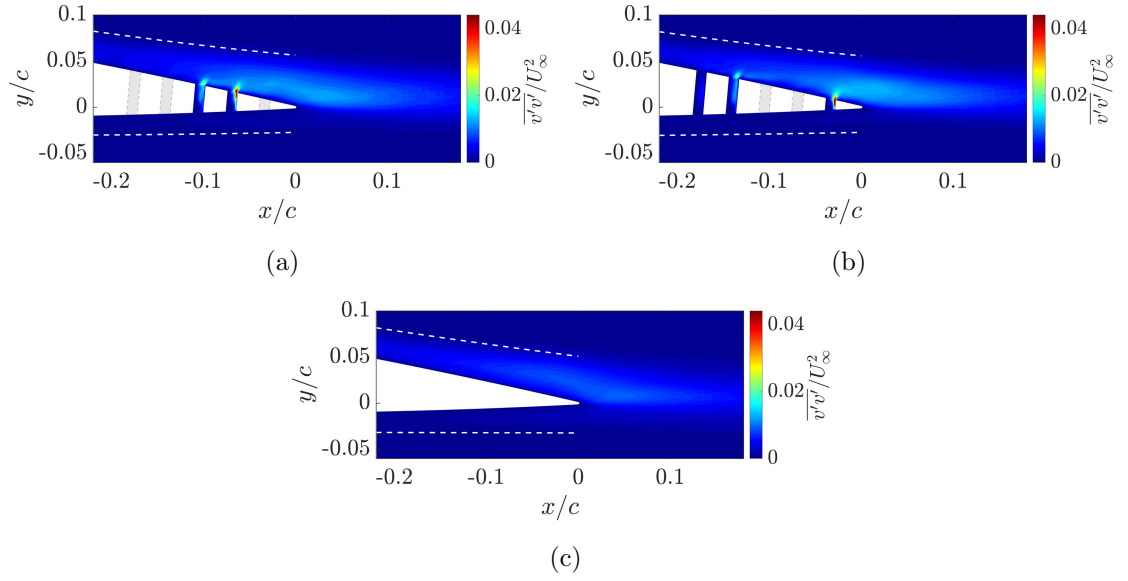


Figure 6.26: Contours of the normalised Reynolds normal-stress $\overline{v'v'}/U_\infty^2$ in spanwise planes at (a) PL1 and (b) PL2 of porous airfoil and (c) midspan plane of reference airfoil. Locations of $U = 0.99U_\infty$ are marked by white dashed lines.

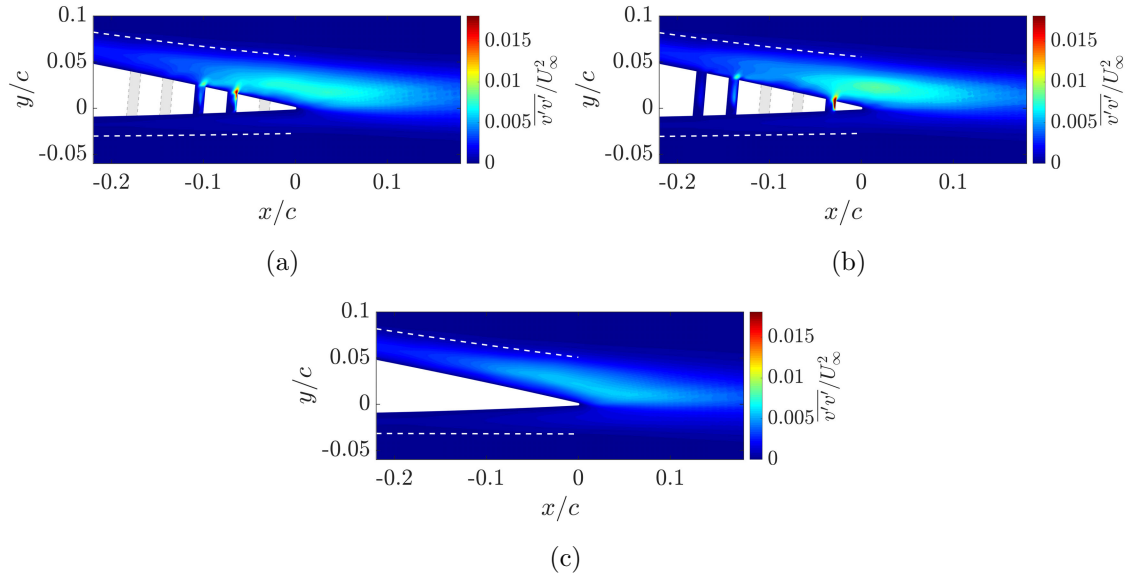


Figure 6.27: Contours of the normalised Reynolds normal-stress $\overline{v'v'}/U_\infty^2$ bandpass-filtered within R_l in spanwise planes at (a) PL1 and (b) PL2 of porous airfoil and (c) midspan plane of reference airfoil. Locations of $U = 0.99U_\infty$ are marked by white dashed lines.

pared with that of the reference airfoil in the midspan plane. For the unfiltered results (Figure 6.26), regions of a high magnitude of $\overline{v'v'}/U_\infty^2$ are observed near the downstream pore walls. Compared with the reference airfoil, the regions downstream of the pores in the suction-side boundary layer and near wake show a higher magnitude of $\overline{v'v'}/U_\infty^2$. The increase in the vertical velocity fluctuations for the porous airfoil indicates the presence of large swirling turbulent structures and highly anisotropic flow at these regions [2]. The

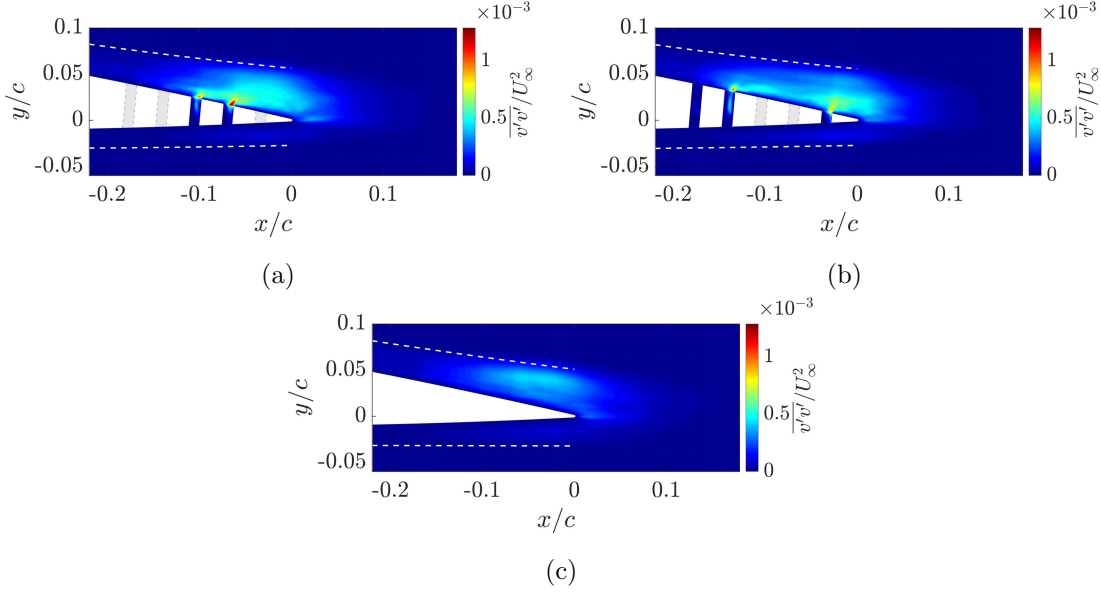


Figure 6.28: Contours of the normalised Reynolds normal-stress $\overline{v'v'}/U_\infty^2$ bandpass-filtered within R_h in spanwise planes at (a) PL1 and (b) PL2 of porous airfoil and (c) midspan plane of reference airfoil. Locations of $U = 0.99U_\infty$ are marked by white dashed lines.

low-frequency (R_l) results (Figure 6.27) show a spatial distribution similar to the unfiltered results (Figure 6.26) except in the wake and outer boundary layer near the TE, where the magnitude of $\overline{v'v'}/U_\infty^2$ relative to regions near the downstream pore wall is increased. However, for the high-frequency (R_h) results (Figure 6.28), high magnitudes of $\overline{v'v'}/U_\infty^2$ are only present in small regions near the junction of the downstream pore wall and airfoil suction surface (pore suction-side open end), indicating the existence of high-energy eddies of frequencies within R_h .

Figure 6.29 illustrates the definition of the cylindrical-polar velocity components u_r and u_θ in the acoustic source term related to Reynolds shear-stress $|-2\widehat{u_r u_\theta}|$ (as described in Ref. [189]), where caret denotes the temporal Fourier transform. This source term can be used to indicate the intensity of noise sources generated by turbulence. Figures 6.30 and 6.31 present the magnitude of the normalised acoustic source term $|-2\widehat{u_r u_\theta}|/U_\infty^2$

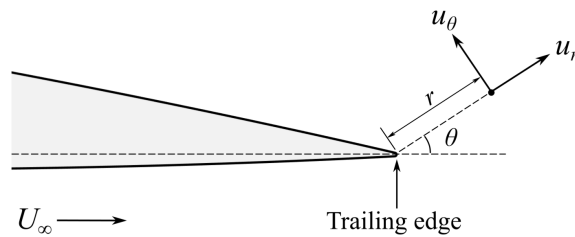


Figure 6.29: Schematic of the polar velocity components about the airfoil TE.

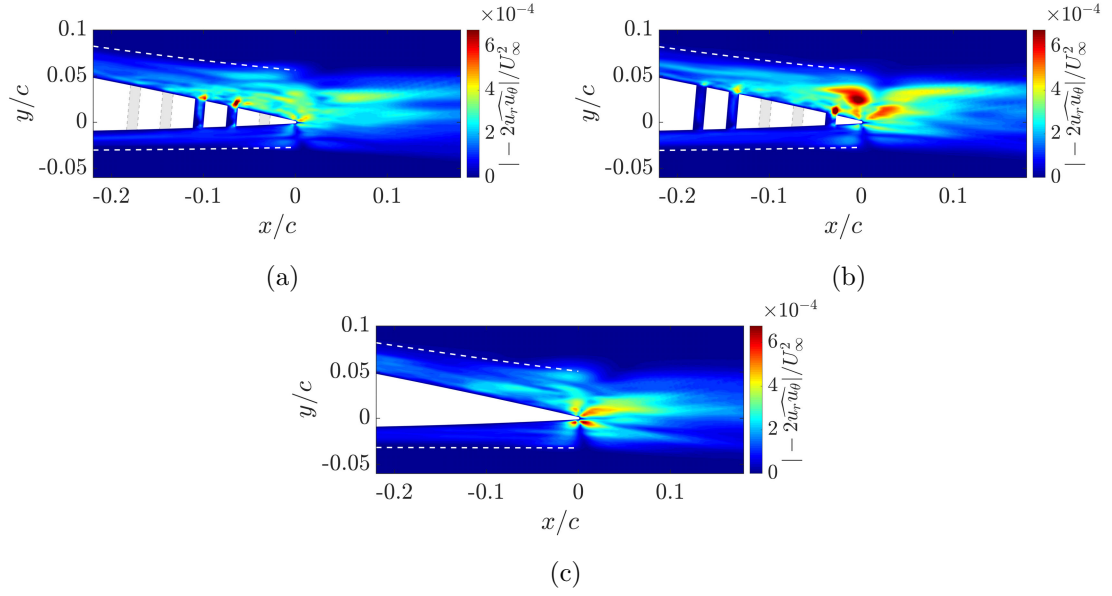


Figure 6.30: Contours of the magnitude of acoustic source term $|-2\widehat{u_r u_\theta}|/U_\infty^2$ in 1/3 octave band at 5 kHz in spanwise planes at (a) PL1 and (b) PL2 of porous airfoil and (c) midspan plane of reference airfoil. Locations of $U = 0.99U_\infty$ are marked by white dashed lines.

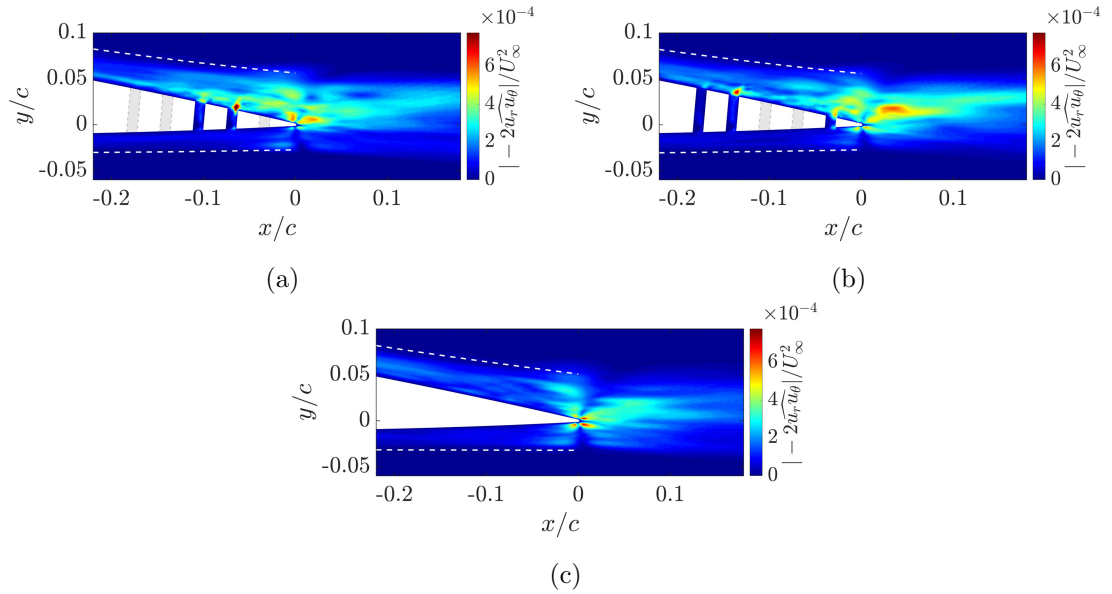


Figure 6.31: Contours of the magnitude of acoustic source term $|-2\widehat{u_r u_\theta}|/U_\infty^2$ in 1/3 octave band at 8 kHz in spanwise planes at (a) PL1 and (b) PL2 of porous airfoil and (c) midspan plane of reference airfoil. Locations of $U = 0.99U_\infty$ are marked by white dashed lines.

in the 5 and 8 kHz 1/3 octave bands where the peak noise reduction and increase are observed, respectively. At both frequencies, the source term of the reference airfoil shows a spatial distribution of four high-magnitude regions near the TE (Figures 6.30c and 6.31c). For the porous airfoil, the magnitude of the quadruple-distributed source regions

is significantly reduced in plane PL1 (Figure 6.30a) at 5 kHz where the peak noise level of FWH predictions is observed. In plane PL2 (Figure 6.30b), the magnitude of the source term is reduced near the pressure surface at the TE but increased in the suction-side TE boundary layer and wake compared with those of the reference airfoil. The increase of acoustic source intensity is likely due to the highly swirled (high intensity of vertical velocity fluctuations) turbulence that permeates through the pore nearest to the TE (Figure 6.27). Moreover, in both planes PL1 and PL2, the acoustic source term is of high magnitude near the pore suction-side open end where high level vertical velocity fluctuations are present (Figure 6.27). At 8 kHz, the peak frequency of the broadband noise increase produced by the porous TE, the intensity of the quadruple-distributed source regions near the TE of reference airfoil (Figure 6.31c) is only slightly reduced by the porous geometries, while a higher magnitude of $|-2\widehat{u_r u_\theta}|/U_\infty^2$ appears near the pore suction-side open end and in the suction-side wake (Figures 6.31a and 6.31b). This, along with the vertical velocity fluctuation results (Figure 6.28), suggest that the high-frequency broadband noise increase observed in experiments and FWH predictions may arise from the interactions between the pore suction-side open end and turbulence permeated through the TE pores from the pressure surface to the suction surface.

Vertical velocity fluctuations are commonly linked to wall pressure fluctuations and therefore, are widely used in the source term of analytical models [5, 37, 162, 179] for TE noise. In a recent experimental study of PIV measurements on an airfoil with porous TE [165], the vertical velocity fluctuations were found to be correlated between the pressure- and suction-sides of the porous metal-foam TE over the frequency range of noise reduction. It was suggested that the vertical flow passing through the porous media contributes to the noise reduction achieved with the porous TE. The vertical flow connects the upstream pressure and suction surfaces, hence reduces the acoustic impedance jump at the edge. To investigate the applicability of these findings for the porous TE in this study, the spatial correlation of the vertical velocity fluctuations $R_{vv,\tau=0}$ has been calculated using a cross-correlation function given by:

$$R_{vv,\tau=0}(\mathbf{x}, \xi) = E[v'(\mathbf{x}, t), v'(\mathbf{x} + \xi, t)], \quad (6.11)$$

where \mathbf{x} stands for the reference point, ξ is a separation vector of the distance relative to

reference point and $E[\]$ denotes the expected value. Figures 6.32 and 6.33 present the spatial correlation maps of vertical velocity fluctuations bandpass-filtered within frequency regions R_l and R_h , respectively. These spatial correlation maps are calculated based on the reference points at the near-wall boundary layer ($\delta_y = 0.1\delta$) and different streamwise locations, where δ_y is the distance from the reference point to wall and δ is the local boundary layer thickness. The regions of low correlation ($R_{vv,\tau=0} < 0.2$) have been masked for clarity. For the results filtered over the frequency region of TE noise reduction (R_l) as shown in Figure 6.32, a region of low spatial correlations appears in the suction-side boundary layer when the corresponding reference points are near the pressure-side open end of the pores. As the reference point moves downstream, higher correlations are observed in the suction-side boundary layer. In the spatial correlation maps filtered over the frequency region of broadband noise increase (R_h), the suction-side low-correlation region is not observed, indicating that the vertical velocity fluctuations over this frequency range fail to propagate from the lower surface to the upper surface through the pores. Despite the differences in TE porous geometries, the spatial correlation maps of the simulated porous TE show similar characteristics to those of the metal-foam TE as reported in [165]. This suggests that the vertical velocity fluctuations that propagate from the pressure surface to the suction surface may be a crucial feature for the noise reduction by porous TEs.

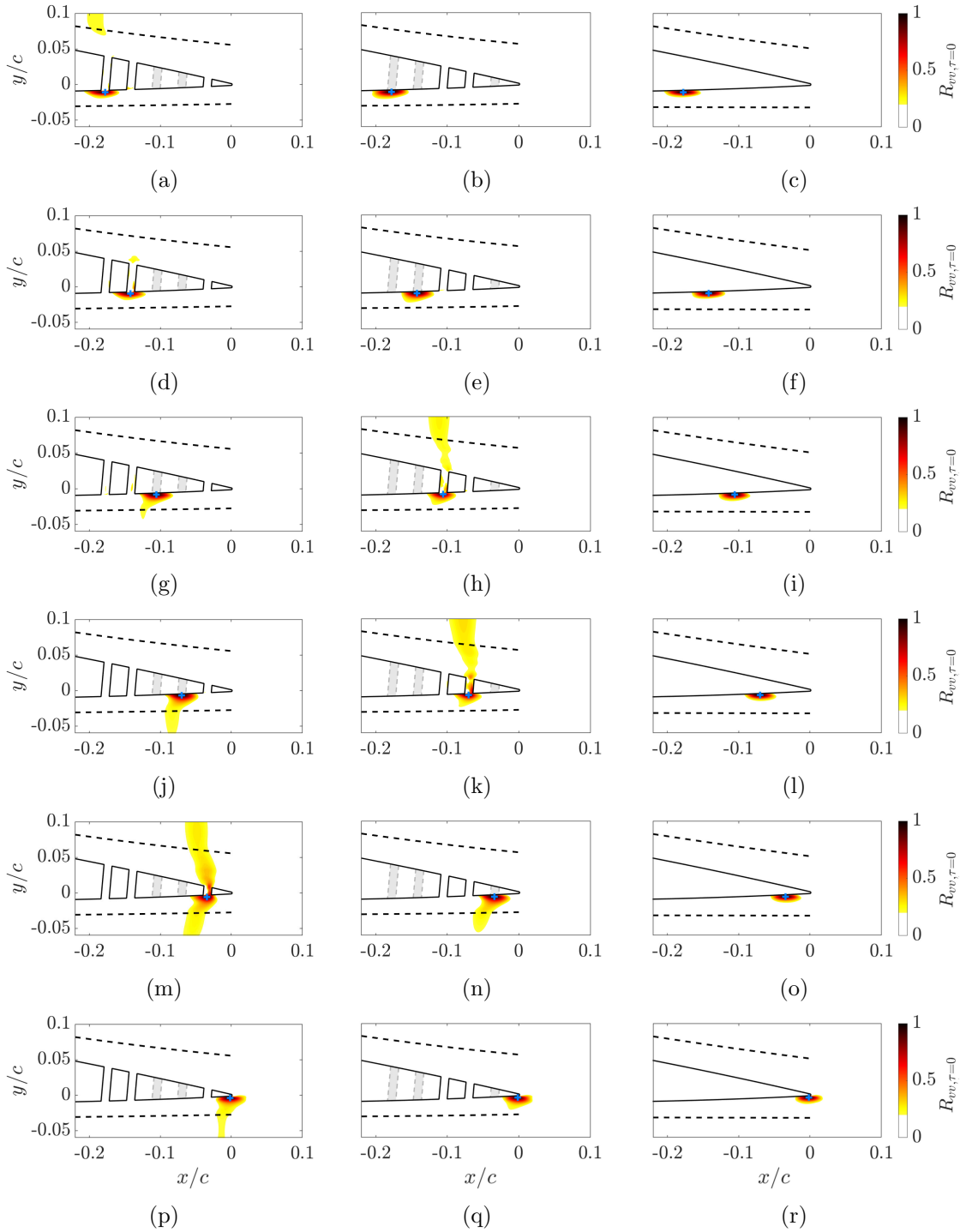


Figure 6.32: Contours of the spatial correlation of the vertical velocity fluctuations bandpass-filtered within frequency region R_l in spanwise planes at PL1 (middle column) and PL2 (left column) of porous airfoil and midspan plane of reference airfoil (right column) with reference points at $\delta_y = 0.1\delta$ and different streamwise location:(a)–(c) $x/c = -0.178$; (d)–(f) $x/c = -0.142$; (g)–(i) $x/c = -0.105$; (j)–(l) $x/c = -0.070$; (m)–(o) $x/c = -0.034$; (p)–(r) $x/c = -0.02$. Locations of the reference point are marked by blue crosses, and the boundary layer edges ($U = 0.99U_\infty$) are marked by black dashed lines.

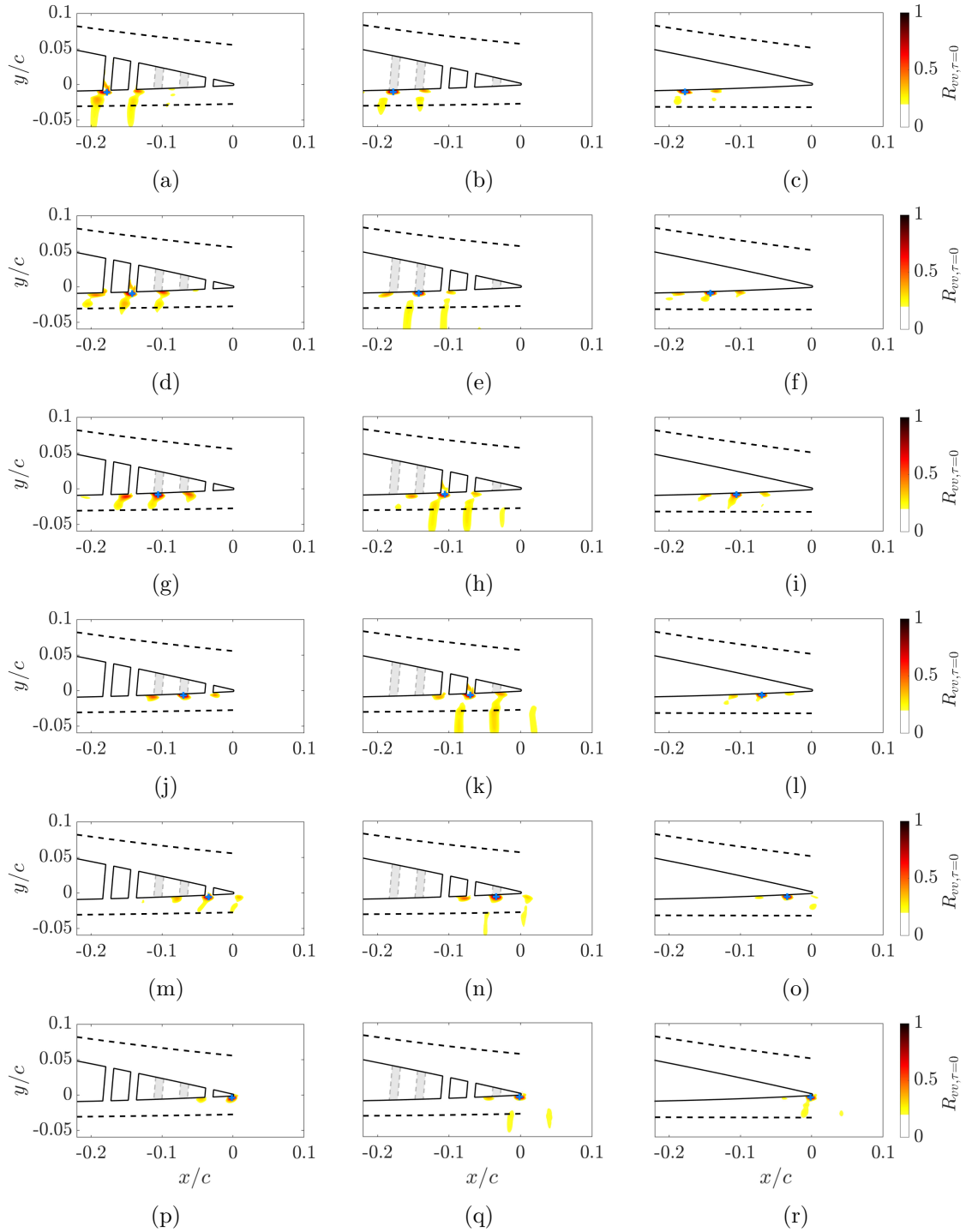


Figure 6.33: Contours of the spatial correlation of the vertical velocity fluctuations bandpass-filtered within frequency region R_h in spanwise planes at PL1 (middle column) and PL2 (left column) of porous airfoil and midspan plane of reference airfoil (right column) with reference points at $\delta_y = 0.1\delta$ and different streamwise location: (a)–(c) $x/c = -0.178$; (d)–(f) $x/c = -0.142$; (g)–(i) $x/c = -0.105$; (j)–(l) $x/c = -0.070$; (m)–(o) $x/c = -0.034$; (p)–(r) $x/c = -0.02$. Locations of the reference point are marked by blue crosses, and the boundary layer edges ($U = 0.99U_\infty$) are marked by black dashed lines.

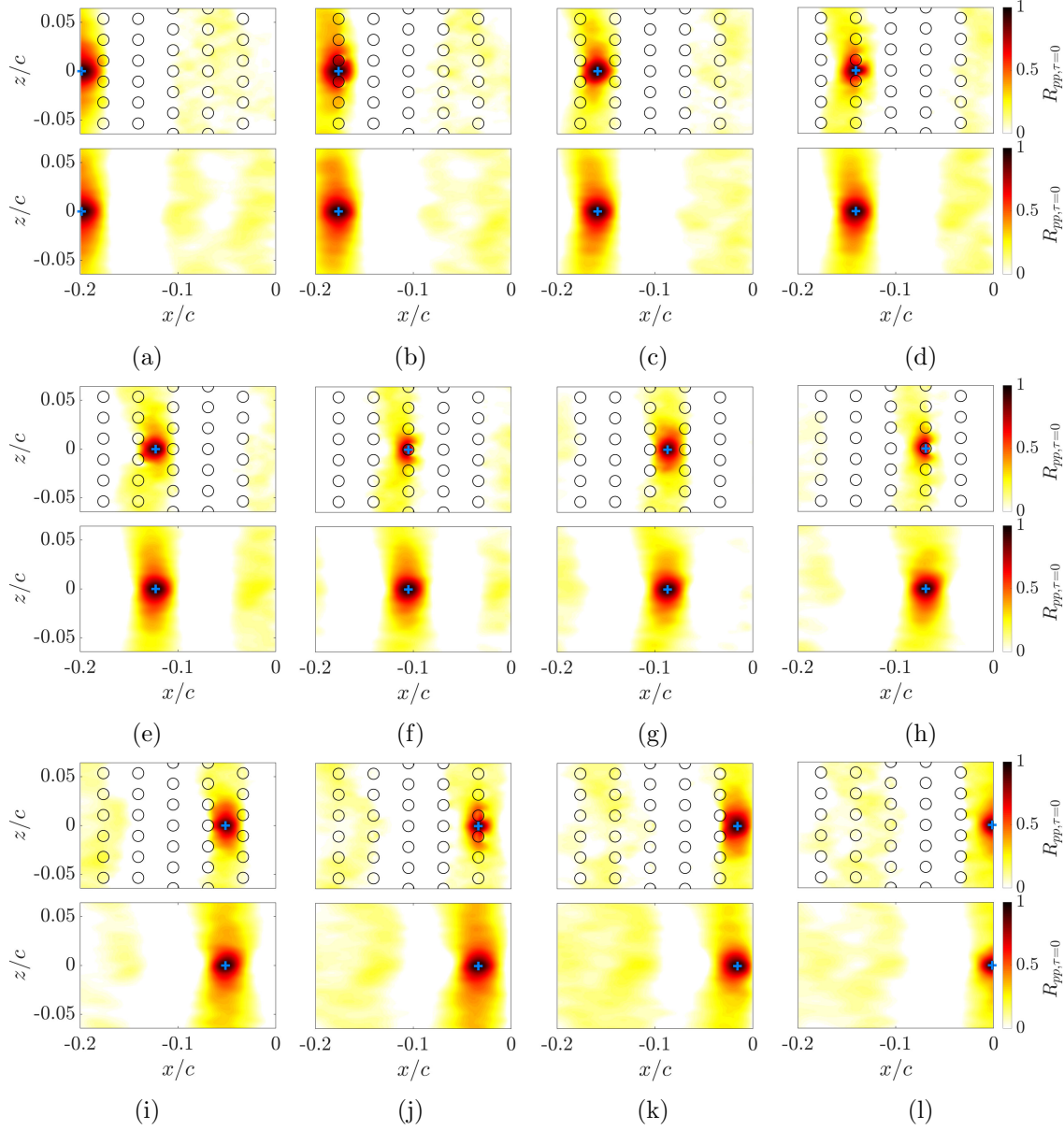


Figure 6.34: Contours of the spatial correlation of the pressure fluctuations bandpass-filtered within frequency region R_l at the suction surface of the porous (top) and reference (bottom) TEs with reference points at different streamwise location: (a) $x/c = -0.199$; (b) $x/c = -0.176$; (c) $x/c = -0.159$ (d) $x/c = -0.14$; (e) $x/c = -0.12$; (f) $x/c = -0.105$ (g) $x/c = -0.087$; (h) $x/c = -0.069$; (i) $x/c = -0.051$; (j) $x/c = -0.034$; (k) $x/c = -0.016$; (l) $x/c = -0.001$. Locations of the reference point are marked by blue crosses, and the pores are marked by black circles.

To further investigate the effects of the permeated flow on wall pressure fluctuations, analysis of the spatial correlation and space-time correlation of the wall pressure fluctuations has been carried out. Both the spatial correlation $R_{pp,\tau=0}$ and space-time correlation R_{pp} are calculated using the cross-correlation function:

$$R_{pp}(\mathbf{x}, \xi, \tau) = E[p'(\mathbf{x}, t), p'(\mathbf{x} + \xi, t + \tau)], \quad (6.12)$$

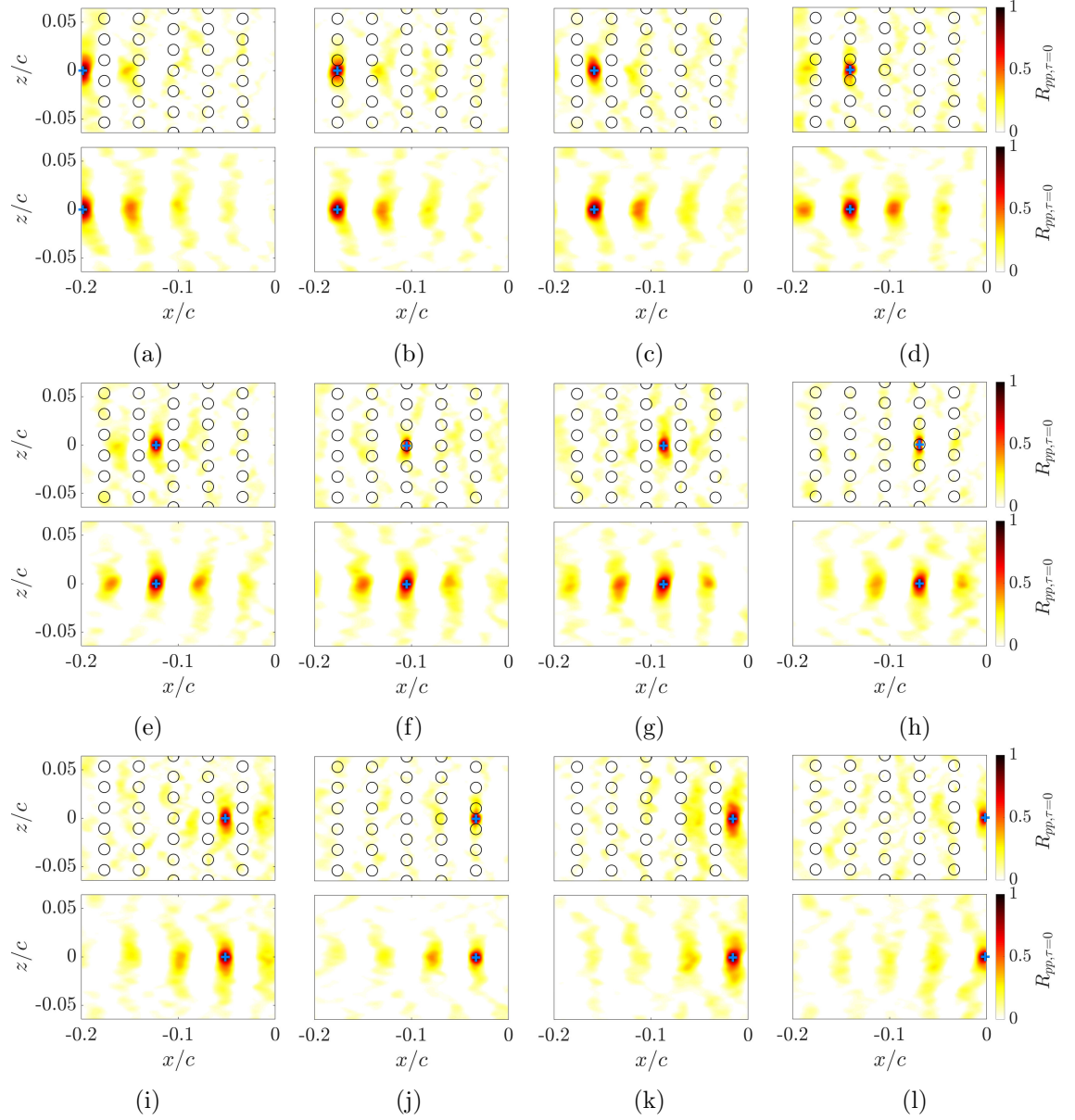


Figure 6.35: Contours of the spatial correlation of the pressure fluctuations bandpass-filtered within frequency region R_h at the suction surface of the porous (top) and reference (bottom) TE with reference points at different streamwise location: (a) $x/c = -0.199$; (b) $x/c = -0.176$; (c) $x/c = -0.159$ (d) $x/c = -0.14$; (e) $x/c = -0.12$; (f) $x/c = -0.105$ (g) $x/c = -0.087$; (h) $x/c = -0.069$; (i) $x/c = -0.051$; (j) $x/c = -0.034$; (k) $x/c = -0.016$; (l) $x/c = -0.001$. Locations of the reference point are marked by blue crosses, and the pores are marked by black circles.

where τ is the temporal lag between signals at the location $\mathbf{x} + \xi$ and reference point \mathbf{x} . The spatial correlation $R_{pp,\tau=0}$ is a special form of Eq. (6.12) when the temporal lag equals to zero: $R_{pp,\tau=0}(\mathbf{x}, \xi) = R_{pp}(\mathbf{x}, \xi, 0)$. Figures 6.34 and 6.35 present the spatial correlation maps of the pressure fluctuations at the suction surface near the TE, in which the pressure fluctuation signals are bandpass-filtered over frequency regions R_l and R_h , respectively.

These spatial correlation maps have been calculated based on reference points at various streamwise locations along the midspan (PL1). For locations at the voids (regions within the black circles), the correlation is calculated using air pressure fluctuations instead of wall pressure fluctuations. For the results filtered within the frequency region of TE noise reduction (R_l) as shown in Figure 6.34, the spanwise correlation of wall pressure fluctuations is significantly reduced by the porous geometries, especially when the reference point is at the void location or its nearby regions. This indicates the reduction of spanwise correlation may be attributed to the geometry discontinuity of porous TE and the flow perturbations propagating from the pressure-side through the pores, which may have destructive effects on the spanwise-coherent turbulent structures. For the results filtered over the frequency region of broadband noise increase (R_h) as shown in Figure 6.35, the spanwise correlation of wall pressure fluctuations is not significantly affected by the porous geometries. Only a minor reduction of spanwise correlation is observed at the void locations. Due to the bandpass filtering over R_h , high spatial correlation is observed at several locations along the streamwise direction for the reference airfoil. The spatial correlation at these locations is significantly reduced by the porous TE, which may also be caused by the flow perturbations induced by porous geometries.

In Figure 6.37, the space-time correlation maps at six upstream reference locations P_{st1} – P_{st6} (as illustrated in Figure 6.36) on the suction surface of the porous and reference TEs are presented. The temporal lag τ and streamwise separation distance relative to the reference point Δx are nondimensionalised by the freestream velocity U_∞ and streamwise

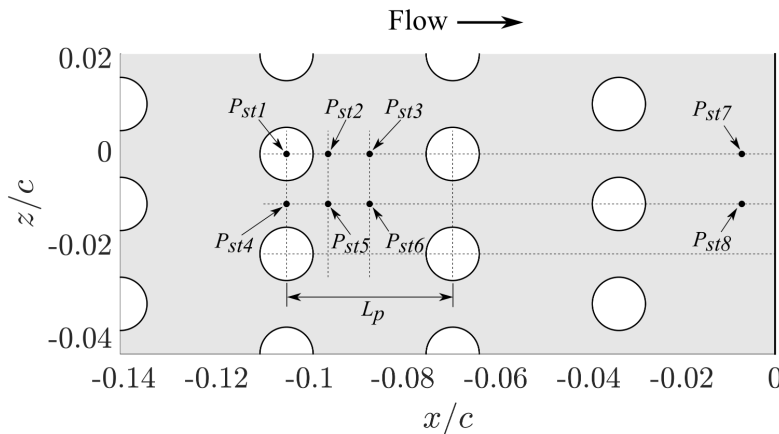


Figure 6.36: Locations of the reference point for analysing the space-time correlation and mean convection velocity.

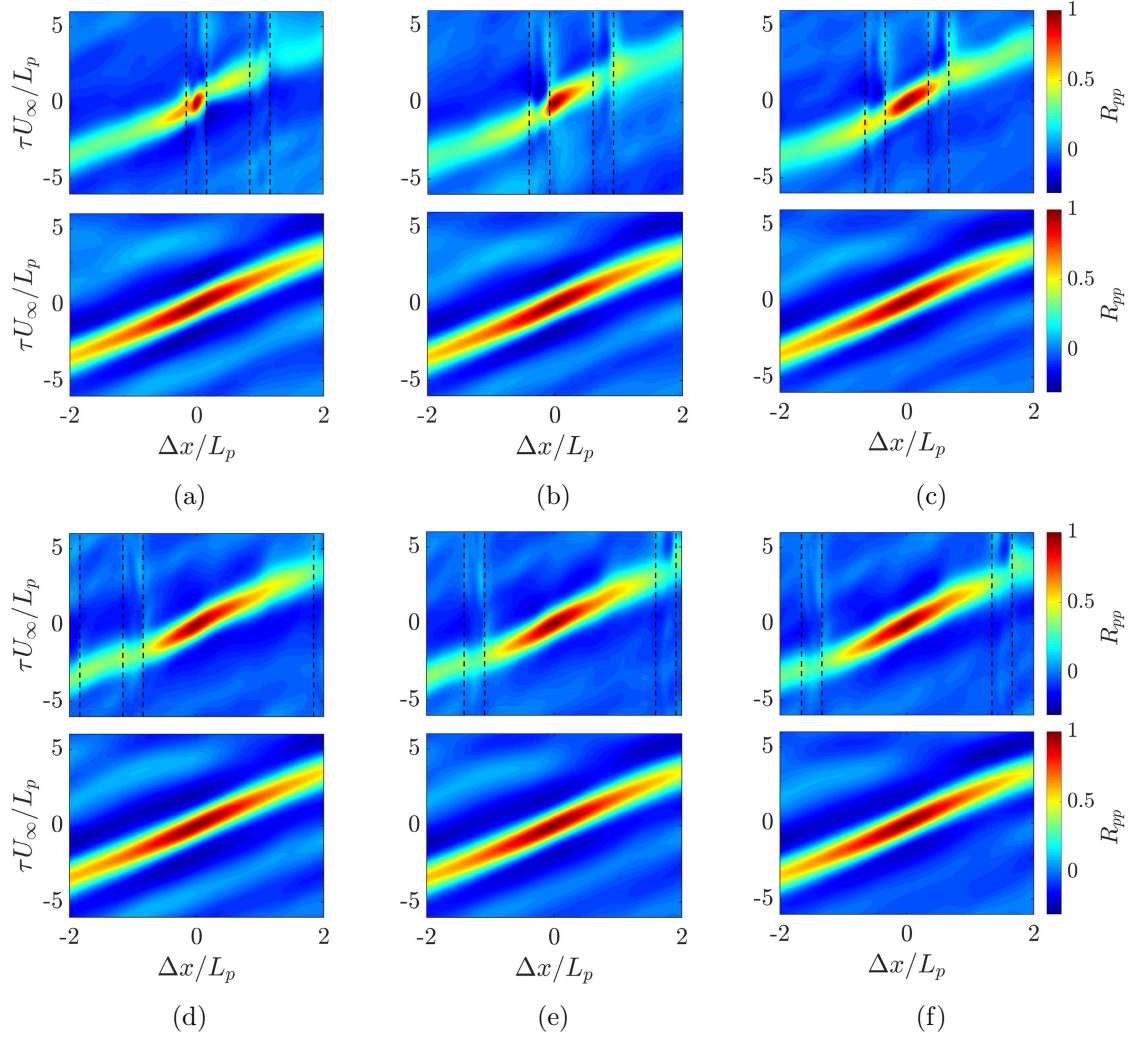


Figure 6.37: Contours of the space-time correlation of the pressure fluctuations on the suction surface of the porous (top) and reference (bottom) TEs with respect to reference points: (a) P_{st1} ; (b) P_{st2} ; (c) P_{st3} ; (d) P_{st4} ; (e) P_{st5} and (f) P_{st6} . Locations of the pore wall are marked by black dashed lines.

spacing between the pores L_p . For the reference point P_{st1} at the center of the pore open end, regions of high correlation are confined within the pore. For other reference points, significant decorrelation of the pressure fluctuations is observed at the pore locations where a discontinuity due to the solid wall is present. In order to relate the wall pressure fluctuations to the TBL-TE noise generation, the local mean convection velocity $\overline{U_c}$ is estimated using the space-time correlation results by [95]:

$$\overline{U_c}(\Delta x) = \Delta x / \tau_{max}(\Delta x) , \quad (6.13)$$

where τ_{max} is the temporal lag of the maximum correlation for a fixed streamwise separation distance Δx . Figure 6.38 presents the normalised mean convection velocity

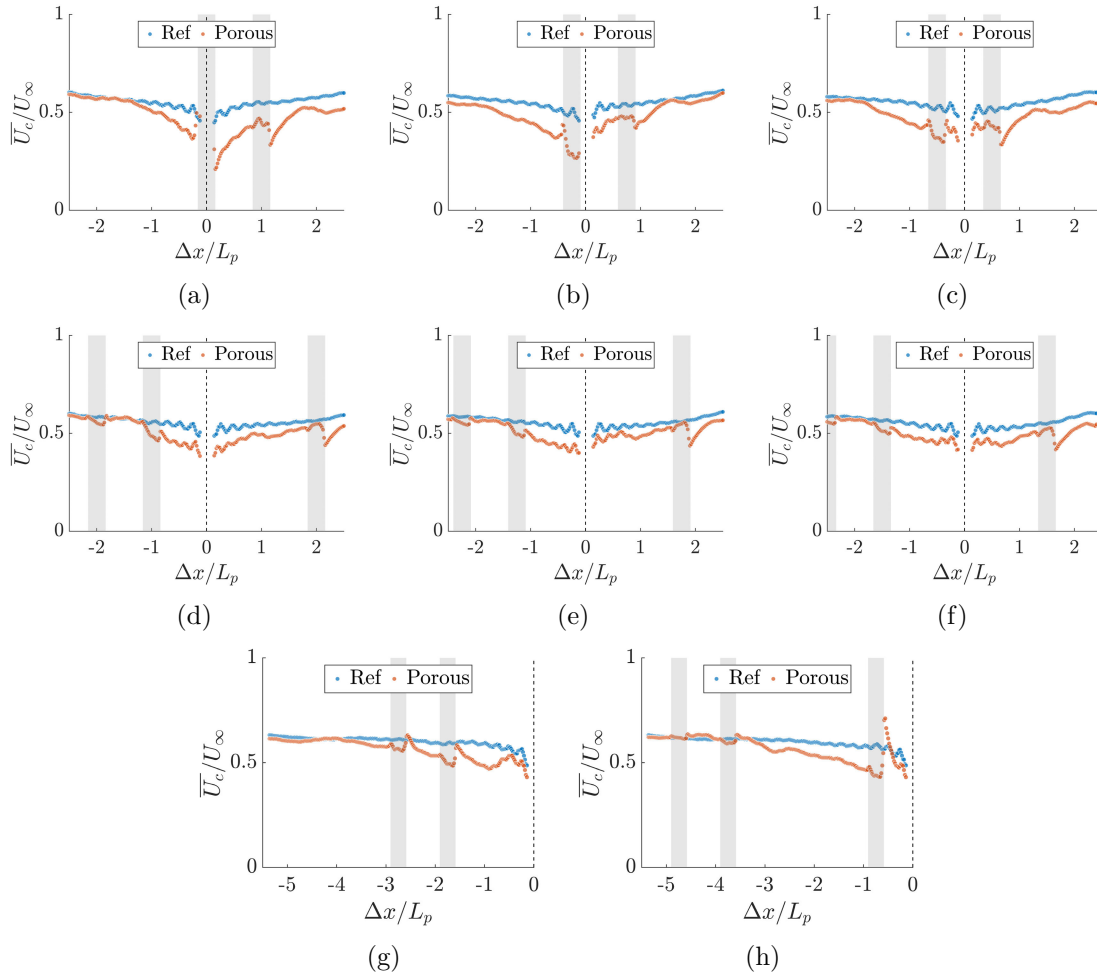


Figure 6.38: Normalised mean convection velocity \overline{U}_c/U_∞ on the suction surface of the porous and reference TE with respect to reference points: (a) P_{st1} ; (b) P_{st2} ; (c) P_{st3} ; (d) P_{st4} ; (e) P_{st5} ; (f) P_{st6} ; (g) P_{st7} and (h) P_{st8} . Locations of the pore are marked in grey.

\overline{U}_c/U_∞ calculated at six upstream reference points and two reference points near the TE. At upstream reference points P_{st1} – P_{st6} (Figures 6.38a–6.38f), the mean convection velocities of the turbulence convected from upstream and to downstream locations are both significantly reduced. When the turbulence is convected from upstream locations ($\Delta x < 0$) to the reference point, a sudden recovery of convection velocity occurs at the suction surface downstream of the pore. When the turbulence is convected from the reference point to downstream locations ($\Delta x > 0$), a sudden decrease of convection velocity occurs within the pore region near the downstream pore wall. Similar characteristics are observed at reference points P_{st7} and P_{st8} near the TE (Figures 6.38g and 6.38h) where the mean convection velocity reduces in the pore regions and suddenly recovers at the suction surface downstream of the pore. Overall, the mean convection velocity over the TE region ($-0.2 < x/c < 0$) is significantly reduced by the porous geometries.

Spanwise correlation length and convection velocity, as components of the source terms in many analytical models for TBL-TE noise [4, 6, 162, 179], play an important role in noise generation and scattering. The convection velocity results, along with the spatial correlation maps of wall pressure fluctuations, suggest that the noise reduction by a porous TE is mainly due to reductions in spanwise correlation [23] and convection velocity [35], which may arise from the flow perturbations that propagate through the pores [34] and the flow induced by the discontinuity of porous geometries.

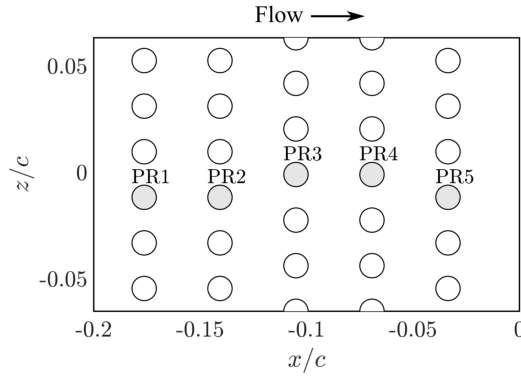


Figure 6.39: Locations of the selected pores for flow characterisation (marked in grey).

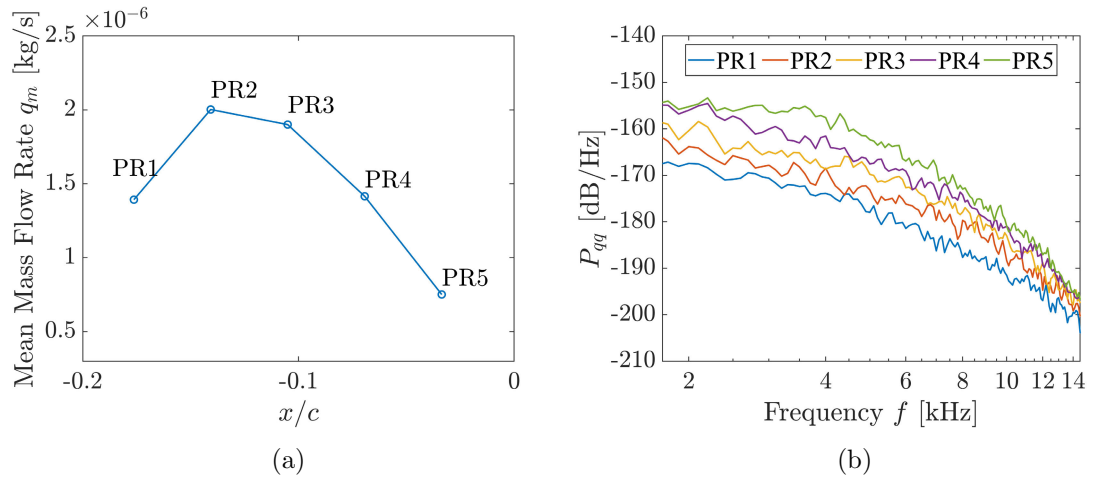


Figure 6.40: Characteristics of the mass flow rate through pores PR1–PR5: (a) mean mass flow rate q_m ; (b) power spectral density of mass flow rate P_{qq} .

In order to investigate the generation mechanism of the broadband noise increase over frequency region R_h , the mass flow rate of the flow permeation through five pores PR1–PR5 at different streamwise locations (as illustrated in Figure 6.39) and the surface pressure fluctuation on the interior wall of these pores are analysed. Figure 6.40 presents the mean mass flow rate q_m and the power spectral density of the mass flow rate P_{qq} of

pores PR1–PR5. The maximum mean mass flow rate is observed at the second pore PR2. In the region downstream of PR2, the mass flow rate decreases gradually, indicating flow permeation reduces as the flow develops towards the TE. However, the fluctuations of mass flow rate gradually intensify in the downstream pores, showing broadband increases of power spectral density over a wide range of frequencies (2–14 kHz). At the frequency region of the broadband noise increase (R_h), the power spectral density of the mass flow rate does not noticeably increase. Therefore, a direct relationship between mass flow rate and broadband noise increase is not evident.

As discussed in Sec. 6.4.1, additional dipole noise sources are observed over frequency region R_h in the noise directivity results predicted by the FWH acoustic analogy (Fig-

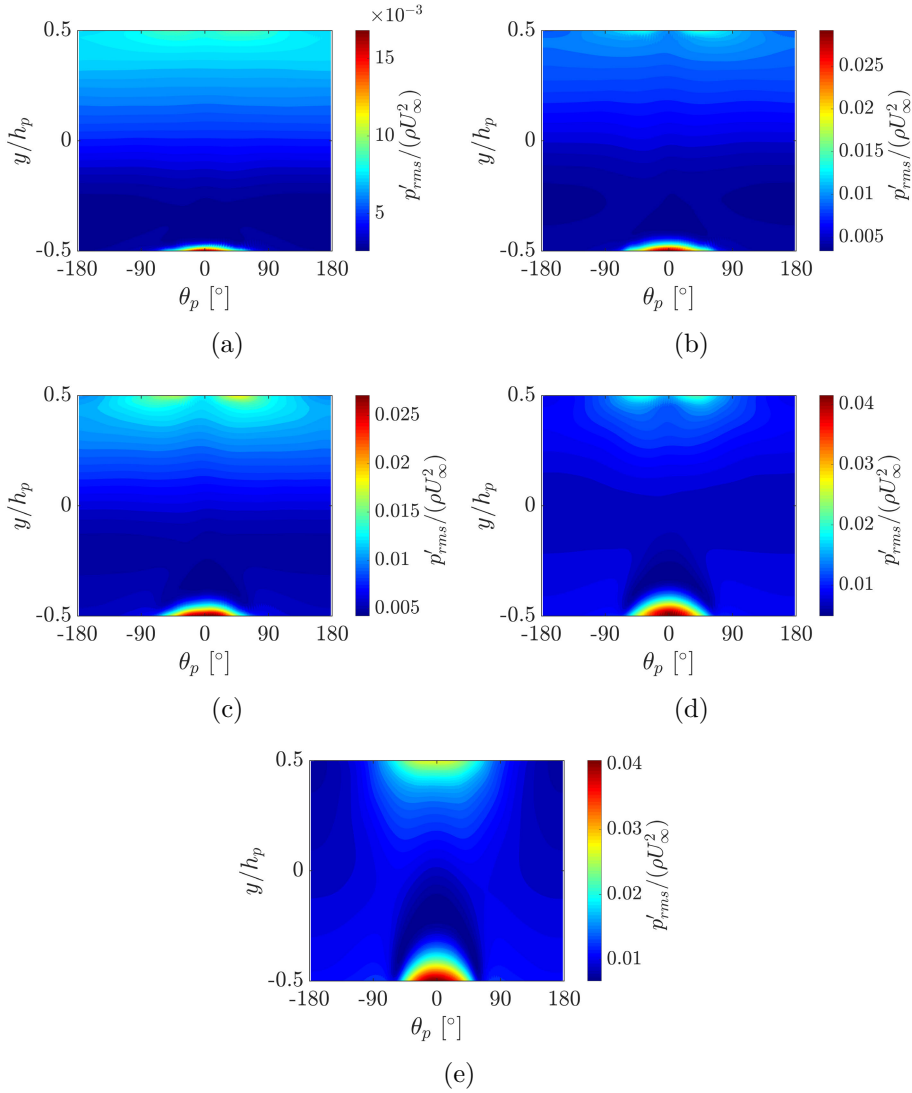


Figure 6.41: Contours of the normalised RMS of wall pressure fluctuations bandpass-filtered within frequency region R_l in pores (a) PR1, (b) PR2, (c) PR3, (d) PR4 and (e) PR5.

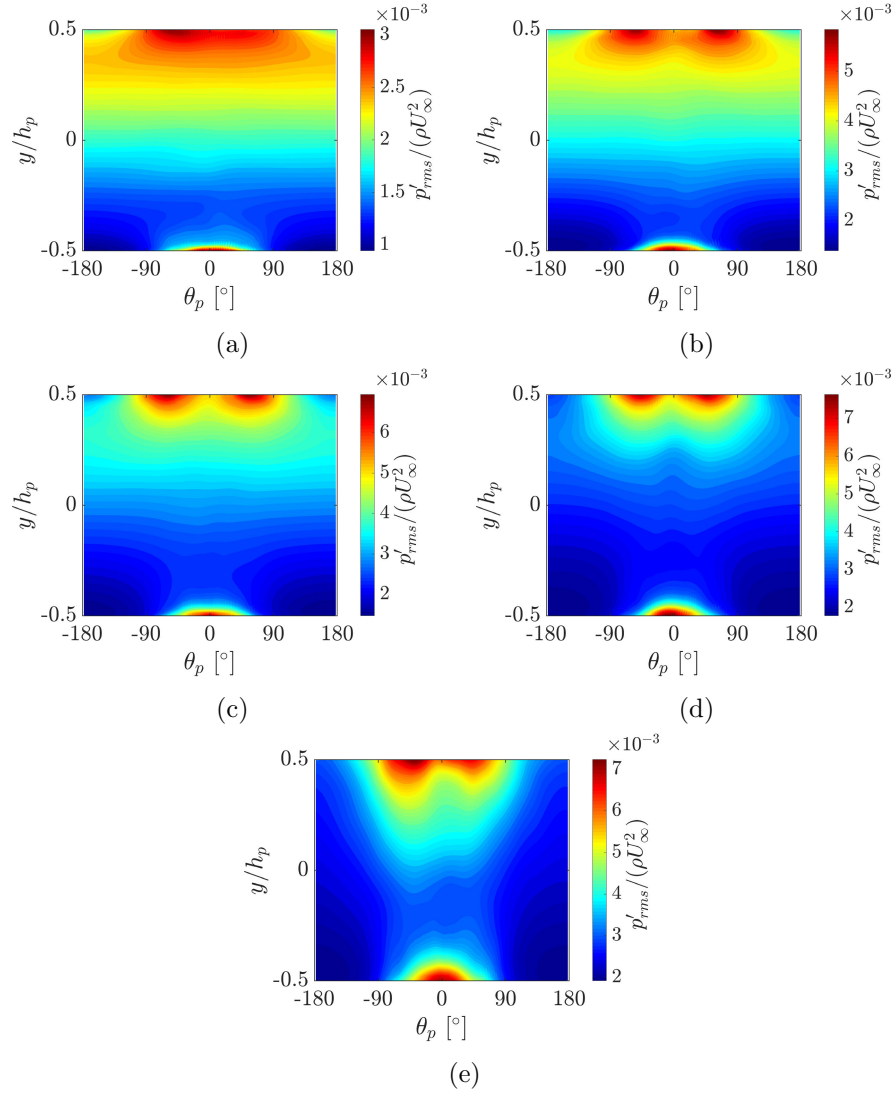


Figure 6.42: Contours of the normalised RMS of wall pressure fluctuations bandpass-filtered within frequency region R_h in pores (a) PR1, (b) PR2, (c) PR3, (d) PR4 and (e) PR5.

ure 6.18). Since the dipole sources of aerodynamic noise are directly related to the unsteady surface pressure [196], the distribution of surface pressure fluctuations can indicate the locations where the flow structures contribute the most to the dipole noise sources. Figures 6.41 and 6.42 present the spatial distributions of root mean square (RMS) of the bandpass-filtered (within R_l and R_h) pressure fluctuations $p'_{rms}/\rho U_\infty^2$ at the wall of pores PR1–PR5. The spatial distribution results are presented in a cylindrical coordinate system, where the radial location $r_p = d_p/2$ (pore wall location), θ_p is the azimuth angle and y/h_p is the vertical location normalised by the local pore height h_p (distance from pressure surface to suction surface). For the results presented in Figures 6.41 and 6.42, locations $\theta_p = 0$ and $\theta_p = 180^\circ$ correspond to the downstream and upstream locations of the pore

wall, and locations $y/h_p = -0.5$ and $y/h_p = 0.5$ correspond to the locations of the pressure surface and suction surface, respectively. For the results filtered within frequency region R_l (Figure 6.41), the highest magnitude of p'_{rms} appears at a region near the junction of the downstream pore wall and the pressure surface ($\theta_p = 0$, $y/h_p = -0.5$) between azimuth angle $\theta_p = -45 - 45^\circ$. On the wall of pores PR2–PR5, a second region of high p'_{rms} magnitude appears near the suction-side downstream wall junction ($\theta_p = 0$, $y/h_p = 0.5$). For the results filtered within the frequency region of broadband noise increase R_h (Figure 6.41), the region near the suction-side downstream wall junction ($\theta_p = 0$, $y/h_p = 0.5$) between azimuth angle $\theta_p = -90 - 90^\circ$ becomes the dominant dipole source region, showing a significantly higher magnitude of p'_{rms} compared to regions near the pressure surface. The high-level pressure fluctuations in these regions could arise from the impingement of upstream turbulence and edge-induced flow separation [196]. Moreover, in pores PR2–PR5, the high-magnitude region near the suction surface develops into two sub-regions symmetrical to each other, which indicates that the edge-induced flow separation is intensified as the flow develops further downstream.

Figures 6.43 and 6.44 present the normalised RMS of the bandpass-filtered (within R_l and R_h) wall pressure fluctuations $p'_{rms}/\rho U_\infty^2$ on the suction surface of the porous and reference TEs. Note that p'_{rms} in the voids (regions within the black circles) is calculated using air pressure fluctuations instead of wall pressure fluctuations. For both frequency regions, the results of porous TE show a significantly higher level of wall pressure fluctuations compared to the reference TE. Starting from the downstream of the first column of

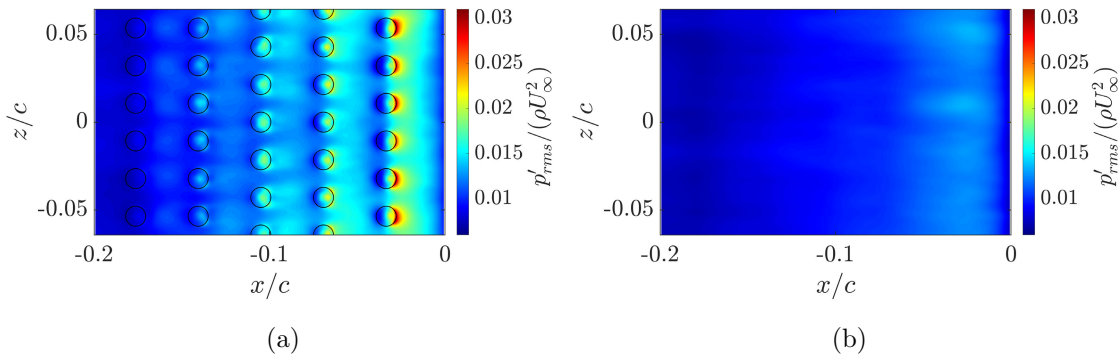


Figure 6.43: Contours of the normalised RMS of wall pressure fluctuations bandpass-filtered within frequency region R_h on the suction surface of the (a) porous and (b) reference TEs. Locations of the pore are marked by black circles.

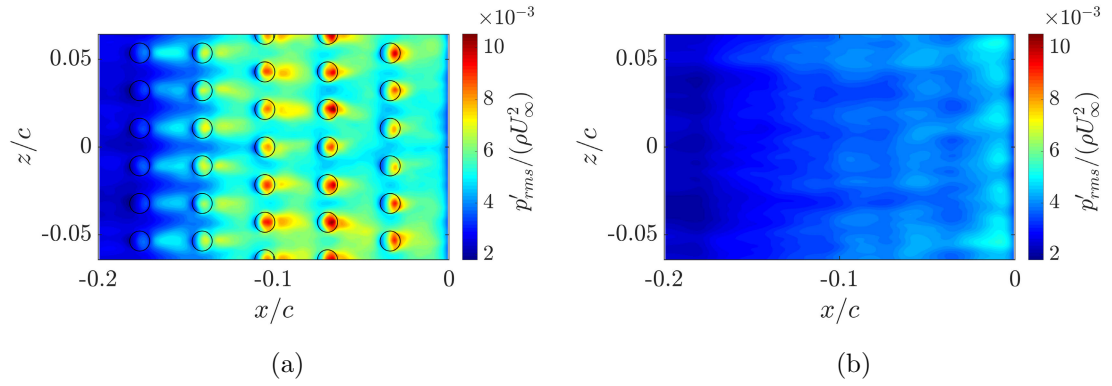


Figure 6.44: Contours of the normalised RMS of wall pressure fluctuations bandpass-filtered within frequency region R_h on the suction surface of the (a) porous and (b) reference TEs. Locations of the pore are marked by black circles.

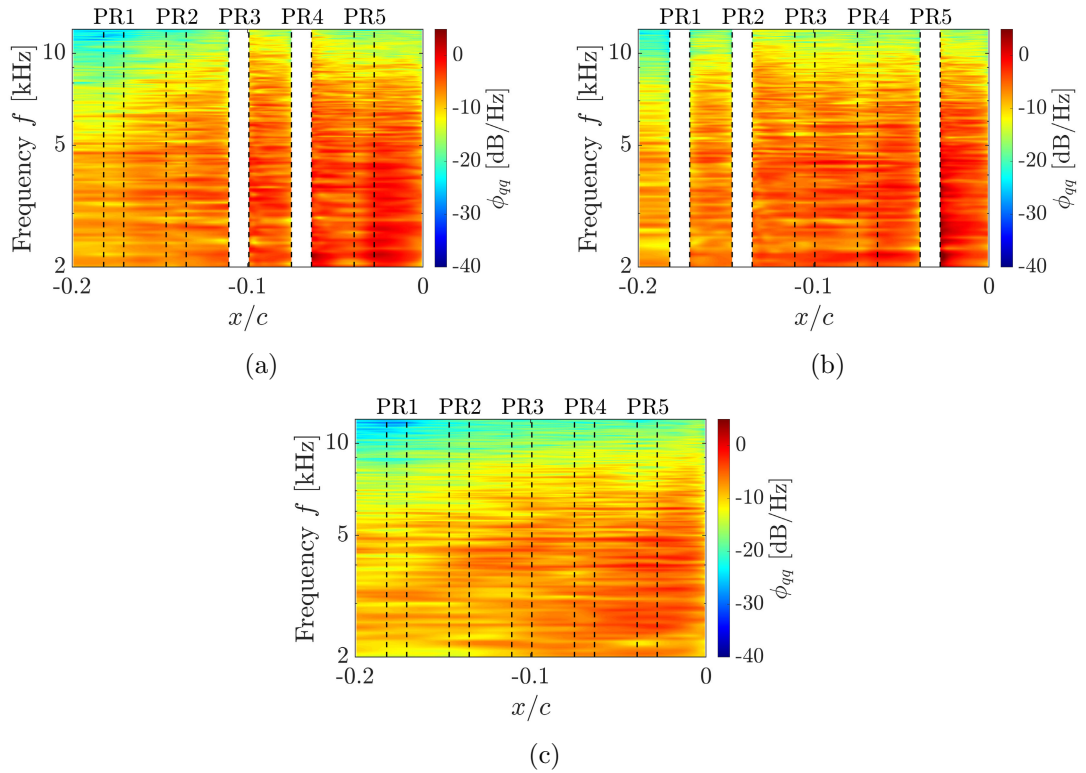


Figure 6.45: Contours of the power spectral density of wall pressure at different streamwise locations on the suction surface of the porous TE at spanwise locations (a) PL1 and (b) PL2; and (c) the reference TE at PL1. The Locations of pores PR1–PR5 are marked by black dashed lines, and locations of PL1 and PL2 are illustrated in Figure 6.21.

pores, high levels of p'_{rms} appear at the vicinity of the pore suction-side TE and the suction surface downstream of the pores. For frequency region R_h , locations of the highest p'_{rms} are shifted from the suction surface to the void near the pore suction-side TE, which illustrates the contribution of flow permeation to the broadband noise increase. The results of p'_{rms} on the pore walls and suction surface suggest that the broadband noise increase of

the porous TE originates from the interactions between the pore suction-side TE and turbulence from the upstream boundary layer and pore flow permeation. Figure 6.45 shows the results of wall pressure power spectral density on the suction surface of the porous and reference TEs at different streamwise locations. An increase in the level of wall pressure fluctuation is observed at locations immediately downstream of the pores over the entire frequency range from 2–12 kHz. The highest level of the increase occurs at the frequency region R_h (7.8–11 kHz), further indicating that the excessive high-frequency noise is likely attributed to the unsteady flow permeation and pore TE geometry.

6.5 Summary

This chapter has summarised results of the flow characteristics around the porous and serrated TEs investigated in this study, which includes: experimental results of flow measurements in UAT Campaign 1a and UAT Campaign 1b, and numerical simulation results of LES Case 1 and LES Case 2.

In UAT Campaign 1a, both mean and fluctuating velocity measured in the near wake of different novel TE extensions (attached to a naturally-transitioned NACA 0012 airfoil) vary significantly, illustrating that the spanwise-variant edge geometries have altered the flow structure at the TE. Moreover, both the frequency and intensity of the peaks in the velocity spectra are highly correlated with the LBL-TE noise measured in the far-field. This indicates that a reduction of LBL-TE noise by novel TE extensions is achieved by altering the flow structures related to the amplification of T-S waves. In addition, the boundary layer profile measured at 1 mm upstream of the TE extensions is almost identical to that of the baseline extension. This suggests that the effects of the TE extension on the development of the upstream boundary layer are insignificant.

In UAT Campaign 1b, where TE extensions are attached to a forced-transitioned NACA 0012 airfoil, flow characteristics in a near-wake plane are characterised in terms of mean velocity, turbulence intensity and turbulence integral length scale. Near-wake mean velocity profiles and velocity distributions in the near-wake plane have revealed the existence of turbulent flow traveling from the pressure surface to suction surface, which is likely induced by the permeable porous geometries for the extension P and the serrated

geometries adjacent to the tip of a serration for serrated extensions NS and CS. However, the gradually varying porous geometries of serrated-porous extension CSP only has a minor effect on mean velocity and turbulence intensity, showing a spatial distribution comparable to that of the straight baseline extension. The integral length scale in the inner region of the near wake (vicinity of edges) is reduced by all treated extensions, which may arise from their complex porous geometries or serrated sharp edges, breaking up large turbulent eddies into smaller scales. Moreover, a noise intensity factor is proposed to account for the effects of turbulence intensity, integral length scale and mean velocity on TBL-TE noise generation. This noise intensity factor can be used to identify the contribution of local flow characteristics to the TBL-TE noise generation. Moreover, the integral of noise intensity factor over the near-wake plane has shown a good consistency with TBL-TE noise results for different TE extensions presented in Sec. 5.3. This integration approach can account for the spanwise-variations induced by treated edge geometries, and relate the effects of treated TE extensions on near-wake velocity statistics to their TBL-TE noise reduction.

In the LES simulations, flow around the straight (LES Case 1) and porous (LES Case 2) TEs of a forced-transitioned NACA 0012 airfoil at $\alpha = 5^\circ$ and $U_\infty = 50$ m/s have been simulated. The far-field noise levels predicted by FWH acoustic analogy are in a reasonably good agreement with experimental data, showing a prediction error of less than 5 dB over 2 to 8 kHz. The frequency regions of noise reduction and increase by the porous TE have been accurately captured by FWH predictions. The predicted noise directivity pattern reveals that the porous TE reduces the strength of TBL-TE noise without significantly changing its radiation pattern at 1.6, 2 and 4 kHz. At higher frequencies ($f > 5$ kHz), the noise directivity has been significantly changed by porous TE, likely due to the effects of additional noise sources associated porous geometries. Moreover, high-vorticity turbulent flow is observed to travel through the porous geometries from the pressure surface to suction surface. As a result, the magnitude of Reynolds normal-stress is increased near the junction of the pore wall and suction surface. However, the strength of the acoustic source term related to Reynolds shear-stress in the vicinity of the TE is significantly reduced. Furthermore, the wall pressure fluctuation results illustrate that the spanwise correlation length and convection velocity, as components of the source terms in many analytical models for TBL-TE noise [4, 6, 162, 179], have also been significantly

reduced in the TE region due to the flow perturbations propagating through the pores. This is considered to be the main reason for the TBL-TE noise reduction by the porous TE. Finally, the RMS of wall pressure fluctuations on the pore walls and suction surface suggest that the high-frequency broadband noise originates from the interactions between the pore suction-side TE geometries and the turbulence from upstream boundary layer and pore flow permeation.

Chapter 7

Rotor Noise Reduction using Porous and Serrated Trailing-Edge Treatments

7.1 Overview

The main purpose of this chapter is to evaluate the aeroacoustic performance of the proposed porous trailing edge (TE) as a rotor application. The geometry of the porous TE is determined by the acoustic characterisation experiments as described in Chapter 4. A rotor with a NACA 0012 profile, 0.07 m constant chord and 1.04 m diameter has been characterised as the reference case for turbulent boundary layer trailing-edge (TBL-TE) noise and laminar-transitional boundary layer trailing-edge (LBL-TE) noise comparisons. The noise attenuation capability of the porous TE is compared with that of a recently proposed cut-serrated TE [45] and the well-known extended-serrated TE, which has been applied in the wind turbine industry for TBL-TE noise reduction [149]. Details of the facility, measurement setup and signal processing methods have been described in Sec. 3.4.

This chapter is structured as follows. First, the sound map results obtained from conventional beamforming (details in Sec. 3.3.3), phase-averaged beamforming (details in Sec. 3.4.3) algorithms PABF 1 and PABF 2 are presented in Sec. 7.2. The most dominant noise sources at various frequencies were localised using PABF 2. This information, together with the BPM predictions presented in Sec. 7.3, are used to determine the frequency range for TBL-TE noise comparisons. In Sec. 7.3, the noise spectra obtained by integrating the sound pressure over the dominant source region in the beamforming

sound maps, have also been presented. The noise attenuation capability of the tested TE treatments are then quantified from these noise spectra. After that, Sec. 7.4 discusses the potential effects of the porous structures' sound absorption on TE noise attenuation. Finally, the aeroacoustic performance of the treated blades and their effect on TBL-TE noise and LBL-TE noise are summarised in Sec. 7.5.

7.2 Beamforming Sound Maps

Three beamforming methods: Conventional Beamforming (CBF), Phase-Averaged Beamforming Method 1 (PABF 1) and Method 2 (PABF 2) have been adopted to analyse the data acquired in the rotor rig experimental campaign. The formulation of these beamforming algorithms have been presented in Secs. 3.3.3 and 3.4.3. In this section, the case of forced-transitioned blades operating at a pitch angle of 5° and RPM of 900 has been chosen to demonstrate the performance of the beamforming algorithms and the noise source localisation of the rotor trailing-edge (TE) treatments tested in this thesis. The details of the measurement setup have been described in Secs. 3.4.1 and 3.4.2.

Figure 7.1 presents a comparison of the beamforming maps for the reference blades processed using CBF, PABF 1 and PABF 2 at two selected frequencies of 4kHz and 8kHz. All beamforming maps are shown with a dynamic range of 8 dB for ease of comparison. As the rotor test rig and surrounding room were not acoustically treated for this measurement campaign, the acoustic data were acquired using the 64-channel microphone array in a reverberant environment. Consequently, the sound maps processed using CBF are extremely noisy with numerous side lobes at certain frequencies, such as 4 and 8 kHz as shown in Figures 7.1a and 7.1b. However, beamforming methods PABF 1 and PABF 2 use phase-averaging to de-rotate the sound map results to a specific range of angles around the angle of rotation of interest ($\theta_i + [-5^\circ, 5^\circ]$) and perform considerably better than CBF. The reverberation background noise sources have been effectively removed, and the dominant noise sources have been quantified and localised at the blade tip region, especially for PABF 2, as shown in Figures 7.1c–7.1f. The difference in noise levels for PABF 1 and PABF 2 is due to the discrepancy in their background-noise-removal capability. When the rotor is operating in the octagonal test-section, the rotor blades are the dominant noise source, generating and emitting aerodynamic noise according to a certain directivity pattern. In comparison, the directivity of the background noise in a reverberant environment is arbitrary. The phase-averaged beamforming methods manipulate the entire data record into several small data segments corresponding to the rotational angles of interest ($\theta_i + [-5^\circ, 5^\circ]$) for phase averaging. The variation in directivity of the aerodynamic noise sources between data segments is negligible, while the background noise sources are uncor-

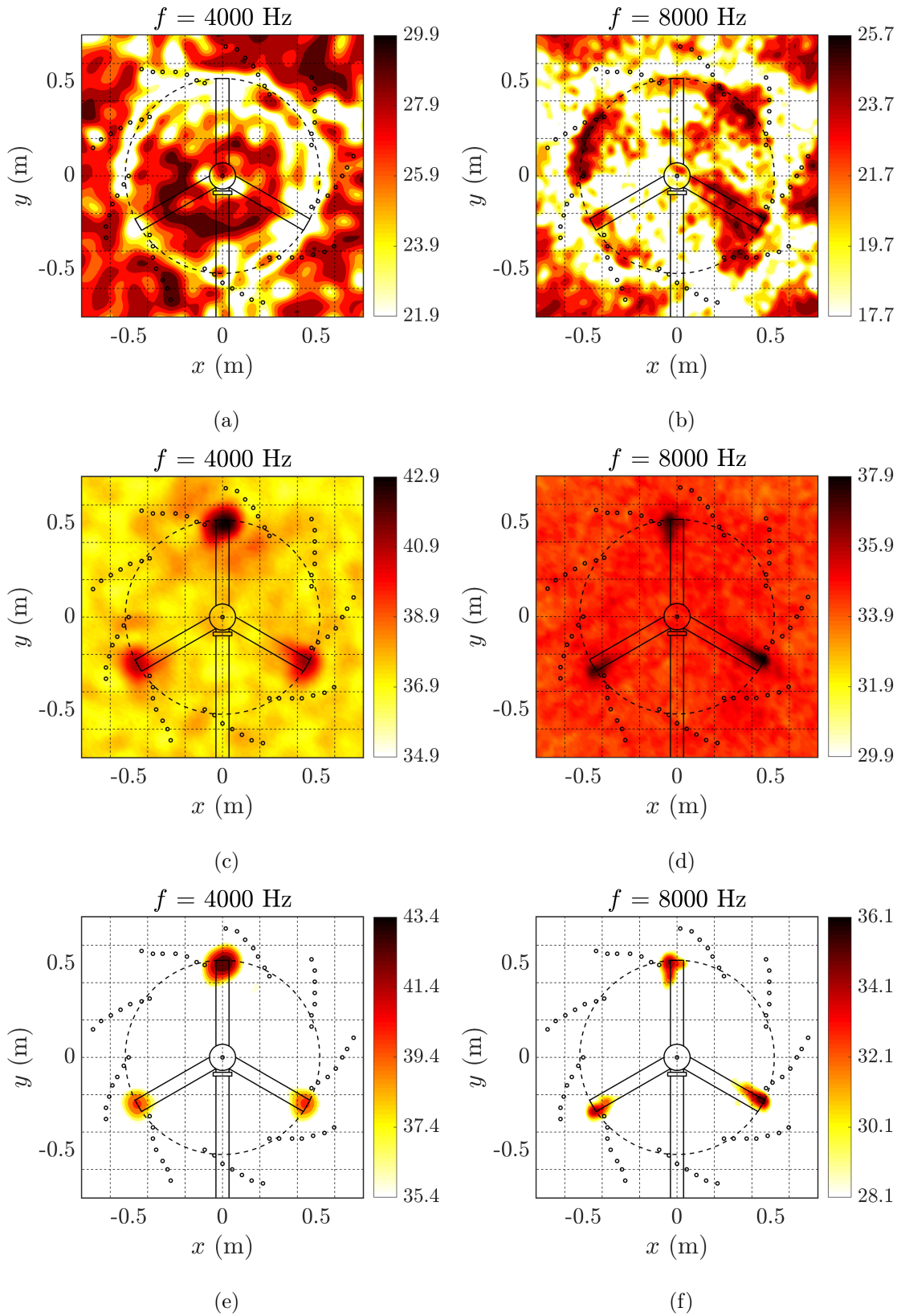


Figure 7.1: One-third-octave band beamforming maps at 4 kHz and 8 kHz for reference blades at RPM of 900 and pitch angle of 5°. Each row corresponds to the results processed by (a, b) CBF, (c, d) PABF 1 and (e, f) PABF 2 .

related between data segments. The phase-averaging process helps filter the uncorrelated signals, producing improved sound maps. Moreover, PABF 2 can better distinguish the major aerodynamic noise sources from the background noise, compared to PABF 1 (see Figures 7.1c–7.1f). This is because PABF 2 builds the cross-spectral matrix to account for the coherence between the data records taken from different microphones in the array, contributing to the filtering of uncorrelated acoustic signals and consequently, further dereverberation of the beamforming maps. In this chapter, acoustic data are processed using PABF 2.

Figure 7.2 shows the one-third-octave band sound maps at frequencies of 4, 5.04, 6.35 and 8 kHz for reference blades operating at 900 RPM and 5° pitch angle. In general, the location of maximum noise level moves from blade leading edge (LE) to TE as the frequency increases. The dominant noise source is clearly identified at either LE or TE at frequencies higher than 5.04 kHz. However, it is still difficult to determine the dominant noise source location at 4 kHz due to the large beamwidth of the sound map. Table 7.1 summarises the frequencies when the sound map shows higher noise levels at the TE of forced-transitioned reference blade, which correspond to $f \geq 6.35$ kHz for the scenario shown in Figure 7.2. These results can provide useful information to determine the frequency range for TBL-TE noise comparisons.

Table 7.1: TE-noise-dominant frequency range f_{TE} for the forced-transitioned reference blade.

RPM	800			900		
Pitch angle $[\circ]$	0	5	10	0	5	10
f_{TE} [Hz]	≥ 5040	≥ 5040	≥ 5040	≥ 5040	≥ 6350	≥ 5040

In Figure 7.3, the phase-averaged beamforming maps at 6.35 kHz for the reference blade (Ref) and blades with porous (P), cut-serrated (CutS) and extended-serrated (ExtS) TEs, are presented as a typical example of TBL-TE noise comparison. The geometries of these blades have been described in Sec. 3.4.2. The dynamic range of the beamforming maps for the blades with TE treatments have been adjusted to match that of the blade Ref for comparison. The major noise sources for all blades are located in the blade tip region. The highest noise levels are produced along the blade TE for blades Ref and P. Blade P shows a similar noise source distribution pattern to that of blade Ref but yields a lower

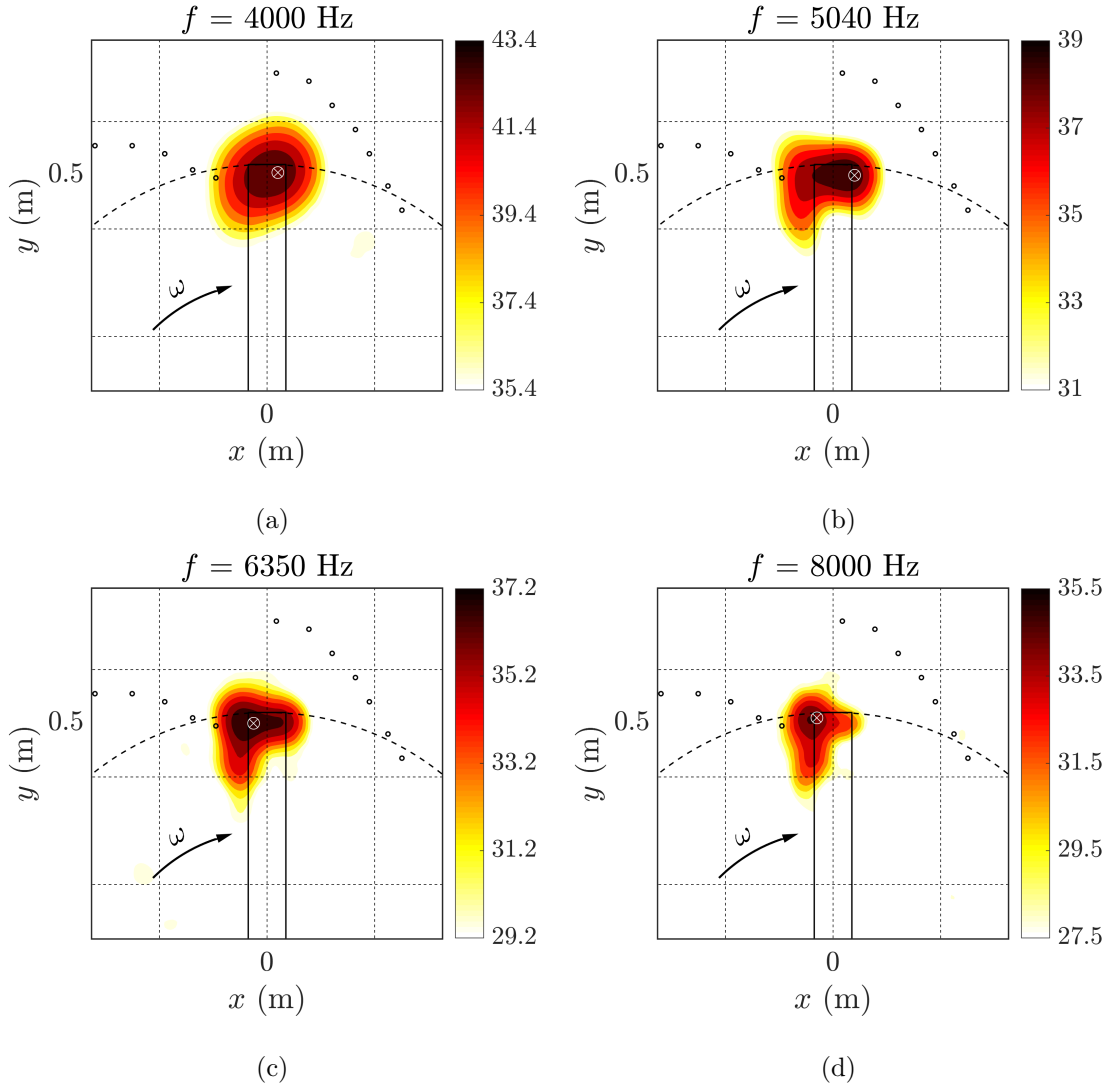


Figure 7.2: One-third-octave band beamforming maps at $f_{1/3} =$ (a) 4 kHz, (b) 5.04 kHz, (c) 6.35 kHz and (d) 8 kHz processed by PABF 2 for forced-transitioned blades Ref operating at RPM of 900 and pitch angle of 5° . The location of maximum noise level is marked by a white circle-cross symbol.

noise level. For serrated blades CutS and ExtS, the highest noise levels are located at the blade LE-tip corner. According to their noise source distribution, both blades reduce the TE noise in-board of the blade tip. CutS also significantly reduces the noise at the TE-tip corner, so that the LE noise component becomes dominant. Although ExtS is efficient in TE noise reduction over the blade in-board region, its LE-tip corner displays the strongest noise source among these sound maps. This may be due to the interaction between the tip vortices and the extended-serrated geometries, which alters the flow characteristics (turbulence intensity, turbulence length scale, etc.) in the wake, giving rise to a higher level of LE-turbulence-interaction noise. It is also possible that the additional lift due to

the longer chord of ExtS alters the local flow conditions (local angle of attack, induced velocity, inflow velocity, etc.), thereby affecting the LE noise generation. Furthermore, the acoustic performance of blades P and CutS are generally consistent over the operating conditions tested in this study. However, the increase in LE noise level for ExtS is only observed at two operating conditions: $\text{RPM} = 800$, $\alpha_{pi} = 10^\circ$; $\text{RPM} = 900$, $\alpha_{pi} = 5^\circ$. A comprehensive spectral analysis for all tested operating conditions will be presented and further discussed in the next Sec. 7.3.

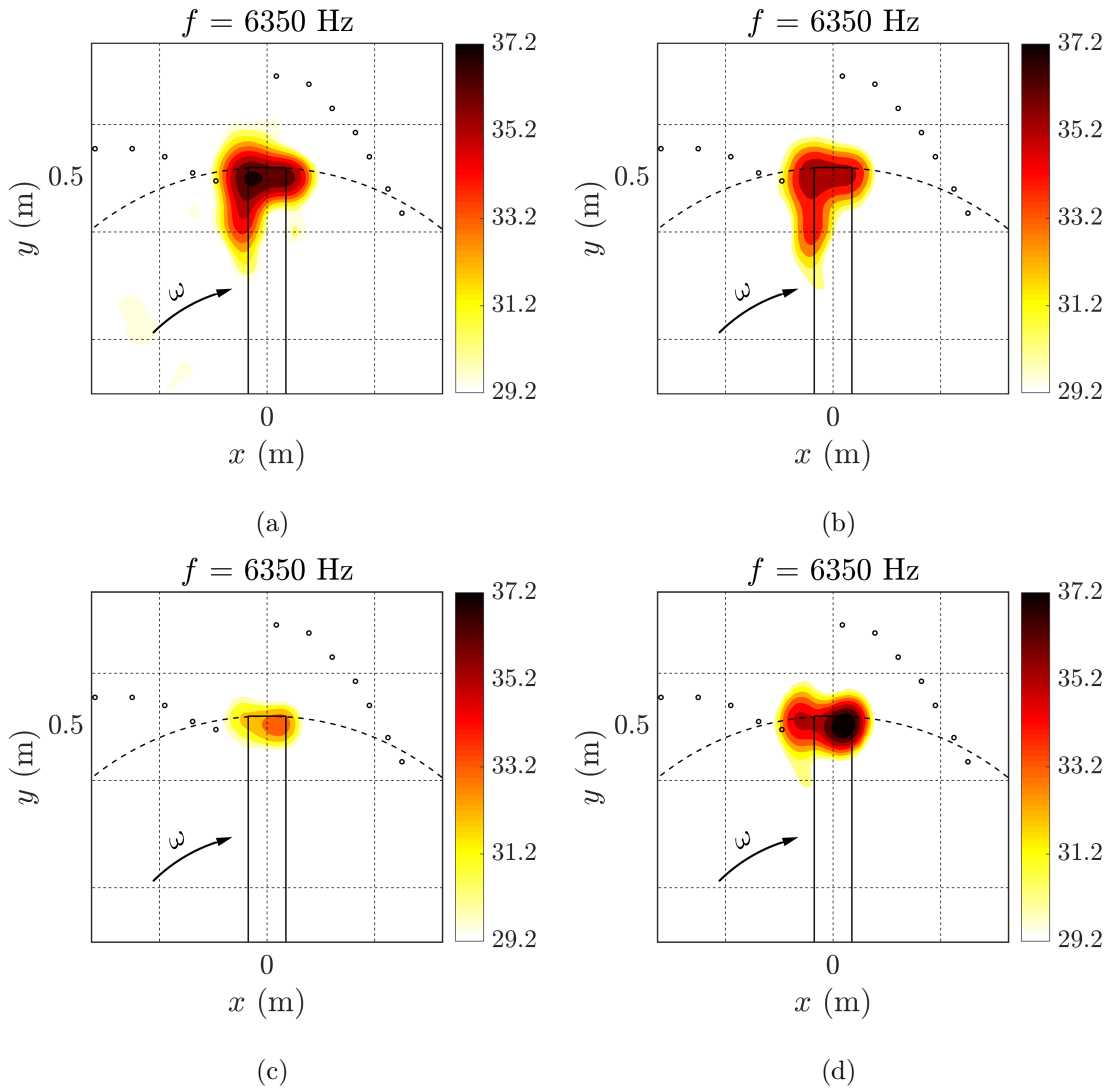


Figure 7.3: One-third-octave beamforming maps at 6.35 kHz processed by PABF 2 for forced-transitioned blades (a) Ref, (b) P, (c) CuS and (d) ExtS operating at RPM of 900 and pitch angle of 5° .

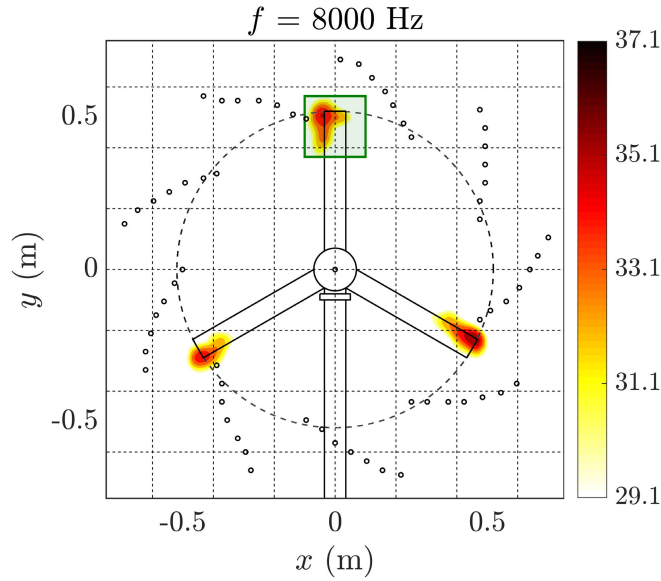


Figure 7.4: Integration region (marked in green rectangle) of rotor beamforming maps.

7.3 Noise Spectra Results

As shown in the beamforming sound maps (Figures 7.1–7.3), the tip region of the rotor blades generates the highest level of TBL-TE noise as it encounters higher incoming flow velocity U_∞ compared to the region much further in-board of the tip. The level of TBL-TE noise theoretically scales with U_∞^5 [190], which means that the TBL-TE noise emitted from the in-board region near to the hub has a much lower level compared to that in the tip region. Therefore, the phase-averaged sound maps are integrated over the tip region (as shown in Figure 7.4) using the source integration method (as described in Sec. 3.3.3) to obtain the one-third-octave band noise spectra for rotor blades Ref, P, CutS and ExtS.

Due to the complexity of the flow environment around the rotor blades, multiple noise sources are generated and dominate at various frequency ranges. For the forced-transition rotor blades investigated in this study, the major noise sources are: (1) blade-tower interaction noise, steady and unsteady loading noise, and thickness noise over low frequencies (up to 0.5 kHz) as discussed in previous rotor noise studies [197, 199]; (2) LE-turbulence-interaction noise over medium frequencies (0.5 to ~ 5 kHz) and (3) TBL-TE noise over high frequencies (~ 5 to 12 kHz). In order to compare the TE noise attenuation capability of TE treatments, it is necessary to identify the TE-noise-dominant frequency range

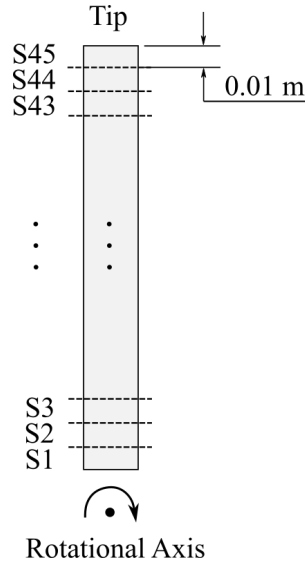


Figure 7.5: Sketch of the rotor blade segmentation.

for the reference blades. As discussed in Sec. 7.2, locations of the dominant noise source at higher frequencies (above 5 kHz) have been determined from the beamforming sound maps. However, the sound maps at lower frequencies (below 5 kHz) fail to accurately localise the dominant noise source to blade edges due to its large beamwidth with respect to blade chord. Therefore, the BPM model[31], which has been proven to be adequate for TBL-TE noise prediction[57, 58, 198], is adopted to predict the level and frequency characteristics of TBL-TE noise for blade Ref. This prediction can provide further indication for determining the frequency range for TE noise comparisons, especially for the data at frequencies below 5 kHz.

The input parameters of the BPM model include local angle of attack, inflow velocity and TE boundary layer displacement thickness. To calculate these values along the blade, a Blade Element Momentum Theory (BEMT) approach [109] is used. The NACA0012 rotor blade is divided into 45 blade segments along the radial direction, and each segment has a radial span of 0.01 m (as shown in Figure 7.5). The local aerodynamic conditions for each segment are obtained by BEMT, in which the rotor model is treated as a hovering rotor. For TBL-TE noise estimation, the BPM model is applied to the segments near the blade tip, corresponding to the source integration region in Figure 7.4. Considering the velocities locally induced by the trailing tip vortices, Prandtl's tip loss function is incorporated into the BEMT solver to increase accuracy.

Figure 7.6 illustrates the local aerodynamic environment of a blade segment, in which

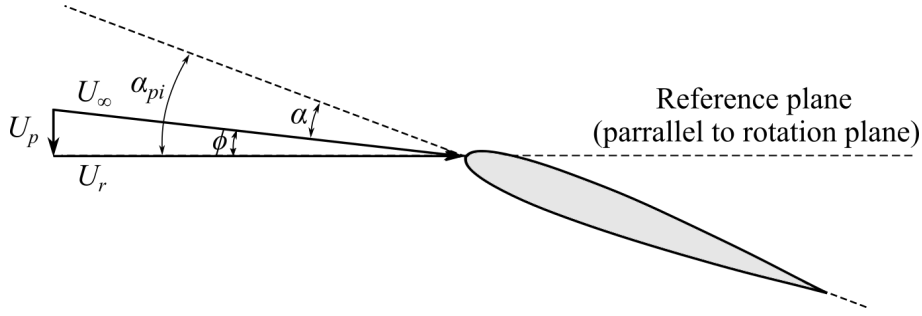


Figure 7.6: Schematic of the local aerodynamic environment of a blade segment.

α_{pi} is the local pitch angle, ϕ is the induced inflow angle, U_p is the induced velocity normal to the rotation plane, U_r is the rotational velocity at radius r , U_∞ and α are the effective inflow velocity and angle of attack. The tip loss effects are taken into account by introducing a correction factor F , which can be determined by

$$F = \left(\frac{2}{\pi}\right) \cos^{-1}(\exp -f), \quad (7.1)$$

$$f = \frac{N_b}{2} \left(\frac{1 - \bar{r}}{\bar{r}\phi} \right), \quad (7.2)$$

$$\bar{r} = r/R_t, \quad (7.3)$$

where N_b is the number of blades, r the local radius of the blade segment, R_t is the rotor radius and \bar{r} is the non-dimensional radial position of the blade segment. The tip loss function F is then incorporated into BEMT as a reduction factor applied to the change in fluid velocity. The induced inflow angle ϕ can be calculated by

$$\phi = \frac{\sigma C_{l\alpha}}{16F\bar{r}} \left(\sqrt{1 + \frac{32F\alpha_{pi}\bar{r}}{8F}} - 1 \right), \quad (7.4)$$

where $C_{l\alpha}$ stands for the local aerodynamic loading defined as the slope of local lift coefficient to angle of attack ($C_{l\alpha} = \partial C_l / \partial \alpha$), and σ is the blade solidity defined by

$$\sigma = \frac{N_b c}{R_t \pi}, \quad (7.5)$$

where c is the local blade chord length. Since F is a function of ϕ , the induced angle ϕ is calculated numerically through iterations over Eqs. (7.1)–(7.5). For the first iteration, Eq. (7.4) is solved by the initial input of $F = 1$, then ϕ from Eq. (7.4) is substituted into

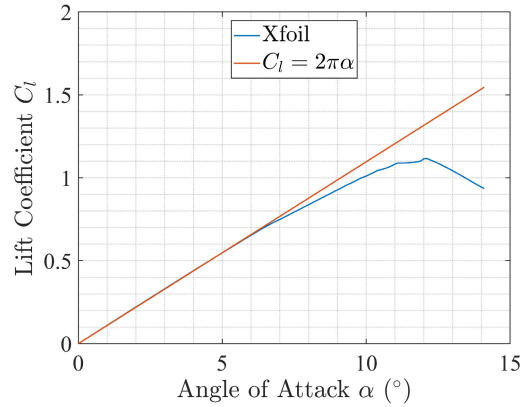


Figure 7.7: Lift coefficient estimations using Xfoil for a NACA0012 blade segment (tripped at 10% chord) at $Re_c = 2.08 \times 10^5$ in comparison with thin airfoil approximation.

Eqs. (7.1) and (7.2) to recalculate tip loss correction factor F until the numerical solution is converged. The convergence criteria of residual for F is set to 10^{-3} . The numerical solution usually converges rapidly and within 10 iterations. Once F is determined, the induced angle ϕ can be calculated from Eq. (7.4) accordingly. The local effective angle of attack α and inflow velocity U_∞ are then determined by

$$\alpha = \alpha_{pi} - \phi, \quad (7.6)$$

$$U_\infty = U_r / \cos \phi. \quad (7.7)$$

During the iterations, the aerodynamic loading $C_{l\alpha}$ is assumed to be 2π , which is an approximation for a thin airfoil. Figure 7.7 shows results of the lift coefficient as a function of angle of attack for a NACA0012 blade tip segment ($Re_c = 2.08 \times 10^5$) estimated by Xfoil [59] in comparison with the thin airfoil approximation ($C_{l\alpha} = 2\pi$). In the Xfoil estimation, the boundary layer transition point is set at 10% chord on both sides of the airfoil, which is consistent with the tripping location in the experiment. The slope of the lift coefficient shows excellent agreement with the thin airfoil approximation for angles of attack of up to 6° (the error of C_l is less than 1%). The BEMT results under this assumption for the forced-transitioned reference blade at pitch angles of 5° and 10° are presented in Figure 7.8, which shows that the effective angles of attack along the blade radius for both pitch angles are lower than 6° (Figure 7.8a). This have further demonstrated the applicability of the 2π assumption for aerodynamic loading $C_{l\alpha}$.

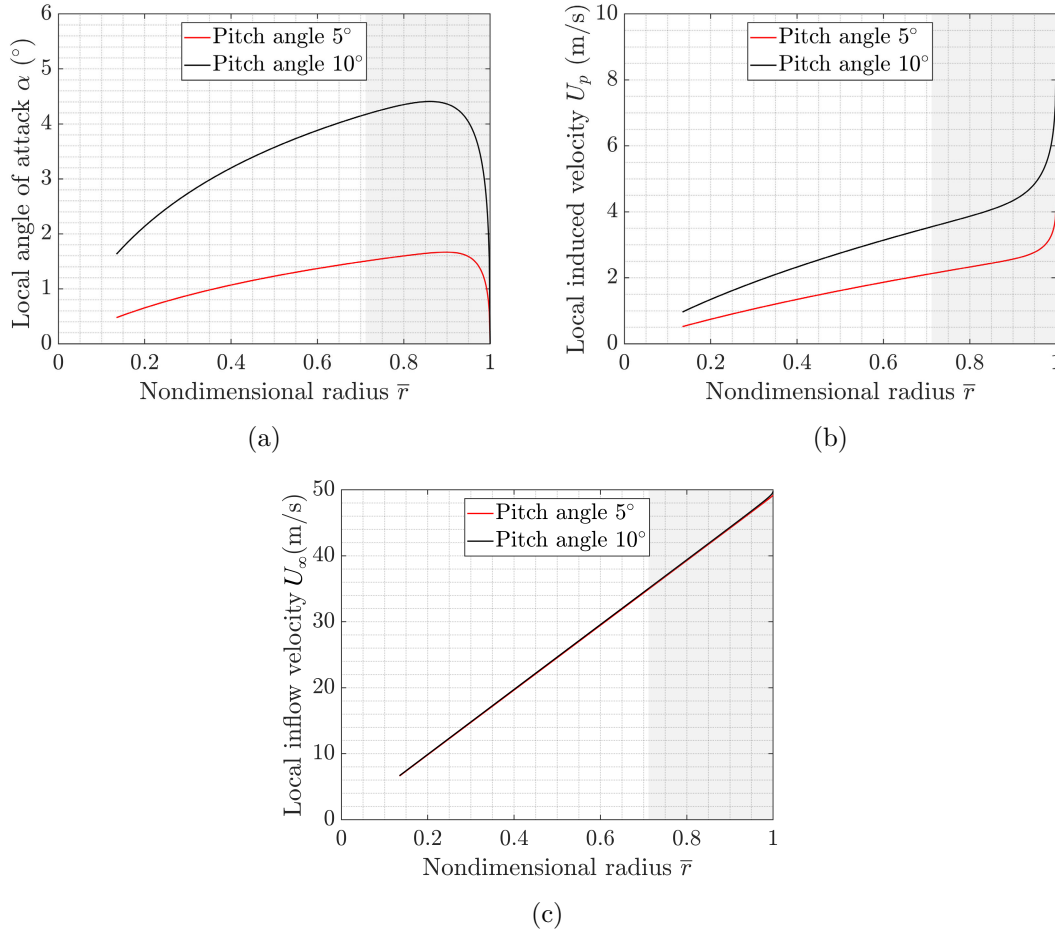


Figure 7.8: BEMT results for the forced-transitioned reference blade at RPM of 900 and pitch angles of 5° and 10°: (a) local angle of attack, (b) induced velocity and (c) inflow velocity (data used for BPM predictions are marked in grey).

The BEMT results of local angle of attack α and inflow velocity U_∞ at the blade tip region (marked in grey in Figure 7.8) are used for BPM prediction of TBL-TE noise. To account for the turbulence development over the local blade segment, the TE displacement boundary layer thickness δ^* , as another input parameter of BPM TBL-TE noise model, is estimated using Xfoil and the local BEMT results. The total TBL-TE noise prediction is then obtained by summing the local BPM prediction for each blade segment within this region. The tip vortex formation noise is estimated using BPM flat-tip noise model. The averaged angle of attack over the outermost 2% of the blade ($0.98 \leq \bar{r} \leq 1$) is used as the input for tip noise predictions. Figure 7.9 shows the results of the BPM prediction and integrated noise spectra for the tip region of blade Ref operating at an RPM of 900 and pitch angles of 0°, 5° and 10°. The TE-noise-dominant frequency range f_{TE} determined by the beamforming maps (as presented in Table 7.1) are marked in grey. The results of the

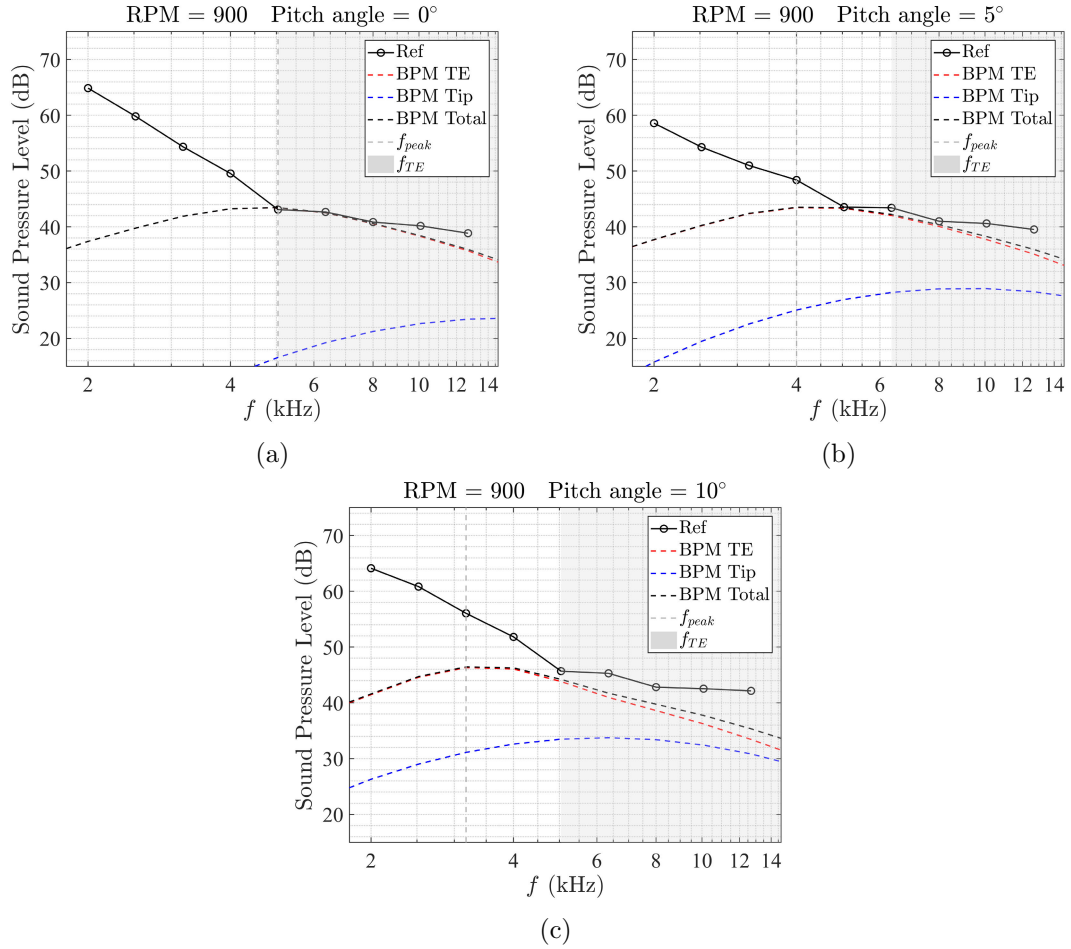


Figure 7.9: BPM noise prediction compared with the integrated one-third-octave noise spectra for reference blade at RPM of 900 and pitch angles of (a) 0°, (b) 5° and (c) 10° (The TE-noise-dominant frequency range determined from the beamforming sound map is marked in grey).

integrated spectra and BPM predictions for pitch angles of 0° and 5° show good agreement over f_{TE} , while a larger deviation is observed for the case of 10° pitch angle. The deviation is likely due to the BPM tip noise prediction underestimating the tip noise level as reported in [135]. As the pitch angle increases, the passage of turbulence over the TE of the blade tip will be intensified, generating higher levels of tip vortex formation noise. Therefore, the deviation between the BPM predictions and integrated spectra increase as the blade is set at a higher pitch angle. For frequencies below the peak frequency of the BPM prediction f_{peak} , the discrepancy between BPM prediction and measured noise spectra becomes considerably large (over 10 dB at $\alpha_{pi} = 5^\circ, 10^\circ$), indicating that TE noise is completely masked here. This frequency range is likely dominated by the LE-turbulence-interaction noise originating from the interaction between the blade LE and the impinging turbulence (see Figures 7.2a and 7.2b). For frequencies between f_{peak} and f_{TE} , the total

sound pressure levels are contributed from both LE and TE noise sources. The attenuation of TBL-TE noise over this frequency range will still give rise to noticeable changes in the total noise levels. Therefore, to account for all potential TBL-TE noise attenuation, the noise spectra at frequencies higher than f_{peak} are chosen to compare the TBL-TE noise performance of blades Ref, P, CutS and ExtS. Note that similar comparisons between BPM prediction and measured noise spectra are observed for 800 RPM, and the corresponding frequency range for TBL-TE noise comparison is determined using the same criteria.

Figure 7.10 presents the results of the noise attenuation performance for blades P, CutS and ExtS with forced-transitioned boundary layer. The region marked in grey indicates the frequency range that is dominated by the TBL-TE noise. The acoustic performance of these treated blades is quantified by the change in sound pressure level ΔSPL compared to that of blade Ref according to

$$\Delta SPL = SPL_{Ref} - SPL_{Treated} , \quad (7.8)$$

where SPL_{Ref} and $SPL_{Treated}$ refer to the integrated sound pressure levels of the reference blade and the blade with TE treatments, respectively. Figure 7.10 shows the CutS blades perform similarly for all operating conditions. They increase the noise levels by up to 10.9 dB at lower frequencies (up to 5 kHz) and reduce the high-frequency component (above 5 kHz) of TE noise by up to 8.4 dB. The significant noise increase observed is likely due to bluntness vortex-shedding noise originating from the blunt root of the cut serrations (as reported in [45] for a stationary cut-serrated airfoil). ExtS blades can achieve appreciable noise reductions of up to 9.2 dB over frequencies dominated by TE noise (marked in grey) for most operating conditions (as shown in Figures 7.10a, 7.10b, 7.10c and 7.10f). However, they produce an excessive noise level increase of up to 6.2 dB at lower frequencies (up to 6 kHz) when operating at 900 RPM, 5° pitch (Figure 7.10d) and 800 RPM, 10° pitch (Figure 7.10e). This noise increase may result from a higher level of LE-turbulence-interaction noise (see Figure 7.3d) caused by the extended-serrated geometries.

The beamforming map of ExtS at 900 RPM and 5° pitch angle has shown higher noise levels at the blade LE compared to the reference blade (as shown in Figures 7.3a and 7.3d). The porous blades show consistent noise reductions of up to 2.2 dB over lower frequencies (up to 6 kHz for 800 RPM and 7 kHz for 900 RPM) but an increase in noise level of up to 6.2

dB at higher frequencies. As reported in previous studies on porous TE treatments [35, 86], high-frequency noise increases are likely due to the excessive ‘roughness’ noise originating from the interaction between the TE boundary layer and the roughness elements produced by the porous geometries. Moreover, the serrated blades CutS and ExtS are found to be less effective in high-frequency TE noise reduction as the pitch angle increases, while the porous blade P becomes more efficient in low-frequency TE noise reduction when a pitch angle is present.

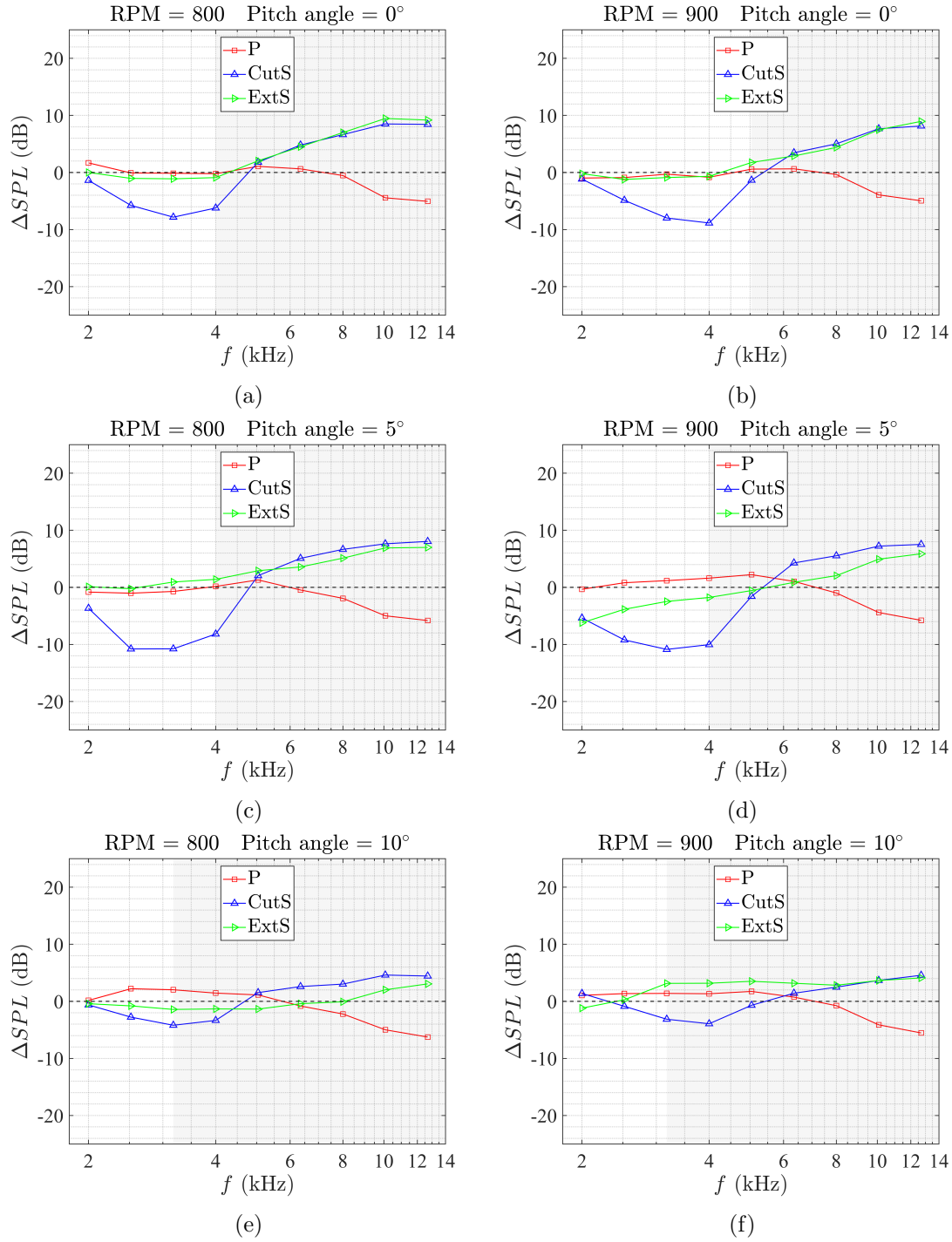


Figure 7.10: One-third-octave band noise reduction ΔSPL for forced-transitioned blades P, ExtS and CutS at 800 RPM: pitch angles of (a) 0°, (c) 5° and (e) 10°, and 900 RPM: pitch angles of (b) 0°, (d) 5° and (f) 10°. (the frequency range for TBL-TE noise comparison is marked in grey)

The range of Reynolds numbers based on chord $Re_c(1.4\text{--}2.3 \times 10^5)$ and effective angle of attack ($0\text{--}4.4^\circ$) for the blade tip region falls into the tonal envelope presented in [10, 122], where LBL-TE noise is likely to occur with natural boundary layer transition. Figure 7.11 shows the effects of boundary layer tripping on the TE noise generation for the reference blade at RPM of 900 and pitch angles of 0° , 5° and 10° . The noise level for the reference blade with natural-transition is significantly (up to 14.1 dB) higher than that of the forced-transition case due to the production of high-amplitude tonal LBL-TE noise. Data at frequencies where the naturally-transitioned blade yields higher noise levels (marked in grey in Figure 7.11) are adopted to evaluate the effects of blades P, CutS and ExtS on LBL-TE noise.

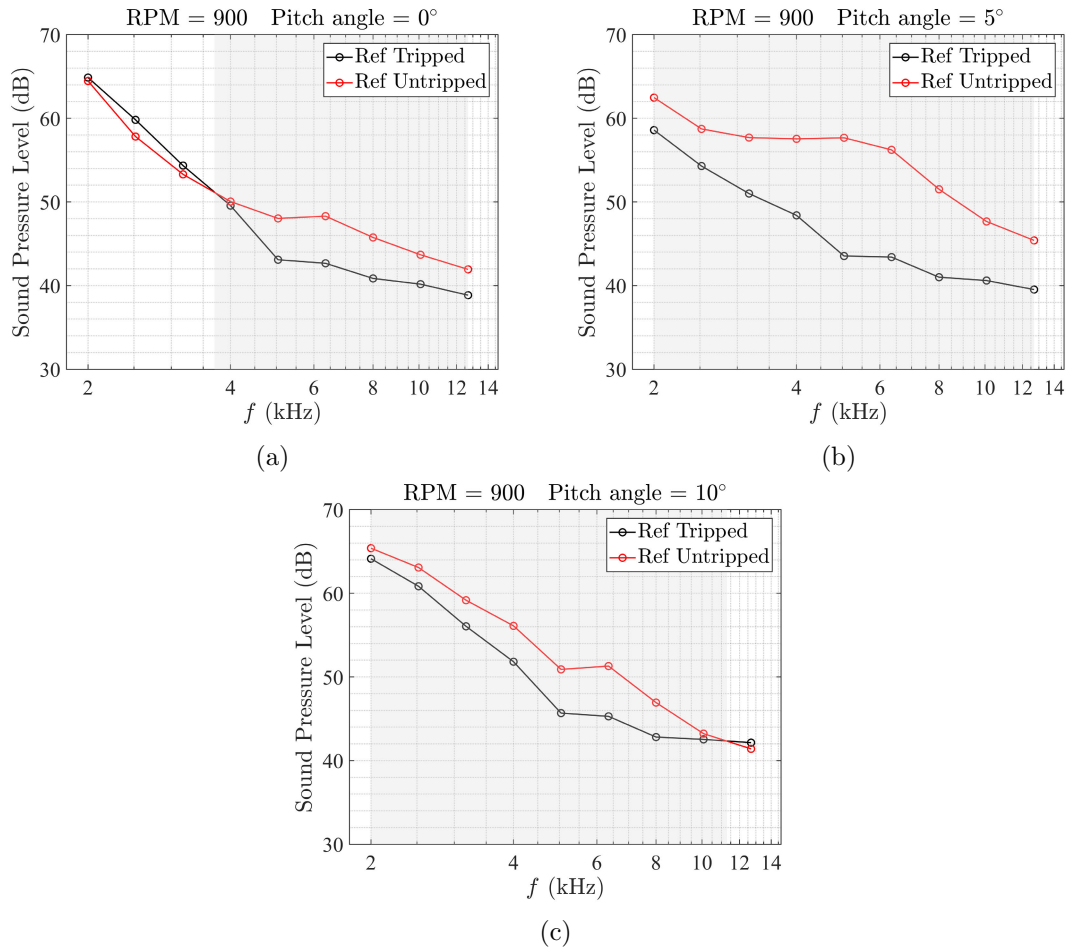


Figure 7.11: Integrated noise spectra in one-third-octave band for the reference blade with naturally and forced transitioned boundary layers at RPM of 900 and pitch angles of (a) 0° , (b) 5° and (c) 10° .

In Figure 7.12, the results of the noise attenuation performance ΔSPL of blades P, CutS and ExtS with naturally-transitioned boundary layer are presented. The grey region marked in this figure indicates the frequency range dominated by the LBL-TE noise (as determined from Figure 7.11). Similar to the forced-transitioned cut-serrated blade, the

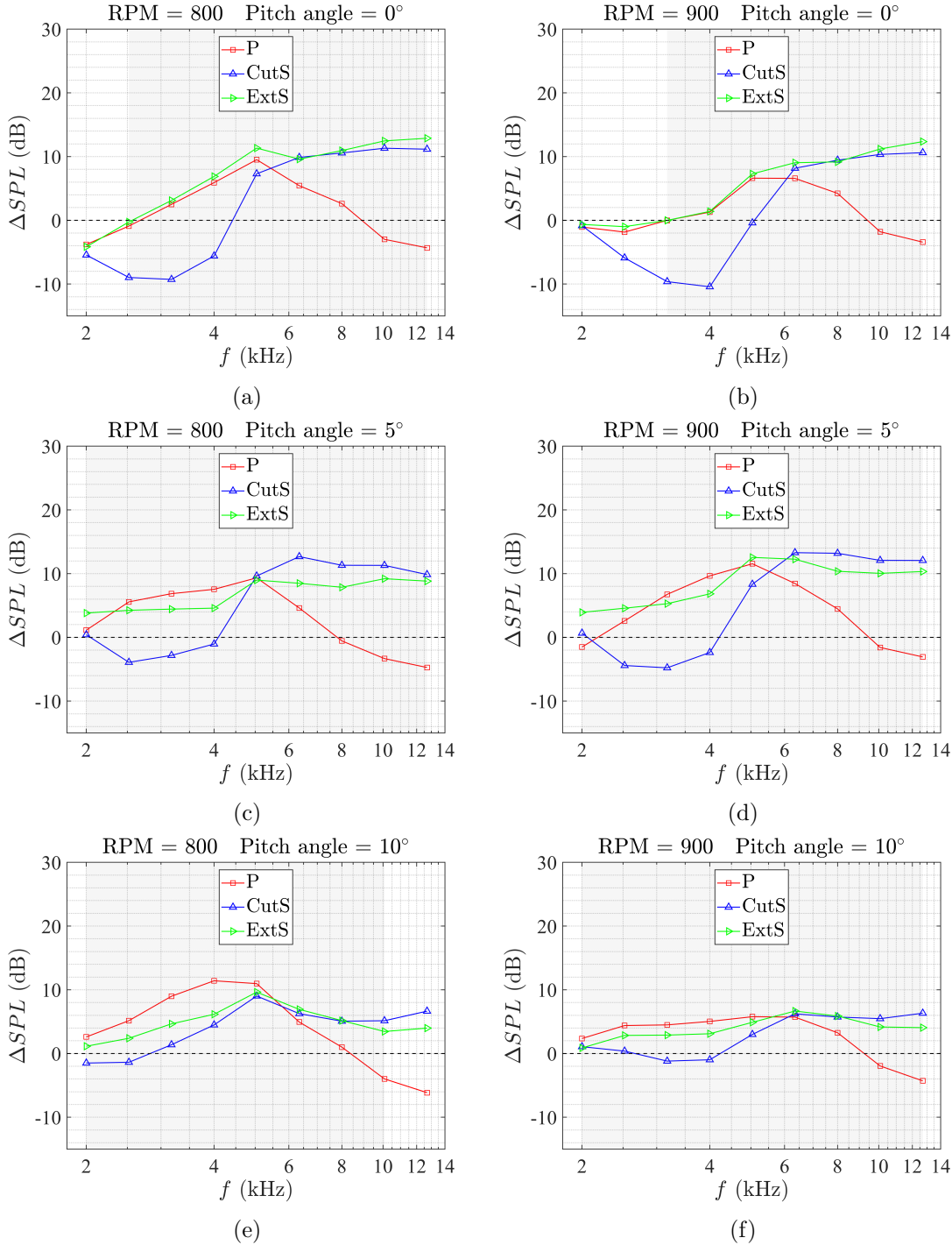


Figure 7.12: One-third-octave band noise reduction ΔSPL for naturally transitioned (un-tripped) blades P, ExtS and CutS at 800 RPM: pitch angles of (a) 0°, (c) 5° and (e) 10°, and 900 RPM: pitch angles of (b) 0°, (d) 5° and (f) 10°. (The frequency range for LBL-TE noise comparison is marked in grey).

bluntness vortex-shedding noise gives rise to a significant noise increase of up to 10.4 dB over lower frequencies (up to 5 kHz) for the naturally-transitioned blade at pitch angle of 0° (Figures 7.12a and 7.12b). The level of the excessive bluntness noise reduces as pitch angle increases. However, the LBL-TE noise can be significantly reduced by blade CutS at higher frequencies (over 5 kHz) by up to 13.3 dB. Blade ExtS achieves a prominent noise reduction of up to 12.9 dB at all operating conditions over the entire frequency range where LBL-TE noise is dominant. Blade P suppresses the LBL-TE noise efficiently over lower frequencies (up to 8 kHz for 800 RPM and 9 kHz for 900 RPM), achieving an even higher level of noise reduction at non-zero pitch angles compared to blades CutS and ExtS (Figures 7.12c–7.12f). However, the noise attenuation at higher frequencies is still limited by the excessive ‘roughness’ noise produced by the porous geometries as discussed previously.

Figure 7.13 shows the overall acoustic performance in terms of TBL-TE noise for the forced-transitioned blades P, CutS and ExtS, which is calculated as the change in overall sound pressure levels $\Delta OASPL$ over the frequency range for TBL-TE noise comparison ($f > f_{peak}$):

$$\Delta OASPL = OASPL_{Ref} - OASPL_{Treated} , \quad (7.9)$$

where $OASPL_{Ref}$ and $OASPL_{Treated}$ are the overall sound pressure levels for the reference blade and the blade with TE treatments, respectively. As shown in Figure 7.13, blade CutS fails to achieve an overall noise reduction at all operating conditions. Instead, this blade increases the overall noise level by up to 7.1 dB due to the introduction of high-level bluntness vortex-shedding noise. Although porous blade P achieves a noise reduction over lower frequencies, it can only lower the overall noise level by up to 0.7 dB at pitch angle of 10°, limited by excessive high-frequency ‘roughness’ noise. Blade ExtS is found to be the most effective in TBL-TE noise reduction, achieving significant overall noise reductions of up to 3.2 dB at most operating conditions except the cases of 800 RPM, 10° pitch and 900 RPM, 5° pitch. For the operating conditions of increased overall noise level, the LE-turbulence-interaction noise may be strengthened by the extended serration geometries as discussed previously.

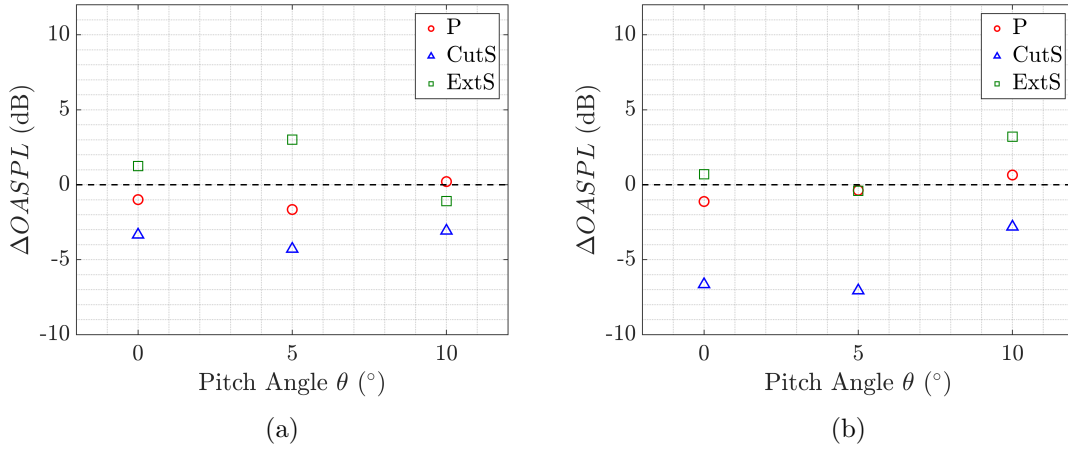


Figure 7.13: Reduction in overall sound pressure level $\Delta OASPL$ over TE-turbulence-noise-sensitive frequencies for forced-transitioned blades with TE treatments at RPM of (a) 800 and (b) 900.

Figure 7.14 presents the overall acoustic performance $\Delta OASPL$ of the natural-transitioned blades P, CutS and ExtS over frequencies where LBL-TE noise is dominant. Similar to the forced-transitioned scenario, an increase in overall noise level (up to 7.8 dB) has been observed for CutS at most operating conditions except the case of 900 RPM and 10° pitch angle. However, the additional noise produced by this blade decreases at higher pitch angles as the effective bluntness becomes smaller with respect to the direction of the in-flow velocity, weakening the bluntness vortex-shedding noise. Blades ExtS and P are both effective in LBL-TE noise reduction, achieving an overall noise reduction of up to 5.6 dB and 5.1 dB at all operating conditions, respectively. When a pitch angle is present, the

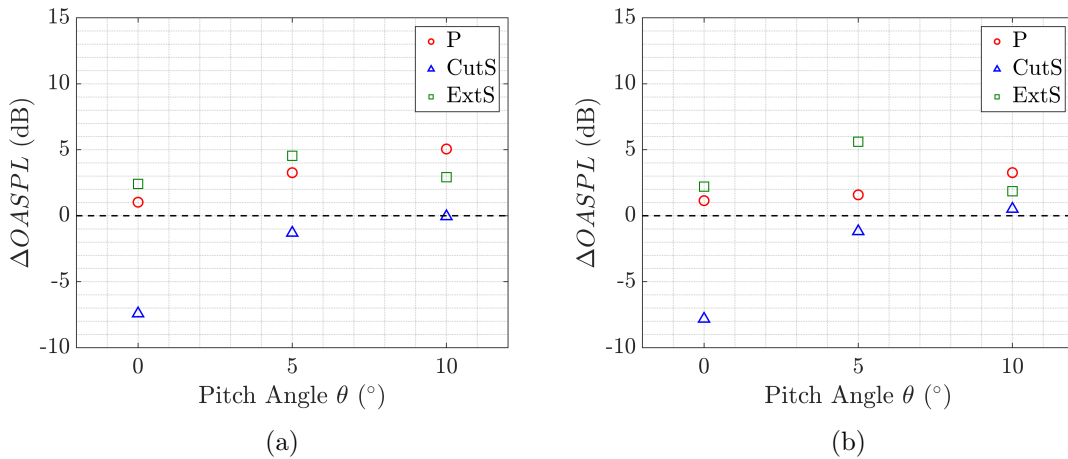


Figure 7.14: Reduction in overall sound pressure level $\Delta OASPL$ over TE-instability-noise-dominant frequencies for natural-transitioned blades with TE treatments at RPM of (a) 800 and (b) 900.

overall noise reduction $\Delta OASPL$ of blade ExtS is found to decrease with increasing pitch angle, while the $\Delta OASPL$ of blade P increases as the blade pitches at a higher angle.

7.4 The Relationship between Noise Reduction and Sound Absorption Coefficient for the Porous Blade

As described in Sec. 3.4.2, the geometry of blade P's porous TE has been designed according to the geometrical parameters of impedance tube specimen P4 (see Sec. 3.2 for details). P4 was characterised to have good sound absorption (where the sound absorption coefficient $\alpha_p > 0.3$) over a frequency range of 4 to 6.4 kHz. Figure 7.15 presents the noise reduction performance ΔSPL of blade P at all operating conditions tested in this experimental campaign. For the forced- and natural-transition scenarios, a noise reduction of up to 2.2 and 11.6 dB can be achieved over the high sound absorption frequency range of 4 to 6.4 kHz (the grey region in Figure 7.15), respectively. Except for the case of 800 RPM and 10° pitch angle, the noise reduction ΔSPL at all other operating conditions peaks within this frequency range (4–6.4 kHz), indicating that the high sound absorption coefficient may contribute to the TE noise reduction by altering the acoustic scattering efficiency of the blade TE.

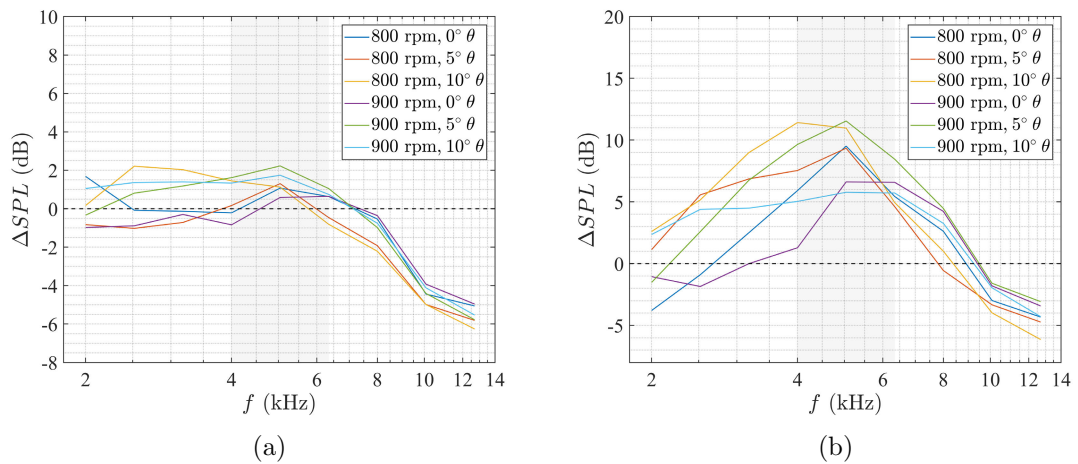


Figure 7.15: One-third-octave band noise reduction ΔSPL for (a) forced-transitioned and (b) natural-transitioned blade P at RPM of 800 and 900 and pitch angles of 0°, 5° and 10° (high-sound-absorption region marked in grey).

7.5 Summary

The TE noise generated from four sets of rotor blades with straight, porous, cut-serrated and extended-serrated TE has been measured using a 64-channel microphone array and processed by three beamforming algorithms: CBF, PABF 1 and PABF 2. This experimental campaign investigated two scenarios; that of forced and natural boundary layer transition corresponding to the generation of TBL-TE noise and LBL-TE noise, respectively. Phase-averaged beamforming method 2 (PABF 2) has been found to remove the background noise efficiently and distinctly localise the noise sources on the rotation plane. The beamforming results processed by PABF 2 have shown that the highest noise levels for all blade sets are present at TE in the blade tip regions. Therefore, the beamforming maps of these blade sets are integrated over this region for comparison of their TE noise generation.

The BPM model has been used to determine the frequency range dominated by TBL-TE noise for the reference blade (Ref). As the inputs to the BPM model, the local aerodynamic conditions along the blade span were calculated using blade element momentum theory (BEMT) and Xfoil. BPM prediction results and the integrated spectra of blade Ref are in reasonably good agreement over frequencies higher than the peak frequency of BPM predictions. Hence, this frequency range is chosen to evaluate the effects of blades CutS, ExtS and P on the TBL-TE noise. The naturally-transitioned blade Ref has shown significantly (up to 14.1 dB) higher noise level compared to the forced-transitioned case due to the high-amplitude tonal LBL-TE noise. The frequency range where naturally-transitioned Ref shows higher noise levels is therefore chosen for LBL-TE noise comparisons.

The acoustic performance of blades CutS, ExtS and P for TBL-TE noise and LBL-TE noise have been summarised as follows:

- **Cut-Serrated TE (CutS):** CutS is the most acoustically efficient TE treatment over high frequencies (above 5 kHz for 800 RPM and 6 kHz for 900 RPM) compared to ExtS and P, achieving noise reductions in TBL-TE noise of up to 8.4 dB and LBL-TE noise of up to 13.3 dB. However, this edge treatment can lead to noise increases at low frequencies due to the presence of bluntness vortex-shedding noise,

induced by the bluntness at the roots of the serration. As a result, CutS fails to achieve an overall noise reduction for both TE noise sources, increasing the overall sound pressure levels by up to 7.1 dB for TBL-TE noise and 7.8 dB for LBL-TE noise.

- **Extended-Serrated TE (ExtS):** ExtS can achieve noise reduction ΔSPL over the entire frequency range of interest for both TBL-TE noise and LBL-TE noise at the majority of operating conditions. However, for the scenarios of forced-transitioned blade at 800 RPM, 10° pitch and 900 RPM, 5° pitch, ExtS fails to reduce the overall noise level, instead, slightly raise the $OASPL$ of up to 1.1 dB. The noise increases are likely due to an increase in the level of LE-turbulence-interaction noise attributed to the extended serration geometries. Despite the minor overall noise increase at the aforementioned two scenarios, ExtS still has the best overall noise attenuation performance compared to other TE treatments, achieving an overall noise reduction of up to 3.2 dB in TBL-TE noise and 5.6 dB in LBL-TE noise.
- **Porous TE (P):** P can consistently achieve TBL-TE noise reductions of up to 2.2 dB over lower frequencies (up to 6 kHz for 800 RPM and 7 kHz for 900 RPM) for all forced-transitioned scenarios. In terms of LBL-TE noise, P yields highest noise reduction of up 11.6 dB over lower frequencies (up to 8 kHz for 800 RPM and 9 kHz for 900 RPM) when a pitch angle is present. However, the noise attenuation performance of P is limited by the presence of high-frequency 'roughness' noise produced by its porous geometry. P can only achieve limited overall TE-turbulence reductions of up to 0.7 dB when pitched at 10° . For the LBL-TE noise, despite the high-frequency noise increase, P can still reduce the overall sound level by up to 5.1 dB for all natural-transitioned scenarios due to its significant low-frequency noise attenuation. The overall LBL-TE noise reduction for P has been found to increase with the pitch angle, while ExtS yields less overall noise reduction as the blade pitches at a higher angle. Moreover, P can effectively control the noise levels for both TE noise sources over the frequency range (4–6.4 kHz) corresponding to that where its porous structures have good sound absorption ($\alpha_p > 0.3$). In fact, P achieves its peak noise reduction within this frequency range for most operating conditions (except 800 RPM, 10° pitch). This indicates that the sound absorption of

the TE geometries may play a role in TE noise attenuation by altering the acoustic scattering efficiency of the blade TE.

Chapter 8

Prediction Model for Wind Turbine Noise

8.1 Overview

In this chapter, a wind turbine noise prediction model, which integrates a noise scaling approach with the BPM model, is developed and detailed. The proposed model estimates the wind turbine noise by scaling wind tunnel acoustic and aerodynamic data to a full-scale wind turbine based on non-dimensional constraints. This model serves the purpose of improving the accuracy of the Class II prediction method (as described in Ref. [82]) that only relies on the semi-empirical BPM model for the turbulent boundary layer trailing-edge (TBL-TE) noise prediction.

This chapter is structured as follows. First, the aerodynamic results of the airfoils tested in UAT Campaign 2 are presented in Sec. 8.2, which includes the aerodynamic force and near-wake velocity results. The acoustic results, as the major input for the noise prediction model, are then presented and discussed in Sec. 8.3. The following Sec. 8.4 details the method and procedure of the noise prediction model as well as the corrections of sound propagation. After that, the prediction results for a full-scale wind turbine are presented and compared with field-test data and the predictions from the classic BPM model in Sec. 8.5. Finally, the findings and potential further improvements of the proposed prediction model are summarised in Sec. 8.6.

8.2 Aerodynamic Results

As described in Sec. 3.3.2, the aerodynamic performance of 5 cambered airfoils (S1–S5) with the profiles from 5 tip regions of a Goldwind[®] wind turbine blade is obtained. All measurements are conducted at a freestream velocity $U_\infty = 30$ m/s and geometric angles of attack from 0 to 16° , incrementing by 2° .

The main purpose of the aerodynamic measurements is to correct for the open-jet effects on the geometric angles of attack to ensure the acoustic data are scaled properly. Table 8.1 shows the results corrected from (Eqs. (3.29)–(3.31) in Sec. 3.3.6).

Table 8.1: Corrected angles of attack for wind turbine airfoils S1–S5.

Geometric angle of attack α_g ($^\circ$)	Corrected angle of attack α_c ($^\circ$)				
	S1	S2	S3	S4	S5
0	-0.1	-0.2	-0.3	-0.4	-0.7
2	1.4	0.9	0.9	0.8	0.5
4	2.5	2.1	2.1	1.9	1.7
6	3.7	3.3	3.2	3.0	2.9
8	4.9	4.6	4.5	4.3	4.1
10	6.1	5.7	5.7	5.6	5.4
12	7.4	7.1	6.9	6.8	6.6
14	8.8	8.4	8.2	8.1	7.9
16	10.3	9.7	9.6	9.4	9.1

Figures 8.1a–8.1d show the comparison of the aerodynamic performance of the 5 airfoils, in which S1 corresponds to the region near the hub and S5 corresponds to the blade tip region. Although the lift curve slope (Figure 8.1a) does not appear to change significantly, the amount of lift generated at a particular angle of attack is lowest for S1 and highest for S5. Figure 8.1b shows the results of drag coefficient as a function of α_c . The drag coefficients for the test models are comparable at low angles of attack ($0 < \alpha_c < 6^\circ$); however, at high lift angles of attack, the drag increases in the same proportion as the lift. Figure 8.1c compares the lift-to-drag ratio (L/D) of these airfoil models as a function of angle of attack. The maximum L/D values increase only slightly between S1 and S5, however, the L/D peak angle of attack ($\alpha_{L/D,max}$) differs from one airfoil to another with

the near-hub airfoil S1 showing the highest $\alpha_{L/D,max}$ and near-tip S5 showing the lowest. The result indicates the optimum configuration for achieving maximum L/D is to set tip region S1 and hub region S5 to lowest and highest angles of attack, and gradually increase the angle of attack from tip to hub. This agrees with the typical characteristic for a wind turbine blade as the tip region runs at higher linear velocity, hence the pitch angle of this region is usually set to be lower to generate less loading. The drag polar results are shown in Figure 8.1d. The curves of these airfoils show similar shapes and collapse together, indicating that the overall lift-to-drag performance for these airfoils is similar, however, the airfoils must be set at different angles of attack to achieve similar L/D . Table 8.2 summarises the maximum L/D values and the corresponding angles of attack.

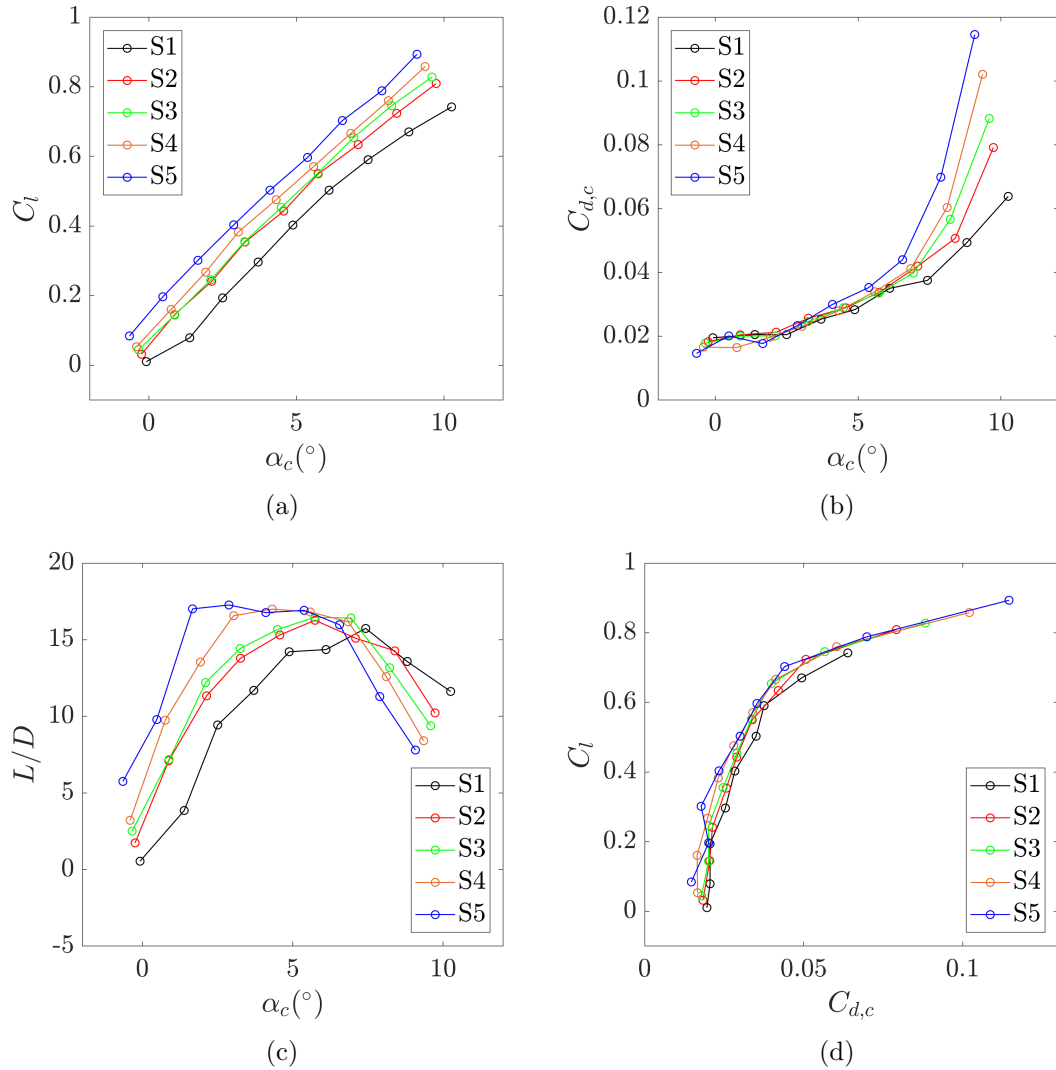


Figure 8.1: Aerodynamic performance for airfoils S1 to S5: (a) Lift curves, (b) drag curves, (c) lift to drag ratio and (d) drag polar.

Table 8.2: The maximum L/D and the corresponding angle of attack for airfoils S1 to S5

Airfoil model	S1	S2	S3	S4	S5
Maximum L/D	15.74	16.27	16.46	17	17.27
Peak angle of attack $\alpha_{L/D,max}$	7.4	5.7	5.7	4.3	2.9

8.2.1 Boundary Layer Properties

The velocity profile in the very near wake (0.7% chord downstream of the trailing edge) was measured for airfoil models S1 and S5 using a pitot probe as described in Sec. 3.3.2. The boundary layer properties were calculated from the very near wake data which is considered to be close enough for representing the boundary layer at the airfoil trailing edge (TE). The measurements serve the purpose of evaluating the accuracy of Xfoil predictions which were used for the noise scaling in the wind turbine noise prediction. For each case, two geometric angles of attack equal to 0° and 10° were considered. The corrected angles of attack corresponding to $\alpha_g = 0^\circ$ and 10° for S1 and S5 are presented in Table 8.1.

Figure 8.2 shows the boundary layer profiles for S1 and S5 on both sides of the airfoil at angles of attack $\alpha_g = 0^\circ$ and 10° . In order to extract the boundary layer thickness (δ), the momentum thickness (θ), the displacement thickness (δ^*) and the shape factor (H_s), a shape-preserving spline with 5000 points was fitted to the measured data as shown in Figure 8.2a. This spline was also extrapolated to $y = 0$ in order to numerically integrate the velocity profile down to the surface. The boundary layer parameters extracted from these profiles towards the suction and the pressure sides of the airfoil are shown in Tables 8.3 and 8.4 respectively. The boundary layer displacement thickness predicted using Xfoil is in reasonable agreement (typical error $\leq 20\%$) with the measured data (especially for tip region airfoil S5), indicating that the prediction from Xfoil is adequate to represent the displacement thickness at the airfoil TE for the purpose of noise scaling.

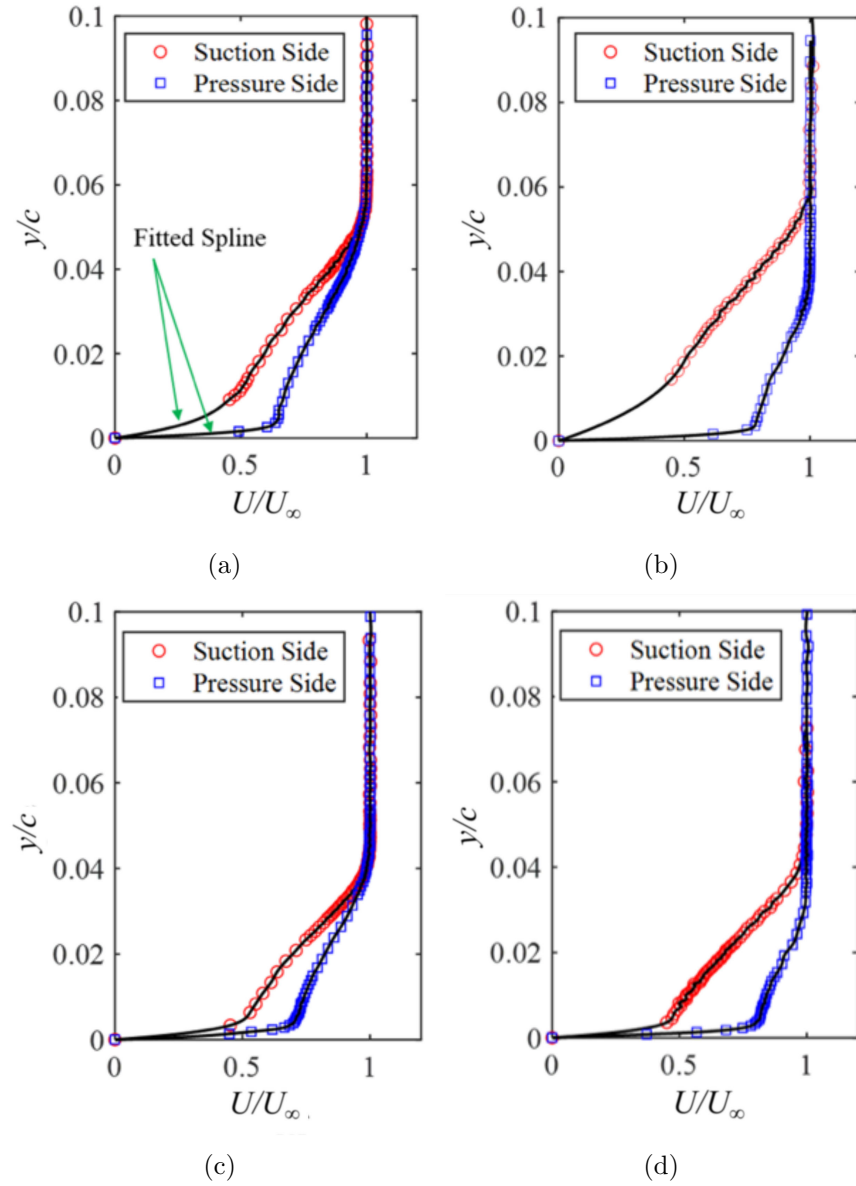


Figure 8.2: Boundary layer velocity profiles on both sides of the airfoil for S1 at (a) $\alpha_g = 0^\circ$ and (b) 10° , and S5 at (c) $\alpha_g = 0^\circ$ and (d) 10° .

Table 8.3: Boundary layer parameters towards the suction-side for S1 and S5

$\alpha_g (^\circ)$	Airfoil	δ (mm)	δ^* (mm)	δ^* (mm)	θ (mm)	H_s
				from Xfoil		
0	S1	10.7	3.6	2.9	1.8	2
10	S1	11.5	4.6	5.2	1.8	2.6
0	S5	8.3	2.4	2.9	1.4	1.8
10	S5	11.8	5.0	5.3	2.1	2.4

Table 8.4: Boundary layer parameters towards the pressure-side for S1 and S5

$\alpha_g(^{\circ})$	Airfoil	δ (mm)	δ^* (mm)	δ^* (mm) from Xfoil	θ (mm)	H_s
0	S1	10.8	2.2	3.2	1.5	1.5
10	S1	6.6	1	1.1	0.7	1.4
0	S5	8.3	1.5	1.3	1.1	1.4
10	S5	6.7	0.8	0.6	0.6	1.4

8.3 Acoustic Results

8.3.1 Beamforming Maps

Microphone array measurements have been conducted on these 5 cases (S1–S5) and post-processed using conventional beamforming methodology as discussed in Secs. 3.3.2 and 3.3.3. The acoustic data were taken simultaneously with the aerodynamic data, which were for the airfoils at $U_{\infty} = 30$ m/s and $\alpha_g = 0$ – 16° (with an increment of 2°) as mentioned before. The beamforming maps at 1260 Hz for the acoustic data of the airfoils at $\alpha_g = 0^{\circ}$ and $U_{\infty} = 30$ m/s are presented in Figures 8.3a–8.3e, in which the sound pressure levels on the TE plane are mapped with a dynamic range of 10 dB. The dominant noise sources for all cases have been clearly localised at the TE of the model (green rectangle) with the flow direction from left to right. To prevent the undesired noise sources from the airfoil-wall junctions and the gaps between the turn-table and end-plate from being taken into account for the noise scaling, the beamforming maps were integrated using the method described in Sec. 3.3.3.

8.3.2 Source Integration Results

Figure 8.4 shows the 1/3 octave band noise spectra integrated over the TE region as shown in Figure 8.3, and the noise prediction results from BPM model [31] for S1 at $\alpha_g = 0$ – 16° and $U_{\infty} = 30$ m/s. XFOIL [59] was utilised to estimate the boundary layer parameters in the BPM model. As shown in the figure, the spectra of integrated sources and BPM prediction share a similar spectral shape but the level is different (difference within 10

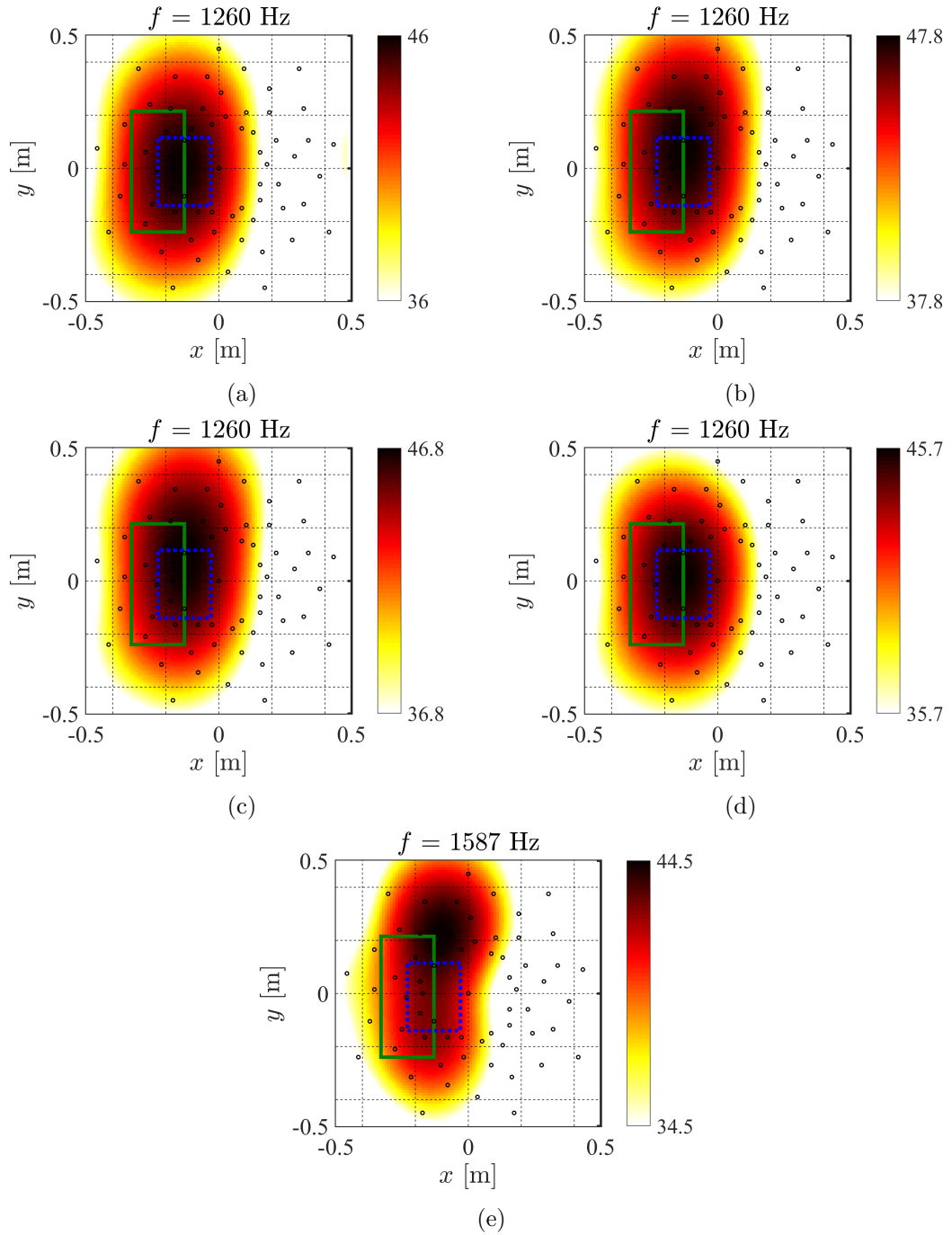


Figure 8.3: Beamforming maps (color bar scale in dB) at 1260 Hz for airfoil models (a) S1, (b) S2, (c) S3, (d) S4 and (e) S5 at $\alpha_g = 0$ and $U_\infty = 30$ m/s. Flow comes from left to right. Green rectangle is the position of airfoil model, and the TE integration region is marked by a blue-dashed rectangle (x and y correspond to horizontal (streamwise) and vertical coordinates).

dB). The other 4 airfoils (S2–S5) have also shown a similar comparison as S1 does (see Figure 8.5). In fact, the disparity between experimental results and BPM prediction is expected as the BPM model was developed for a NACA0012 airfoil rather than for general designs. This also indicates that directly using the acoustic data obtained from the BPM model for wind turbine noise prediction can introduce errors, therefore the acoustic data from wind tunnel measurements are necessary for an accurate prediction of wind turbine noise.

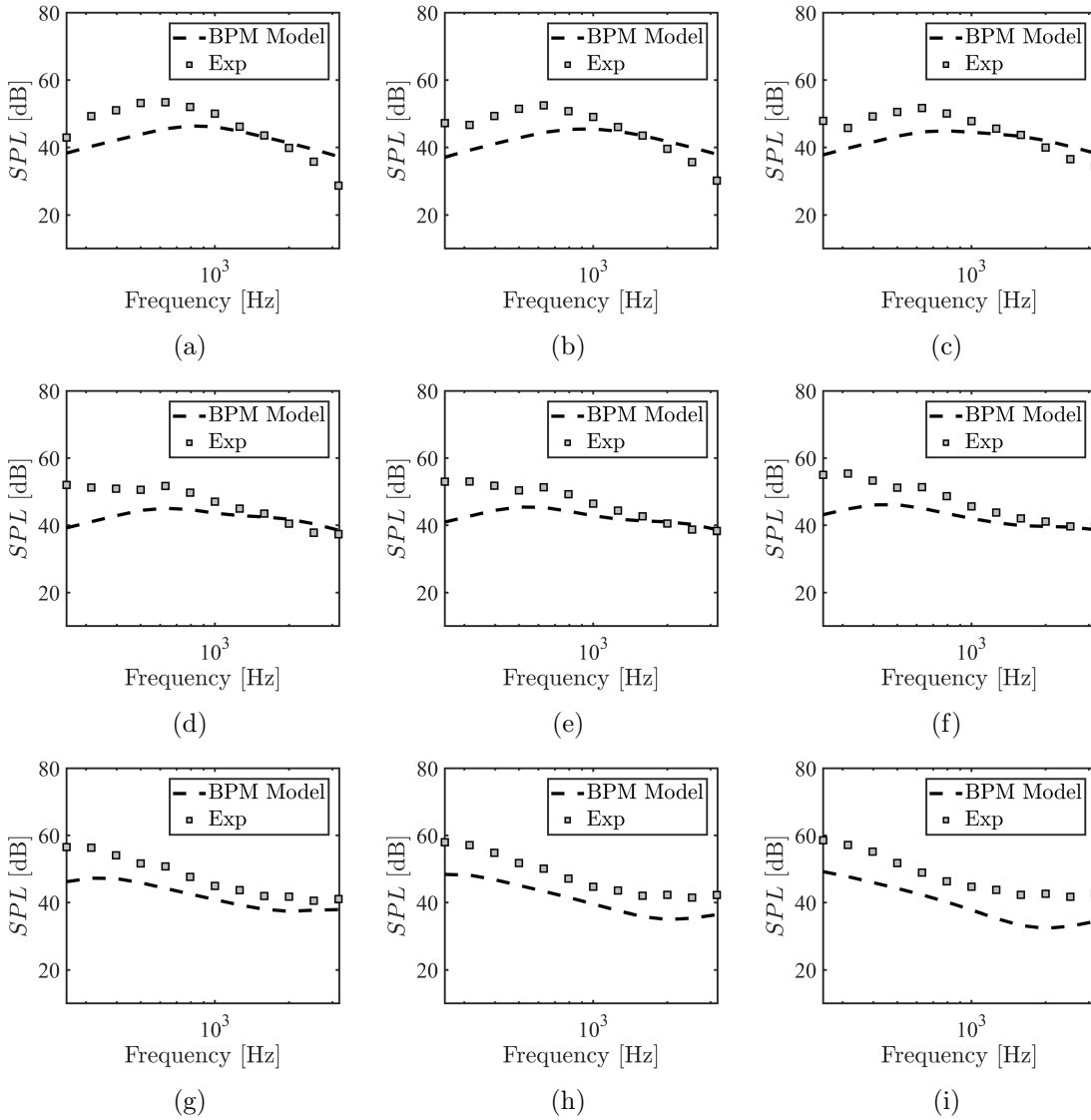


Figure 8.4: Integrated 1/3 octave band spectra (green squares) and spectra from BPM model (black dashed line, boundary layer parameters estimated by Xfoil) for S1 at the geometric angle of attack $\alpha_g =$ (a) 0° ; (b) 2° ; (c) 4° ; (d) 6° ; (e) 8° ; (f) 10° ; (g) 12° ; (h) 14° and (i) 16° at $U_\infty = 30$ m/s.

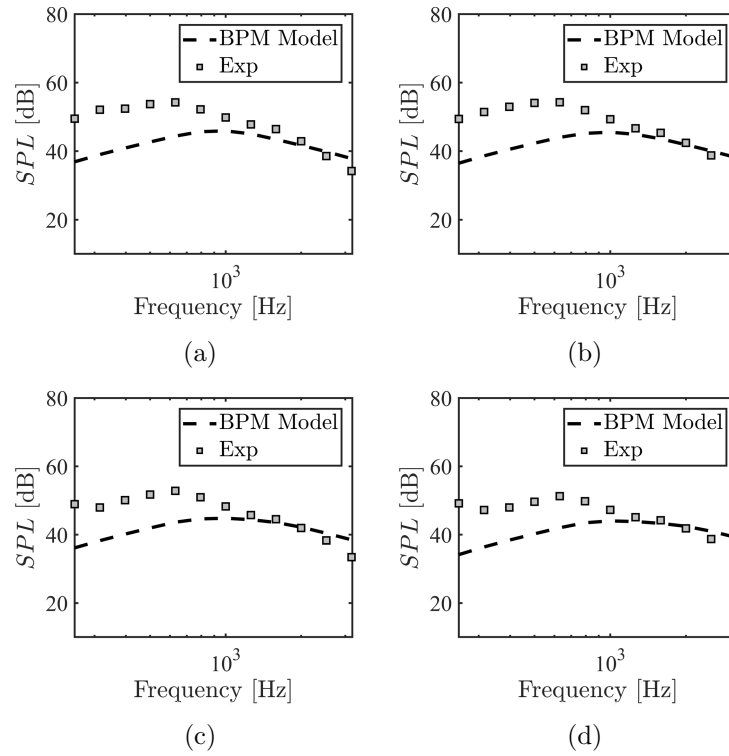


Figure 8.5: Integrated 1/3 octave band spectra (green square) and spectra from BPM model (black dashed line, boundary layer parameters estimated by Xfoil) for (a) S2; (b) S3; (c) S4 and (d) S5 at $\alpha_g = 0^\circ$ and $U_\infty = 30$ m/s.

8.4 Wind Turbine Noise Prediction Method

The wind turbine noise prediction methodology is based on the one outlined in Ref [82]. However, instead of using the BPM model [31] for airfoil TBL-TE noise prediction, the acoustic and aerodynamic results from UAT Campaign 2 (details described in Sec. 3.3) were used with a scaling procedure to improve the prediction accuracy. This section details the principle and procedure for this prediction method.

8.4.1 Principle

The overall noise emitted from a wind turbine blade can be regarded as the sum of several noise sources along the blade span. Based on this concept, the blade is first divided into n segments (see Figure 8.6), then the angle of attack and incoming velocity for each segment along the blade radius are predicted using Blade Element Momentum Theory (BEMT) based on the operating conditions, geometries (provided by Goldwind[®]) and

aerodynamics estimated using Xfoil. Next, the angle of attack and incoming velocity, as the inputs for Xfoil, are used to estimate the boundary layer properties at the TE of each segment. After that, the inflow turbulence noise and airfoil TBL-TE noise, as the two most dominant noise sources for a wind turbine, are determined using the information obtained above. Finally, the predicted noise from each segment are summed to produce the total noise emitted from the wind turbine. In addition, corrections of sound propagation are also taken into account to improve the prediction results. The following sections will further discuss the details of each component of this method.

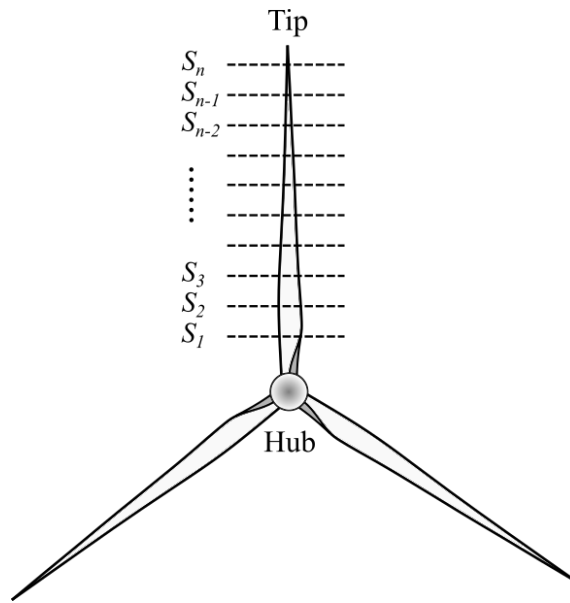


Figure 8.6: Schematic of the discretisation of a wind turbine blade into n segments: $S_1, S_2, S_3, \dots, S_n$.

Blade Element Momentum Theory

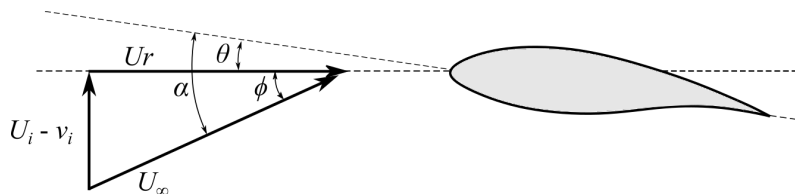


Figure 8.7: Schematic of the flow condition encountered by a wind turbine blade element

In order to estimate the noise generated from a blade segment, the incoming flow condition is required. Blade element momentum theory [109] is a method that performs a momentum balance across the rotor to determine the flow conditions encountered by each

segment of the rotor. In Figure 8.7, U_i is the local wind velocity approaching the blade element, v_i is the the local induced velocity from the energy extracted from the wind and U_r is the linear velocity due the movement of the blade segment, which can be determined by

$$U_r = \omega_r r , \quad (8.1)$$

where ω_r is the rotational rate of the rotor and r is the radius from the local blade segment to the rotor hub. The local pitch angle (blade pitch angle + local twist angle) for a blade segment is defined as θ , the angle of attack α of the blade segment can be determined by

$$\alpha = \theta + \phi , \quad (8.2)$$

where ϕ is the local inflow angle which varies along the blade span. It can be expressed as

$$\phi = \tan^{-1} \left(\frac{U_i - v_i}{U_r} \right) = \tan^{-1} \left(\frac{U_i - v_i}{\omega_r r} \right) \approx \frac{U_i - v_i}{\omega_r r} = \left(\frac{U_i - aU_i}{\omega_r R_t} \right) \left(\frac{\omega_r R_t}{\omega_r r} \right) = \frac{1 - a}{\bar{r} X_{TSR}} , \quad (8.3)$$

Here, the small angle assumption is used and a is the local induction factor defined as $a = v_i/U_i$ and $\bar{r} = r/R_t$, where r is the local radius of the local blade segment and R_t is the rotor radius. X_{TSR} is the tip-speed ratio defined as

$$X_{TSR} = \frac{\omega_r R_t}{U_i} . \quad (8.4)$$

The local induction factor a can be calculated as follows

$$a(\bar{r}, X_{TSR}) = \sqrt{\left(\frac{\sigma X_{TSR} C_{l_\alpha}}{16} + \frac{1}{2} \right)^2 - \frac{\sigma X_{TSR} C_{l_\alpha} (X_{TSR} \theta \bar{r} + 1)}{8}} + \frac{\sigma X_{TSR} C_{l_\alpha}}{16} + \frac{1}{2} . \quad (8.5)$$

Here, σ is the local solidity defined by $\sigma = N_b c$, where N_b is the number of blades of the rotor and c is the chord length of the local blade segment. The local aerodynamics are taken into account using the derivative

$$C_{l_\alpha} = \frac{\partial C_l}{\partial \alpha} , \quad (8.6)$$

where C_l is the lift coefficient.

For better accuracy, the rotor-tip loss effects can be taken into account [109] by introducing a tip-loss factor F defined as

$$F = \frac{2}{\pi} \arccos(\exp(-\varphi)), \quad (8.7)$$

where

$$\varphi = \frac{N_b}{2} \left(\frac{\bar{r} - \bar{r}_0}{1 - a} \right) X_{TSR}, \quad (8.8)$$

where $\bar{r}_0 = r_0/R$ is the non-dimensional root-cut-out distance, and r_0 is the distance between the center of the rotor hub and the root of the rotor blade. The local induction factor can then be determined by the equations modified from Eq. (8.5). When $0 \leq a \leq 0.5$, it can be determined by

$$a(\bar{r}, X_{TSR}, F) = \sqrt{\left(\frac{\sigma X_{TSR} C_{l_\alpha}}{16F} + \frac{1}{2} \right)^2 - \frac{\sigma X_{TSR} C_{l_\alpha} (X_{TSR} \theta \bar{r} + 1)}{8F}} + \frac{\sigma X_{TSR} C_{l_\alpha}}{16F} + \frac{1}{2}, \quad (8.9)$$

and when $0.5 < a \leq 1$, the expression is modified to

$$a(\bar{r}, X_{TSR}, F) = \sqrt{\left(\frac{\sigma X_{TSR} C_{l_\alpha}}{16F} - \frac{1}{2} \right)^2 - \left(\frac{1}{2} - \frac{\sigma X_{TSR} C_{l_\alpha} (X_{TSR} \theta \bar{r} + 1)}{8F} \right)} - \frac{\sigma X_{TSR} C_{l_\alpha}}{16F} + \frac{1}{2} \quad (8.10)$$

The local angle of attack α and incoming velocity U (as shown in Figure 8.7) for each blade segment can be determined by iterations over Eqs.(8.1)-(8.4) and (8.6)- (8.10), in which the local aerodynamic characteristics are estimated using Xfoil.

Inflow Turbulence Noise Prediction

Inflow turbulence noise is the dominant low-frequency noise source for a large-scale wind turbine. Based on an analytical model of a flat-plate first proposed by Amiet [5], the inflow turbulence-interaction noise is estimated using the modified formulation of Amiet's model presented by Buck [33]. For a blade segment that has a large chord with respect to an acoustic wavelength (high frequencies), the estimated 1/3 octave-band sound pressure level generated by the inflow turbulence noise can be determined by

$$SPL_H = 10 \log_{10} \left[\rho_0^2 c_0^4 \frac{r \delta_{ILS}}{2r_e^2} M_l^5 I_{uu} \frac{(k/k_e)^3}{(1 + (k/k_e)^2)^{7/3}} D \right] + 78.4, \quad (8.11)$$

where ρ_0 is the freestream density, c_0 is the speed of sound, r_e is the distance from the source to the observer, r is the blade segment radius, I_{uu} is the turbulence intensity, δ_{ILS} is the turbulence integral length scale and M_l is the local Mach number. The turbulence intensity I_{uu} is defined as $I_{uu} = \overline{u'}/U_i$, where u' is fluctuating velocity of the incoming wind. The directivity function D will be discussed in Sec. 8.4.2. The turbulence wavenumber [89] k and the energy-containing wavelength scale of turbulence k_e are defined as follows

$$k_e = \frac{\sqrt{\pi}\Gamma(5/6)}{\delta_{ILS}\Gamma(1)}, \quad (8.12)$$

where Γ stands for the Gamma function. For the predictions in this thesis, the turbulence integral length scale δ_{ILS} is assumed to be $2.45 h_r$ [49, 139], where h_r is the height of the rotor hub. The full expression of inflow turbulence noise SPL_{inflow} , including the low-frequency, noncompact airfoil correction factor and the minor correction factor for finite angle of attack [140], is determined by the following equations (8.13)–(8.16):

$$SPL_{inflow} = SPL_H + 10 \log_{10} \left(\frac{LFC}{1 + LFC} \right), \quad (8.13)$$

$$LFC = 10S^2(1 + 9\alpha^2)M_l \left(\frac{kc}{2} \right)^2 \beta^{-2}, \quad (8.14)$$

$$S^2 = \left[\frac{2\pi kc}{2\beta^2} + \left(1 + 2.4 \frac{kc}{2\beta^2} \right)^{-1} \right]^{-1}, \quad (8.15)$$

$$\beta = 1 - M_l^2, \quad (8.16)$$

where LFC is the low-frequency correction factor and S is an approximation of the compressible Sears function [124]; α and c are the angle of attack and local chord length as mentioned before.

A correction based on the interpolation of the Guidati model for inflow turbulence-interaction noise from airfoils of finite thickness [81] is then considered in the prediction, which gives the final expression of the predicted inflow turbulence noise $SPL_{inflow,c}$ as follows:

$$SPL_{inflow,c} = SPL_{inflow} + \Delta SPL_G + 10\text{dB}, \quad (8.17)$$

$$\Delta SPL_G = -[1.123(T_{1\%} + T_{10\%}) + 5.317(T_{1\%} + T_{10\%})^2](kc + 5) \quad (8.18)$$

where $T_{1\%}$ and $T_{10\%}$ are the airfoil non-dimensional thickness (normalised by chord length) at chord locations 1% and 10%, respectively.

Turbulent Boundary Layer Trailing-Edge Noise Prediction

Airfoil TBL-TE noise is usually the dominant noise source for wind turbines [148, 174]. In this prediction method, two models are used to estimate the TBL-TE noise generated from different radial positions of the turbine blades. For the hub region ($\bar{r} < 0.6$) of the blades, it moves at a relatively lower velocity and therefore acts as a less dominant noise source (TBL-TE noise level is scaled with the fifth power of velocity [190]). The TBL-TE noise generated from this region is estimated using the Brooks, Pope and Marcolini (BPM) model [31]. For the tip region ($\bar{r} \geq 0.6$), as a more dominant noise source, its contribution to the total TBL-TE noise level is estimated using a more accurate noise scaling model that scales the acoustic data measured in anechoic wind tunnel to the full-scale conditions. Figure 8.8 illustrates the noise prediction models employed in different blade regions. The principle and formulations of these two models will be introduced in the following sections.

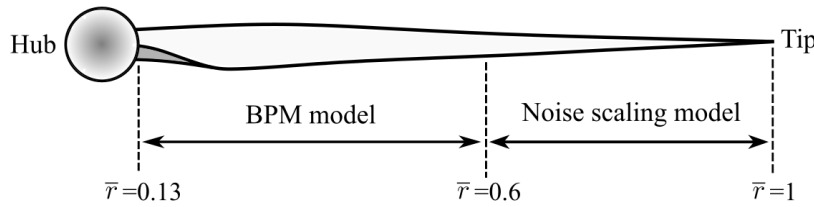


Figure 8.8: TBL-TE noise prediction models employed in different radial positions along the blade.

BPM Model In the BPM model, the sound pressure level of the TBL-TE noise SPL_{TE} is proportional to the boundary layer displacement thickness δ^* and the fifth power of the local Mach number M_l^5 and inversely proportional to the square of the distance between the airfoil segment TE and the observer r_e^2 . The total TBL-TE noise estimation SPL_{TE} consists of three parts: the estimations of the TBL-TE noise originating from the pressure-side boundary layer SPL_p , suction-side boundary layer SPL_s and angle of attack SPL_α , which can be determined by the following Eqs. (8.19) to (8.22):

$$SPL_{TE} = 10 \log_{10}(10^{SPL_p/10} + 10^{SPL_s/10} + 10^{SPL_\alpha/10}), \quad (8.19)$$

$$SPL_p = 10 \log_{10} \left(\frac{\delta_p^* M^5 L D}{r_e^2} \right) + A \left(\frac{St_p}{St_1} \right) + (K_1 - 3) + \Delta K_1, \quad (8.20)$$

$$SPL_s = 10 \log_{10} \left(\frac{\delta_s^* M^5 L D}{r_e^2} \right) + A \left(\frac{St_s}{St_1} \right) + (K_1 - 3), \quad (8.21)$$

$$SPL_\alpha = 10 \log_{10} \left(\frac{\delta_s^* M^5 L D}{r_e^2} \right) + B \left(\frac{St_s}{St_2} \right) + K_2. \quad (8.22)$$

here, A , B , St_1 , St_2 , K_1 , ΔK_1 and K_2 are the empirical functions, where K_1 , ΔK_1 and K_2 depend on the Mach and Reynolds numbers of the blade segment. More details of these functions refer to the original report [31] for BPM model. The span of the local blade segment is L , and D is the directivity function that will be discussed in Sec. 8.4.2. The Strouhal numbers based the displacement thickness of the boundary layers on pressure side δ_p^* and suction side δ_s^* at the airfoil TE are represented by St_p and St_s , respectively. They are defined as

$$St_p = \frac{f \delta_p^*}{U_\infty}, \quad St_s = \frac{f \delta_s^*}{U_\infty} \quad (8.23)$$

where f is frequency and U_∞ stands for the incoming velocity for the blade segment (as illustrated in Figure 8.7).

Noise scaling model based on wind tunnel data The TBL-TE noise emitted from the blade tip region (spanwise locations presented in Table 3.5), as the dominant noise source, is estimated by the acoustic data from wind tunnel measurements (presented in Sec. 8.3) and the noise scaling functions established on the basis of the characteristics of airfoil TBL-TE noise.

Based on the scaling law of TBL-TE noise described in Ref. [31], the noise scaling approach assumes that TBL-TE noise measured at a particular angle of attack and Reynolds number, in each 1/3 octave band can be scaled as,

$$SPL_{1/3} - 10 \log_{10} \left(\frac{\delta_l^* M_l^5 L}{r_e^2} \right) = F(St) + K = NSF(St, \alpha) \quad (8.24)$$

Where $F(St)$ is a spectral function depending on Strouhal number, K is an amplitude function and the combination is the noise scaling function NSF . The empirical noise scaling function (NSF) for airfoil segment is derived and calculated using the acoustic

data measured in UAT (denoted by subscript UAT),

$$NSF(\alpha, St_{\text{UAT}}) = [SPL_{1/3}]_{\text{UAT}} - 10 \log_{10} \left[\frac{\delta_s^* M_l^5 L}{r_e^2} \right]_{\text{UAT}} - K_{\text{corr}} \quad (8.25)$$

Where NSF is a function depending on airfoil angle of attack and strouhal number, M_l is the local Mach number, δ_s^* is the suction-side TE boundary layer height, r_e is the distance from the TE of the airfoil segment to the observer and L is the airfoil span of the test model which refers to the spanwise length of the beamforming integration region (as shown in Figure 8.3) in this prediction. The effect of Reynolds number (Re_c , based on chord c) is estimated using a correction factor K_{corr} derived from the Reynolds-number-based amplitude function K_1 in BPM model [31],

$$K_1 = \begin{cases} -4.31 \log_{10}(Re_c) + 156.3 & (Re_c < 2.47 \times 10^5) \\ -9.0 \log_{10}(Re_c) + 181.6 & (2.47 \times 10^5 \leq Re_c \leq 8.0 \times 10^5) \\ 128.5 & (Re_c > 8 \times 10^5). \end{cases} \quad (8.26)$$

$$(8.27)$$

$$(8.28)$$

In order to account for the noise level difference caused by the Reynolds number (Re_c , based on chord c) difference between the airfoil model in small-scale wind tunnels ($Re_c \leq 8.0 \times 10^5$) and the full-scale wind turbine blade in fields ($Re_c > 8.0 \times 10^5$), the correction factor K_{corr} can be obtained by subtracting Eq. (8.28) from Eqs. (8.26) and (8.27)

$$K_{\text{corr}} = \begin{cases} 27.7 - 4.31 \log_{10}([Re_c]_{\text{UAT}}) & ([Re_c]_{\text{UAT}} < 2.47 \times 10^5) \\ 53.1 - 9.0 \log_{10}([Re_c]_{\text{UAT}}) & (2.47 \times 10^5 \leq [Re_c]_{\text{UAT}} \leq 8.0 \times 10^5), \end{cases} \quad (8.29)$$

$$(8.30)$$

where $[Re_c]_{\text{UAT}}$ is the Reynolds number based on chord in wind tunnel experiments. The acoustic measurements performed in UAT Campaign 2 correspond to a Reynolds number of 4×10^5 , therefore, the correction factor K_{corr} is calculated using Eq. (8.30).

Assuming similarity, the frequency and level between wind tunnel measurements and wind turbine predictions can be directly translated using

$$St_{\text{UAT}} = \left[\frac{f \delta_s^*}{U_\infty} \right]_{\text{UAT}} = St_{\text{WT}} = \left[\frac{f \delta_s^*}{U_\infty} \right]_{\text{WT}} \quad (8.31)$$

$$[SPL_{1/3}]_{\text{WT}} = NSF(\alpha, St_{\text{WT}}) + 10 \log_{10} \left[\frac{\delta_s^* M_l^5 L D}{r_e^2} \right]_{\text{WT}} \quad (8.32)$$

where the subscript WT indicates wind turbine, D is the directivity function as before, and $[L]_{\text{WT}}$ stands for the span of the local blade segment when scaling the wind tunnel results using Eq. 8.32.

Sound power is estimated by integrating the sound intensity projected onto a sphere of radius r_e about the turbine. Before converting the sound pressure level to intensity, the sound pressure levels are A-weighted. The corrections of sound propagation are also taken into account and will be discussed in the following section.

8.4.2 Corrections of Sound Propagation

When considering the sound propagation of the noise emitted from a wind turbine, two factors need to be taken into account: the directivity of noise emitted from the wind turbine and the losses during the sound propagation from the noise source to the observer.

Noise Directivity

According to Standard IEC 61400-11 [50], the observer is always positioned at a fixed location when evaluating the noise level of a wind turbine, therefore the directivity of the noise emission needs to be considered when comparing the prediction with the field measurement.

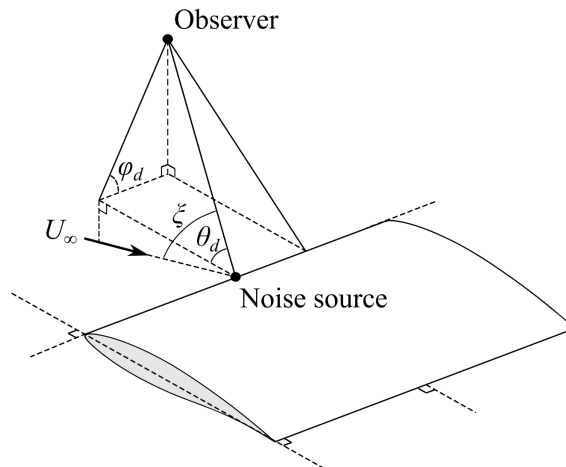


Figure 8.9: Schematic of the angle definitions for the noise directivity function

For noise at very low frequency, of which acoustic wavelengths are large with respect to the airfoil segment chord length, the aerodynamic noise from the wind turbine is modelled

as a dipole source. The directivity function of a dipole source is given by [26, 31, 32, 175]

$$D_l = \frac{\sin^2 \theta_d \sin^2 \varphi_d}{(1 - M_l \cos \xi)^4}. \quad (8.33)$$

The definition of θ_d and φ_d , which refer to the relative position between the noise source and observer, are shown in Figure 8.9; θ_d is the angle between the sound ray and the chord line of the airfoil segment. However, ξ refers to the angle of the ray relative to the local inflow velocity. The directivity function for noise at high frequency is determined by [26, 32]

$$D_h = \frac{2 \sin^2(\theta_d/2) \sin^2 \varphi_d}{(1 - M_l \cos \xi)^4}. \quad (8.34)$$

The inflow noise directivity can be calculated using Eqs. (8.33) and (8.34). However, when calculating the directivity function of TBL-TE noise, θ_d and ξ are replaced by $\pi - \theta_d$ and $\pi - \xi$, respectively, due to the fact that the inflow noise and TBL-TE noise are radiated from opposite edges: inflow turbulence noise is generated from the interaction between the atmospheric turbulence and the discontinuity brought by the leading edge, while the TBL-TE noise originates from the interaction between the TE and the turbulence in the boundary layer.

Atmospheric Absorption

As the sound propagates from the wind turbine to the far-field observer, the amplitude of the sound wave attenuates as some of the energy is lost to the air in the atmosphere. These energy losses are due to the thermal-viscous effects caused by the molecular collision and relaxation processes that absorb some of the kinetic energy of the sound wave [60].

The excess attenuation from atmospheric absorption A_{atm} is determined by [82]

$$A_{\text{atm}} = a_a r_e \quad (\text{dB}) \quad (8.35)$$

where r_e is the distance from the noise source to the observer, and a_a is the attenuation in dB per meter for a pure tone frequency f which is given according to ANSI/ASA S1.26

by

$$a_a = 8.686f^2 \left\{ \left[1.84 \times 10^{-11} \left(\frac{P_a}{P_r} \right)^{-1} \left(\frac{T_a}{T_r} \right)^{1/2} \right] + \left(\frac{T_a}{T_r} \right)^{-5/2} \times \right. \\ \left. \left[0.01275e^{-2239.1/T_a} \left(\frac{f_{r0}}{f_{r0}^2 + f^2} \right) + 0.1068e^{-3352/T_a} \left(\frac{f_{rN}}{f_{rN}^2 + f^2} \right) \right] \right\} \quad (\text{dB}/m) , \quad (8.36)$$

where T_a is ambient atmospheric temperature in Kelvin, T_r is the reference temperature (293.15 K), P_a is the ambient atmospheric pressure, P_r is the reference atmospheric pressure (101325 Pa), and f_{r0} and f_{rN} are determined by

$$f_{r0} = \left(\frac{P_a}{P_r} \right) \left[24 + \frac{(4.04 \times 10^4 h)(0.02 + h)}{0.391 + h} \right] \quad (8.37)$$

$$f_{rN} = \left(\frac{T_a}{T_r} \right)^{-1/2} \left(\frac{P_a}{P_r} \right) \left\{ 9 + 280he^{-4.170[(T_a/T_r)^{-1/3} - 1]} \right\} , \quad (8.38)$$

where h is the molar concentration of water vapour that can be calculated from relative humidity h_r by

$$h = h_r \left(\frac{P_{sat}}{P_r} \right) \left(\frac{P_a}{P_r} \right)^{-1} , \quad (8.39)$$

where

$$\frac{P_{sat}}{P_r} = 10^V \quad (8.40)$$

and

$$V = 10.79586 \left[1 - \left(\frac{273.16}{T_a} \right) \right] - 5.02808 \log_{10} \left(\frac{T_a}{273.16} \right) \\ + 1.50474 \times 10^{-4} \left\{ 1 - 10^{-8.29692[(T/273.16) - 1]} \right\} \\ + 0.42873 \times 10^{-3} \left\{ 1 - 10^{4.76955[1 - (273.16/T)]} \right\} - 2.2195983 \quad (8.41)$$

,which can be approximated by

$$V = -6.8346 \left(\frac{273.16}{T_a} \right)^{1.261} + 4.6151 . \quad (8.42)$$

The error for the approximation is small enough to be negligible for the wind turbine noise prediction.

Since the results for both the prediction and field measurement are acquired in 1/3-octave bands, a correction for 1/3-octave band analysis is also taken into account by the

following equation [82]:

$$A_{\text{atm},1/3} = A_{\text{atm}}(1.0053255 - 0.00122622A_{\text{atm}})^{1.6} \quad (\text{dB}), \quad (8.43)$$

where A_{atm} is the excess atmospheric attenuation at the center frequency of 1/3-octave band and $A_{\text{atm},1/3}$ is the corrected 1/3-octave attenuation employed in the noise prediction code.

8.4.3 Prediction Procedure

The sound power level for the full-scale wind turbine can be calculated as shown in Figure 8.10. The detailed procedure is presented as follows

- (1) Input the profile, pitch angle, local twist angle of each blade segment as well as the wind turbine operating conditions, including rpm, incoming wind speed and weather conditions of the field-test.
- (2) Calculate inflow velocity U_{∞} and local angle of attack α for each blade segments based on BEMT, which can be achieved by iterations over Eqs. (8.1)-(8.10).
- (3) Input U_{∞} and α , obtained in step (2), for each blade segment into Xfoil to get the estimation of boundary layer displacement thickness δ^* .
- (4) Input data of the airfoil test models S1–S5 (blade segments in tip region) acquired in UAT Campaign 2 and estimated using Xfoil, which includes the corrected angle of attack α_c , freestream velocity U_{∞} , sound pressure level $[SPL_{1/3}]_{\text{UAT}}$ in 1/3 octave-band integrated over the TE region (as shown in Figure 8.3) and the corresponding frequency f from wind tunnel measurements and the boundary layer displacement thickness δ^* from Xfoil.
- (5) Generate a look-up table of the noise scaling function from the data input from step (4) using Eqs. (8.25) and (8.30). In the look-up table, a NSF value can be found for any arbitrary angle of attack α and frequency f within the table's range through data interpolation.

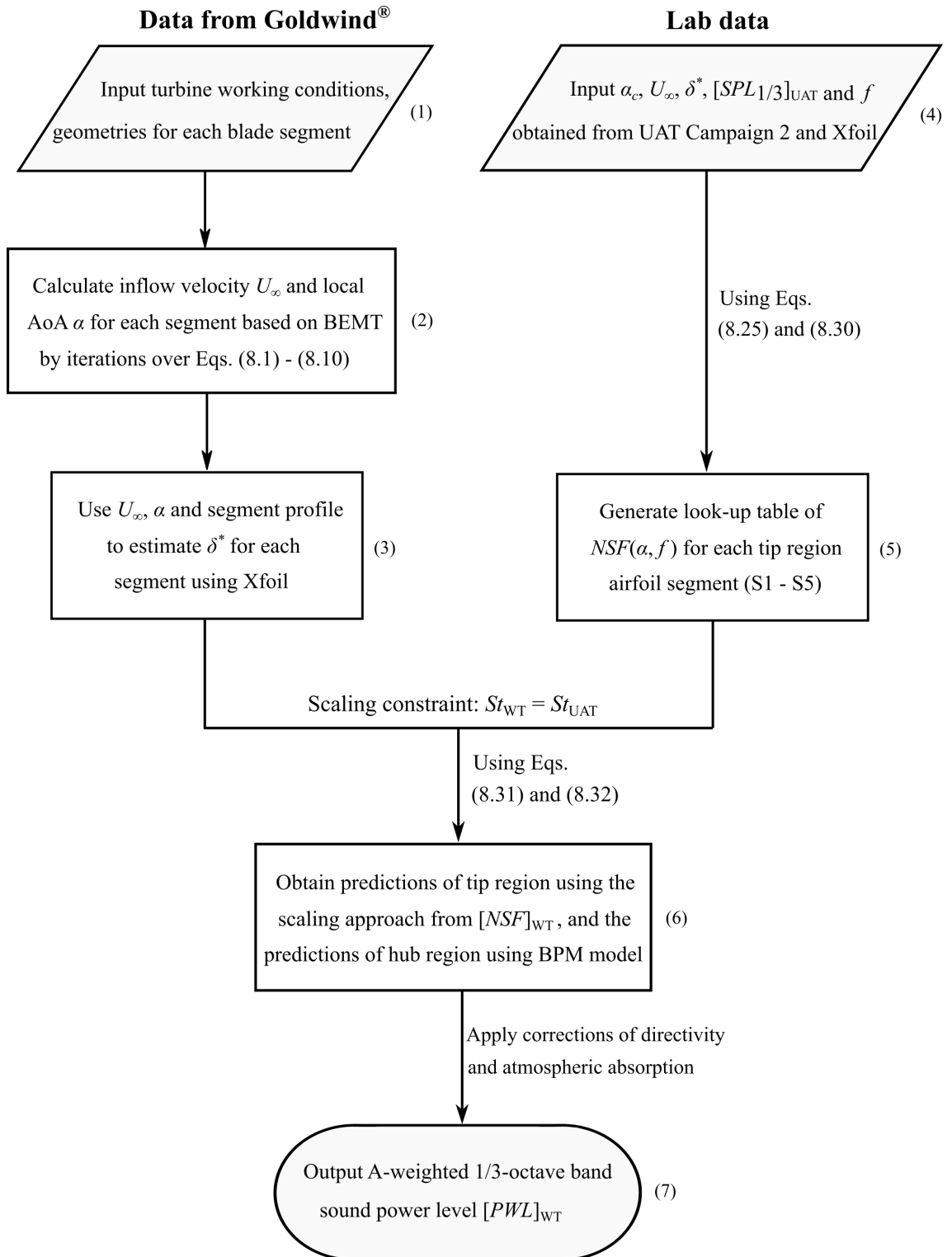


Figure 8.10: Flow chart for the wind turbine noise prediction program using noise scaling function (NSF) and BPM model.

- (6) Based on the data obtained from steps (2), (3) and (5), scale the lab acoustic data to the sound pressure level of the blade tip region using Eqs. (8.31) and (8.32), of which the scaling constraint is $St_{WT} = St_{UAT}$. Calculate the sound pressure level for the blade hub region using BPM model and data obtained from previous steps.
- (7) Apply the corrections of the noise directivity and atmospheric absorption to the sound pressure level obtained in step (6) and convert the sound pressure level to A-weighted sound power level $[PWL]_{WT}$.

8.5 Prediction Results

This section presents the prediction results obtained using both the noise scaling and BPM model, which includes the noise spectra and the overall sound power level for the wind turbine operating at wind speed U_i of 7, 8, 9 and 9.5 m/s. Prediction results are then compared with the field-test data measured according to the setup shown in Figure 8.11, where the microphone was positioned 170 m downwind of the turbine tower on the ground. The field test was conducted according to Standard IEC 61400-11[50].

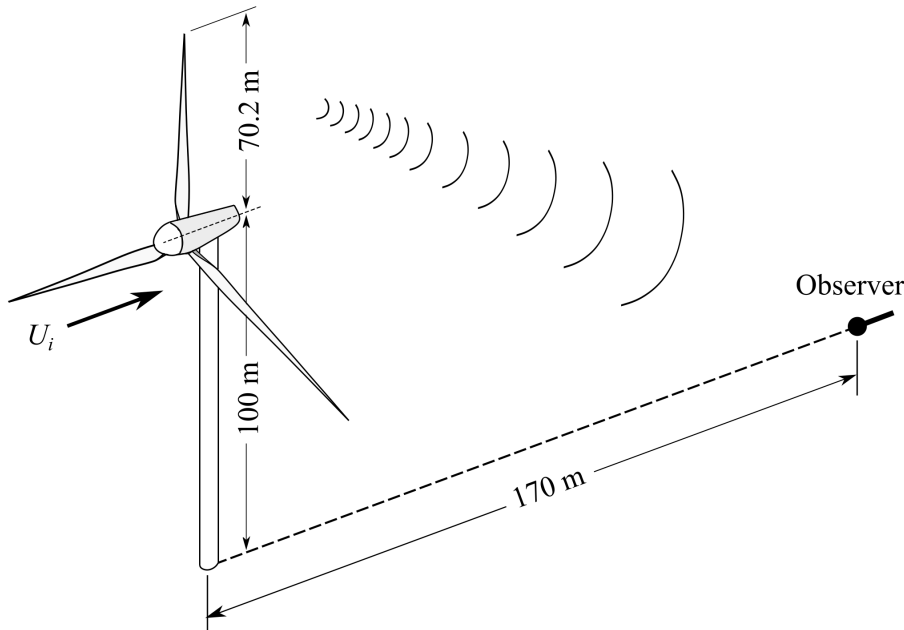


Figure 8.11: Schematic of the field-test setup.

8.5.1 Effects of Sound Propagation Corrections

The corrections for noise directivity and atmospheric absorption were applied in the prediction model as discussed in Sec. 8.4.2. Figure 8.12 shows the *NSF* prediction results for the wind turbine operating at rated RPM of 12 with a tip-speed ratio of 9.3, which corresponds to a wind speed U_i of 9.5 m/s. Figure 8.12a presents the uncorrected *NSF* prediction, which is in good agreement with the experimental data over frequencies up to 800 Hz. The predicted noise spectrum starts to deviate from the field-test spectrum over higher frequencies, overpredicting the noise levels of up to 30 dB at 10 kHz. The prediction results corrected by directivity function are shown in Figure 8.12b, where the peak levels of the noise spectrum (over 300 to 800 Hz) show a closer comparison with the field-test data. Atmospheric loss is more significant at higher frequencies. The deviation at the

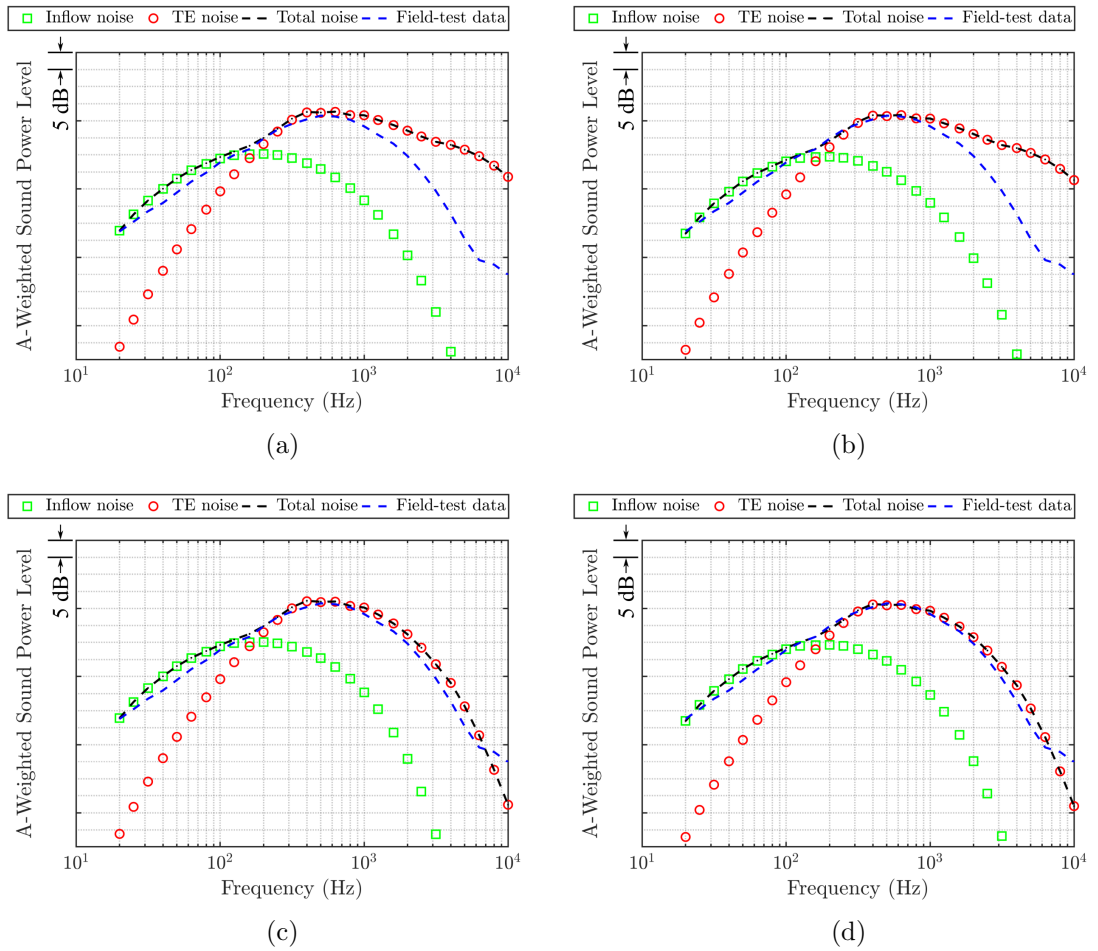


Figure 8.12: Wind turbine noise prediction results using *NSF* with (a) no correction; (b) directivity correction; (c) atmospheric correction; (d) directivity and atmospheric corrections for wind turbine operating at $U_i = 9.5$ m/s

higher frequency range (800 Hz to 10000 Hz) is corrected effectively (see Figure 8.12c) using the method described in Sec. 8.4.2 for the weather condition (ambient temperature $T_a = 288.15$ K, ambient pressure $P_a = 89150$ Pa and relative humidity $h_r = 20$ %) provided by Goldwind[®]. The prediction results with corrections of both the noise directivity and atmospheric loss (see Figure 8.12d) show good agreement with the experimental data over the entire frequency range.

8.5.2 Improvement of Wind Turbine Noise Prediction

As discussed in Sec. 8.4, the noise prediction model proposed in this thesis uses a noise scaling function NSF , combined with the semi-empirical BPM model, for wind turbine noise prediction. This model aims to improve the accuracy of the classic semi-empirical method which only uses BPM model for turbine noise prediction.

Figure 8.13a shows the comparison of predicted wind turbine noise spectra between NSF prediction, BPM prediction and field-test data for the wind turbine operating at $U_i = 9.5$ m/s. The NSF prediction yields better consistency with the field-test data, improving the prediction accuracy by up to 3 dB at the peak level of the noise spectra. Figure 8.13b presents the A-weighted overall sound power level of the NSF and BPM predictions compared with the field-test data at wind speed $U_i = 7$ –9.5 m/s. Here, the uncertainty of the field-test measurements is represented as error bars. The NSF method can accurately predict the overall sound power level with errors that are within the uncertainty of the

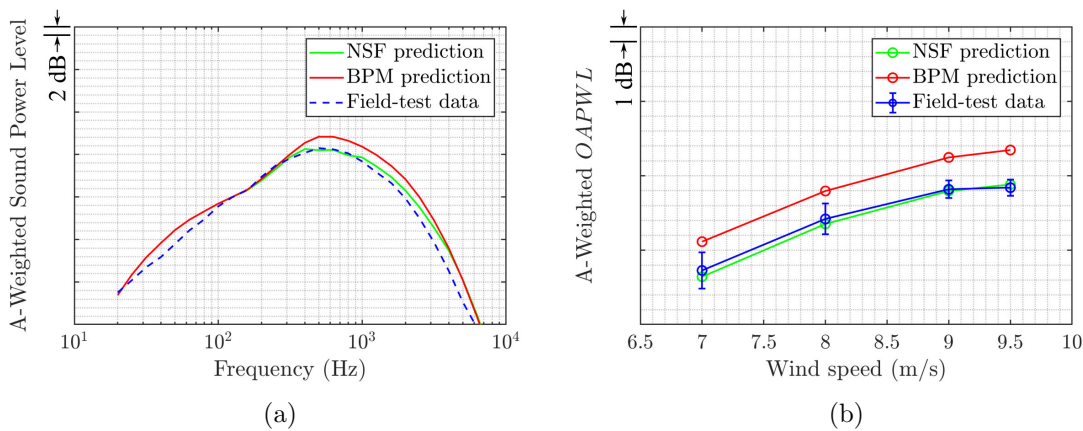


Figure 8.13: Comparison of the prediction results between NSF method and BPM model: (a) predicted noise spectra for the wind turbine operating at wind speed of 9.5 m/s; (b) predicted A-weighted overall sound power level for the wind turbine operating at wind speeds U_i from 7 to 9.5 m/s

experimental data, and improve the overall sound power prediction accuracy by 2–2.5 dB compared to BPM model.

8.6 Summary

The noise generated from a full-scale industrial wind turbine at operating conditions of incoming wind speeds of $U_i = 7\text{--}9.5\text{ m/s}$ and tip-speed ratio $X_{TSR} = 9.3$ is predicted using a noise prediction model based on the proposed noise scaling method and the semi-empirical BPM model. In this model, the TBL-TE noise from the blade tip region, as the most dominant noise source for the wind turbine, is estimated by a noise scaling function (NSF) using the information from the acoustic and aerodynamic data measured in UAT for five airfoil test models, which have profiles identical to five wind turbine blade segments at the tip region.

The acoustic and aerodynamic measurements for the airfoil test models are taken at a freestream velocity of $U_i = 30\text{ m/s}$ and geometric angles of attack of $\alpha_g = 0\text{--}16^\circ$ (with an increment of 2°) in the open-jet anechoic wind tunnel UAT. To account for the changes in angle of attack due to the open-jet effects, aerodynamic data are used for the angle of attack correction. The corrected angles of attack α_c are then used to scale the acoustic data of the airfoil test model to that of the wind turbine blade segment using NSF and the aerodynamics of the blade segments estimated using blade element momentum theory (BEMT) and Xfoil.

The details of the proposed prediction method have also been presented in this chapter, including the BEMT, inflow noise model, BPM model, TBL-TE noise scaling model, corrections of noise directivity and atmospheric absorption as well as the prediction procedure. According to the weather conditions provided by Goldwind[®], the atmospheric loss of the field test is considered to be significant at high frequencies from 800 to 10000 Hz. After the corrections of sound propagation, the NSF prediction results of both the noise spectra and overall sound power levels have shown excellent agreement with the field-test data at all incoming wind speeds $U_i = 7\text{--}9.5\text{ m/s}$, and an improvement of accuracy by up to 2–2.5 dB compared with the BPM prediction results.

Chapter 9

Conclusions

Airfoil trailing-edge (TE) noise, generated by the interaction of boundary layer turbulence or instabilities with the trailing edge, is an important noise source for airfoil applications such as wind turbines, aeroengine fans, propellers and drones. Effective TE noise control requires either altering the turbulent flow structures and strength in the boundary layer or reducing the acoustic scattering efficiency of the edge.

Based on these two principles, novel porous structures have first been acoustically characterised to facilitate the design of porous TE geometries. Next, the aeroacoustic performance and near-wake flow characteristics of a series of flat-plate TE extensions (attached to a NACA 0012 airfoil) with novel porous and serrated geometries have been examined in the UNSW anechoic wind tunnel (UAT). In addition to experimental investigations, the near-field flow and far-field sound pressure for a NACA 0012 airfoil with novel porous TE have been numerically simulated. After that, novel TE treatments have been applied to a set of rotor blades with a NACA 0012 profile. The aeroacoustic performance of the treated rotor blades has been evaluated on the UNSW rotor rig. Finally, a wind turbine noise prediction method has been developed. The prediction results have been compared with the field-test data for a full-scale industrial wind turbine. The following sections summarise the major conclusions and suggest potential future work.

9.1 Thesis Summary

The major achievements and findings are summarised as follows:

- **Sound absorption of additively manufactured novel porous structures for airfoil and rotor TE noise control**

Two types of novel porous structures have been designed, additively manufactured

and acoustically characterised (Chapter 4). For the micro-tube porous structure, good sound absorption ($\alpha_p=0.25-0.9$) can be achieved over higher frequencies (3.2–6.4 kHz). Two geometric design criteria for this structure have been established: 1) the peak frequency of the sound absorption coefficient can be shifted to lower frequencies by decreasing the porosity; 2) for the micro-tube structure with a certain porosity, a maximum sound absorption coefficient can be achieved by selecting an optimal pore aspect ratio (0.1 for specimens examined in this study). This micro-tube structure has been applied in airfoil and rotor TE noise control as presented in Chapters 5–7.

The other novel porous structure (PF structure) consists of a micro-perforated housing and a Basotech[®] acoustic foam infill. Such structure can provide efficient broadband sound absorption with a limited specimen thickness, where the peak sound absorption can be effectively predicted by Maa's model. Therefore, the peak sound absorption for such a structure can be tuned to the desired frequency range by optimally designing the micro-perforated geometries based on Maa's model.

- **The noise reduction performance of novel TE designs on airfoil LBL-TE noise**

The performance of eleven treated TE designs (including sawtooth-serrated, novel serrated, porous, porous-serrated and serrated-porous TEs as illustrated in Table. 3.4) in reducing LBL-TE noise of a natural-transitioned NACA 0012 airfoil at low-to-moderate Reynolds numbers ($1.9-3.2 \times 10^5$) have been assessed using the identical experimental setup in UAT (Sec. 5.2). Among these designs, the curved-serrated TE has the best performance in attenuating TE noise, showing an overall noise reduction (integrated over 0.25–10 kHz) of up to 16.4 dB over the entire Reynolds number range ($1.9-3.2 \times 10^5$). Traditional saw-tooth serrated TEs are shown to reduce the overall noise level at low Reynolds numbers, but introducing more high-level tonal noise at moderate Reynolds number ($2.9-3.2 \times 10^5$). For slitted, porous, porous-serrated TEs, they both fail to reduce the overall noise level over the entire Reynolds number range due to numerous excessive tones. However, serrated-porous TEs are found to consistently reduce the overall noise level by up to 14.2 dB over the entire Reynolds number range, in spite of a noise increase observed

at high frequencies ($St_b > 0.175$).

- **The noise reduction performance of novel TE designs on airfoil TBL-TE noise**

The performance of five treated TE designs in reducing TBL-TE noise of a forced-transitioned NACA 0012 airfoil at moderate Reynolds numbers ($3.2\text{--}8 \times 10^5$) have been assessed using the identical experimental setup in the UAT (Sec. 5.3). The overall noise reduction for frequency regions dominated by different noise mechanisms are evaluated. All five designs can efficiently reduce the overall noise level at frequencies dominated by TBL-TE noise over the entire Reynolds number range. The curved-serrated TE shows a greatest TBL-TE noise reduction of up to 4 dB, which is 1.4 dB more than that of the traditional saw-tooth serrated TE with the same value of λ/h . For the TE designs with porous geometries, their noise attenuation performance is compromised by the excessive noise observed at high frequencies ($St_b > 0.16$).

- **The role of porous geometries of a flat-plate TE extension in airfoil TE noise control**

According to the analytical study [99], the rigid flat-plate porous TE can effectively reduce the TBL-TE noise level at low frequencies. This has been confirmed by the measurements in Sec. 5.3. However, a high-frequency noise increase is observed for all TE designs with porous geometries as reported above. The level of the excessive noise is found to increase with the area of porous geometries, indicating that this noise increase originating from the porous geometries. When applying porous geometries in TE noise control, the inherent high-frequency noise associated with their geometries should be considered.

- **Flow characteristics related to the LBL-TE noise reduction by treated TE extensions**

Mean and fluctuating velocities have been measured in the near-wake of the natural-transitioned airfoil with treated TE extensions at a Reynolds number of 2.9×10^5 (Sec. 6.2). The spanwise-variant edge geometries are found to alter the flow structure at the TE, since both mean and fluctuating velocities vary significantly for different

treated TE extensions. Moreover, both the frequency and intensity of the peaks in the near-wake velocity spectra are highly correlated with the LBL-TE tonal noise measured in the far-field (Sec. 5.2). This indicates that a reduction of LBL-TE noise by treated TE extensions is achieved by altering the flow structures related to the amplification of T-S waves, hence suppressing the aeroacoustic feedback loop.

- **Noise intensity factor for relating near-wake flow statistics to TBL-TE noise generation**

The flow characteristics in a near-wake plane of the forced-transitioned airfoil with treated TE extensions at a Reynolds number of 5.8×10^5 are characterised in terms of mean velocity, turbulence intensity and turbulence integral length scale (Sec. 6.3). A noise intensity factor is proposed to estimate the combined effects of these flow statistics on TBL-TE noise generation. This noise intensity factor is integrated over the near-wake plane of treated TEs to account for the spanwise-variations induced by treated edge geometries and relate the near-wake flow statistics to the TBL-TE noise reduction by treated TEs. The integration results are consistent with the TBL-TE noise results in Sec. 5.3.

- **Mechanisms of the noise reduction and increase by the micro-tube porous TE**

Flow fields around the straight and micro-tube porous TEs of a forced-transitioned NACA 0012 airfoil at $\alpha = 5^\circ$ and $U_\infty = 50$ m/s have been numerically simulated (Sec. 6.4). The far-field noise levels predicted by the FWH acoustic analogy are in a reasonably good agreement (error < 5 dB over 2–8 kHz) with experimental data, and the frequency regions of noise reduction and increase by the porous TE have been accurately captured.

A detailed analysis of the flow and acoustic results reveals that the noise reduction by the porous TE may be attributed to 1) reduced magnitudes of the acoustic source term related to Reynolds shear-stress, 2) reduced spanwise correlations of wall pressure fluctuations and 3) reduced turbulence convection velocity near the TE. These changes are considered to be mainly due to the flow perturbations propagating through the pores, breaking up coherent turbulent flow structures and reducing the

acoustic impedance jump at the TE. The wall pressure fluctuation results suggest that the excessive high-frequency broadband noise originates from the interactions between the pore suction-side TE geometries with turbulence from the upstream boundary layer and pore flow permeation.

- **Aeroacoustic performance for rotor blades with different TE designs**

The TE noise generated from four sets of rotor blades with straight (reference), porous, cut-serrated and extended-serrated TEs has been measured and processed using a phase-averaged beamforming method (Chapter 7). The cut-serrated TE is the most acoustically efficient design at high frequencies. However, due to the high-intensity bluntness vortex-shedding noise at low frequencies, cut-serrated TE increases the overall noise level by up to 7.8 dB and 7.1 dB for the natural- and forced-transitioned rotor blades. The extended-serrated TE can achieve the greatest overall noise reduction of up to 5.6 dB and 3.2 dB for the natural- and forced-transitioned rotor blades. The porous TE has the greatest potential in reducing low-frequency noise. However, the excessive high-frequency noise (as discussed above) is also observed for porous rotor blades, compromising their overall noise reduction to less than 5.1 dB and 0.7 dB for the natural- and forced-transitioned regimes.

- **The potential role of sound absorption in TE noise control**

The micro-tube porous TE of rotor blades can effectively control the noise levels for both LBL-TE and TBL-TE noise sources over the frequency range from 4 to 6.4 kHz (Sec.7.4), where its porous structures (based on specimen P4 in Chapter 4) have good sound absorption ($\alpha_p > 0.3$). In fact, porous rotor blades achieve their peak noise reduction within this frequency range for most operating conditions (except 800 RPM, 10° pitch). These indicate that the sound absorption of the TE geometries may play a role in TE noise attenuation by reducing the TE acoustic scattering efficiency.

- **TBL-TE noise scaling model for wind turbine noise prediction**

A noise scaling model tailored for the TBL-TE noise prediction for full-scale wind turbines is proposed. This model is based on a noise scaling function (NSF), which scales the acoustic results of the airfoil models in the anechoic wind tunnel to the

full-scale wind turbine in the field. After the corrections of sound propagation, the NSF prediction results have shown excellent agreement with the field-test data at all incoming wind speeds (7–9.5 m/s). Compared to the prediction method based on the BPM model, an improvement in prediction accuracy by up to 2–2.5 dB is achieved by the proposed NSF method.

9.2 Future Work

There are many potential future working themes and research methods to be extended, some of which are described here:

- The great potential of porous treatments in TE noise control has been confirmed. Different from past studies, porous structures are characterised in terms of their sound absorption coefficient instead of flow resistivity (permeability). The potential effect of sound absorption on TE noise generation have been investigated, however, not yet confirmed. To further justify it, a parametric study on porous TE structures with a similar flow resistivity but different sound absorption coefficient can be conducted. A good starting point would be the comparison between TEs made of the PF structure (broadband sound absorption), micro-tube structure (sound absorption in a relatively narrow bandwidth) and metal foam (no sound absorption) with a similar flow resistivity.
- The excessive high-frequency noise (as reported in past studies) has been observed for all TEs with porous structures in experiments and numerical simulations. Numerical results suggest that this noise source is caused by the interaction between the pore edge geometries and the turbulent flow that passes over it. Further studies can focus on how to attenuate the excessive noise source by modifying the pore edge geometries (such as bevelling and rounding).
- The flow statistics in the near-wake of treated novel TEs have been related to TBL-TE noise generation by the proposed noise intensity factor. However, this factor is not capable of predicting the TBL-TE noise to the exact level due to the lack of surface pressure fluctuation data. To gain a deeper understanding of the noise

reduction mechanisms for treated novel TEs, information on surface pressure fluctuations is important. Due to the complex geometries of novel TEs, it is extremely difficult to implement sufficiently small pressure sensors on their surface without introducing significant intrusive effects. Therefore, the non-intrusive time-resolved stereoscopic or tomographic PIV system can be good choice to measure and link the near-wall vertical velocity fluctuations to the TBL-TE noise source term related to surface pressure fluctuations.

- To apply low-noise TE treatments in realistic applications (such as wind turbines), their effect on the aerodynamic performance is important. This is because it can change the aerodynamic environment of the local blade segment, hence affecting the noise generation. A comprehensive aerodynamic force measurement can be performed to further verify the applicability of the novel TEs for TE noise control.
- The wind turbine noise prediction method based on the proposed noise scaling model has significantly improved the prediction accuracy of the method based on the BPM model. However, considering the uncertainties from the open-jet effects on the angle of attack and the Reynolds number difference between the airfoil test models and the full-scale wind turbine blade segments, further improvements can be potentially achieved by: 1) minimising the open-jet effects using a kevlar-wall anechoic wind tunnel; 2) applying a more accurate Reynolds number correction obtained from large-scale ($Re_c > 5 \times 10^5$) anechoic wind tunnel measurements. Moreover, this NSF method can be extended to predict the noise from full-scale wind turbines with novel TE treatments.

References

- [1] ACARE. Aeronautics and air transport: Beyond vision 2020 (towards 2050). Advisory Council for Aeronautics Research in Europe, 2010.
- [2] S. A. S. Ali, M. Azarpeyvand, and C. R. I. da Silva. Trailing-edge flow and noise control using porous treatments. Journal of Fluid Mechanics, 850:83–119, 2018.
- [3] S. A. S. Ali, M. Azarpeyvand, and C. R. I. da Silva. Trailing edge bluntness noise reduction using porous treatments. Journal of Sound and Vibration, 474:115257, 2020.
- [4] R. Amiet. Effect of the incident surface pressure field on noise due to turbulent flow past a trailing edge. 1978.
- [5] R. K. Amiet. Acoustic radiation from an airfoil in a turbulent stream. Journal of Sound and Vibration, 41(4):407–420, 1975.
- [6] R. K. Amiet. Noise due to turbulent flow past a trailing edge. Journal of Sound and Vibration, 47(3):387–393, 1976.
- [7] H. Arbey and J. Bataille. Noise generated by airfoil profiles placed in a uniform laminar flow. Journal of Fluid Mechanics, 134:33–47, 1983.
- [8] F. Archibald. The laminar boundary layer instability excitation of an acoustic resonance. Journal of Sound and Vibration, 38(3):387–402, 1975.
- [9] E. Arcondoulis, C. Doolan, and A. C. Zander. Airfoil noise measurements at various angles of attack and low reynolds number. In Proceedings of ACOUSTICS, pages 23–25, 2009.
- [10] E. Arcondoulis, C. Doolan, A. Zander, and L. Brooks. A review of trailing edge noise generated by airfoils at low to moderate reynolds number. Acoustics Australia, 38(3), 2010.
- [11] R. Arina, R. Della Ratta Rinaldi, A. Iob, and D. Torzo. Numerical study of self-noise produced by an airfoil with trailing-edge serrations. In 18th AIAA/CEAS Aeroacoustics Conference (33rd AIAA Aeroacoustics Conference), page 2184, 2012.
- [12] F. Avallone, S. Pröbsting, and D. Ragni. Three-dimensional flow field over a trailing-edge serration and implications on broadband noise. Physics of Fluids, 28(11):117101, 2016.

- [13] F. Avallone, W. Van der Velden, and D. Ragni. Benefits of curved serrations on broadband trailing-edge noise reduction. Journal of Sound and Vibration, 400:167–177, 2017.
- [14] F. Avallone, W. Van der Velden, D. Ragni, and D. Casalino. Noise reduction mechanisms of sawtooth and combed-sawtooth trailing-edge serrations. Journal of Fluid Mechanics, 848:560–591, 2018.
- [15] L. J. Ayton. Acoustic scattering by a finite rigid plate with a poroelastic extension. Journal of Fluid Mechanics, 791:414–438, 2016.
- [16] L. J. Ayton. Analytic solution for aerodynamic noise generated by plates with spanwise-varying trailing edges. Journal of Fluid Mechanics, 849:448–466, 2018.
- [17] M. Azarpeyvand, M. Gruber, and P. Joseph. An analytical investigation of trailing edge noise reduction using novel serrations. In 19th AIAA/CEAS Aeroacoustics Conference, page 2009, 2013.
- [18] T. Bachmann, S. Klän, W. Baumgartner, M. Klaas, W. Schröder, and H. Wagner. Morphometric characterisation of wing feathers of the barn owl *tyto alba pratincola* and the pigeon *columba livia*. Frontiers in Zoology, 4(1):23, 2007.
- [19] Y. Bae and Y. J. Moon. Effect of passive porous surface on the trailing-edge noise. Physics of Fluids, 23(12):126101, 2011.
- [20] C. Bahr, T. Yardibi, F. Liu, and L. Cattafesta. An analysis of different measurement techniques for airfoil trailing edge noise. In 14th AIAA/CEAS Aeroacoustics Conference (29th AIAA Aeroacoustics Conference), page 2957, 2008.
- [21] C. Bahr, J. Li, and L. Cattafesta. Aeroacoustic measurements in open-jet wind tunnels-an evaluation of methods applied to trailing edge noise. In 17th AIAA/CEAS Aeroacoustics Conference (32nd AIAA Aeroacoustics Conference), page 2771, 2011.
- [22] J. B. Barlow, W. H. Rae, and A. Pope. Low-speed wind tunnel testing. Wiley New York, 1999.
- [23] P. Bernicke, R. Akkermans, V. Ananthan, R. Ewert, J. Dierke, and L. Rossian. A zonal noise prediction method for trailing-edge noise with a porous model. International Journal of Heat and Fluid Flow, 80:108469, 2019.
- [24] W. K. Blake. Mechanics of flow-induced sound and vibration, Volume 2: Complex flow-structure interactions. Academic press, 2017.
- [25] W. K. Blake and J. L. Gershfeld. The aeroacoustics of trailing edges. In Frontiers in Experimental Fluid Mechanics, pages 457–532. Springer, 1989.

- [26] T. Brooks and C. Burley. Rotor broadband noise prediction with comparison to model data. In 7th AIAA/CEAS Aeroacoustics Conference and Exhibit, page 2210, 2001.
- [27] T. Brooks and W. Humphreys, Jr. Effect of directional array size on the measurement of airframe noise components. In 5th AIAA/CEAS Aeroacoustics Conference and Exhibit, page 1958, 1999.
- [28] T. F. Brooks and T. Hodgson. Trailing edge noise prediction from measured surface pressures. Journal of Sound and Vibration, 78(1):69–117, 1981.
- [29] T. F. Brooks and W. M. Humphreys. A deconvolution approach for the mapping of acoustic sources (damas) determined from phased microphone arrays. Journal of Sound and Vibration, 294(4-5):856–879, 2006.
- [30] T. F. Brooks and M. A. Marcolini. Scaling of airfoil self-noise using measured flow parameters. AIAA Journal, 23(2):207–213, 1985.
- [31] T. F. Brooks, D. S. Pope, and M. A. Marcolini. Airfoil self-noise and prediction. 1989.
- [32] S. Buck, S. Oerlemans, and S. Palo. Experimental characterization of turbulent inflow noise on a full-scale wind turbine. Journal of Sound and Vibration, 385: 219–238, 2016.
- [33] S. Buck, S. Oerlemans, and S. Palo. Experimental validation of a wind turbine turbulent inflow noise prediction code. AIAA Journal, 56(4):1495–1506, 2018.
- [34] A. R. Carpio, F. Avallone, D. Ragni, M. Snellen, and S. van der Zwaag. Mechanisms of broadband noise generation on metal foam edges. Physics of Fluids.
- [35] A. R. Carpio, R. M. Martínez, F. Avallone, D. Ragni, M. Snellen, and S. van der Zwaag. Experimental characterization of the turbulent boundary layer over a porous trailing edge for noise abatement. Journal of Sound and Vibration, 443:537–558, 2019.
- [36] K. Chandiramani. Diffraction of evanescent waves, with applications to aerodynamically scattered sound and radiation from un baffled plates. the Journal of the Acoustical Society of America, 55(1):19–29, 1974.
- [37] D. M. Chase. Sound radiated by turbulent flow off a rigid half-plane as obtained from a wavevector spectrum of hydrodynamic pressure. the Journal of the Acoustical Society of America, 52(3B):1011–1023, 1972.
- [38] D. M. Chase. Noise radiated from an edge in turbulent flow. AIAA Journal, 13(8): 1041–1047, 1975.

- [39] T. Chong, P. Joseph, and M. Kingan. An investigation of airfoil tonal noise at different reynolds numbers and angles of attack. Applied Acoustics, 74(1):38–48, 2013.
- [40] T. P. Chong and E. Dubois. Optimization of the poro-serrated trailing edges for airfoil broadband noise reduction. the Journal of the Acoustical Society of America, 140(2):1361–1373, 2016.
- [41] T. P. Chong and P. Joseph. An experimental study of tonal noise mechanism of laminar airfoils. In 15th AIAA/CEAS Aeroacoustics Conference (30th AIAA Aeroacoustics Conference), page 3345, 2009.
- [42] T. P. Chong and P. F. Joseph. An experimental study of airfoil instability tonal noise with trailing edge serrations. Journal of Sound and Vibration, 332(24):6335–6358, 2013.
- [43] T. P. Chong and A. Vathylakis. On the aeroacoustic and flow structures developed on a flat plate with a serrated sawtooth trailing edge. Journal of Sound and Vibration, 354:65–90, 2015.
- [44] T. P. Chong, P. Joseph, A. Vathylakis, and M. Gruber. On the noise and wake flow of an airfoil with broken and serrated trailing edges. In 17th AIAA/CEAS Aeroacoustics Conference (32nd AIAA Aeroacoustics Conference), page 2860, 2011.
- [45] T. P. Chong, A. Vathylakis, P. F. Joseph, and M. Gruber. Self-noise produced by an airfoil with nonflat plate trailing-edge serrations. AIAA Journal, 51(11):2665–2677, 2013.
- [46] J. Chung and D. Blaser. Transfer function method of measuring in-duct acoustic properties. i. theory. the Journal of the Acoustical Society of America, 68(3):907–913, 1980.
- [47] I. Clark, W. J. Devenport, J. Jaworski, C. Daly, N. Peake, and S. A. Glegg. The noise generating and suppressing characteristics of bio-inspired rough surfaces. In 20th AIAA/CEAS Aeroacoustics Conference, page 2911, 2014.
- [48] I. A. Clark, W. N. Alexander, W. Devenport, S. Glegg, J. W. Jaworski, C. Daly, and N. Peake. Bioinspired trailing-edge noise control. AIAA Journal, 55(3):740–754, 2017.
- [49] I. E. Commission et al. Wind turbine generator systems-part 1: Safety requirements. IEC 61400-1, 1999.
- [50] I. E. Commission et al. Wind turbine generator systems-part 11: Acoustic noise measurement techniques. IEC 61400-11, 2012.

-
- [51] I. B. Crandall. Theory of vibrating systems and sound. D. Van Nostrand Company, 1926.
- [52] D. Crighton and F. Leppington. Scattering of aerodynamic noise by a semi-infinite compliant plate. Journal of Fluid Mechanics, 43(4):721–736, 1970.
- [53] N. Curle. The influence of solid boundaries upon aerodynamic sound. In Proceedings of the Royal Society of London A: Mathematical, Physical and Engineering Sciences, volume 231, pages 505–514. The Royal Society, 1955.
- [54] T. Dassen, R. Parchen, J. Bruggeman, and F. Hagg. Results of a wind tunnel study on the reduction of airfoil self-noise by the application of serrated blade trailing edges. 1996.
- [55] G. Desquesnes, M. Terracol, and P. Sagaut. Numerical investigation of the tone noise mechanism over laminar airfoils. Journal of Fluid Mechanics, 591:155–182, 2007.
- [56] W. Devenport, R. Burdisso, H. Camargo, E. Crede, M. Remillieux, M. Rasnick, and P. Van Seeters. Aeroacoustic testing of wind turbine airfoils. National Renewable Energy Laboratory (NREL), Blacksburg, Virginia, 2010.
- [57] W. J. Devenport, R. A. Burdisso, A. Borgoltz, P. A. Ravetta, M. F. Barone, K. A. Brown, and M. A. Morton. The kevlar-walled anechoic wind tunnel. Journal of Sound and Vibration, 332(17):3971–3991, 2013.
- [58] C. J. Doolan and D. J. Moreau. A review of airfoil trailing edge noise with some implications for wind turbines. International Journal of Aeroacoustics, 14(5-6):811–832, 2015.
- [59] M. Drela. Xfoil: An analysis and design system for low reynolds number airfoils. In Low Reynolds number aerodynamics, pages 1–12. Springer, 1989.
- [60] L. Evans, H. Bass, and L. Sutherland. Atmospheric absorption of sound: Theoretical predictions. the Journal of the Acoustical Society of America, 51(5B):1565–1575, 1972.
- [61] R. Ewert, C. Appel, J. Dierke, and M. Herr. Rans/caa based prediction of naca 0012 broadband trailing edge noise and experimental validation. In 15th AIAA/CEAS Aeroacoustics Conference (30th AIAA Aeroacoustics Conference), page 3269, 2009.
- [62] B. W. Fassmann, C. Rautmann, R. Ewert, and J. Delfs. Prediction of porous trailing edge noise reduction via acoustic perturbation equations and volume averaging. In 21st AIAA/CEAS Aeroacoustics Conference, page 2525, 2015.

- [63] J. E. Ffowcs Williams and D. L. Hawkings. Sound generation by turbulence and surfaces in arbitrary motion. Philosophical Transactions of the Royal Society of London. Series A, Mathematical and Physical Sciences, 264(1151):321–342, 1969.
- [64] A. Finez, M. Jacob, E. Jondeau, and M. Roger. Broadband noise reduction with trailing edge brushes. In 16th AIAA/CEAS Aeroacoustics Conference, page 3980, 2010.
- [65] M. R. Fink. Experimental evaluation of theories for trailing edge and incidence fluctuation noise. AIAA Journal, 13(11):1472–1477, 1975.
- [66] P. Freymuth and L. M. Fingerson. Hot-wire anemometry at very high frequencies: effect of electronic noise. Measurement Science and Technology, 8(2):115, 1997.
- [67] M. Germano, U. Piomelli, P. Moin, and W. H. Cabot. A dynamic subgrid-scale eddy viscosity model. Physics of Fluids A: Fluid Dynamics, 3(7):1760–1765, 1991.
- [68] T. Geyer, E. Sarradj, and C. Fritzsche. Measurement of the noise generation at the trailing edge of porous airfoils. Experiments in Fluids, 48(2):291–308, 2010.
- [69] T. Geyer, E. Sarradj, and C. Fritzsche. Porous airfoils: noise reduction and boundary layer effects. International Journal of Aeroacoustics, 9(6):787–820, 2010.
- [70] T. Geyer, E. Sarradj, and C. Fritzsche. Silent owl flight: acoustic wind tunnel measurements on prepared wings. In 18th AIAA/CEAS Aeroacoustics Conference (33rd AIAA Aeroacoustics Conference), page 2230, 2012.
- [71] T. F. Geyer and E. Sarradj. Trailing edge noise of partially porous airfoils. In 20th AIAA/CEAS Aeroacoustics Conference, page 3039, 2014.
- [72] S. Glegg and W. Devenport. Aeroacoustics of low Mach number flows: fundamentals, analysis, and measurement. Academic Press, 2017.
- [73] X. Gloerfelt and T. Le Garrec. Trailing edge noise from an isolated airfoil at a high reynolds number. In 15th AIAA/CEAS Aeroacoustics Conference (30th AIAA Aeroacoustics Conference), page 3201, 2009.
- [74] L. Goines and L. Hagler. Noise pollution: a modem plague. South Med J, 100(3):287–94, 2007.
- [75] R. Graham. The silent flight of owls. The Aeronautical Journal, 38(286):837–843, 1934.
- [76] M. Gruber. Airfoil noise reduction by edge treatments. PhD thesis, University of Southampton, 2012.

- [77] M. Gruber, M. Azarpeyvand, and P. F. Joseph. Airfoil trailing edge noise reduction by the introduction of sawtooth and slitted trailing edge geometries. integration, 10:6, 2010.
- [78] M. Gruber, P. Joseph, and T. P. Chong. Experimental investigation of airfoil self noise and turbulent wake reduction by the use of trailing edge serrations. In 16th AIAA/CEAS Aeroacoustics Conference, page 3803, 2010.
- [79] M. Gruber, P. Joseph, and T. Chong. On the mechanisms of serrated airfoil trailing edge noise reduction. In 17th AIAA/CEAS Aeroacoustics Conference (32nd AIAA Aeroacoustics Conference), page 2781, 2011.
- [80] M. Gruber, P. Joseph, and M. Azarpeyvand. An experimental investigation of novel trailing edge geometries on airfoil trailing edge noise reduction. In 19th AIAA/CEAS Aeroacoustics Conference, page 2011, 2013.
- [81] G. Guidati, R. Bareiss, S. Wagner, R. Parchen, G. Guidati, R. Bareiss, S. Wagner, and R. Parchen. Simulation and measurement of inflow-turbulence noise on airfoils. In 3rd AIAA/CEAS Aeroacoustics Conference, page 1698, 1997.
- [82] C. H. Hansen, C. J. Doolan, and K. L. Hansen. Wind farm noise: measurement, assessment, and control. John Wiley & Sons, 2017.
- [83] M. Herr. Design criteria for low-noise trailing-edges. In 13th AIAA/CEAS Aeroacoustics Conference (28th AIAA Aeroacoustics Conference), page 3470, 2007.
- [84] M. Herr and W. Dobrzynski. Experimental investigations in low-noise trailing edge design. AIAA Journal, 43(6):1167–1175, 2005.
- [85] M. Herr, R. Ewert, and J. Dierke. Trailing-edge noise data quality assessment for caa validation. In 16th AIAA/CEAS Aeroacoustics Conference, page 3877, 2010.
- [86] M. Herr, K.-S. Rossignol, J. Delfs, N. Lippitz, and M. Mößner. Specification of porous materials for low-noise trailing-edge applications. In 20th AIAA/CEAS Aeroacoustics Conference, page 3041, 2014.
- [87] A. Herrig, W. Würz, T. Lutz, and E. Krämer. Trailing-edge noise measurements using a hot-wire based coherent particle velocity method. In 24th AIAA Applied Aerodynamics Conference, page 3876, 2006.
- [88] A. Herrig, W. Würz, E. Krämer, and S. Wagner. New cpv-results of naca 0012 trailing-edge noise. In Int. Conference on Methods of Aerophysical Research ICMAR, Novosibirsk, volume 30, 2008.
- [89] J. Hinze. Turbulence, mcgraw-hill, new york, 1975.
- [90] M. Howe. The influence of vortex shedding on the generation of sound by convected turbulence. Journal of Fluid Mechanics, 76(4):711–740, 1976.

- [91] M. S. Howe. A review of the theory of trailing edge noise. Journal of Sound and Vibration, 61(3):437–465, 1978.
- [92] M. S. Howe. Noise produced by a sawtooth trailing edge. the Journal of the Acoustical Society of America, 90(1):482–487, 1991.
- [93] M. S. Howe. Trailing edge noise at low mach numbers. Journal of Sound and Vibration, 225(2):211–238, 1999.
- [94] M. S. Howe. Edge-source acoustic green’s function for an airfoil of arbitrary chord, with application to trailing-edge noise. Quarterly Journal of Mechanics and Applied Mathematics, 54(1):139–155, 2001.
- [95] N. Hu, N. Reiche, and R. Ewert. Simulation of turbulent boundary layer wall pressure fluctuations via poisson equation and synthetic turbulence. Journal of Fluid Mechanics, 826:421–454, 2017.
- [96] F. V. Huthcheson and T. F. Brooks. Measurement of trailing edge noise using directional array and coherent output power methods. International Journal of Aeroacoustics, 1(4):329–353, 2002.
- [97] T. Ikeda, T. Atobe, and S. Takagi. Direct simulations of trailing-edge noise generation from two-dimensional airfoils at low reynolds numbers. Journal of Sound and Vibration, 331(3):556–574, 2012.
- [98] S. A. Janssen, H. Vos, A. R. Eisses, and E. Pedersen. A comparison between exposure-response relationships for wind turbine annoyance and annoyance due to other noise sources. the Journal of the Acoustical Society of America, 130(6):3746–3753, 2011.
- [99] J. W. Jaworski and N. Peake. Aerodynamic noise from a poroelastic edge with implications for the silent flight of owls. Journal of Fluid Mechanics, 723:456–479, 2013.
- [100] J. W. Jaworski and N. Peake. Aeroacoustics of silent owl flight. Annual Review of Fluid Mechanics, 52, 2020.
- [101] L. Jones and R. Sandberg. Numerical investigation of airfoil self-noise reduction by addition of trailing-edge serrations. In 16th AIAA/CEAS Aeroacoustics Conference, page 3703, 2010.
- [102] L. Jones and R. Sandberg. Acoustic and hydrodynamic analysis of the flow around an aerofoil with trailing-edge serrations. Journal of Fluid Mechanics, 706:295–322, 2012.

- [103] L. Jones, R. Sandberg, and N. Sandham. Investigation and prediction of transitional airfoil self-noise. In 15th AIAA/CEAS Aeroacoustics Conference (30th AIAA Aeroacoustics Conference), page 3104, 2009.
- [104] L. Jones, R. Sandberg, and N. Sandham. Stability and receptivity characteristics of a laminar separation bubble on an aerofoil. Journal of Fluid Mechanics, 648:257, 2010.
- [105] L. E. Jones and R. D. Sandberg. Numerical analysis of tonal airfoil self-noise and acoustic feedback-loops. Journal of Sound and Vibration, 330(25):6137–6152, 2011.
- [106] M. J. Kingan and J. R. Pearse. Laminar boundary layer instability noise produced by an aerofoil. Journal of Sound and Vibration, 322(4-5):808–828, 2009.
- [107] A. Kisil and L. J. Ayton. Aerodynamic noise from rigid trailing edges with finite porous extensions. Journal of Fluid Mechanics, 836:117–144, 2018.
- [108] T. Le Garrec, X. Gloerfelt, and C. Corre. Direct noise computation of trailing edge noise at high reynolds numbers. In 14th AIAA/CEAS Aeroacoustics Conference (29th AIAA Aeroacoustics Conference), page 2914, 2008.
- [109] G. J. Leishman. Principles of helicopter aerodynamics with CD extra. Cambridge university press, 2006.
- [110] A. C. Leon, F. Avallone, S. Pröbsting, and D. Ragni. Piv investigation of the flow past solid and slitted sawtooth serrated trailing edges. In 54th AIAA Aerospace Sciences Meeting, page 1014, 2016.
- [111] C. A. León, D. Ragni, S. Pröbsting, and F. Scarano. Flow field around a serrated trailing edge at incidence. In 33rd Wind Energy Symposium, page 0991, 2015.
- [112] C. A. León, R. Merino-Martínez, D. Ragni, F. Avallone, and M. Snellen. Boundary layer characterization and acoustic measurements of flow-aligned trailing edge serrations. Experiments in Fluids, 57(12):182, 2016.
- [113] C. A. León, D. Ragni, S. Pröbsting, F. Scarano, and J. Madsen. Flow topology and acoustic emissions of trailing edge serrations at incidence. Experiments in Fluids, 57(5):91, 2016.
- [114] C. A. León, R. Merino-Martínez, D. Ragni, F. Avallone, F. Scarano, S. Pröbsting, M. Snellen, D. G. Simons, and J. Madsen. Effect of trailing edge serration-flow misalignment on airfoil noise emissions. Journal of Sound and Vibration, 405:19–33, 2017.
- [115] C. A. León, R. Merino-Martínez, S. Pröbsting, D. Ragni, and F. Avallone. Acoustic emissions of semi-permeable trailing edge serrations. Acoustics Australia, 46(1): 111–117, 2018.

- [116] L. Leylekian, M. Lebrun, and P. Lempereur. An overview of aircraft noise reduction technologies. 2014.
- [117] M. J. Lighthill. On sound generated aerodynamically i. general theory. Proceedings of the Royal Society of London. Series A. Mathematical and Physical Sciences, 211 (1107):564–587, 1952.
- [118] M. J. Lighthill. On sound generated aerodynamically ii. turbulence as a source of sound. Proceedings of the Royal Society of London. Series A. Mathematical and Physical Sciences, 222(1148):1–32, 1954.
- [119] G. Lilley. A study of the silent flight of the owl. In 4th AIAA/CEAS Aeroacoustics Conference, page 2340, 1998.
- [120] D. K. Lilly. A proposed modification of the germano subgrid-scale closure method. Physics of Fluids A: Fluid Dynamics, 4(3):633–635, 1992.
- [121] X. Liu, H. Kamliya Jawahar, M. Azarpeyvand, and R. Theunissen. Aerodynamic performance and wake development of airfoils with serrated trailing-edges. AIAA Journal, pages 3669–3680, 2017.
- [122] M. Lowson, S. Fiddes, and E. Nash. Laminar boundary layer aero-acoustic instabilities. In 32nd Aerospace Sciences Meeting and Exhibit, page 358, 1994.
- [123] M. Lowson, A. McAlpine, and E. Nash. The generation of boundary layer instability noise on aerofoils. In 36th AIAA Aerospace Sciences Meeting and Exhibit, page 627, 1998.
- [124] M. V. Lowson. Assessment and prediction of wind turbine noise. Technical report, Flow Solutions Ltd., 1993.
- [125] B. Lyu, M. Azarpeyvand, and S. Sinayoko. Prediction of noise from serrated trailing edges. Journal of Fluid Mechanics, 793:556–588, 2016.
- [126] D.-Y. Maa. Theory and design of microperforated panel sound-absorbing constructions. Scientia Sinica, 18(1):55–71, 1975.
- [127] D.-Y. Maa. Microperforated-panel wideband absorbers. Noise Control Engineering Journal, 29(3):77–84, 1987.
- [128] D.-Y. Maa. Potential of microperforated panel absorber. the Journal of the Acoustical Society of America, 104(5):2861–2866, 1998.
- [129] O. Marsden, C. Bogey, and C. Bailly. Direct noise computation of the turbulent flow around a zero-incidence airfoil. AIAA Journal, 46(4):874–883, 2008.

- [130] A. McAlpine, E. Nash, and M. Lowson. On the generation of discrete frequency tones by the flow around an aerofoil. Journal of Sound and Vibration, 222(5):753–779, 1999.
- [131] P. Migliore and S. Oerlemans. Wind tunnel aeroacoustic tests of six airfoils for use on small wind turbines. J. Sol. Energy Eng., 126(4):974–985, 2004.
- [132] D. Moreau and C. Doolan. The generation of tonal noise from sawtooth trailing-edge serrations at low reynolds numbers. The Aeronautical Journal, 120(1228):971–983, 2016.
- [133] D. J. Moreau and C. J. Doolan. Noise-reduction mechanism of a flat-plate serrated trailing edge. AIAA Journal, 51(10):2513–2522, 2013.
- [134] D. J. Moreau, L. A. Brooks, and C. J. Doolan. Broadband trailing edge noise from a sharp-edged strut. the Journal of the Acoustical Society of America, 129(5):2820–2829, 2011.
- [135] D. J. Moreau, C. J. Doolan, W. N. Alexander, T. W. Meyers, and W. J. Devenport. Wall-mounted finite airfoil-noise production and prediction. AIAA Journal, pages 1637–1651, 2016.
- [136] S. Moreau and M. Roger. Effect of airfoil aerodynamic loading on trailing edge noise sources. AIAA Journal, 43(1):41–52, 2005.
- [137] S. Moreau and M. Roger. Back-scattering correction and further extensions of amiet’s trailing-edge noise model. part ii: Application. Journal of Sound and Vibration, 323(1-2):397–425, 2009.
- [138] P. Moriarty. Nafnoise: a program for calculating 2d airfoil noise. Design code, National Wind Technology Center, USA, 2003.
- [139] P. Moriarty and P. Migliore. Semi-empirical aeroacoustic noise prediction code for wind turbines. Technical report, National Renewable Energy Lab., Golden, CO.(US), 2003.
- [140] P. Moriarty, G. Guidati, and P. Migliore. Recent improvement of a semi-empirical aeroacoustic prediction code for wind turbines. In 10th AIAA/CEAS Aeroacoustics Conference, page 3041, 2004.
- [141] T. Mueller, C. Allen, W. Blake, R. Dougherty, D. Lynch, P. Soderman, and J. Underbrink. Aeroacoustic Measurements. Springer, 2002.
- [142] T. Nakano, N. Fujisawa, and S. Lee. Measurement of tonal-noise characteristics and periodic flow structure around naca0018 airfoil. Experiments in Fluids, 40(3):482–490, 2006.

- [143] E. C. Nash, M. V. Lowson, and A. McAlpine. Boundary-layer instability noise on aerofoils. Journal of Fluid Mechanics, 382:27–61, 1999.
- [144] A. A. Oberai, F. Roknaldin, and T. J. Hughes. Computation of trailing-edge noise due to turbulent flow over an airfoil. AIAA Journal, 40(11):2206–2216, 2002.
- [145] S. Oerlemans. Reduction of wind turbine noise using blade trailing edge devices. In 22nd AIAA/CEAS Aeroacoustics Conference, page 3018, 2016.
- [146] S. Oerlemans and P. Migliore. Aeroacoustic wind tunnel tests of wind turbine airfoils. In 10th AIAA/CEAS Aeroacoustics Conference, page 3042, 2004.
- [147] S. Oerlemans, J. Schepers, G. Guidati, and S. Wagner. Experimental demonstration of wind turbine noise reduction through optimized airfoil shape and trailing-edge serrations. 2001.
- [148] S. Oerlemans, P. Sijtsma, and B. M. López. Location and quantification of noise sources on a wind turbine. Journal of Sound and Vibration, 299(4-5):869–883, 2007.
- [149] S. Oerlemans, M. Fisher, T. Maeder, and K. Kögler. Reduction of wind turbine noise using optimized airfoils and trailing-edge serrations. AIAA Journal, 47(6):1470–1481, 2009.
- [150] K. Ohlenforst and G. W. E. Council. Global wind report 2018, 2019.
- [151] T. Padois, C. Prax, and V. Valeau. Numerical validation of shear flow corrections for beamforming acoustic source localisation in open wind-tunnels. Applied Acoustics, 74(4):591–601, 2013.
- [152] R. R. Parchen. Progress report DRAW: A prediction scheme for trailing edge noise based on detailed boundary layer characteristics. TNO Institute of Applied Physics, 1998.
- [153] R. W. Paterson, P. G. Vogt, M. R. Fink, and C. L. Munch. Vortex noise of isolated airfoils. Journal of Aircraft, 10(5):296–302, 1973.
- [154] A. Powell. On the aerodynamic noise of a rigid flat plate moving at zero incidence. the Journal of the Acoustical Society of America, 31(12):1649–1653, 1959.
- [155] Z. Prime, C. Doolan, and B. Zajamsek. Beamforming array optimisation and phase averaged sound source mapping on a model wind turbine. In Inter-Noise and Noise-Con Congress and Conference Proceedings, volume 249, pages 1078–1086. Institute of Noise Control Engineering, 2014.
- [156] Z. Prime, C. Doolan, and B. Zajamsek. Beamforming array optimisation and phase averaged sound source mapping on a model wind turbine. In Inter-Noise and Noise-Con Congress and Conference Proceedings, volume 249, pages 1078–1086. Institute of Noise Control Engineering, 2014.

- [157] S. Pröbsting and S. Yarusevych. Laminar separation bubble development on an airfoil emitting tonal noise. Journal of Fluid Mechanics, 780:167–191, 2015.
- [158] J. W. S. B. Rayleigh. The theory of sound, volume 2. Macmillan, 1896.
- [159] L. F. Richardson and J. A. Gaunt. The deferred approach to the limit. Philosophical Transactions of the Royal Society of London. Series A, containing papers of a mathematical or physical character, 226(636-646):299–361, 1927.
- [160] P. J. Roache. Quantification of uncertainty in computational fluid dynamics. Annual review of fluid Mechanics, 29(1):123–160, 1997.
- [161] M. Roger and S. Moreau. Broadband self noise from loaded fan blades. AIAA Journal, 42(3):536–544, 2004.
- [162] M. Roger and S. Moreau. Back-scattering correction and further extensions of amiet’s trailing-edge noise model. part 1: theory. Journal of Sound and Vibration, 286(3):477–506, 2005.
- [163] L. Rossian, B. W. Fassmann, R. Ewert, and J. Delfs. Prediction of porous trailing edge noise reduction using acoustic jump-conditions at porous interfaces. In 22nd AIAA/CEAS Aeroacoustics Conference, page 2920, 2016.
- [164] L. Rossian, R. Ewert, and J. Delfs. Evaluation of acoustic jump conditions at discontinuous porous interfaces. In 23rd AIAA/CEAS Aeroacoustics Conference, page 3505, 2017.
- [165] A. Rubio Carpio, F. Avallone, D. Ragni, M. Snellen, and S. van der Zwaag. Mechanisms of broadband noise generation on metal foam edges. Physics of Fluids, 31(10):105110, 2019.
- [166] S. G. Saddoughi and S. V. Veeravalli. Hot-wire anemometry behaviour at very high frequencies. Measurement Science and Technology, 7(10):1297, 1996.
- [167] R. Sandberg and L. Jones. Direct numerical simulations of low reynolds number flow over airfoils with trailing-edge serrations. Journal of Sound and Vibration, 330(16):3818–3831, 2011.
- [168] R. Sandberg, L. Jones, and N. Sandham. Direct numerical simulations of noise generated by turbulent flow over airfoils. In 14th AIAA/CEAS Aeroacoustics Conference (29th AIAA Aeroacoustics Conference), page 2861, 2008.
- [169] R. D. Sandberg and N. D. Sandham. Direct numerical simulation of turbulent flow past a trailing edge and the associated noise generation. Journal of Fluid Mechanics, 596:353–385, 2008.

- [170] M. Sanjosé, C. Méon, S. Moreau, A. Idier, and P. Laffay. Direct numerical simulation of acoustic reduction using serrated trailing-edge on an isolated airfoil. In 20th AIAA/CEAS Aeroacoustics Conference, page 2324, 2014.
- [171] E. Sarradj. Three-dimensional acoustic source mapping with different beamforming steering vector formulations. Advances in Acoustics and Vibration, 2012, 2012.
- [172] E. Sarradj and T. Geyer. Noise generation by porous airfoils. In 13th AIAA/CEAS Aeroacoustics Conference (28th AIAA Aeroacoustics Conference), page 3719, 2007.
- [173] E. Sarradj, C. Fritzsche, and T. Geyer. Silent owl flight: bird flyover noise measurements. AIAA Journal, 49(4):769–779, 2011.
- [174] J. Schepers, A. Curvers, S. Oerlemans, K. Braun, T. Lutz, A. Herrig, W. Wuerz, A. Mantecanz, L. Garcillan, M. Fischer, et al. Sirocco: silent rotors by acoustic optimisation. In Second International Meeting on Wind Turbine Noise, Lyon, France, volume 2021, 2007.
- [175] R. Schlinker and R. Amiet. Helicopter rotor trailing edge noise. In 7th Aeroacoustics Conference, page 2001, 1981.
- [176] J. H. Seo and Y. J. Moon. Aerodynamic noise prediction for long-span bodies. Journal of Sound and Vibration, 306(3-5):564–579, 2007.
- [177] P. Sijtsma. Clean based on spatial source coherence. International Journal of Aeroacoustics, 6(4):357–374, 2007.
- [178] J. Smagorinsky. General circulation experiments with the primitive equations: I. the basic experiment. Monthly Weather Review, 91(3):99–164, 1963.
- [179] O. Stalnov, P. Chaitanya, and P. F. Joseph. Towards a non-empirical trailing edge noise prediction model. Journal of Sound and Vibration, 372:50–68, 2016.
- [180] C. Tam and N. Reddy. Sound generated in the vicinity of the trailing edge of an upper surface blown flap. Journal of Sound and Vibration, 52(2):211–232, 1977.
- [181] C. K. Tam. Discrete tones of isolated airfoils. the Journal of the Acoustical Society of America, 55(6):1173–1177, 1974.
- [182] C. Van Dam, D. L. Kahn, and D. E. Berg. Trailing edge modifications for flatback airfoils. SAND2008-1781, Sandia National Laboratories, Albuquerque, NM, 2008.
- [183] W. C. van der Velden and S. Oerlemans. Numerical analysis of noise reduction mechanisms on improved trailing edge serrations using the lattice boltzmann method. In 35th Wind Energy Symposium, page 1379, 2017.

- [184] W. C. van der Velden, A. van Zuijlen, and D. Ragni. Flow topology and noise emission around straight, serrated and slitted trailing edges using the lattice boltzmann methodology. In 22nd AIAA/CEAS Aeroacoustics Conference, page 3021, 2016.
- [185] J. Van Doormaal and G. Raithby. Enhancements of the simple method for predicting incompressible fluid flows. Numerical heat transfer, 7(2):147–163, 1984.
- [186] A. Vathylakis, T. P. Chong, and P. F. Joseph. Poro-serrated trailing-edge devices for airfoil self-noise reduction. AIAA Journal, 53(11):3379–3394, 2015.
- [187] A. Vathylakis, C. C. Paruchuri, T. P. Chong, and P. Joseph. Sensitivity of aerofoil self-noise reductions to serration flap angles. In 22nd AIAA/CEAS Aeroacoustics Conference, page 2837, 2016.
- [188] C. Wagner, T. Hüttl, and P. Sagaut. Large-eddy simulation for acoustics, volume 20. Cambridge University Press, 2007.
- [189] M. Wang and P. Moin. Computation of trailing-edge flow and noise using large-eddy simulation. AIAA Journal, 38(12):2201–2209, 2000.
- [190] J. F. Williams and L. Hall. Aerodynamic sound generation by turbulent flow in the vicinity of a scattering half plane. Journal of Fluid Mechanics, 40(4):657–670, 1970.
- [191] J. Winkler, S. Moreau, and T. Carolus. Large-eddy simulation and trailing-edge noise prediction of an airfoil with boundary-layer tripping. In 15th AIAA/CEAS Aeroacoustics Conference (30th AIAA Aeroacoustics Conference), page 3197, 2009.
- [192] J. Winkler, S. Moreau, and T. Carolus. Airfoil trailing edge noise prediction from large-eddy simulation: influence of grid resolution and noise model formulation. In 16th AIAA/CEAS Aeroacoustics Conference, page 3704, 2010.
- [193] W. R. Wolf and S. K. Lele. Trailing-edge noise predictions using compressible large-eddy simulation and acoustic analogy. AIAA Journal, 50(11):2423–2434, 2012.
- [194] W. R. Wolf, J. L. F. Azevedo, and S. K. Lele. Convective effects and the role of quadrupole sources for aerofoil aeroacoustics. Journal of Fluid Mechanics, 708: 502–538, 2012.
- [195] T. Wu and L. Lee. A direct boundary integral formulation for acoustic radiation in a subsonic uniform flow. Journal of sound and vibration, 175(1):51–63, 1994.
- [196] Q. Yang and M. Wang. Boundary-layer noise induced by arrays of roughness elements. Journal of Fluid Mechanics, 727:282–317, 2013.
- [197] Y. Yauwenas, B. Zajamšek, J. Reizes, V. Timchenko, and C. J. Doolan. Numerical simulation of blade-passage noise. the Journal of the Acoustical Society of America, 142(3):1575–1586, 2017.

-
- [198] B. Zajamsek, C. J. Doolan, D. J. Moreau, J. Fischer, and Z. Prime. Experimental investigation of trailing edge noise from stationary and rotating airfoils. the Journal of the Acoustical Society of America, 141(5):3291–3301, 2017.
- [199] B. Zajamsek, Y. Yauwenas, C. J. Doolan, K. L. Hansen, V. Timchenko, J. Reizes, and C. H. Hansen. Experimental and numerical investigation of blade–tower interaction noise. Journal of Sound and Vibration, 443:362–375, 2019.